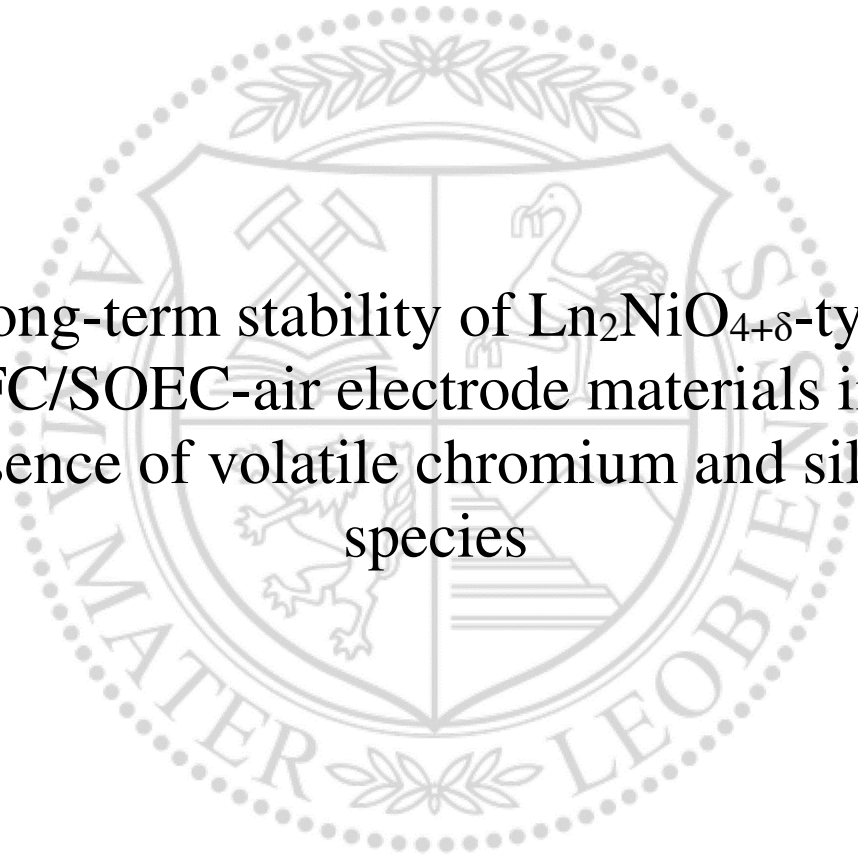Chair of Physical Chemistry

Doctoral Thesis

# Long-term stability of $Ln_2NiO_{4+\delta}$-type SOFC/SOEC-air electrode materials in the presence of volatile chromium and silicon species

Dipl.-Ing. Nina Schrödl, BSc

March 2019

## Eidesstattliche Erklärung

Ich erkläre an Eides statt, dass ich diese Arbeit selbständig verfasst, andere als die angegebenen Quellen und Hilfsmittel nicht benutzt, und mich auch sonst keiner unerlaubten Hilfsmittel bedient habe.

Ich erkläre, dass ich die Richtlinien des Senats der Montanuniversität Leoben zu "Gute wissenschaftliche Praxis" gelesen, verstanden und befolgt habe.

Weiters erkläre ich, dass die elektronische und gedruckte Version der eingereichten wissenschaftlichen Abschlussarbeit formal und inhaltlich identisch sind.

## Affidavit

I declare on oath that I wrote this thesis independently, did not use other than the specified sources and aids, and did not otherwise use any unauthorized aids.

I declare that I have read, understood, and complied with the guidelines of the senate of the Montanuniversität Leoben for "Good Scientific Practice".

Furthermore, I declare that the electronic and printed version of the submitted thesis are identical, both, formally and with regard to content.

Date 06.03.2019

Signature author
Nina Schrödl
Matriculation number: 00430109

# Acknowledgement

Last but not least I would like to thank my family and especially my partner Robert for continuously supporting me in all my endeavors.

# Abstract

This dissertation examines the long-term stability of $Ln_2NiO_{4+\delta}$-type rare earth nickelates with respect to their application as oxygen electrode materials in solid oxide fuel and electrolyzer cells. Special emphasis is put on electrode poisoning caused by volatile Cr- and Si-compounds, which is a well-known degradation mechanism that significantly shortens the operating-life of solid oxide cells.

Several long-term experiments on dense samples and porous electrodes were conducted to investigate the detrimental effects of Cr- and Si-poisoning.

The long-term stability was assessed by monitoring the oxygen exchange kinetics on dense nickelate samples using the dc-conductivity relaxation (CR) technique, as well as by measuring the area specific resistance of porous electrodes by means of electrochemical impedance spectroscopy (EIS).

Dense samples of $La_2NiO_{4+\delta}$ (LNO) were tested at 700°C and 800°C for subsequent periods of 1000 h in dry and humidified oxygen/argon atmospheres, with and without the presence of a Cr- and a Si-source. Changes in surface morphology and chemistry were analyzed using atomic force microscopy, X-ray photoelectron spectroscopy, scanning electron microscopy with energy dispersive X-ray spectroscopy and high-resolution scanning transmission electron microscopy with energy dispersive X-ray and electron energy loss spectroscopy.

LNO demonstrates excellent stability under dry conditions even when a Cr-source is present. Increasing the humidity of the surrounding $O_2$/Ar gas mixture, however, results in a rapid decline of the chemical surface exchange coefficient ($k_{chem}$) of oxygen, which could be attributed to the decomposition of LNO into several secondary phases at the sample surface.

Cr-poisoning was tested under realistic SOEC/SOFC operating conditions on symmetrical button cells with LNO, $Pr_2NiO_{4+\delta}$ (PNO) and $LNO-Ce_{0.9}Gd_{0.1}O_{2-\delta}$ (LNO-GDC) composite electrodes at 800°C under open current conditions as well as under current load. Similar to the experiments on dense samples the cells were subjected to dry and humidified $O_2$/Ar gas mixtures for periods of several hundred hours, with and without Cr being present.

Additionally, cell tests with reference electrodes were conducted to investigate the influence of electrode polarization on Cr-poisoning. Extensive post-test analyses were performed using SEM- and STEM-EDX-EELS. The performance of all cells remained stable under dry conditions, even under current load. However, with humidity and in presence of Cr the cell performance degraded and the polarization resistance contribution of one electrode increased significantly. EIS-measurements and post-test analyses revealed a correlation between Cr-deposition and electrode performance.

# Kurzfassung

Im Rahmen dieser Dissertation wurde die Langzeitstabilität von Seltenerdnickelaten des $Ln_2NiO_{4+\delta}$-Strukturtyps im Hinblick auf die Anwendung als Sauerstoffelektrode in Festoxidbrennstoffzellen und -elektrolyseuren untersucht. Der Schwerpunkt der Studie wurde hierbei auf die Vergiftung der Sauerstoffelektrode durch flüchtige Cr- und Si-Verbindungen gelegt, welche einen bekannten Degradationsmechanismus darstellt, der die Lebensdauer von Festoxidzellen deutlich herabsetzt.

Mehrere Langzeitexperimente an dichten Proben und porösen Elektroden wurden durchgeführt, um die schädlichen Einflüsse der Cr- und Si-Vergiftung zu untersuchen. Die Langzeitstabilität wurde einerseits anhand der Sauerstoffaustauschkinetik, die mittels Leitfähigkeitsrelaxationsmessungen an dichten Proben bestimmt wurde, und andererseits durch Aufzeichnung des flächenbezogenen, elektrischen Widerstands poröser Elektroden mittels elektrochemischer Impedanzspektroskopie (EIS) charakterisiert.

Dichte $La_2NiO_{4+\delta}$ (LNO)-Proben wurden für jeweils 1000 h bei 700°C und 800°C in trockener und befeuchteter Sauerstoff/Argon-Atmosphäre mit und ohne Cr-Quelle getestet. Änderungen der Oberflächenmorphologie und -chemie wurden mittels Rasterkraftmikroskopie, Röntgenphotoelektronenspektroskopie, Rasterelektronen- mikroskopie mit energiedispersiver und hochaufgelöster Rastertransmissionselektronenmikroskopie in Kombination mit energiedispersiver Röntgen- und Elektronenenenergieverlustspektroskopie untersucht.

LNO weist eine hervorragende Stabilität in trockener Gasatmosphäre, auch in Gegenwart einer Cr-Quelle, auf. Wird das umgebende $O_2/Ar$-Gasgemisch jedoch befeuchtet, nimmt der chemische Oberflächenaustauschkoeffizient des Sauerstoffs ($k_{chem}$) enorm ab, was auf die Zersetzung von LNO in mehrere chemische Verbindungen an der Probenoberfläche zurückgeführt werden konnte.

Weiters wurde die Cr-Vergiftung unter für Festoxidbrennstoffzellen und -elektrolyseure realistischen Betriebsbedingungen an symmetrischen Knopfzellen mit LNO, $Pr_2NiO_{4+\delta}$ (PNO) und $LNO$-$Ce_{0.9}Gd_{0.1}O_{2-\delta}$ (LNO-GDC) Kompositelektroden bei 800°C untersucht. Dabei wurden die Zellen unter konstanter Stromlast gehalten. Die Zellen wurden in jeweils für mehrere hundert Stunden trockener, befeuchteter und Cr-hältiger Gasatmosphäre ausgesetzt. Bei den Zelltests konnte durch den Einsatz einer Referenzelektrode ein Einfluss der Elektrodenpolarität auf die Cr-Vergiftung bestimmt werden. Nach den elektrochemischen Messungen wurden die Zellen mit elektronenmikroskopischen Methoden untersucht. Der gemessene Zellwiderstand aller Zellen blieb in trockener Atmosphäre über mehrere hundert Stunden stabil. Befeuchtung des Testgases in Gegenwart einer Cr-Quelle führte jedoch zu einem Anstieg des Polarisationswiderstands einer der beiden Elektroden, was zu einem sich ebenfalls im Anstieg des gesamten Zellwiderstands äußerte. Durch die Kombination von EIS-Messungen mit Post-Test Analysen konnte eine Korrelation zwischen der Cr-Abscheidung und dem Elektrodenwiderstand nachgewiesen werden.

# Table of contents

# 1  Introduction

The increase in energy consumption due to the continuous growth of the world's population has initiated concerns about climate change and limited fossil fuel deposits and has led to an increasing share of renewable energy sources, like wind and solar power, in energy production. The intermittent nature of these energy sources causes an imbalance between electricity supply and demand, creating the necessity for energy storage on a large scale to provide a stable power grid. Solid oxide fuel cells and electrolyzers are highly efficient, low emission energy conversion devices, which can provide a valuable link between energy production and demand. Surplus electricity from renewable resources or conventional energy production during low demand hours can be converted into hydrogen via e. g. high-temperature electrolysis and stored or redistributed into the natural gas grid. The production of hydrogen in solid oxide electrolysis cells (SOECs) can be highly efficient, especially if the required thermal energy can be provided by excess heat from existing power plants or industrial factories. Stored hydrogen, on the other hand, can be easily converted into electricity via a solid oxide fuel cell (SOFC) during times of high energy demand in a decentralized setting [1]. At the moment hydrogen production via water electrolysis is not economically competitive in comparison to conventional methods like steam reformation of methane, due to the high price of grid electricity. It is, however, one of the most environmentally friendly and sustainable ways to produce hydrogen.

## 1.1  Fuel cells

Fuel cells are highly efficient devices, which continually and directly convert chemical into electrical energy as long as reactants are supplied. The physical principle behind the fuel cell was contemporaneously discovered by the British physico-chemist Sir William Robert Grove [2] and the German chemist Christian Friedrich Schönbein [3] between 1839 and 1842, while performing electrolytical experiments in aqueous acidic solutions. In the simplest case, hydrogen gas as fuel and oxygen from the air as oxidant react according to the following chemical equation

$$H_2 + \frac{1}{2} O_2 \rightarrow H_2O \qquad\qquad 1.1$$

In a fuel cell, the electrons, which are exchanged in this hydrogen oxidation reaction are separated and driven through an external circuit to provide useful work. In order to utilize the transferred electrons, the hydrogen combustion reaction must be split into two electrochemical half reactions.

$$H_2 \leftrightarrow 2H^+ + 2e^-$$ 1.2

$$\frac{1}{2}O_2 + 2H^+ + 2e^- \leftrightarrow H_2O$$ 1.3

In the first half-reaction (eq. 1.2) hydrogen gas is oxidized to hydrogen ions giving two electrons per mole of hydrogen gas, which are used in the second reaction (eq. 1.3) to reduce oxygen under the formation of water. The terms oxidation and reduction refer to the removal and addition of electrons from or to a species, respectively.

In many ways fuel cells are comparable to batteries, as the internal structure and function are practically identical. Fuel cells consist of two electrodes, i.e. anode and cathode, which are electronically conducting, porous structures providing an electrocatalytically active surface for the reactions occurring in the fuel cell. By definition, the anode is the electrode where oxidation reactions occur while on the cathode reduction reactions take place. Both electrodes are in contact with a purely ion conducting material, the electrolyte, which allows for the aforementioned separation of the oxidation and the reduction reaction. Electrode reactions are not limited to the examples presented above. The exact nature of the oxidation and the reduction reaction depends on the type of fuel cell, or rather the employed electrolyte.

In general, fuel cells are classified based on the type of electrolyte and the resulting operational conditions that are applied. Table 1.1 provides an overview of the operating characteristics of the five most common types of fuel cells. Fuel cells are also commonly categorized into low-temperature (T < 250°C) and high-temperature (500 ≤ T/°C ≤ 1000) devices.

*Table 1.1: Most common types of fuel cells [4].*

| Type | Electrolyte | Typical operating temperature /°C | Charge carrier | Fuel | Catalyst |
|---|---|---|---|---|---|
| Polymer electrolyte membrane fuel cell (PEMFC) | Polymer membrane | 80 | $H^+$ | $H_2$, methanol | Platinum |
| Phosphoric acid fuel cell (PAFC) | Immobilized $H_3PO_4$ | 200 | $H^+$ | $H_2$ | Platinum |
| Alkaline fuel cell (AFC) | Immobilized KOH | 60-220 | $OH^-$ | $H_2$ | Platinum |
| Molten carbonate fuel cell (MCFC) | Molten carbonate | 650 | $CO_3^{2-}$ | $H_2$, $CH_4$ | Nickel |
| Solid-oxide fuel cell (SOFC) | Ceramic | 600-1000 | $O^{2-}$ | $H_2$, $CH_4$, CO | Perovskites, Nickel |

The low-temperature fuel cells, which include the PEMFC, the PAFC and the AFC, are usually operated with pure hydrogen, emitting only water vapor as exhaust gas. With the exception of the PEMFC these fuel cell types use fairly inexpensive electrolyte materials. However, due to the low activity for the hydrogen oxidation in this temperature range, expensive noble metal catalysts like Pt must be applied, which significantly contribute to the overall cost of fuel cells. In addition, the use of Pt makes this fuel cells susceptible to sulfur and carbon monoxide poisoning, which limits the fuel options to pure hydrogen. In the high-temperature regime, however, alcohols, hydrocarbons or carbon monoxide can also serve as fuel, which results in the co-emission of carbon dioxide. Although the emission of $CO_2$ seems to somewhat contradict the ecologically beneficial aspects of the technology, fuel cells directly convert chemical into electrical energy with high efficiency, as opposed to mechanical energy in the case of a combustion engine, thus producing comparatively lower $CO_2$ emissions. Furthermore, using renewable hydrocarbons from fermented biomass (e.g. bio methane, methanol, ethanol) as fuel is considered to be $CO_2$ neutral, since the produced $CO_2$ was originally consumed by the growing biomass. An efficiency comparison to other current energy conversion technologies is provided in Fig. 1.1.
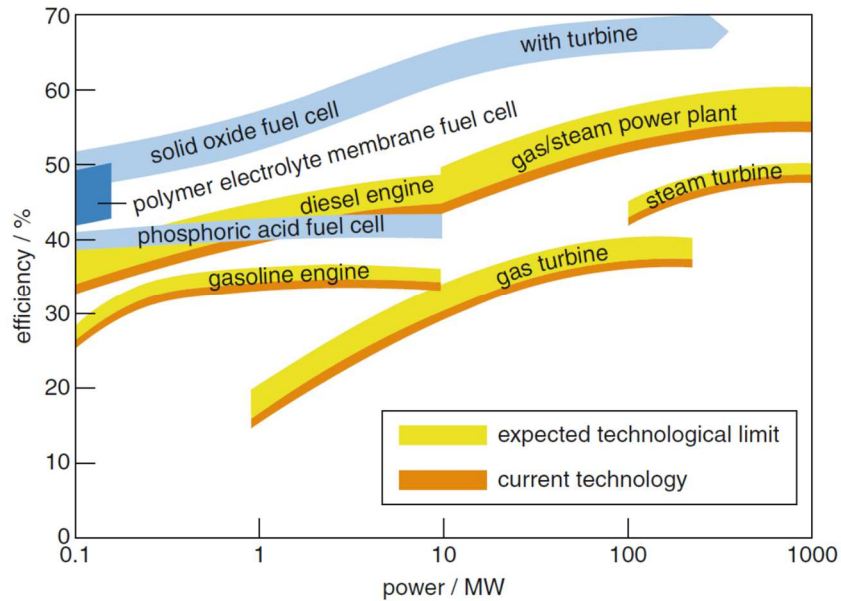
*Fig. 1.1: Efficiency vs. power for fuel cells and other energy conversion technologies [5].*

## 1.2 Solid oxide fuel cells

The following paragraphs provide a short introduction to the function and materials for solid oxide fuel cells (SOFCs). Since this work focuses on devices using oxygen ion conductors, the proton-conducting solid oxide fuel cells are not discussed here.

Generally, SOFCs can be categorized based on operating temperature into low- (500 – 650°C), intermediate- (650°C – 800°C) and high-temperature (800 – 1000°C) devices [6]. In contrast to other fuel cell types, the main components in SOFCs are solid state ceramic materials. The electrolyte is comprised of a dense, oxygen-conducting ceramic, whereas the electrodes feature high porosity to allow for efficient gas transport and a large reactive surface. High operating temperatures are necessary to achieve sufficient ionic and electronic conductivity in solid electrolytes and electrodes. In contrast to the earlier described PEMFC, the oxygen reduction reaction takes place at the cathode. Molecular oxygen is reduced to $O^{2-}$ ions and transported across the electrolyte to the anode where hydrogen is oxidized, and water is formed. The functional principle of a SOFC is illustrated in Fig. 1.2.
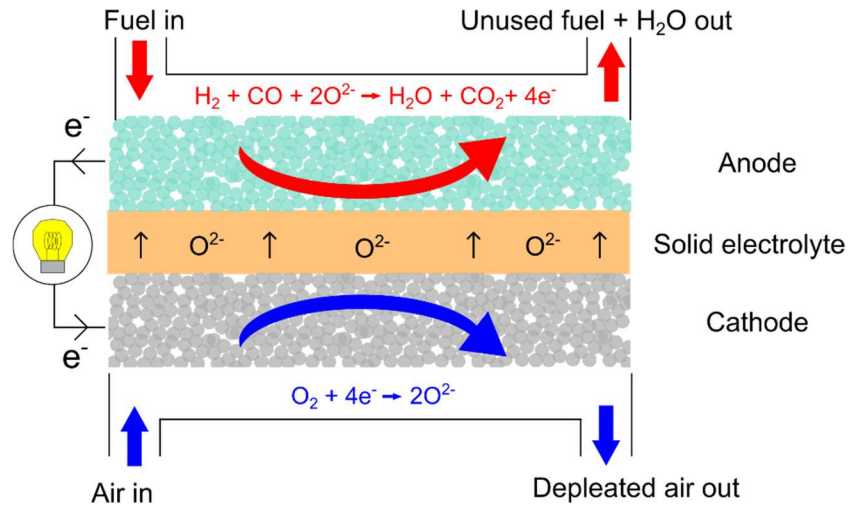
*Fig. 1.2: Working principle of an SOFC.*

The main advantage of SOFCs over other fuel cells is their ability to use hydrogen as well as carbon-based fuels [7], which allows for a wide range of stationary [8-10] and mobile applications [11-13]. Due to the high operating temperatures, methane and even higher hydrocarbons can be reformed internally to hydrogen and carbon-monoxide, which act as fuel gas for the anode reaction [14]. The occurring reactions are summed up below.

| | | |
|---|---|---|
| Anode | $H_2 + O^{2-} \leftrightarrow H_2O + 2e^-$ | 1.4 |
| | $CO + O^{2-} \leftrightarrow CO_2 + 2e^-$ | 1.5 |
| Cathode | $\frac{1}{2}O_2 + 2e^- \leftrightarrow O^{2-}$ | 1.6 |
| Overall reactions | $H_2 + \frac{1}{2}O_2 \leftrightarrow H_2O$ | 1.7 |
| | $CO + \frac{1}{2}O_2 \leftrightarrow CO_2$ | 1.8 |

In most cases SOFCs are fabricated either as flat sheets or tubes. Additionally, cells can be designed as self-supporting, whereby one of the cell components is fabricated as support structure to provide the required mechanical stability. Alternatively, an external support (interconnect) is used. Fig. 1.3 depicts a selection of SOFCs with different support structures.
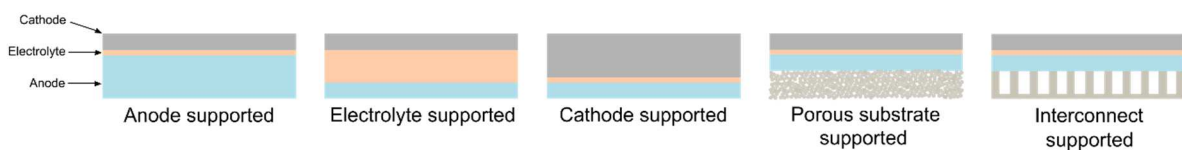


*Fig. 1.3: SOFC cell designs with different support structures.*

The cell design is to some extend based on the desired operating temperature, i.e. an electrolyte-supported cell has to be operated at higher temperatures to minimize ohmic losses than an anode-supported cell [14]. Alternatively, one of the electrodes might serve as scaffold, which allows for the application of a thin electrolyte layer. However, in the case of the anode, re-oxidation of the anode-material might lead to structural damage, and thicker cathodes and anodes might introduce polarizations due to mass transport limitations. Since a single fuel cell only provides a voltage of approximately 1 V, several flat or tubular cells are assembled and connected in series in a so-called fuel cell stack. Interconnect plates act as an electrical connection between neighboring cells and, in the case of a planar fuel cell stack, also as separation between reducing and oxidizing atmospheres. A good interconnect material is required to provide high electrical conductivity, microstructural, chemical, thermal and mechanical stability, imperviousness for oxygen and hydrogen, a comparable thermal expansion coefficient to the electrode material. Additionally, it should be low-cost and easy to manufacture [6]. Despite the high cost, lanthanum-chromite-based interconnects are usually used in high-temperature SOFC applications. Partial substitution of La with Mg, Ca or Sr significantly enhances the electronic conductivity of the material.

In recent years efforts have been made to lower SOFC operating temperatures to an intermediate temperature regime where metallic alloys can be used as interconnect material [15]. Metallic interconnect materials are preferable due to their mechanical strength, high thermal and electrical conductivity. A significant disadvantage of metals is their stability towards oxidation under SOFC operating conditions. Therefore, only alloys, which form continuous, protective oxide scales are suitable for SOFC applications [6]. Cr-based or -containing alloys with a minimum Cr-content of 15-25 wt-% provide the required oxidation stability while maintaining sufficient electrical conductivity [16]. Nevertheless, excessive growth and subsequent spallation of chromia scales, as well as volatilization of Cr, can severely impact long-term stack performance.

### 1.2.1 Electrolyte materials for SOFCs

Suitable electrolyte materials for SOFCs are good oxygen ion conductors with negligible electronic conductivity, which can be sintered to dense ceramic layers to prevent the mixing of fuel and oxidant gases. Ideally, electrolyte materials should be chemically stable under high temperatures and varying oxygen partial pressures and inert towards other cell components [17]. The most commonly used materials are stabilized $ZrO_2$ and doped $CeO_2$. Both ceramics possess the fluorite structure, which can occur in monoclinic, tetragonal or cubic symmetry [6,18,19]. The highest oxygen conductivity in this material is achieved via stabilization of the cubic lattice by adding dopants such as $Y_2O_3$, CaO or $Sc_2O_3$. The substitution of Zr by aliovalent

dopants leads to an increase in oxygen vacancies as presented in eq. 1.9 in Kröger-Vink notation.

$$Y_2O_3 \rightarrow 2Y'_{Zr} + 3O_O^x + V_O^{\cdot\cdot} \hspace{4cm} 1.9$$

The highest achievable conductivity in yttria stabilized $ZrO_2$ (YSZ) is reached at a concentration of 8 mol-% $Y^{3+}$. Higher dopant concentrations lead to trapping of oxygen vacancies by negatively charged defects, which effectively limits the mobility of oxygen vacancies [19]. Scandia stabilized $ZrO_2$ (ScSZ) shows higher ionic conductivity compared to YSZ [20,21]. A disadvantage of stabilized $ZrO_2$ electrolytes is their tendency to react with almost all cathode materials, which results in the formation of electrically insulating phases, e.g. $La_2Zr_2O_7$ or $SrZrO_3$ [22,23].

To avoid undesired side reactions with electrode materials, a thin, dense layer of doped $CeO_2$, which also exhibits the cubic fluorite structure, is usually applied between the cathode and a zirconia-based electrolyte [24,25]. Doped ceria can only be used as electrolyte in the low-temperature range (below 600°C), because at higher temperatures and low oxygen partial pressures (fuel side) the $Ce^{4+}$ cations are partially reduced to $Ce^{3+}$, which results in a non-negligible electronic conductivity. Thus, cells with a pure ceria electrolyte suffer from losses due to current leakage, if operated at temperatures above 600°C in atmospheres with low oxygen partial pressures [6].

Similar to zirconia-based electrolytes, partial substitution of $Ce^{4+}$ ions by aliovalent rare earth elements (e.g. Sm, Gd), increases the oxygen vacancy concentration (see eq. 1.10). The highest ionic conductivity in this material can be achieved by choosing a dopant with similar ionic radius to $Ce^{4+}$ [26].

$$Gd_2O_3 \rightarrow 2Gd'_{Ce} + 3O_O^x + V_O^{\cdot\cdot} \hspace{4cm} 1.10$$

Another type of electrolyte material is based on the perovskite structure. The chemical formula of perovskites is $ABO_3$, where A is a 12-fold and B a 6-fold coordinated cation. In general, perovskites are mixed ionic and electronic conductors (MIEC) and are therefore more suitable as cathode materials. As electrolyte the most promising compound of this category is Sr and Mn doped $LaGaO_3$ (LSGM) [6]. While the ionic conductivities of LSGM and doped ceria are similar, LSGM exhibits superior stability at low oxygen partial pressures, and does not form secondary phases with electrode materials. However, secondary phase formation during preparation and interdiffusion of ions between both electrodes and LSGM has been reported [27,28].

### 1.2.2 Anode materials for SOFCs

SOFC anodes provide the reaction sites for the oxidation of hydrogen and the formation of water, which not only requires good electronic and ionic conductivity, but also sufficient porosity to ensure fast transport of reactants and products to and from the active sites of the electrode. In addition to the thermal, chemical, and mechanical stability criteria for ceramic fuel cell components, SOFC anodes also have to show exceptional stability against carbon and sulfur deposition [6,29]. The selection of an appropriate anode material is to a large extent determined by the fuel used to operate the fuel cell. The most common anode material for pure hydrogen fuel is a Ni-YSZ cermet, which is fabricated using NiO and YSZ particles [30]. NiO is reduced in-situ to Ni metal during the first operation with hydrogen, which results in additional porosity. In this composite anode Ni provides electronic conductivity, as well as the catalytic properties for the $H_2$ oxidation. YSZ serves as structural support and substrate for the separation of the Ni particles, which otherwise would agglomerate at high temperatures over time. Additionally, YSZ provides oxygen ion conductivity, which allows for oxygen transport the reaction sites within the anode, as well as excellent adhesion to the electrolyte [29]. The main degradation issues of Ni-YSZ anodes are coarsening and re-oxidation of the Ni-particles [31,32], in case the fuel supply is interrupted. Despite the many advantages of Ni-YSZ anodes, they are not well suited for carbon-containing fuels, due to carbon formation on Ni-particles [33]. Sulfur-containing fuel contaminants tend to adsorb to Ni-particles [34-36], which partially inactivates the anode. However, sulfur-poisoned anodes can be almost completely regenerated by removing the sulfur-source [34]. Carbon deposits can be formed by catalytical decomposition of $CH_4$, by reaction of CO with $H_2$ or disproportionation of CO (Boudouard reaction) [6]. The deposited carbon blocks the catalytically active sites of the anode and has to be avoided. Carbon formation can be suppressed by adding large amounts of steam to the fuel gas by operating the fuel cell at high current densities, which increases the amount of produced water in the anode [37]. In order to avoid carbon formation completely alternative anode materials have been proposed in the literature, e.g. perovskite ceramics like La-doped $SrTiO_3$ [38,39] or replacing Ni with Cu in YSZ-based cermets [40,41]. However, Cu shows a tendency towards agglomeration [41] and a significantly reduced catalytic activity for the hydrogen oxidation [40,42]. Also, addition of precious metals to Ni-anodes seems to improve carbon stability [43].

### 1.2.3 Cathode materials for SOFCs

Cathode materials should exhibit high activity for the oxygen reduction reaction, as well as high electronic and ionic conductivity to minimize the resistance contribution of the cathode

to the total cell resistance. Furthermore, good cathode materials should be chemically compatible with the used electrolyte to prevent the formation of poorly conducting compounds at the electrolyte-cathode interface. To avoid the delamination of the cathode from the electrolyte, the thermal expansion coefficient of both materials should be within a similar range [6].

The majority of suitable cathode materials are members of the perovskite structure family. Strontium-doped lanthanum manganate (LSM) is the most common cathode material for high-temperature SOFCs [44]. The rather poor electronic conductivity of pure $LaMnO_3$ can be enhanced via partial substitution of $La^{3+}$ with a lower valence cation, e.g. alkaline earth metal ions (e.g. $Ca^{2+}$, $Sr^{2+}$), which leads to the formation of an electric hole on the Mn-ion (p-type conductivity). The electronic conductivity of $La_{1-x}Sr_xMnO_3$ varies with Sr content, with a maximum at the composition x=0.5 [45]. Due to the negligible ionic conductivity of LSM the oxygen reduction reaction is limited to the electrode-electrolyte interface in a pure LSM electrode. Therefore, LSM is almost exclusively used in conjunction with a good ionic conductor like YSZ in a composite-electrode, which dramatically increases the triple phase boundary where cathode, electrolyte and gas phase intersect [46,47]. LSM tends to form zirconate phases with YSZ at high temperatures, especially during sintering, but also during long-term operation, which significantly reduces cathode performance over time [22,48,49]. However, the formation of zirconates can be effectively suppressed by using A-site deficient LSM [50,51]. The performance of LSM-YSZ composite electrodes is satisfactory in the high temperature regime, however, below 800°C cathode materials with higher catalytical activity are necessary to overcome the increased polarization resistances at lower operating temperatures [6]. This can be accomplished by increasing the active surface area in the cathode, either by using nanocrystalline composite electrodes or by employing materials, which feature ionic and electronic conductivity, which effectively extends the triple phase boundary to the entire surface of the cathode [52]. MIECs like $La_{1-x}Sr_xCoO_{3-\delta}$ (LSC) have been considered as a highly active substitute for LSM in the intermediate- to low temperature regime [53,54]. In LSC the substitution of $La^{3+}$ by $Sr^{2+}$ enhances oxygen ion conductivity as well as electronic conductivity via the formation of electron holes as well as oxygen vacancies. A severe disadvantage of LSC is the large TEC mismatch to most electrolyte materials, which can result in electrode delamination [54] and the chemical reactivity with YSZ (zirconate formation) [55]. Moreover, LSC tends to Sr-segregation and thus, decomposition of the active cathode material at SOFC operating temperatures [56-59].

Sr-doped $LaFeO_3$ [60,61] has been proposed as a more chemically stable, but also less active alternative to LSC. Sr substitution on the A-site introduces negatively charged defects, which are compensated by oxygen vacancies or $Fe^{4+}$ ions. Similar to LSC, this leads to an increase in

electronic and ionic conductivity. Further advantages of LSF are a lower TEC and its significantly lower reactivity with $ZrO_2$ in comparison to LSC [62,63]. However, LSF can incorporate $Zr^{4+}$ into the B-site of the perovskite structure, which leaves an A-site depleted material with lower conductivity [62-64].

The A- and B-site doped $La_{1-x}Sr_xCo_{1-y}Fe_yO_{3-\delta}$ (LSCF) exhibits a lower TEC than pure LSC, as well as lower reactivity with YSZ [6]. The B-site substitution of Co with Fe, results in a lowered electronic conductivity in comparison to pure LSC. Despite being less reactive with YSZ, a ceria interlayer between LSCF cathode and $ZrO_2$-base electrolyte is still necessary. LSCF shows superior electrode performance as cathode in the intermediate temperature regime [65] and can be further improved by composite formation with electrolyte material [52,66] or by infiltration with nanoparticles [67,68]. However, similar to LSC, LSCF also exhibits Sr-segregation, which can result in reduced long-term stability [69-73].

A Sr-free alternative to the aforementioned perovskites are $Ln_2NiO_{4+\delta}$ rare earth nickelates (Ln = La, Pr, Nd) with $K_2NiF_4$-structure. This structure type features $LnNiO_3$ perovskite layers alternating with Ln-O rock salt layers. Without the need for dopants rare earth nickelates incorporate additional oxygen atoms and feature high ionic and sufficiently electronic conductivities to be employed as cathode materials in SOFCs [74,75]. In contrast to perovskite materials, ion conductivity in these structures mainly takes place via oxygen interstitials within the rock salt layers of the crystal structure [76]. $La_2NiO_{4+\delta}$ (LNO), $Pr_2NiO_{4+\delta}$ (PNO) and $Nd_2NiO_{4+\delta}$ (NNO) have been investigated as promising cathode materials [24,75,77-83]. PNO cathodes exhibit the lowest area specific resistances [83] but lack thermodynamic stability at temperatures above 700°C [84-86]. Nickelates have been reported to be thermally compatible with YSZ and GDC [74,87,88], however, studies indicate a chemical reactivity of LNO, PNO and NNO with YSZ and GDC [89,90].

## 1.3 Solid oxide electrolyzer cells

Solid oxide electrolyzer cells (SOECs) can be described as SOFCs, which are operated in reverse mode, i.e. decomposing water vapor into hydrogen and oxygen gas using electricity. Since water splitting is a strongly endothermic non-spontaneous reaction, it is advantageous to perform electrolysis at elevated temperatures in order to decrease overpotentials. While the total energy demand for the decomposition of steam is almost temperature independent, the electrical energy demand decreases dramatically with increasing operating temperature. Therefore, SOECs can reach efficiencies of approximately 90% [91], especially if residual heat

from power plants or factories is available to evaporate water and to contribute to steam preheating. The ideal operating temperature is within the range of 700 – 900°C [92].

Solid oxide electrolyzers can also be employed to directly convert $CO_2$ into $CO$. However, the electrolysis of pure $CO_2$ is disadvantageous as it requires even more energy than water splitting, due to the high stability of the $CO_2$ molecule. Moreover, carbon deposition on the SOEC cathode causes rapid performance degradation in cells, as a result of disproportionation of $CO$ into $CO_2$ and carbon. A summary of the most important electrode reactions occurring during $H_2O$ and $CO_2$ electrolysis is given below.

| | | |
|---|---|---|
| Cathode | $H_2O + 2e^- \leftrightarrow H_2 + O^{2-}$ | 1.11 |
| | $CO_2 + 2e^- \leftrightarrow CO + O^{2-}$ | 1.12 |
| Anode | $O^{2-} \leftrightarrow \frac{1}{2} O_2 + 2e^-$ | 1.13 |
| Overall Reaction | $H_2O \leftrightarrow H_2 + \frac{1}{2} O_2$ | 1.14 |
| | $CO_2 \leftrightarrow CO + \frac{1}{2} O_2$ | 1.15 |

Far more energy efficient is the co-electrolysis of $CO_2$ and steam for the in-situ production of synthesis gas ($CO+H_2$). The simultaneous electrolysis of $CO_2$ and steam requires less power than pure $CO_2$ electrolysis, because the reverse water gas shift reaction (eq. 1.16), which occurs as a side reaction, plays a substantial role in the formation of $CO$ [93,94].

$$H_2 + CO_2 \rightarrow H_2O + CO \qquad \Delta H^0_{298K} = 42.1 \text{ kJ mol}^{-1} \qquad 1.16$$

Additionally, the presence of steam effectively suppresses the aforementioned carbon formation on the SOEC anode, which significantly increases the lifetime of SOECs. Co-electrolysis is considered a promising $CO_2$ utilization technique and has the potential to contribute to the reduction of $CO_2$ emissions while providing syn gas, which can be used in the Fischer-Tropsch process to produce synthetic liquid fuels. Liquid hydrocarbons are not only easier to store but also easier to transport than hydrogen. The functional principle of an SOEC is illustrated in Fig. 1.4.

$H_2O + CO_2$ in       $H_2 + CO$ out

$H_2O + CO_2 + 4e^- \rightarrow H_2 + CO + 2O^{2-}$

Cathode

$\downarrow$   $O^{2-}$   $\downarrow$    $O^{2-}$   $\downarrow$   $O^{2-}$   $\downarrow$   Solid electrolyte

Anode

$2O^{2-} \rightarrow O_2 + 4e^-$

Air in       Enriched air out
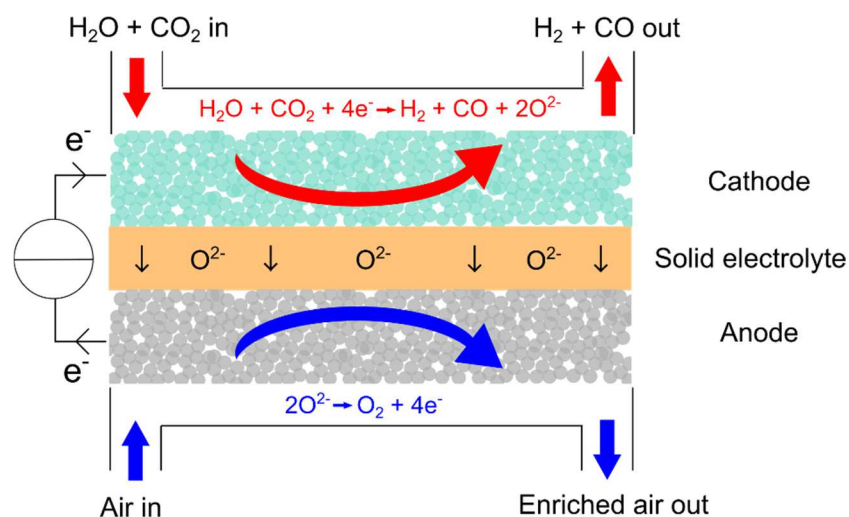
*Fig. 1.4: Functional principle of a solid oxide electrolyzer cell.*

A gas mixture of $CO_2$ and steam is reduced at the cathode to $H_2$ and CO, while $O^{2-}$ ions are transported through the solid electrolyte to the anode where oxygen is formed. Usually, $H_2$ is added to the initial cathode gas mixture to promote CO formation via the reverse water gas shift reaction as well as to suppress cathode re-oxidation. The ceramic materials applied in SOECs are the same as in SOFCs. The most common electrolyte material is YSZ [95,96], but ScSZ [97,98] and LSGM [99,100] have also been investigated. Ceria based electrolyte materials, e.g. GDC and SDC, are only applicable as interlayer between electrolyte and oxygen electrode [101]. The oxygen electrode is often a perovskite type material like LSM or LSCF [102,103]. Most SOEC cathodes are Ni-based cermets, however, due to the susceptibility of Ni to carbon impurities, several perovskite-based materials, e.g. (La, Sr)(Cr, Mn)$O_3$ [104-107], (La, Sr)V$O_3$ [108], $Sr_2Fe_{1.5}Mo_{0.5}O_6$ [109-111] and (La, Sr)Ti$O_3$ [112] have been considered as alternatives.

## 1.4   Scope of this thesis

The aim of this thesis was to investigate the long-term stability of unsubstituted rare earth nickelates against the combined effects of chromium and silicon poisoning with respect to the application in a solid oxide fuel or electrolyzer cell. The first chapter provides a short introduction into the functional principle of fuel cells and describes in more detail the function and components of solid oxide fuel and electrolyzer cells. Chapter 2 starts with the description of factors limiting the lifetime of SOFCs. Additionally, Chapter 2 summarizes the properties of rare earth nickelates and their application as SOFC cathode materials. The last part of Chapter 2 deals with the methods applied for the electrochemical characterization of samples on a material and cell level. Chapter 3 presents in detail procedures used for sample preparation, electrochemical characterization and post-test analyses. The obtained results are shown and

discussed in Chapter 4. Chapter 5 gives a short summary of the results and the main conclusions drawn from the conducted studies. The publications, which originated within the scope of this thesis are attached in the appendix.

# 2 Theoretical background

## 2.1 Electrochemical characterization of air electrode materials

### 2.1.1 Conductivity measurements

The electrochemical properties of dense ceramic samples were investigated via electrical conductivity measurements, which were performed in four contact mode. Two of these contacts are used to apply a constant current, while the other two are operated as current free voltage probes. The contacts are made from Au-wires and Au-paste, due to the inactivity of gold in the oxygen exchange reaction. Two different measurement techniques featuring different contacting schemes and sample geometries were applied in this study (see Fig. 2.1).
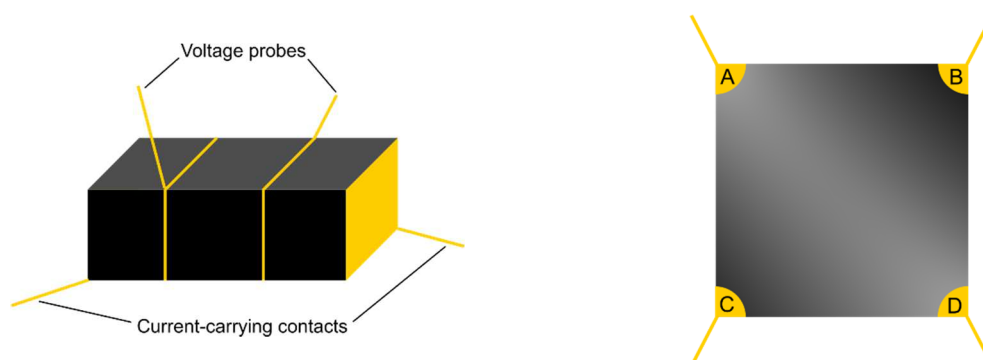


*Fig. 2.1: Bar-shaped sample contacted in linear four-point arrangement (left) and van der Pauw geometry (right).*

#### 2.1.1.1 Linear four-point geometry

For the linear four-point technique the sample is prepared in a rectangular bar shape. The two current-carrying contacts are attached to the smaller faces, whereas the voltage probes are placed in between around the sample circumference at a sufficient distance from the current-sourcing contacts. This is necessary to minimize errors arising from compositional inhomogeneities introduced by direct currents in mixed ionic-electronic conductors when purely electronic contacts are used [113]. The presence of these compositional gradients, which are highest close to the current-carrying contacts, is usually referred to as polarization. At the same time, it is necessary to maintain a sufficiently large distance between the voltage probes to obtain a measurable voltage signal. To accommodate both requirements Dudley and Steele [114] recommend attaching the voltage probes symmetrically at a third of the bar length measured from each end. The electrical conductivity is determined based on the well-known relation

$$\sigma = \frac{1}{R}\frac{d}{A}$$

2.1

with R, A and d denoting the measured resistance in Ω, the cross-section area of the bar-shaped sample in cm$^2$ and the distance between the voltage probes in cm. The resistance value is obtained by measuring several voltages at increasing currents. According to Ohm's law

$$V_d = RI$$

2.2

with I being the applied current and $V_d$ the measured voltage difference between the voltage probes, the resistance is determined from the slope of the current-voltage curve via linear regression analysis.

### 2.1.1.2 Van der Pauw geometry

The second sample geometry used was originally developed by van der Pauw [115] for conductivity and Hall effect measurements. For this technique four contacts are positioned around the outer rim of a thin slab. The thin sample can be of arbitrary shape, provided it features a constant sample thickness and no discontinuities, e.g. isolated holes. Deviations from ideal, point-like electronical contacts lead to errors in the measured conductivity. However, these errors do not exceed 10%, if the radius of each contact remains below one fifth of the sample's radius [113]. In this work, the four contacts, marked as A, B, C, and D in Fig. 2.1, are placed at the corners of a square, flat sample. The electric current is first sourced through contacts A and B, while contacts C and D serve as voltage probes, which provides the resistance labeled as $R_{AB,CD}$. In the next step the contacting arrangement is changed by 90°, i.e. contacts B and C serve as current source and sink, while the potential difference is measured between D and A, providing the resistance $R_{BC,DA}$. Each measurement is performed twice with the direction of the current reversed to account for thermal offsets of the measured voltages. The conductivity is then calculated based on the following relation

$$e^{-\pi d\sigma R_{AB,CD}} + e^{-\pi d\sigma R_{BC,DA}} = 1$$

2.3

Since there is no analytical solution when $R_{AB,CD} \neq R_{BC,DA}$, this equation is solved for σ by numerical methods, with R=$(R_{AB,CD} + R_{BC,DA})/2$ as a starting value.

### 2.1.2 Conductivity relaxation measurements

The dc-electrical conductivity relaxation technique is a useful method to determine the oxygen exchange kinetics in oxide ceramics and was originally described by Dünwald and Wagner [116]. Dense ceramic samples are equilibrated in a quartz glass reactor at a certain temperature and oxygen partial pressure and the conductivity is measured in either linear four-point or van der Pauw geometry. After recording the conductivity until a stable baseline is established, the oxygen partial pressure in the reactor is changed abruptly, which causes the MIEC to release or take up oxygen, depending on the direction of the partial pressure change, until a new equilibrium is reached. In this regard a change to a higher $pO_2$ leads to incorporation of oxygen into the crystal lattice, whereas the decrease in $pO_2$ causes the sample to release oxygen, which corresponds to an oxidation and a reduction step. The change in oxygen content influences the electronic charge carrier concentrations and thus also the electronic conductivity of the sample. Compared to the fast $pO_2$ change, the conductivity response is delayed while the sample relaxes into its new equilibrium state.

The conductivity response is normalized according to

$$\sigma_n = \frac{\sigma(t) - \sigma_0}{\sigma_\infty - \sigma_0} \qquad\qquad 2.4$$

were $\sigma_0$ and $\sigma_\infty$ correspond to the measured conductivities before and after the relaxation process, respectively. Fig. 2.2 depicts the applied oxygen step and the corresponding normalized conductivity response for an oxidation reaction.
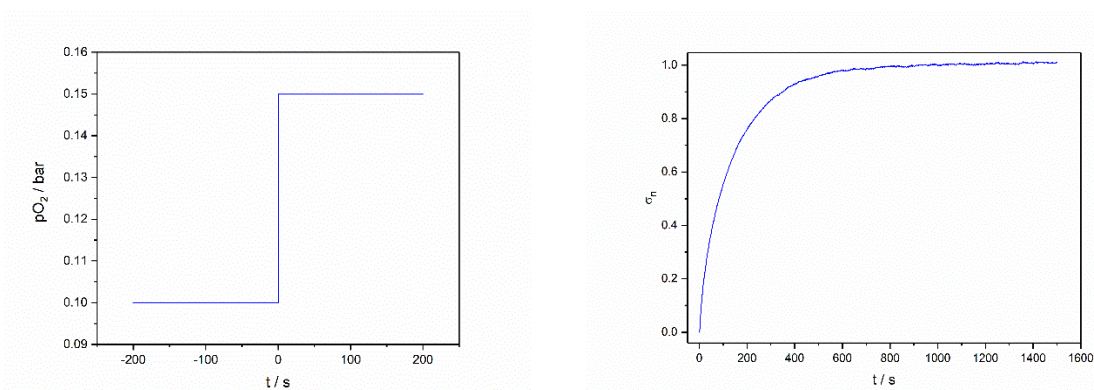


*Fig. 2.2: Ideal oxidative $pO_2$ step (left) and corresponding normalized conductivity response (right).*

The chemical surface exchange ($k_{chem}$) and diffusion coefficients ($D_{chem}$) of oxygen are then extracted by nonlinear least-square fitting of a suitable solution of the diffusion equation to the normalized conductivity transients. The proper solution for the diffusion equation is

selected based on the sample geometry. In van der Pauw arrangement, the oxygen diffusion is restricted to one dimension, whereas in linear four-point geometry oxygen can diffuse in two directions through the sample, as the small faces of the bar-shaped samples are completely covered by gold sheets, which block oxygen diffusion along this direction (see Fig. 2.3).
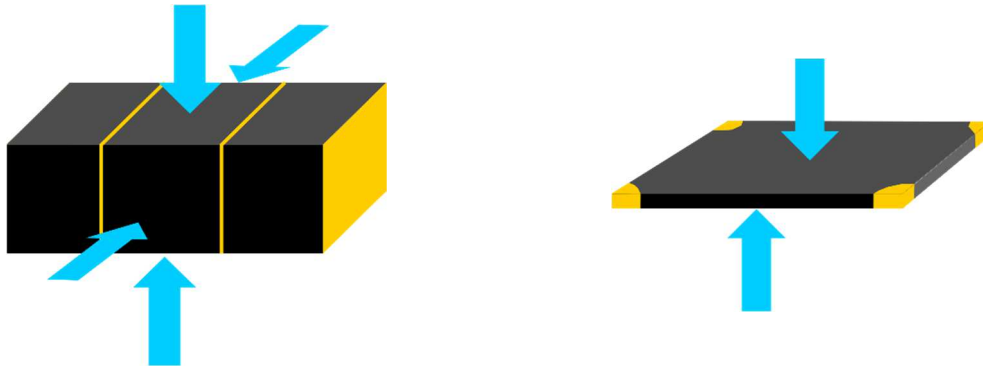


*Fig. 2.3: Possible oxygen diffusion paths through a bar shaped (left) and a van der Pauw sample (right).*

The main advantage of the van der Pauw geometry is that less material is needed for the sample preparation in comparison to the bar-shaped samples used for linear four-point measurements. However, bar-shaped samples can easily be prepared with sufficient thickness to allow for the simultaneous determination of $k_{chem}$ and $D_{chem}$.

### 2.1.3 Oxygen diffusion

Oxygen intake from the gas phase into a dense ceramic is essentially dominated by two main processes connected in series, i.e. the surface exchange and the chemical diffusion within the bulk of the material. The latter can be described by Fick's first law for 1-dimensional diffusion

$$J = -D_{chem}\frac{\partial c}{\partial x}$$
2.5

where J is the oxygen particle flux density and c the concentration of oxygen.

Plugging eq. 2.5 into the continuity equation yields the partial differential equation known as Fick's second law of diffusion.

$$\frac{\partial c}{\partial t} = D_{chem}\frac{\partial^2 c}{\partial x^2}$$
2.6

Here it is assumed that $D_{chem}$ is independent of concentration.

For 1-dimensional diffusion through a sample with the thickness 2a, perpendicular to the sample surface the following boundary conditions can be defined

$$J(a) = -D_{chem} \left. \frac{\partial c}{\partial x} \right|_{x=a} = k_{chem}[c(a) - c_\infty] \qquad 2.7$$

$$J(-a) = -D_{chem} \left. \frac{\partial c}{\partial x} \right|_{x=-a} = -k_{chem}[c(-a) - c_\infty] \qquad 2.8$$

where $c_\infty$ denotes the equilibrium concentration of oxygen after the relaxation.

This linear rate law does not reflect a strict physical relationship and holds true only for small $pO_2$ changes. Ideally, if both surface exchange and diffusion contribute to the conductivity relaxation in roughly the same manner, both kinetic parameters can be obtained simultaneously from the conductivity transient.

However, the relaxation process can also be dominated by the surface exchange reaction or the diffusion within the solid, i.e. the oxygen exchange kinetics is either surface or diffusion controlled, or in other words becomes rate determining.

As a means to distinguish between diffusion, surface and mixed-controlled kinetics Bouwmeester et al. [117] suggested a characteristic sample thickness $L_c$ based on

$$L_c = \frac{RT}{8F^2} \frac{t_e t_{ion} \sigma_{total}}{j_{ex}^0} = \frac{D^*}{k} \qquad 2.9$$

with $t_e$, $t_{ion}$ being the electronic and ionic transfer numbers, $\sigma_{total}$ the electrical conductivity, $j_{ex}^0$ the surface oxygen exchange rate, $D^*$ the tracer diffusion coefficient and $k$ the surface exchange coefficient of oxygen. $L_c$ represents an oxygen membrane thickness at, which surface exchange and diffusion process equally contribute to the conductivity relaxation.

Den Otter et al. [118] adopted this characteristic length scale for conductivity relaxation measurements

$$L_c = \frac{D_{chem}}{k_{chem}} \qquad 2.10$$

From this relation a dimensionless transport number involving half the sample distance is derived

$$L_\alpha = \frac{a k_{chem}}{D_{chem}} \qquad 2.11$$

At L$_\alpha$ values below 0.03 the kinetics are dominated by the surface exchange reaction, whereas at L$_\alpha$ values above 30 the kinetics are shifted to a diffusion-controlled regime. For 0.03 ≤ L$_\alpha$ ≤ 30 the oxygen kinetics is under mixed-control [118].

## 2.2 Electrochemical characterization of cells

### 2.2.1 Current voltage measurements

The standard technique to evaluate the overall performance of a fuel cell is to record a current-voltage (I-V) curve. In general, I-V measurements are conducted by drawing a defined current from the cell, measuring the resulting voltage response and plotting the obtained voltages against the current density. I-V curves are a quick way to determine the performance of a fuel cell, provided that the measurements were performed under steady state conditions, i.e. the voltage can relax to the steady-state value after the current is increased. The cell performance is judged based on the deviation from the theoretical Nernst potential. A schematic representation of an I-V curve is depicted in Fig. 2.4.
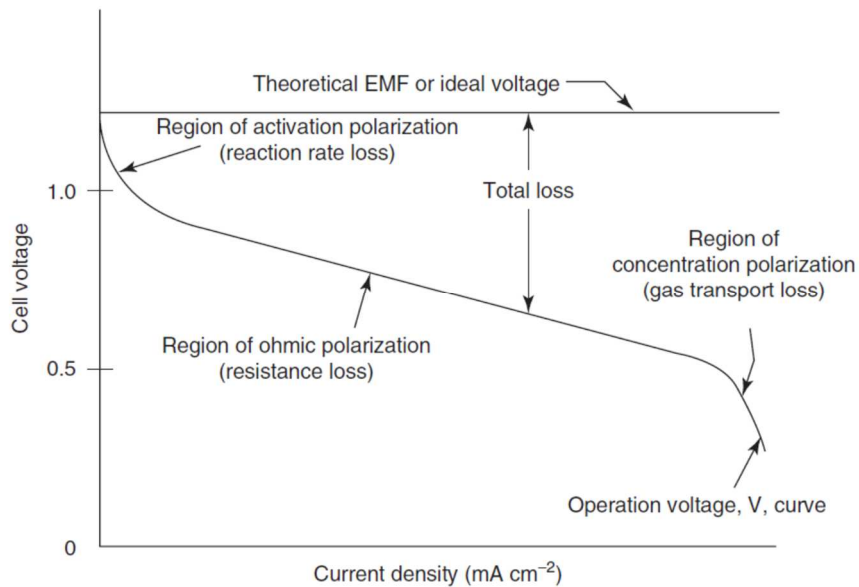


*Fig. 2.4: Schematic I-V-curve of a fuel cell. Image taken from [119].*

The deviations from the ideal potential are called polarization losses or overpotentials. The mathematical description of the I-V-curve is given by

$$V = E^0 - \eta_{ohm} - \eta_{act,anode} - \eta_{act,cathode} - \eta_{conc,anode} - \eta_{conc,cathode} \qquad 2.12$$

where V is the measured voltage, E$^0$ the theoretical Nernst potential, $\eta_{ohm}$, $\eta_{act}$ and $\eta_{conc}$ the losses caused by ohmic, activation and concentration polarization, for both electrodes. At low

19

current densities the I-V curve is dominated by losses due to activation polarization, which are caused by the activation barrier that impedes the electrochemical reaction. Ohmic polarizations govern the mid current density range and are mainly caused by the limited ionic and electronic conduction of the electrode and the electrolyte. At very high current densities the voltage is limited due to insufficient mass transport of reactants to the electrode/electrolyte interface.

In addition to the electrochemical information that can be extracted from an I-V curve, it can also be used to track changes in cell or electrode resistance in long-term stability experiments.

## 2.2.2 Electrochemical impedance spectroscopy

Electrochemical impedance spectroscopy (EIS) is a powerful characterization method for the investigation of electrode processes and transport properties of materials [120]. EIS allows for the separation of the contributions of different processes to the overall resistance in a fuel cell.

### 2.2.2.1 Definition of impedance

Essentially, impedance can be described as a frequency-dependent resistance. Similar to Ohm's law (eq. 2.2), the impedance Z can be defined in terms of a ratio between a voltage and a current, which are both functions of time

$$Z = \frac{V(t)}{I(t)} \qquad\qquad 2.13$$

Usually, the impedance is determined via the application of a sinusoidal excitation voltage with a defined frequency, which can be expressed as

$$V_t = V_0 \sin(\omega t) \qquad\qquad 2.14$$

$$\omega = 2\pi f \qquad\qquad 2.15$$

where $V_t$, $V_0$, $\omega$ and f are the voltage at a time t, the amplitude, radial frequency and the frequency. If the system is linear and time-invariant the resulting current response is recorded, which is also a sinus-wave with the same radial frequency $\omega$, but different amplitude. Unless a purely ohmic resistance is measured the obtained current signal shows a phase shift compared to the excitation signal, which is denoted by the phase angle $\varphi$ in the following expression

$$I_t = I_0 \sin(\omega t - \varphi) \qquad\qquad 2.16$$

where $I_t$ is the current at a given time t and $I_0$ the amplitude of the wave. Combination of eq. 2.13, 2.14 and 2.16 leads to the following expression

$$Z = \frac{V_t}{I_t} = \frac{V_0 \sin(\omega t)}{I_0 \sin(\omega t + \varphi)} = Z_0 \frac{\sin(\omega t)}{\sin(\omega t + \varphi)} \qquad 2.17$$

These relations can also be expressed as complex numbers by applying Euler's relationship

$$e^{j\varphi} = cos\varphi + j\ sin\varphi \qquad 2.18$$

with j being the imaginary number ($j \equiv \sqrt{-1}$), leading to

$$V_t = V_0\ e^{j\omega t} \qquad 2.19$$

$$I_t = I_0 e^{j\omega t - j\varphi} \qquad 2.20$$

Plugging eq. 2.19 and 2.20 into eq. 2.13 results in

$$Z = Z_0 \exp(j\varphi) = Z_0(cos\varphi + jsin\varphi) \qquad 2.21$$

### 2.2.2.2  *Measurement and interpretation of impedance data*

To characterize an electronic or electrochemical system impedance measurements are carried out automatically over many frequencies, ranging from the MHz to the mHz regime. Based on eq. 2.21 the impedance can be represented as vectors in the complex plane with $Z_{Re}=|Z_0|*cos\varphi$ as real and $Z_{Im}=|Z_0|*sin\varphi$ as imaginary part where the phase angle $\varphi$ is defined according to

$$\varphi = arctan\frac{Z_{Im}}{Z_{Re}} \qquad 2.22$$

This type of graphical representation in the complex plane shown in Fig. 2.5 is called an Argand diagram or Nyquist plot.
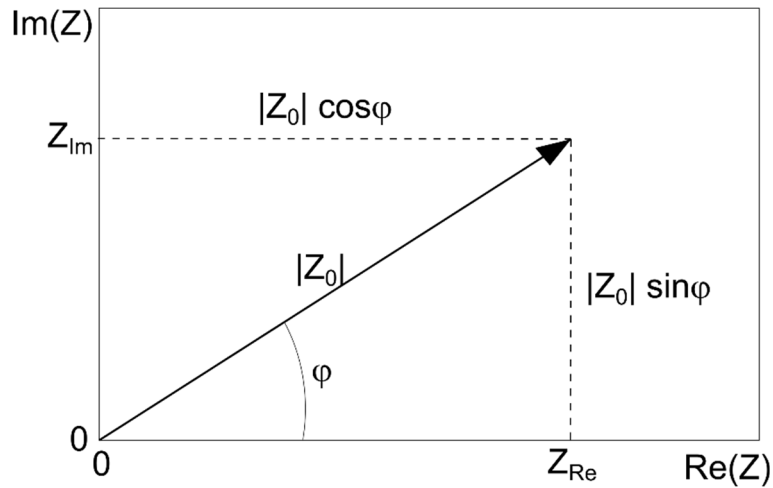
*Fig. 2.5: Complex plane representation of impedance Z plotted as vector.*

Alternatively, impedance data can also be presented as Bode plot, which usually shows the logarithm of the impedance magnitude and the phase angle as a function of the applied AC frequency.

To obtain meaningful impedance results it is crucial that a linear relationship between the electrical excitation and the measured response is established. Most real systems involving chemical reactions are not linear. However, by keeping the excitation voltage or current amplitude small, i.e. below the thermal voltage $V_T$=RT/F=kT/e [121], the system becomes pseudolinear as only a very small portion of the I-V-curve is probed. Therefore, small signal amplitudes, usually between 1 and 20 mV, are chosen. Impedance spectra can be interpreted by applying models based on electrical circuit analogs, which are comprised of passive circuit elements. The most basic passive elements are the resistor, the inductor and the capacitor. Circuit elements should not be chosen arbitrarily to obtain the best fit result with the measured data but should be based on physically meaningful processes taking place in the analyzed system. To obtain a suitable model, the basic circuit elements are connected in series or in parallel and the total impedance is calculated from Kirchhoff's laws. The impedance of two circuit elements connected in series is given by

$$Z = Z_1 + Z_2 \qquad\qquad 2.23$$

In the case of a parallel connection of two circuit elements, the impedance is

$$\frac{1}{Z} = \frac{1}{Z_1} + \frac{1}{Z_2} \qquad\qquad 2.24$$

22

### 2.2.2.3 The ideal resistor

The impedance of the ideal resistor follows Ohm's law (eq. 2.2), is independent of the applied AC voltage frequency and thus has no imaginary component. Simply put, the impedance of an ideal resistor can be expressed as

$$Z = R \tag{2.25}$$

Fig. 2.6 displays the Argand and Bode diagrams for an ohmic resistor of 100Ω. In the complex-plane plot the resistor is depicted as a single dot on the x-axis. Since the impedance only has a real component the resulting current response is always in phase with the applied excitation voltage, i.e. the phase angle amounts to zero.
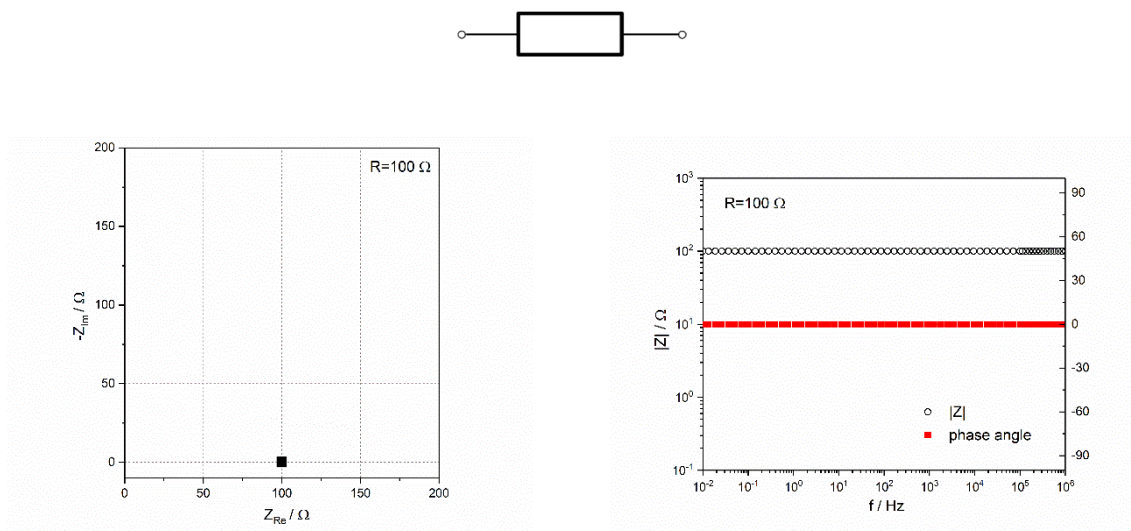




*Fig. 2.6: Argand and Bode diagram for an ohmic resistor of R = 100Ω.*

### 2.2.2.4 The ideal inductor

The ideal inductor can be described as a coil with zero resistance, which produces an electromagnetic force opposed to changes in current. The voltage is directly proportional to the change in current and is given according to

$$V_t = L\frac{dI_t}{dt} \tag{2.26}$$

with L being the inductance in henrys (H). The impedance response of an ideal inductor to a sinusoidal voltage signal is given as

$$Z = j\omega L \tag{2.27}$$

Fig. 2.7 depicts the Argand and Bode diagrams for an inductor with L=1 µH. Given that the impedance of a pure inductor has no real part it can be represented as a straight line along the y-axis in the complex-plane plot. The phase angle is independent of the AC frequency and amounts to +90°. As indicated by eq. 2.27 the impedance of the inductor increases with increasing frequency in the Bode representation.
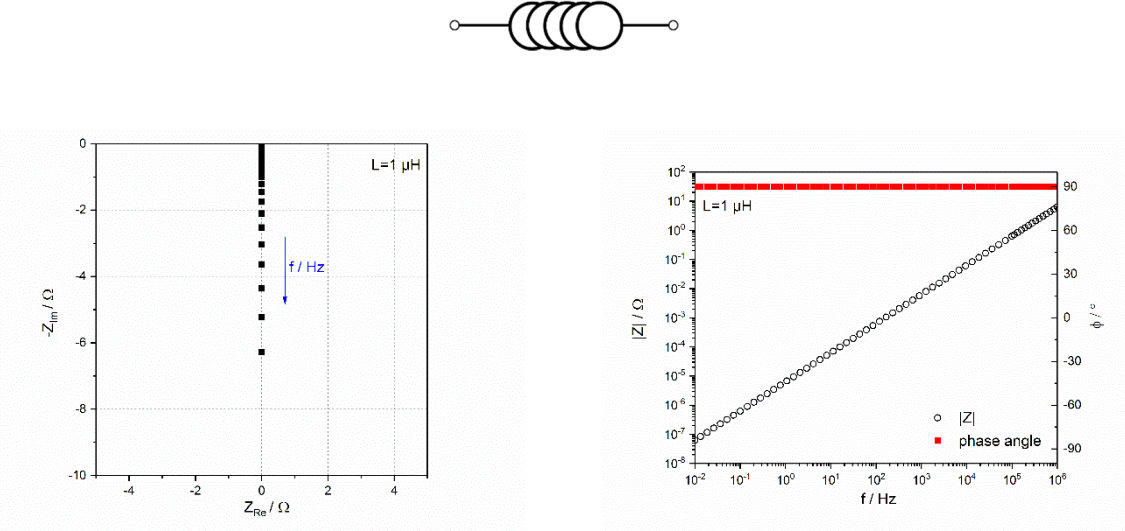




*Fig. 2.7: Argand (left) and Bode (right) diagram for an inductor of L = 1µH.*

### 2.2.2.5   The ideal capacitor

The current-voltage relation for a capacitor can be described by

$$V_t = \frac{Q_t}{C} = \frac{1}{C}\int_0^t I_t dt \qquad\qquad 2.28$$

with Q being the accumulated charge in the capacitor and C the capacitance in farads (F). Ideal capacitors have only an imaginary impedance, which leads to a current phase shift of -90° for the capacitor with respect to the applied voltage signal.

$$Z = \frac{1}{j\omega C} \qquad\qquad 2.29$$

Argand and Bode plots for the basic circuit elements are presented in Fig. 2.8. Similar to the inductor, the impedance of the capacitor is also straight line along the y-axis in the complex-plane plot, but in the opposite direction (see Fig. 2.8). The Bode diagram clearly shows that the impedance of the capacitor decreases with increasing frequency, which is also predicted by eq. 2.29.
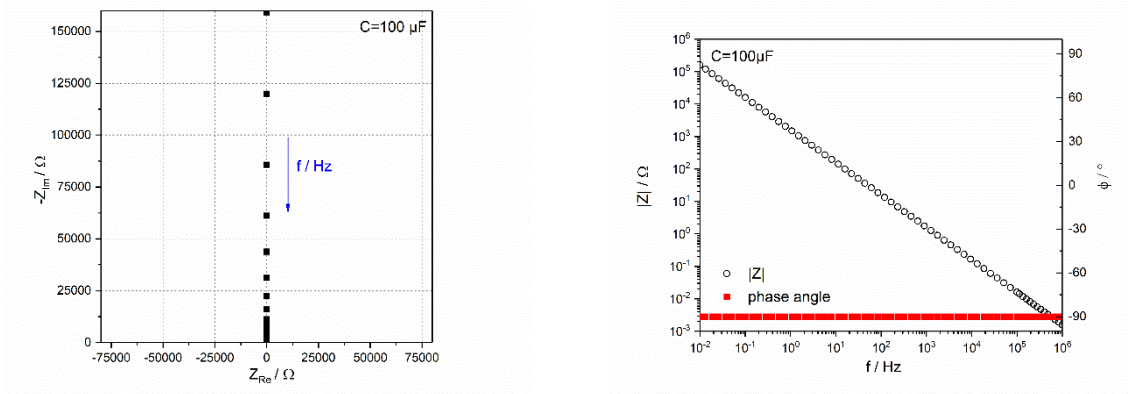
Fig. 2.8: Argand (left) and Bode (right) diagrams of a 100 µF capacitor.

### 2.2.2.6 Constant phase element (CPE)

Due to inhomogeneous current flows in materials, capacitors are often better described by constant phase elements (CPE). The name of this circuit element can be attributed to its AC frequency independent and thus constant phase angle (-απ/2). According to [122] a widespread mathematical expression for the CPE is

$$Z = \frac{1}{Q(j\omega)^\alpha} \qquad\qquad 2.30$$

In general, real electrodes are not uniformly active, due to their microstructure and inhomogeneities in chemical composition [122], and thus distribution of resistances [123]. Porosity [124], rough surfaces [125], defects, but also adsorbed species [126] can lead to a distribution of relaxation times for a single electrode process [121]. However, the physical explanations for the CPE behavior have been heavily disputed in the literature [127-129]. A complex- plane and a Bode plot for the CPE are depicted in Fig. 2.9.

25
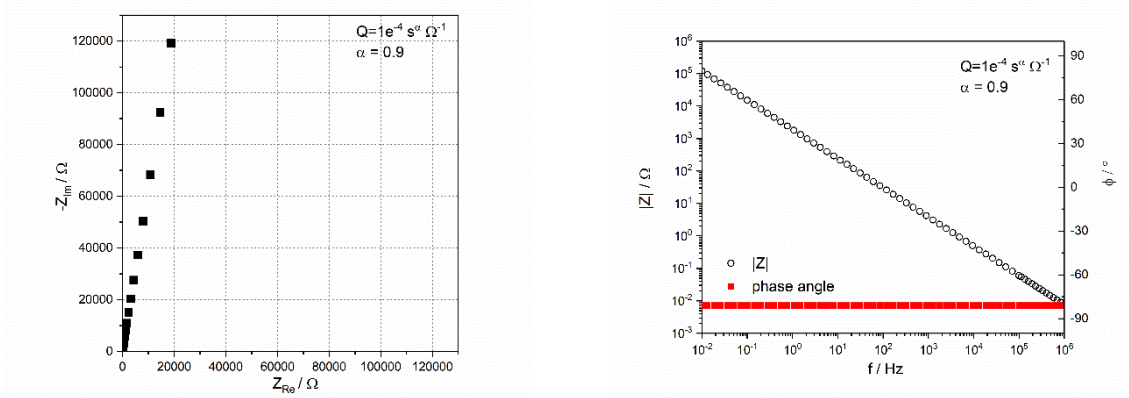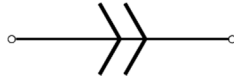
Fig. 2.9: Argand (left) and Bode diagrams (right) for a CPE with $Q=10^{-4}\ s^{\alpha}\ \Omega^{-1}$ and $\alpha=0.9$.

The expression for the impedance response of a CPE is shown in eq. 2.30. In general, the exponent $\alpha$ of a CPE can vary between 0 and 1. Depending on the value of the exponent $\alpha$, the CPE can be used to describe different circuit elements. For $\alpha=1$ the equation yields the impedance of a pure capacitor, whereas for $\alpha=0$ the impedance of an ideal resistor is obtained. In the case of $\alpha=0.5$ the expression simplifies to [130]

$$Z = \frac{1}{Q\sqrt{j\omega}} = \frac{\sigma'}{\sqrt{j\omega}}$$
2.31

which represents the Warburg impedance for semi-infinite diffusion with the mass transfer coefficient $\sigma'=1/Q$ [130]. For n<1 the Q parameter is not equal to the capacity, however, an effective capacity can be determined based on [131,132]

$$C_{eff} = \frac{1}{R}(RQ)^{\frac{1}{\alpha}}$$
2.32

It is important to note that the use of the CPE has certain limitations. As mentioned before the CPE can be used to fit a wide variety of impedance data. However, the physical processes underlying the CPE are not well understood, and it is often applied simply to obtain a better fit, and not necessarily based on a solid, physically meaningful model.

### 2.2.2.7   Warburg impedance (W)

Generally, a Warburg-type impedance occurs when a reaction is limited by mass transport [133]. This type of distributed element was first described by Warburg in 1899 [134] based on Fick's second law for one-dimensional diffusion under the assumption of an infinite diffusion

length. However, diffusion lengths in real electrochemical systems are usually limited. Solutions for a finite diffusion length lead to the more general expression [122]

$$Z = R_W \frac{\tanh \sqrt{\frac{j\omega L^2}{D}}}{\sqrt{\frac{j\omega L^2}{D}}}$$

2.33

which represents the case of a transmissive boundary, i.e. the diffusing species immediately react at the electrode interface [122]. $R_W$, L and D denote the diffusion resistance, the diffusion length and the diffusion coefficient, respectively. Fig. 2.10 shows the complex-plane and Bode plots for the finite length Warburg impedance (eq. 2.33).
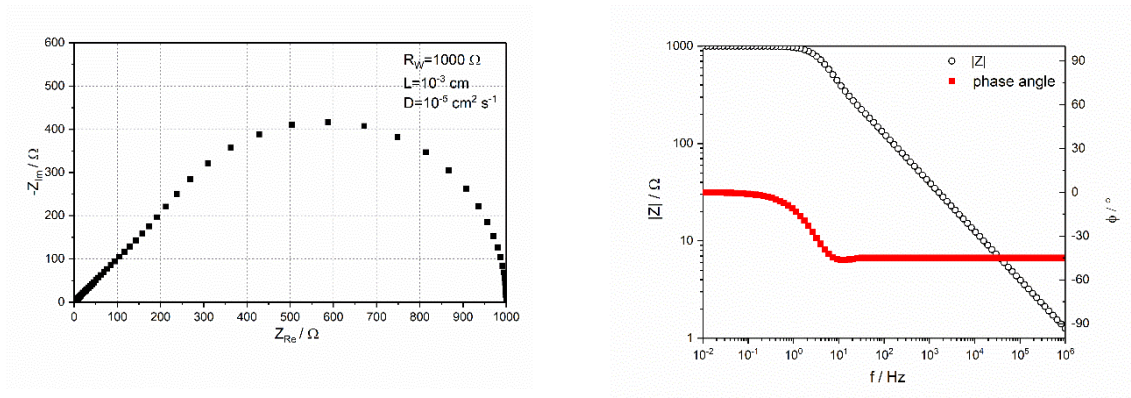




*Fig. 2.10: Argand (left) and Bode diagrams (right) for a finite length Warburg element with $R_W$=1000 Ω, L=$10^{-3}$ cm and D=$10^{-5}$ cm$^2$ s$^{-1}$. Data simulated using ZView [135].*

### 2.2.2.8 Gerischer impedance (G)

Another type of impedance element that is often applied to porous mixed-conducting SOFC cathodes is the Gerischer impedance. A general expression for this type of impedance is [136]

$$Z = \frac{Z_0}{(k + j\omega)^n}$$

2.34

where n is close to 0.5. This type of circuit element, which was originally proposed for an inert electrode in aqueous electrolyte [137], describes the combination of a diffusion process in conjunction with a chemical reaction [136], where the parameter k corresponds to the effective transfer rate of the chemical reaction. Adler et al. [138] proposed a physical model based on microstructural (e.g. porosity and tortuosity) and kinetic parameters for the impedance of mixed ionic and electronic conductors with high ionic conductivity. The resulting

27

impedance can be mathematically expressed as a Gerischer-type impedance. This model has successfully been applied to perovskite electrodes containing Fe and Co but is of limited use for cathode materials with poor ionic conductivity, like LSM [138]. With of a slope of 45° in the high frequency range the Gerischer element bears resemblance to a Warburg impedance (see Fig. 2.11). However, the shape of the arc is different in the low frequency regime.
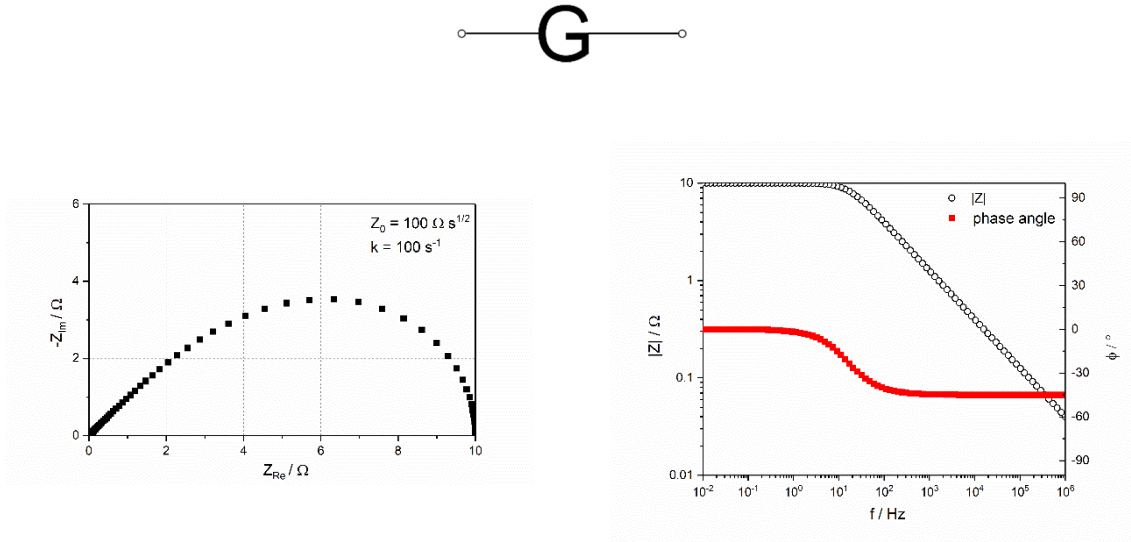




Fig. 2.11: Argand and Bode plots of a Gerischer element with $Z_0$ = 100 $\Omega s^{1/2}$ and k = 100 $s^{-1}$. Data points simulated with ZView [135].

### 2.2.2.9 RC-circuit elements

In the simplest case electrochemical reactions can be approximated by a parallel combination of a resistor and a capacitor, which represent the Faradaic resistance ($R_f$) and the double layer capacitance ($C_{dl}$) at the electrode/electrolyte interface [4]. The Faradaic resistance is the result of the kinetics of the electrochemical reaction, while the double-layer capacitance reflects the charge separation processes at the electrode/electrolyte interface. By combining eq. 2.25, 2.29 and 2.24 the impedance of this resistor-capacitance (R|C) element is given by

$$Z = \frac{1}{\frac{1}{R_f} + j\omega C_{dl}}$$

2.35

Separating the total impedance into a real and an imaginary contribution results in the following expressions [122]

$$Z_{Re} = \frac{R_f}{1 + (\omega R_f C_{dl})^2}$$

2.36

28

$$Z_{Im} = -\frac{\omega R_f^2 C_{dl}}{1 + (\omega R_f C_{dl})^2}$$ 2.37

The corresponding complex-plane and Bode plots for an R|C element featuring a resistor of R=100Ω and a capacitor with C=1µF are depicted in Fig. 2.12.
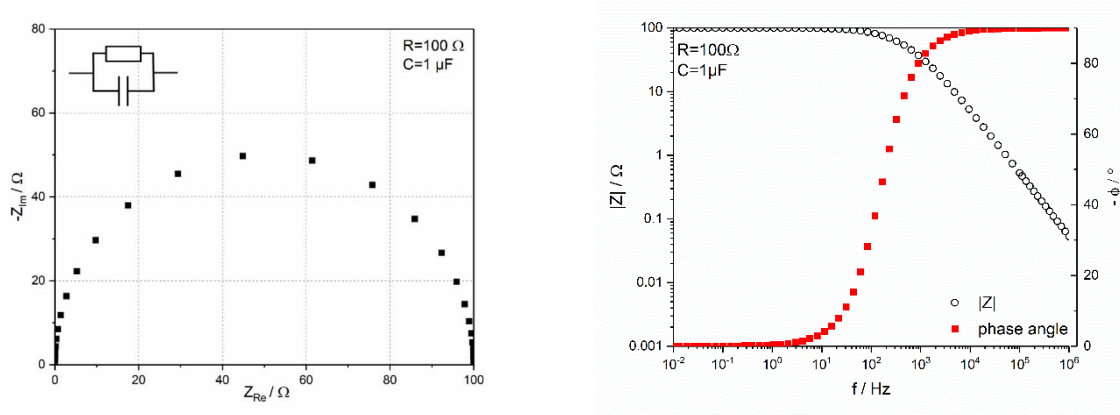


Fig. 2.12: Complex-plane representation with corresponding equivalent circuit (left) and Bode plot of an R|C element with R =100Ω and C=1µF.

Each point in the Argand diagram refers to the impedance at one specific frequency, which increases from right to left in the graph. A more comprehensive representation is provided by a 3-dimensional graph of frequency, real and imaginary part, which is depicted in Fig. 2.13.
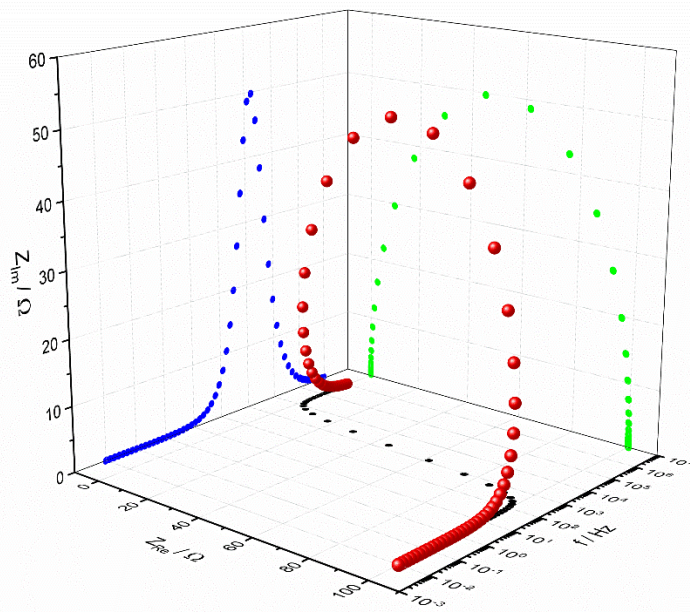


Fig. 2.13: 3-D representation of impedance data of an R|C element with R =100Ω and C=1µF.

The basic R|C element is characterized by a time constant τ, which equals τ=RC. The peak frequency of the impedance arc in the complex plane is also known as the characteristic circular frequency and is calculated according to $\omega_c$=1/τ. Dividing $\omega_c$ by 2π gives the critical relaxation frequency $f_c$.

In the case of a parallel arrangement of a resistor and a capacitor the partitioning of the total current through the two branches, depends on the frequency. The phase angle in the Bode plot indicates that at high frequencies (ω→∞) the impedance is purely capacitive, and the current flows through the capacitor. With decreasing frequency, the impedance of the capacitor increases, thus forcing part of the current through the resistor. At very small frequencies (ω→0) the capacitor completely blocks the current and the impedance is dominated by the resistor. If the impedance response of an R|C element is a perfect semicircle it represents a process with a single time constant. However, if the center of the arc does not fall on the real axis, but rather has a positive imaginary component, the semicircle appears to be depressed. In this case the impedance response includes either more than one process with only slightly different time constants or non-ideal processes with distributed properties. To determine whether there are one or more processes, it is useful to plot the imaginary part of the impedance as a function of the AC frequency f. The existence of multiple processes is indicated by distinct peaks in the imaginary impedance function. Plotting log $Z_{Im}$ vs. log f allows for the identification of non-ideal processes with distributed relaxation times [122,123]. Above the critical relaxation frequency $f_c$ the resulting curve is a straight line (see Fig. 2.14). The slope between the line and the x-axis can be calculated according to

$$\alpha = arctan \frac{\Delta \log Z_{IM}}{\Delta \log f}$$
2.38

If the value of α is equal to 1, which corresponds to a -45° angle in the graph, $Z_{Im}$ reflects the influence of an ideal capacitor, whereas any deviation from this value points towards a single non-ideal process.
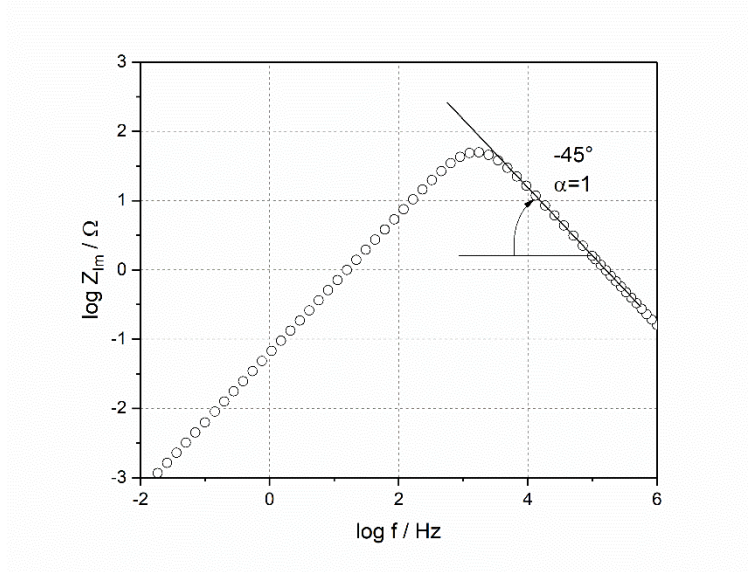
*Fig. 2.14: Log of $Z_{Im}$ vs. log frequency for an R|C element with R =100Ω and C=1µF. Adapted from [122].*

Usually, real systems require the application of more complex circuit elements because real processes show a dispersion of time constants instead of a clearly defined, single time constant.

### 2.2.2.10 R|CPE circuit elements

The CPE is often used instead of the ideal capacitor in a parallel arrangement to a resistor to represent an electrode reaction. Isolating the real and imaginary parts of the impedance of an R|CPE circuit yields [127]

$$Z_{Re} = \frac{R \cdot \left(1 + RQ\omega^{\alpha} \cdot \cos\left(\frac{\alpha\pi}{2}\right)\right)}{1 + 2RQ\omega^{\alpha} \cdot \cos\left(\frac{\alpha\pi}{2}\right) + (RQ\omega^{\alpha})^2} \qquad 2.39$$

$$Z_{Im} = -\frac{R^2 Q\omega^{\alpha} \cdot \sin\left(\frac{\alpha\pi}{2}\right)}{1 + 2RQ\omega^{\alpha} \cdot \cos\left(\frac{\alpha\pi}{2}\right) + (RQ\omega^{\alpha})^2} \qquad 2.40$$

Similar to the R|C equivalent circuit, the R|CPE arrangement also results in a semicircular curve in the complex-plane plot. The effects of the varying exponent α on the impedance are shown in Fig. 2.15. Lowering the α-parameter leads to an apparent suppression of the impedance arc in the Nyquist representation.

31
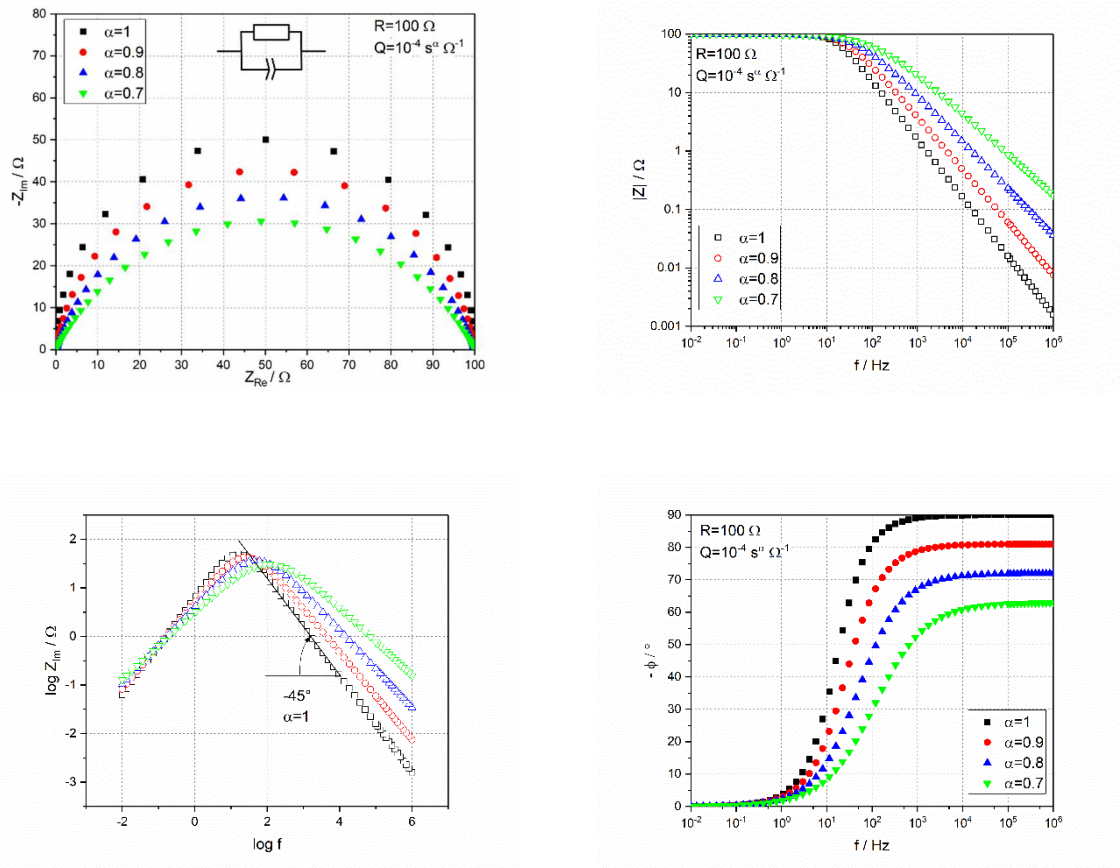
*Fig. 2.15: Nyquist (top, left), Bode (top, right and bottom right) and log $Z_{Im}$ vs log f plots of R|CPE circuits at varying α-values.*

## 2.3   Long-term stability of SOFC cathodes and SOEC anodes

A major obstacle to the application of solid oxide cell technology is the long-term degradation of SOFC and SOEC systems. Minimum operational lifetime targets of approximately 40,000 h for stationary and approximately 10,000 h for mobile SOFC applications are regarded as requirement for successful market entry [139]. Over time, solid oxide cells exhibit performance degradation, which is caused by a deterioration of physical, chemical or mechanical properties of cell components [139,140]. Performance degradation is usually expressed as rate of increasing ASR in single cell tests or as a reduction in power, voltage or efficiency at the stack level. Degradation phenomena are closely related to the applied operating conditions. Microstructural or chemical changes are often caused by abrupt changes in temperature or oxygen partial pressure. Solid oxide cell degradation is a complex issue, which is usually not confined to a single cell component. However, since this thesis is primarily concerned with the long-term stability of oxygen electrodes, the following sections are limited to degradation phenomena occurring in SOFC cathodes and SOEC anodes.

The most common degradation modes are microstructure coarsening, chemical reactions of electrodes with other cell components, decline of ionic or electronic conductivity due to changes in crystal structure or chemical composition, electrode delamination and the chemical reaction of electrode materials with extrinsic impurities [141].

Microstructure coarsening is primarily an issue for composite [142,143] and infiltrated electrodes [144], but has also been reported for Ni-based perovskite electrodes under long-term operation [145] and high current densities [146]. Densification and subsequent delamination of an LSM-YSZ functional layer was observed after electrolyzer operation at high current densities [147].

Sr-doped perovskites show a tendency towards material decomposition due to segregation of Sr to the electrode surface [148-150]. This leads in general to a decrease in ionic and electronic conductivity, as well as less catalytic activity for the oxygen exchange reaction. The minimization of lattice strain and surface charge is commonly regarded as the driving force for Sr-segregation [151]. The Sr-segregation related performance deterioration seems to be enhanced in the presence of moisture [150,152] and has been attributed the loss of Sr due to the formation of volatile hydroxide species [153]. Sr-segregation has been confirmed in cell test under anodic and cathodic bias [59,153,154].

A common problem for oxygen electrode materials is the chemical reactivity with zirconia-based electrolyte materials. LSM tends to form $La_2Zr_2O_7$, whereas LSC and LSCF electrodes form mostly $SrZrO_3$ during the initial sintering, as well as during long-term operation at more moderate temperatures. These reactions can be suppressed via the application of a ceria-based interlayer between electrode and electrolyte. However, Sr interdiffusion can still occur if the ceria layer is porous [155,156]. The application of dense barrier layers can reduce $SrZrO_3$ formation [156-158], yet there are also reports of zirconate formation despite dense GDC layers [159].

Cation interdiffusion between electrode and electrolyte poses another challenge to electrode durability. In the case of LSM, Mn diffusion into YSZ leads to a decrease in conductivity and crack formation [160]. Interdiffusion was also found for LSM and YSZ under SOEC operating conditions and ascribed to enhanced cation migration under anodic polarization [147]. Furthermore, several groups report the formation of $SrZrO_3$ at the interface between electrolyte and barrier layer [153,161,162] in SOEC mode.

Partial or complete delamination of the electrode is often the result of a mismatch in thermal expansion coefficient between cell components [163,164], which manifests as a steep increase in ohmic resistance [163]. However, delamination can also occur due to current cycling or zirconate deposit formation [165,166].

Electrode delamination is the most common failure for pure LSM anodes in SOECs [101] and has been attributed to high oxygen partial pressures at the electrode-electrolyte interface or excess pressure within the electrolyte close to the interface [101,167]. In some studies, the exsolution of LSM nano-particles at the LSM-YSZ contact areas [167,168] and the electroreduction of YSZ [169] have also been identified as a cause for delamination. Generally, delamination seems to be less common for cobaltate-based SOEC anodes. Nevertheless, partial delamination of an LSCF oxygen electrode has been observed after long-term operation at high current densities [166].

The blocking of active reaction sites and the subsequent deactivation of electrode materials by external impurities is commonly referred to as poisoning. The driving force for this type of interaction are acid-base reactions between gaseous, acidic compounds, i.e. HCl, $SO_2$, $CrO_2(OH)_2$, $CO_2$ and $Si(OH)_4$, which react readily with basic oxide compounds, i.e. segregated SrO [139].

$SO_2$ poisoning leading to the formation of $SrSO_4$ has been reported for all Sr-containing electrodes under SOFC and SOEC operation [170-173], although degradation was found to be more pronounced in SOEC mode, when similar cells were tested under anodic and cathodic polarization [174]. $SrSO_4$ formation has also been associated with electrode delamination [173].

### 2.3.1 Chromium-poisoning

One of the most detrimental degradation modes in SOFCs is poisoning of the cathode by chromium phases. The release of volatile Cr-species from metallic interconnects and balance-of-plant components can lead to the formation of Cr-containing deposits [175]. These deposits can damage the oxygen electrode by blocking active sites for the oxygen exchange reaction or by chemically reacting with the electrode material, thus lowering the activity for the oxygen reduction reaction, as well as the electronic conductivity. Nevertheless, the application of metallic interconnects provides several benefits, e.g. the higher electronic conductivity and the cheaper and easier manufacturing of interconnector plates. Ferritic steels with high Cr-content and Cr-based alloys, which form a $Cr_2O_3$ scale that prevents further oxidation, were developed for this purpose. This scale is formed under cathodic and anodic conditions [176]. Hilpert et al. investigated Cr-volatilization via thermodynamic modeling [176]. They found that under dry, oxidative conditions $CrO_3$ is readily formed, whereas under humid conditions a number of Cr-oxyhydrates are released, of which $Cr_2O_2(OH)_2$ is the dominating vapor species. These hexavalent Cr-species are transported via the gas phase to the cathode where they can undergo cathodic reduction according to the following equations

$$CrO_3 + 3e^- \rightarrow \frac{1}{2}Cr_2O_{3(s)} + \frac{3}{2}O^{2-} \qquad\qquad 2.41$$

$$CrO_2(OH)_{2(g)} + 3e^- \rightarrow \frac{1}{2}Cr_2O_{3(s)} + H_2O_{(g)} + \frac{3}{2}O^{2-} \qquad\qquad 2.42$$
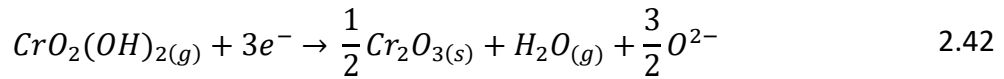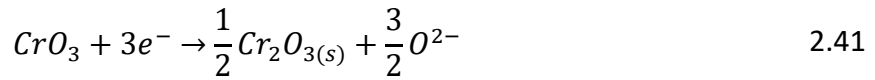
These Cr-species are easily reduced due to the negative Gibbs energy of the reactions, which leads to further vaporization of Cr-species from the interconnect material. Fig. 2.16 shows partial pressures of various Cr(VI) species at different temperatures and levels of humidity as calculated by Hilpert et al. [176].
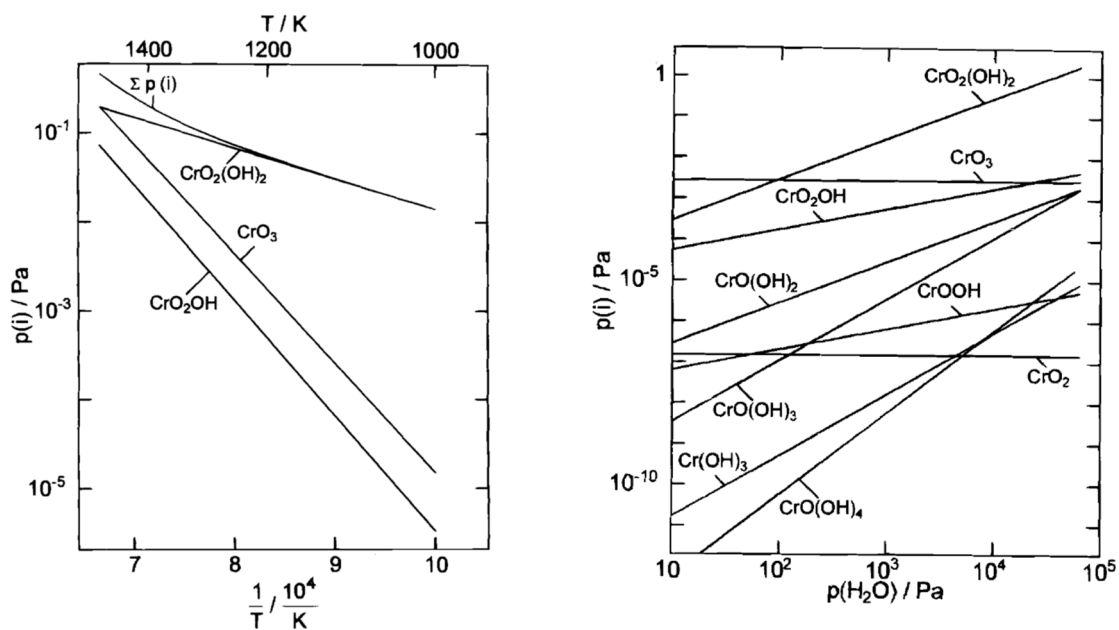


*Fig. 2.16: (Left) Partial pressures of the volatile Cr-species at different temperatures (pO₂ = 2 x 10⁴ Pa, pH₂O = 2 x 10³ Pa) and (right) partial pressured of volatile Cr-species at 1225K at different H₂O partial pressures over Cr₂O₃ scales, taken from [176].*

The vaporization of $CrO_2(OH)_2$ is less dependent on temperature than the release of $CrO_3$. With increasing levels of humidity, the equilibrium vapor pressures of Cr(VI)-oxyhydrates also increase [176,177].

In the literature, numerous reports on the performance degradation of LSM cathodes under Cr-poisoning conditions can be found [178-189]. Zhen et al. investigated Cr-poisoning of pure LSM electrodes on YSZ at 900°C under dry conditions and reported an increase in cathode overpotential over time [178]. Jiang et al. [180] performed button cell tests on LSM-YSZ half cells at 900°C under constant current load in dry atmosphere and found performance degradation under current load, which could be reversed when the current was interrupted. This effect was attributed to the formation of oxygen vacancies under current load, to which

gaseous $CrO_3$ molecules bind via adsorption under polarization [180]. Komatsu et al. found a strong performance degradation of LSM82 electrodes on YSZ electrolytes even at very low current densities, whereas Cr-free cells exhibited low electrode overpotentials at current densities as high as 0.5 $Acm^{-2}$ [182,183]. Park et al reported a rapid decline of the current density of LSM electrodes under constant potential in the presence of a Cr-source, in contrast to Cr-free cells, which showed performance improvement over time [184]. Guan et al. found a direct correlation between the degradation rate of full cells with LSM-YSZ-composite electrodes and the Cr-content in 7-cell stack-tests [185].

In the case of cathode materials, which are predominantly electronic conductors with low oxygen conductivity, e.g. LSM, Cr is accumulated mainly at the triple phase boundary between cathode, electrolyte and gas phase [178-180,182,183,187]. Zhen et al. [178] investigated Cr-poisoning of pure LSM cathodes at 900°C and found significant amounts of Cr-deposits at the electrode after only 20h of testing. Jiang et al. [179,181] reported the formation of Cr-deposit rings on the YSZ-electrolyte along the circumference of LSM electrodes, which grew with time and increasing cathodic potential. SEM-EDXS-analysis of these rings revealed that they were most likely comprised of fine $Cr_2O_3$ crystallites and large, faceted crystals of a $(Cr, Mn)_3O_4$-spinel phase [180,181]. The presence of these phases at the electrode-electrolyte interface was confirmed via XRD-measurements by Komatsu et al. [182]. In contrast, the deposition of Cr in the LSM cathode structure itself is negligible [179,180]. Cr-poisoning experiments by Jiang et al. under anodic and cathodic potential showed that deposit rings are only formed under cathodic potential. Degradation of LSM electrodes under anodic potential resulted in electrode delamination, which was attributed to the evolution of oxygen and subsequent electrode debonding at the triple phase boundary (TPB). However, significant amounts of $Cr_2O_3$, but no signs of Mn were found at the electrolyte. In the absence of cathode polarization, no Cr-deposition occurred at 900°C. After increasing the temperature to 1100°C, however, Cr-species were found [179,181]. The deposition of Cr on LSM electrodes was also demonstrated under anodic polarization, which suggests that the Cr-poisoning mechanism is not solely based on the electrochemical deposition mechanism presented in eq. 2.41 and 2.42 [179,188]. Jiang et al. proposed a reaction mechanism based on the electrochemical reduction of $Mn^{3+}$ to $Mn^{2+}$ under cathodic polarization. The $Mn^{2+}$ species can migrate into the YSZ electrolyte and react with $CrO_3$ to form a Cr-Mn-O species, which acts as nucleation site for further deposition of Cr [179,188]. Ingram et al. [190] investigated button cells with LSM-YSZ composite electrodes in different ceramic housings and found that Cr-gas phase transport is enhanced in the presence of a potassium source. They reported a cell potential drop of 85%/500h in the presence of a metallic interconnect and a K-containing housing.
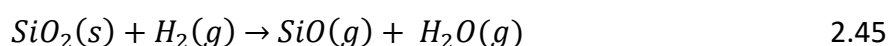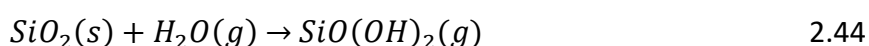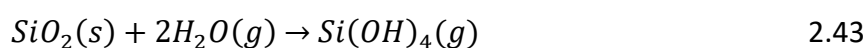
So far, only few Cr-poisoning studies on $K_2NiF_4$-type nickelates have been published in the literature [191-194]. The influence of a sputtered layer of Cr in direct contact with $La_{0.6}Sr_{0.4}CoO_{3-\delta}$ (LSC) and $Nd_2NiO_{4+\delta}$ (NNO) has been investigated by Yang et al. [191] using conductivity relaxation measurements. They found that a 30 nm thick layer of Cr on the NNO surface lead to a decrease in $k_{chem}$ by a factor of 2 in comparison to a fresh, polished sample. The observed decline in surface activity was dramatically less severe in comparison to the tested LSC sample, which indicates a higher stability of NNO against Cr-poisoning. Schuler et al. [192,193] tested symmetrical button cells with $Nd_{1.95}NiO_{4+\delta}$ electrodes at 700°C and 500 $mAcm^{-2}$ in dry and humidified air with a Cr-based alloy as a Cr-source, which had no direct contact to the electrode. EIS-measurements revealed an increase in polarization resistance with time due to Cr-poisoning. In TEM-studies of the degraded cell, the formation of Cr-rich species at the rim of the NNO particles was confirmed. Additionally, Si-rich deposit were also detected, which could be responsible for the detected increase in ASR. Lee et al. [194] studied the effects of different amounts of Cr on $La_2NiO_{4+\delta}$ electrodes after infiltration with a Cr-containing solution, followed by a heat treatment using impedance spectroscopy. They found a rapid increase in polarization resistance when Cr-levels exceeded 0.2%. However, in comparison to similar studies conducted on LSC electrodes, the LNO electrode was significantly less affected by Cr, indicating a higher stability of LNO against Cr-poisoning.

### 2.3.2 Silicon poisoning

Another well-known source of performance degradation in solid oxide cells and stack arrangements is the accumulation of Si in electrolyte and electrode materials. Contrary to Cr-poisoning, which can be significantly reduced by barrier coatings on interconnects and BOP components, Si-contamination can hardly be avoided, because Si is the most abundant impurity in raw material for SOFC components [195-199]. Moreover, Si is sometimes added deliberately to improve sintering and densification [200,201]. Si-impurities in electrolytes tend to segregate to the grain boundaries during sintering process or long-time operation, where they form a continuous and blocking layer surrounding the grains, thus lowering the grain boundary conductivity of the material [195,199,201-205]. Although the amount of Si-impurities in electrolyte materials is generally at the ppm level [195,196,199,204], it was found that Si-levels as low as 50 ppm can significantly increase the grain boundary resistivity in ceria electrolytes [204]. Thermodynamic calculations by de Ridder et al. revealed that Si-concentrations as low as 10 ppm are sufficient to cover the entire surface of a sintered YSZ ceramic with a Si-layer [195]. Additionally, these segregated Si-phases are also formed on the electrode-electrolyte interface and the triple phase boundary in composite electrodes, which could account for the variability in reported electrode resistivities [197,199,206]. Since the use

of highly pure electrolyte powders containing less than 50 ppm of Si is economically unviable pertaining to the commercialization of SOFC stacks, several strategies to diminish the deleterious effects of Si-impurities in electrolyte materials have been proposed in the literature. Among these, tailoring the microstructure [200,207,208] and the incorporation of scavenger compounds, which lead to the formation of Si-inclusions at the triple grain junctions and thus suppress the formation of glass-like layers at the grain boundaries [202,204,209,210] show great promise. In commercially available ceramic powders, Si-impurities are often unintentionally introduced during powder processing procedures, e.g. milling, which are known to severely reduce the performance of SOFC cathodes [198,211,212] and oxygen membranes [213]. In addition to the aforementioned endogenous Si-impurities, Si can also be released from a number of different components in experimental setups or cell stacks. Si can be evaporated from SiC and $MoSi_2$ heating elements [214-216], as well as tube furnace materials [217] in high temperature furnaces used for powder calcination, sintering and contacting of samples. Quartz glass parts in measurement setups have also been reported as a source for exogenous Si-impurities in the literature [58,70,218,219]. Precious metal pastes used for electronic contacts often contain glass compounds, which form a bonding layer between the metal and the oxide ceramic [220-223]. Siloxane based greases and silicone oils for vacuum pumps have also been identified as possible Si-sources in high temperature setups [197,224]. A major Si-source in SOFC stacks are the thermal insulation [225,226], balance of plant components [227] and the glass ceramic seals between interconnects, electrolyte and electrode, which are necessary to separate fuel and oxidant gases in planar stacks [228-232]. $SiO_2$-layer formation under $Cr_2O_3$ scales of interconnect materials, which lead to spallation of the chromia scale have also been reported in the literature [227].

Similar to Cr, Si is present as oxide, i.e. $SiO_2$, under high temperature conditions in oxidizing atmosphere. In water-vapor containing environments silica tends to form volatile hydroxides [233], which can be transported via the gas phase and redeposited on active sites of the electrodes. As high temperature fuel cells are usually operated with ambient air, water is always present on the cathode side. Studies indicate that volatilization and redeposition of silica is negligible in the absence of $H_2O$ [217,219,234]. The reactions most likely to occur under SOFC operating conditions are the following [217,233,235,236]

$$SiO_2(s) + 2H_2O(g) \rightarrow Si(OH)_4(g)$$ 2.43

$$SiO_2(s) + H_2O(g) \rightarrow SiO(OH)_2(g)$$ 2.44

$$SiO_2(s) + H_2(g) \rightarrow SiO(g) + H_2O(g)$$ 2.45

Several studies found that the dominant volatile Si-species at temperatures lower than 1300°C and in the presence of $O_2$ and $H_2O$ is orthosilicic acid ($Si(OH)_4$) [233,235,236]. However, Si-

evaporation rates from BOP components determined by Schuler et al. suggest that other Si-species are also contributing to the gas phase transport of Si [227]. Si-evaporation under reducing conditions according to 2.45 has also been observed [217].

The effects of Si-poisoning on the performance of SOFC cathode materials and oxygen permeation membranes have so far been investigated for (La,Sr)MnO$_3$-YSZ composites [227,237,238], La$_{0.6}$Sr$_{0.4}$CoO$_3$ [219,234], (La,Sr)(Co,Fe)O$_3$ [70,218,224,234,239,240], BaCe$_{0.1}$Co$_{0.4}$Fe$_{0.5}$O$_3$ [213] and Nd$_{1.95}$NiO$_4$ [192,211,212]. Viitanen et al. [224] reported that Si released from siloxane-containing grease used in their measurement setup caused severe performance degradation in LSCF6428 oxygen membranes within 80 minutes of testing. Liu et al. [213] observed a decline in permeation flux of a BaCe$_{0.1}$Co$_{0.4}$Fe$_{0.5}$O$_3$ perovskite oxygen membrane, which was attributed to the formation of Si-containing secondary phases caused by endogenous Si-impurities. Bucher et al. who studied the effects of prolonged Si-contamination on LSCF [58,70,239] and LSC [219,234,241] found a drop in surface activity for the oxygen exchange reaction, which was caused in part by the formation of La-Sr-silicate phases. Perz et al. [240] performed long-term stability tests on a button cell with an LSCF cathode at 700°C and simulated Si-poisoning by applying a 10 nm Si-layer, which led to a steep increase in area specific resistance.

So far only a few publications have addressed the consequences of Si-contamination on rare earth nickelate electrodes. Schuler et al. [192] and Laguna-Bercero et al. [211] found endogenous Si-contamination in NNO cathodes after sintering, which significantly decreased the active surface of the material. Harris et al.[212] investigated NNO cathodes made from powder containing 2-3 at-% Si-impurities using X-ray nanotomography and determined that 20-30 vol% of the electrode contain Si-poisoned degradation phases after sintering, resulting in a decrease of electrochemically active surface of up to 67%.

The aforementioned examples clearly show that Si-poisoning due to both endogenous and exogenous Si-impurities has to be taken into account, considering that the use of high-purity raw materials and pre-dried air in large stack arrangement is not as common as in laboratory measurement setups.


## 2.4   Ln$_2$NiO$_{4+\delta}$- type rare earth nickelates as cathode materials in SOFCs

Ln$_2$NiO$_{4+\delta}$ nickelates (Ln= La, Pr, Nd) adopt the so-called K$_2$NiF$_4$-structure with the general formula A$_2$BX$_4$. This type of crystal structure was originally investigated by Balz und Plieth [242] and contains layers of ABX$_3$ perovskite building blocks intersected with AX rock salt layers. Generally, the ideal, cubic perovskite structure consists of two differently sized cations, A and B, with A-cations positioned on the corners of cube and the B-cation located at the body-

centered position of the cube, which is octahedrally coordinated by 6 X-anions (see Fig. 2.17, left).
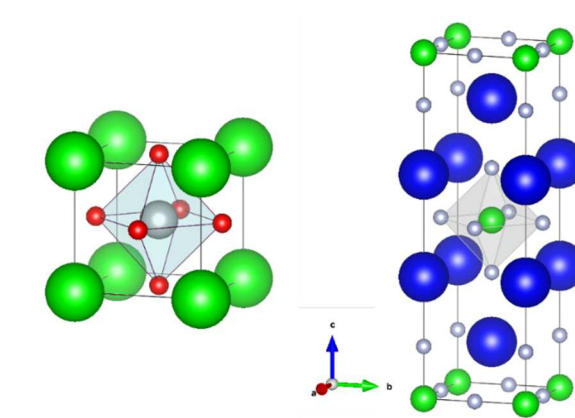


*Fig. 2.17: Crystal structure of the ideal cubic perovskite (left). The A-cations are depicted in green, the B-cation in grey and the anions in red color. Crystal structure of the ideal tetragonal K₂NiF₄-structure (right). The A-cations are shown in blue, the B-cations in green and the anions in grey color. Images generated with VESTA [243].*

The A-cation is usually a main group element, whereas the B-cation is a smaller transition metal. The anion sites can be occupied by oxygen or halides. In reality, perovskite structured materials often are distorted in comparison to the ideal cubic structure. The deviation from the cubic lattice can be expressed by the Goldschmidt tolerance factor t (see eq.2.46) [244].

$$t = \frac{(r_A + r_X)}{\sqrt{2}\,(r_B + r_X)} \qquad\qquad 2.46$$

where $r_A$, $r_B$ and $r_X$ denote the ionic radii of the A- and B-cations and the X-anions, respectively.

The perovskite structure exhibits cubic symmetry within the range of $0.9 \leq t \leq 1$. For slightly lower or higher t-values the lattice is distorted, while below t = 0.71 the structure becomes unstable [245]. The concept of the Goldschmidt tolerance factor has also been applied to describe lattice distortions in the K₂NiF₄-structure with tolerance factors between 0.866 and 1 [246,247].

The unit cell of the structurally-related K₂NiF₄-structure (Fig. 2.17, right) exhibits tetragonal symmetry (*I4/mmm*, space group: 139). The central perovskite block is layered between layers of alternating potassium and fluoride ions, reminiscent of rock salt layers in sodium chloride. The crystal lattice of Ln₂NiO₄ compounds, on the other hand, deviates from the ideal tetragonal structure due to a mismatch between the lengths of Ln-O bonds in the rock salt and Ni-O bonds in the perovskite layers. This causes mechanical stress within the structure, which is partly relieved by a slight rotation of the oxygen octahedra along the c axis [248]. The mismatch can be minimized either by stretching the Ln-O bonds or compressing the perovskite layer. Incorporation of excess oxygen into interstitial sites in the rock salt layer accomplishes

both, by increasing the Ln-O bond length and partially oxidizing $Ni^{2+}$ to $Ni^{3+}$, which results in a shorter Ni-O bond [248,249]. Neutron diffraction studies determined that $La_2NiO_{4+\delta}$ (LNO) crystallizes in the orthorhombic *F*mmm space group [249,250] and undergoes a phase transformation into the tetragonal *I*4/mmm structure around 430 K [249,251]. The stoichiometric compound $La_2NiO_4$, however, is better described by the less symmetric orthorhombic *B*mab space group [250,252].

The bond length mismatch is even more pronounced for the Pr- and Nd-analogs. Therefore $Pr_2NiO_{4+\delta}$ und $Nd_2NiO_{4+\delta}$ tend to incorporate higher amounts of excess oxygen into the structure to relief stress [253].

The oxygen non-stoichiometry $\delta$ of $Ln_2NiO_{4+\delta}$ compounds is dependent on cation composition, temperature as well as oxygen partial pressure and can range between $\delta=0$ for and $\delta=0.25$ for fully oxidized samples [254].

A homologous series of related structures with the general composition $A_{n+1}B_nO_{3n+1}$ was first described by Ruddlesden and Popper for $Sr_2TiO_4$ compounds [255,256]. The first three members of this so-called Ruddlesden-Popper structure family, which are characterized by an increasing number of interlayered perovskite building blocks are depicted in Fig. 2.18.
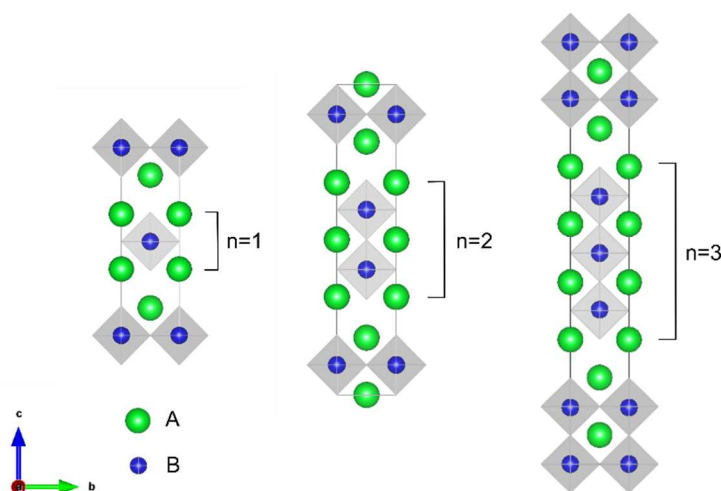


*Fig. 2.18: Unit cells of the first three Ruddlesden-Popper structures with the general formula $A_{n+1}B_nO_{3n+1}$. The A- and B-cations are shown in green and blue, respectively. The O-ions, which are located at the corners of the grey tetrahedrons were omitted for clarity. Structures represent $Sr_2TiO_4$, $Sr_3Ti_2O_7$ and $Sr_4Ti_3O_{10}$ in the space group I4/mmm. Images generated with VESTA [243].*

A number of higher-order Ruddlesden-Popper structures of $La_{2-x}Pr_xNiO_{4+\delta}$ ($0\leq x\leq 2$) have recently been investigated as SOFC cathode materials [77,88,257-261].

In contrast to perovskite materials like La$_{1-x}$Sr$_x$MO$_{3-\delta}$ (M=Mn, Co, Fe), in which oxygen diffusion takes place via vacancies, oxygen in Ln$_2$NiO$_4$-type materials is transported via oxygen interstitials within the rock-salt layer [250].

While La$_2$NiO$_{4+\delta}$ shows high stability at elevated temperatures, Pr$_2$NiO$_{4+\delta}$ incorporates high amounts of oxygen and undergoes thermal decomposition into the third-order Ruddlesden-Popper phase under exsolution of Pr-oxide above 800°C [86,262] according to the following reaction [262]

$$3\ Pr_2NiO_{4+\delta} + xO_2 \leftrightarrow\ Pr_4Ni_3O_{10-\delta\prime} + 2Pr_{1.83-\delta\prime\prime} \qquad\qquad 2.47$$
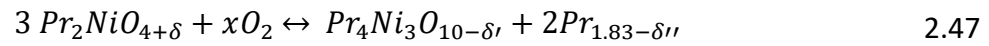
# 3 Experimental

The following section describes in detail the preparation of dense ceramic samples and symmetrical cells for cell testing, as well as the methods used to characterize the raw materials and tested samples. $La_2NiO_{4+\delta}$ (LNO) and $Pr_2NiO_{4+\delta}$ (PNO) powders were obtained from Treibacher Industrie AG (Althofen, Austria) and Marion Technologies (Verniolle, France).

## 3.1 Material characterization

### 3.1.1 Particle size distribution

Particle size distributions of powders were measured using a CILAS 1064 laser diffractometer equipped with a liquid dispersion unit. A suspension of 0.2 g of dry powder sample in 25 ml $H_2O$ deion. with 0.2 g of Na-polyacrylate (NPA 2100, MW = 2100 g $mol^{-1}$) as a dispersant was treated with an ultrasonic rod for 5 min (amplitude 60%, cycle 0.5 s). Approximately 0.5g of dispersant were dissolved in $H_2O$ deion. in the liquid dispersion unit und circulated through the measurement cell. Solvent scattering was corrected by subtraction of a background measurement. Measurements were carried out under ultrasonic agitation.

### 3.1.2 X-ray diffraction

XRD-patterns were recorded on a Bruker AXS D8 Advance Eco equipped with a Cu $K_\alpha$ X-ray source and a 1D-LYNXEYE XE-T detector. The radiation source was operated at 40 kV and 25 mA. Measurements were taken at a step rate of 0.02° and 1s per step. Powder samples were rotated at 30 rpm during measurement. The obtained patterns were evaluated using the commercial crystallographic PDF-4+ data base and the integrated software SIEVE. Quantitative phase analysis was conducted by means of Rietveld refinement using the software package Topas [263].

## 3.2 Long-term stability testing against Cr-/Si on dense samples

### 3.2.1 Sample preparation

Small amounts of ceramic powders were milled in a planetary ball mill (Fritsch Pulverisette 7) in $ZrO_2$-lined cups using $ZrO_2$ milling balls (1.5 mm diameter) or, for larger quantities, in a roller bed mill in polyethylene bottles using $ZrO_2$ milling balls (3 mm diameter) in ethanol. The particle size distribution was determined using a particle size analyzer (CILAS 1064), which

operates based on laser-diffractometry. The milled powders were isostatically pressed into cylindrical pellets in rubber molds for 10 min at 200 MPa and sintered twice for 10 h at 1350°C in air with heating and cooling rates of 2 K min$^{-1}$ in a high temperature furnace (Carbolite RHF1400). The obtained sintered pellets exhibited densities of more than 95%, which is often cited as necessity for diffusivity measurements since such samples should not contain any open porosity [264]. For measurements in van-der-Pauw geometry, a thin slice with a 6×6 mm$^2$ cross-section was cut using a diamond wire saw (Well) and subsequently ground with a diamond grinding disk (mean grain size 70 µm). The squared peace was polished on both sides using polymer-embedded diamond lapping films with 30, 6, and 1 µm mean particle size to a final thickness of 412 µm. After polishing the sample was cleaned in hot acetone for 5 min. Gold wires were attached to all four corners as electrical contacts using gold paste (Metalor), which was dried for 10 min at 150°C and then fired for 15 min at 850°C with heating and cooling rates of 2 K min$^{-1}$.



*Fig. 3.1: Sample in van-der-Pauw geometry mounted inside a quartz-glass holder (left: top view, right: side view).*

To ensure a stable sample position and orientation within the measurement setup the sample was fixed in a cylindrical quartz-glass holder using gold paste, as depicted in Fig. 3.1. In addition, the quartz-glass holder provides a platform for additional pieces of the material for further analysis.

For measurements in linear-four-point geometry a rectangular shape was prepared using a diamond wire saw. The four larger faces of the cuboid were polished with diamond lapping films with 30, 6, and 1 µm mean particle size. Electrical contacts (gold wire) were fixed at the smaller faces using two layers of gold foil and gold paste to provide a large contact area for the application of current. The gold foil also acted as diffusion barrier for oxygen to ensure that oxygen diffusion could only take place through the larger faces of the cuboid. The sample was notched around the circumference in two places to provide support for the two voltage

probes, which were attached at a distance of 5.2 mm from one another. This sample was also mounted inside a quartz-glass holder, as shown in Fig. 3.2.
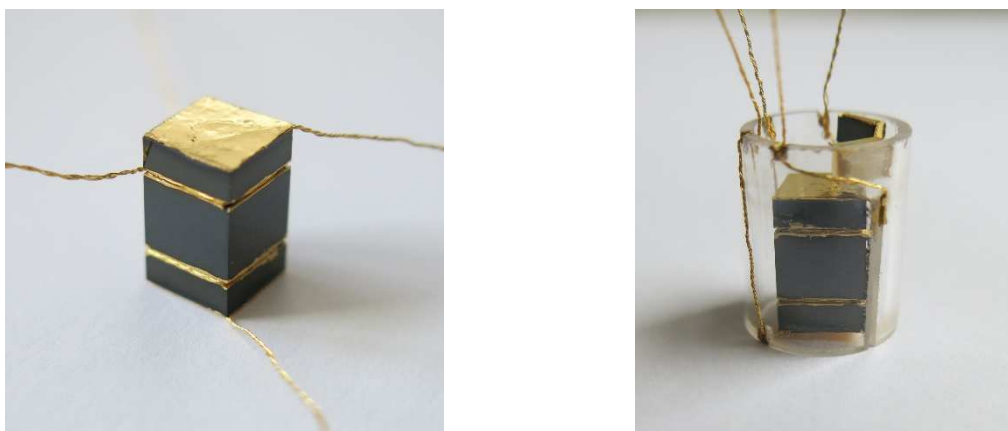


*Fig. 3.2: Rectangularly shaped bar sample for measurements in linear-four-point geometry (left) mounted in quartz-glass holder (right).*

Two addition small pieces of ceramic material were cut and polished to the same finish as the main sample and placed in close proximity to the main sample.

### 3.2.2 Measurement setup

For the determination of the electrical conductivity and the conductivity relaxation curves, the sample was fixed to an alumina sample holder and placed inside a quartz-glass reactor, which was put inside a horizontal tube furnace controlled by a PID controller (Eurotherm Mod. 847). Measurements were performed between 700 and 800°C in $O_2$/Ar gas mixtures as received from the supplier (Linde Gas GmbH) at flow rates of 2 L h$^{-1}$. The gas flow was regulated, depending on the setup, by either ball flowmeters with needle-valves or mass flow controllers. The sample temperature was determined by a mantle S-type thermocouple, which was placed close to the sample. Currents between 200 and 300 mA were applied to the sample using a source meter (Keithley 2400) and the resulting sample voltage was measured using a nano-voltmeter (Keithley 182). The gas atmosphere surrounding the sample was changed by manually switching a four-way valve. For measurements in humid atmospheres the test gases were passed through washing bottles filled with deionized water and thermostatted to 6°C or 17°C, to achieve 30% or 60% relative humidity, respectively. Chromium poisoning was simulated by placing Cr-pellets (99.999%) close to the sample. The quartz-glass reactor and the cylindrical sample mount, and in part the used gold paste, served as an ever-present silicon source.

### 3.2.3 Experimental design

The long-term-stability experiments were usually divided into 3-4 stages to test the ceramic samples under different environmental conditions. For each stage the same main sample was used, therefore it should be taken into account that the effects are somewhat cumulative. An important focus was put on determining the influence of humidity in the presence of a chromium and a silicon source. Two extra pieces of the same material were positioned in the reactor close to the measured sample, which were therefore exposed to the same conditions as the main sample. This allowed for elemental and morphological analysis after each critical step of the experiment, without the need to remove the main sample. The first stage of the long-term experiment usually served to define the intrinsic degradation of the sample surface due to being exposed to high temperatures in dry test gas and without Cr. The influence of Si, though present, can be neglected due to the low volatility of Si under dry conditions [236]. This experimental phase was kept short, since previous examinations of $K_2NiF_4$-type nickelates showed no degradation under these conditions. However, oxygen exchange measurements were performed long enough to establish a proper baseline of $k_{chem}$ for the upcoming stages. The intention was to carry out each subsequent phase of the degradation experiment for at least 1000 hours. At the beginning of the next phase, the sample was cooled down to introduce the Cr-source into the system and subsequently reheated while flushing the sample with 10% $O_2$ in Ar. At this stage of the experiment the focus was mainly put on examining the effects of Cr-poisoning in dry atmosphere. Again, the influence of Si on the oxygen exchange kinetics of the sample should be negligible. After this phase, the sample was cooled down to remove one of the ancillary ceramic samples for surface analysis. During the following two stages the sample was exposed to two different levels of humidity, which leads to an increase in Cr- as well as Si-volatilization. After approximately 1000 hours under moderate humidity, the second ancillary ceramic sample was taken out and analyzed. This allows for the investigation of combined effects of Cr- and Si-poisoning on the surface oxygen exchange, which are expected to emerge during the operation of SOEC/SOFC stacks, as some humidity can be expected during operation at the cathode. A detailed description of the test conditions is given in Table 3.1.

*Table 3.1: Experimental conditions for long-term stability tests on LNO in the presence of Cr and Si. The measurement method used is indicated as vdP (van der Pauw) or L4P (linear four-point) geometry. Measurements were carried out in 10% $O_2$ in Ar.*

| Sample | Method | T / °C | Stage | t / h | pH₂O / r.h. | pH₂O / mbar | Cr | Si |
|---|---|---|---|---|---|---|---|---|
| LNO412 | vdP | 700 | 1 | 312 | 0 | - | - | + |
| | | 700 | 2 | 1176 | 0 | - | + | + |
| | | 700 | 3 | 1200 | 30 | 9.51 | + | + |
| | | 700 | 4 | 1008 | 60 | 19.01 | + | + |
| | | | | | | | | |
| LNO6269×6327 | L4P | 800 | 1 | 528 | 0 | - | - | + |
| | | 800 | 2 | 1008 | 0 | - | + | + |
| | | 800 | 3 | 1200 | 30 | 9.51 | + | + |
| | | 800 | 4 | 1080 | 60 | 19.01 | + | + |

## 3.3 Long-term stability test against Cr on symmetrical half-cells

In addition to the long-term stability experiments on dense samples of LNO, several tests on symmetrical half-cells were conducted. The tests were performed consecutively and with each subsequent experimental procedure, new insights gained in previous experiments were incorporated. The following section describes the preparation of the used cells, the measurement setup, as well as the experimental conditions for each cell test.

### 3.3.1 Cell preparation

To obtain dense electrolyte substrates, $Ce_{0.9}Gd_{0.1}O_{2-\delta}$ (CGO) powder (Treibacher Industrie AG, Althofen, Austria) was preformed into cylindrical pellets in a stainless-steel die (2 or 2.5 cm diameter) using a uniaxial press at 1 ton, which were isostatically repressed at 200-300 MPa for 15 min. The green bodies were sintered at 1450°C for 10 h with heating and cooling rates of 2 K min⁻¹ and 1 K min⁻¹, respectively, which yielded tablets with typical diameters of 16-20 mm and 2 mm thickness with relative densities above 95%. The sintered tablets were ground with diamond and silicon carbide grinding disks to a smooth finish (finest grit P4000) to a final thickness of 1.6-1.8 mm. A thin groove was cut along the circumference of the tablet to provide support for the Pt-reference electrode, which was attached using Pt-paste.

Screen printing pastes were made externally (Fraunhofer IKTS, Germany) and in-house from LNO and PNO powders. The powder was pre-dispersed in a commercial ink-vehicle using a dispersion mixer and the raw paste was homogenized using a triple roll mill (Exakt 50I). Preliminary tests showed that a content of 65 wt-% of ceramic particles with a mean particle size of approximately 0.8 µm gives screen-printing pastes with suitable viscosity for printing as well as crack-free sintered layers. To ensure reproducibility of the printing process and the cathode microstructure, all screen-printing pastes were produced with 65 wt-% solid content of ceramic particles with an approximate mean particle size of 0.8 µm.

For symmetrical cells LNO or PNO electrodes were screen printed using 80T and 55T screens on both sides of the CGO substrate and sintered between 1100 and 1250°C for 2h in air. The mesh dimensions of the screens used for electrode application are listed in Table 3.2. To achieve suitable layer thicknesses, it was usually necessary to print multiple layers per electrode. The resulting electrode layers were between 3 and 30 µm thick, as was determined by SEM imaging of cell cross sections. The adhesion of the sintered layers was tested using the scotch-tape test. Gold grids with wires were attached to the screen-printed electrodes using gold paste as current collectors. The applied cell design is depicted schematically in Fig. 3.3.

*Table 3.2: Mesh dimensions of the applied screens according to the supplier (www.siebdruck-versand.de).*

| Screen | Threads / cm$^{-1}$ | Threads / inch$^{-1}$ | Mesh size / µm | Thread diameter / µm |
|--------|---------------------|------------------------|-----------------|----------------------|
| 55T | 55 | 140 | 124 | 55 |
| 80T | 80 | 200 | 77 | 48 |



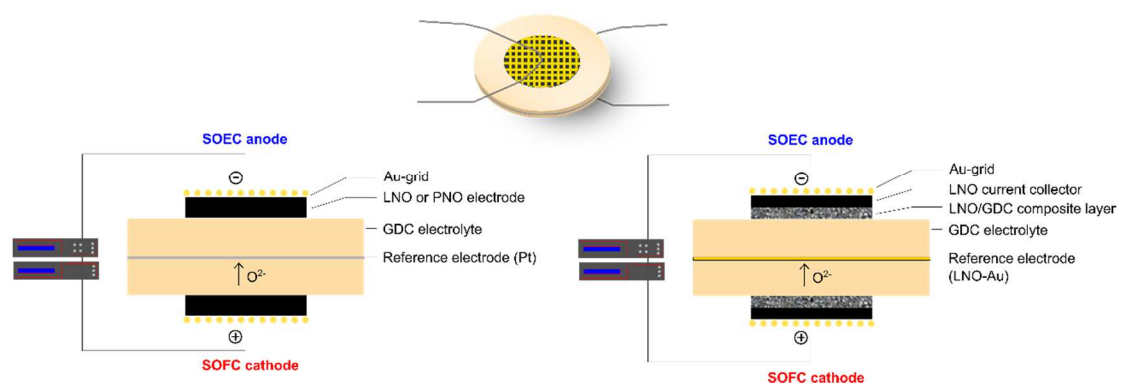*Fig. 3.3: Symmetrical button cell design for impedance measurements.*

### 3.3.2   Measurement setup

The cells were fixed to an alumina sample holder, which was placed inside an alumina tube in a horizontal tube furnace (Reetz GmbH, Mod. LOBA 2050-40-460-1-OW-48V). The furnace was controlled by a PID controller (Eurotherm, Mod. 2416 or 2604) and the sample temperature

was measured using the internal S-type thermocouple of a potentiometric oxygen sensor (Setnag, MicroPoas) or by a sheated S-type thermocouple. Electrochemical impedance spectroscopy and current – voltage measurements were conducted at 800°C in premixed 20% $O_2$/Ar mixtures (Linde Gas GmbH). The gas flow in the reactor was regulated by ball flow meters with needle valves. For long-term stability tests under load, currents between 110 and 500 mA cm$^{-2}$ were applied using an electronic load (TCE 8952 Dual output power supply). For measurements in humid test gases, the gas streams were passed through water filled washing bottles cooled down to 6°C by a thermostat to reach 30% relative humidity before entering the reactor. Chromium poisoning conditions were realized by placing Cr-pellets (99.999%) on an alumina support upstream and in close proximity to the sample mount. Electrochemical impedance spectroscopy (EIS) and current-voltage-characterization were carried out using a potentiostat/galvanostat setup (Novocontrol 15V/10A) coupled with a frequency response analyzer (Novocontrol Alpha-A).

### 3.3.3   Analysis of impedance spectra

Impedance spectra were measured between 10 mHz and 1 MHz under open-circuit-voltage (OCV). The excitation voltage was set to 20 mV (rms). I-V-curves were recorded up to current densities of ±500 mA cm$^{-2}$ with sweep rates of 1 mA s$^{-1}$. Complex non-linear least squares (CLNS) fitting of impedance spectra was performed using the software package WinFit (v.3.4). Impedance spectra were fitted to an equivalent circuit (see Fig. 3.4) consisting of an inductance $L_0$, which is caused by the sample holder, an ohmic resistance $R_0$, which is attributed to the electrolyte, and three RCPE elements, corresponding to at least three electrode processes.
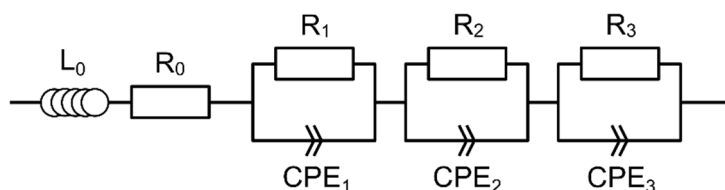


Fig. 3.4: Equivalent circuit used for fitting of impedance spectra.

### 3.3.4   Experimental design

For the long-term endurance tests under Cr-poisoning, the symmetrical half cells were exposed to 3-4 stages of varying operating conditions. During each stage of the experiment the aim was to determine the influence of a different parameter on the area specific resistance (ASR) of the electrodes. The first step of the experiment was usually carried out under dry

49

conditions at 800°C and without current load to define a baseline value for the ASR. The next step introduced either a Cr-source or the application of a constant current load between measurements in dry test gas for at least 600 hours. In the following step, the $O_2$/Ar mixture was humidified to simulate the use of ambient air. In one experiment, the effect of humidity was tested first without the presence of chromium in the reactor, followed by a period with Cr in the reactor present. The cells were kept constantly at 800°C, except when Cr was inserted into the reactor or contacts had to be repaired. A detailed description of the experimental procedures is given in Table 3.3.

*Table 3.3: Experimental conditions for long-term stability tests on porous $Ln_2NiO_4$ electrodes in the presence of Cr. The samples were characterized by impedance spectroscopy and I-V-curves at 800°C in 20% $O_2$ in Ar under dry or humid conditions with and without current load.*

| Sample | Stage | t / h | pH₂O/ r.h. | pH₂O/ mbar | Cr | Load / mA cm⁻² |
|---|---|---|---|---|---|---|
| LNO-sym-2010-1 | 1 | 168 | 0 | - | - | - |
| | 2 | 1176 | 0 | - | - | 110 |
| | 3 | 816 | 30 | 9.51 | + | 110 |
| | | | | | | |
| LNO_LNOGDC5050-sym-2010-4 | 1 | 336 | 0 | - | - | - |
| | 2 | 768 | 0 | - | - | 500 |
| | 3 | 648 | 30 | 9.51 | - | 500 |
| | 4 | 936 | 30 | 9.51 | + | 500 |
| | | | | | | |
| PNO-sym-2010-2 | 1 | 912 | 0 | - | - | - |
| | 2 | 1176 | 0 | - | - | 110 |
| | 3 | 1032 | 30 | 9.51 | + | 110 |

## 3.4 Post-test analysis

### 3.4.1 Sample preparation

For post-test analysis, thin, dense ceramic samples were broken into several pieces. Bar-shaped samples were cut carefully to avoid disturbing the contaminated surfaces into 4 pieces using a diamond wire saw.

Cells were embedded in conductive or non-conductive PMMA resin and cut in half with a diamond cutting wheel. The cut surface of the embedded samples was ground using SiC papers (GRIT 320 – GRIT1200) and subsequently polished using diamond suspensions (9 µm, 3 µm, and 1 µm particle size). The embedded and polished samples were sputtered with a thin layer of gold (Baltek MED 020) and contacted with silver paste to ensure proper sample conductivity. For WDX-analysis, samples were embedded in hot-curing, copper or carbon containing conductive resin.

### 3.4.2 Atomic force microscopy

Surface topography images were obtained on an Asylum Research MFP-3D atomic force microscope (AFM) equipped with planar closed loop scanner in tapping mode at a set-point-to-free amplitude ratio of 0.8 under ambient conditions. Silicon probes (Olympus OMCL-AC160TS) featuring a spring constant of 42 Nm$^{-1}$ and tetrahedral tips with an opening angle of 35° and a nominal tip radius of 7 nm were used. To correct for oblique sample mounting, a step line correction and flattening routine were applied. The root mean square (rms) surface roughness $\sigma_{rms}$ was calculated from topographical data based on

$$\sigma_{rms} = \sqrt{\frac{1}{N^2}\sum_{i=1}^{N}\sum_{j=1}^{N}[z(x_i, y_i) - \mu]^2} \qquad 3.1$$

with x, y and z representing image coordinates, N the number of recorded data points in x- and y-direction and µ the average height level.

As a measure for the change in lateral structure size of surface features, the lateral correlation length ξ is calculated from the height-height correlation function for a random rough surface, which can be expressed as

$$C(x) = \sigma^2_{rms}e^{[-(|x|/\xi)^{2\alpha}]} \qquad 3.2$$

with α being the Hurst-parameter.

Both characteristic properties, $\sigma_{rms}$ and ξ, were usually determined from a mean of three 10x10 µm$^2$ images, unless otherwise stated.

### 3.4.3 X-ray photoelectron spectroscopy

X-ray photoelectron spectroscopy (XPS) combined with Ar$^+$ depth profiling was performed on a Perkin Elmer PHI 5600 ESCA system with hemispherical analyzer, which was operated at a constant pass energy of 58.7 eV. The instrument was equipped with a standard X-ray source

emitting Mg-K$_\alpha$-radiation (1253.6 eV). The analyzed area was restricted to a spot of 400 μm in diameter by an Omnifocus lens. To scan for possible unknown contaminants quick survey scans were performed in advance. For Ar$^+$ sputtering an Atomika WF 421 Microfocus Ion Gun producing a 10 kV Ar$^+$- beam of 150 μm diameter at an ion current of 125 nA was applied. The sputtered area amounted to 1.2 × 1.5 mm$^2$ at an incidence angle of 20° off the surface normal. The sputter rate was estimated based on the Ar$^+$ fluence under the assumption that 2 target atoms per impinging Ar$^+$ atom are released. A Shirley background function was used for background correction and the concentrations of elements were determined based on core-level spectra peak areas applying standard relative sensitivity factors obtained by the manufacturer of the instrument.

### 3.4.4   Scanning electron microscopy

Scanning electron microscopy (SEM) imaging and X-ray analyses were performed on several different electron microscopes. Images of dense ceramic samples and embedded cell cross sections were obtained in secondary electron (SE) and backscattered electron (BSE) mode on a Zeiss Evo 50 microscope at acceleration voltages of 15 kV or on a Zeiss Ultra 55 microscope at acceleration voltages of 5kV. EDXS-survey scans were recorded at acceleration voltages of 10 – 30 kV on both microscopes using either an EDAX Phoenix or an INCA Oxford EDXS-detector. Elemental distribution mappings were recorded on a FEI Quanta 200 SEM with an EDAX Genesis EDXS-detector at 10 kV as well as on the Zeiss Ultra 55 using an EDAX Phoenix detector.

### 3.4.5   Transmission electron microscopy

Thin lamellas for TEM analysis were prepared using a Focused Ion Beam (FIB) NOVA 200 Nanolab dual beam microscope. STEM and TEM investigations were conducted on two high-end microscopes: a FEI Tecnai F20 (operating at 200 keV) equipped with a field emission gun with monochromator, an EDXS-detector (Saphire Si(Li) by EDAX) and an electron energy filter (GIF Quantum by Gatan Inc., energy resolution: 0.1 eV), which can be operated in TEM as well as STEM mode and a FEI Titan3 G2 60-300 (operated at 300 keV) with a Cs probe corrector (DCOR) for high-resolution imaging, equipped with a high sensitivity EDXS-detector (FEI ChemiSTEM with Super-X detector by Bruker), as well as a post-column electron energy filter (GIF Quantum ERSTM by Gatan Inc.). Simulations of selected area diffraction patterns were carried out using the software package JEMS [265].

# 4 Results and discussion

## 4.1 Pre-test material characterization

The following section presents the results of the basic material characterizations, which were carried out before the ceramic powders were processed into sintered pellets or screen-printing pastes. Special emphasis was put on the determination of the particle size distribution, phase composition and the microstructure observed in sintered compacts.

### 4.1.1 Particle size distribution

The raw powders used for dense ceramic pellets and screen-printed cathode layers were characterized regarding their particle size distributions before and after milling. Two batches of LNO powder were obtained from Treibacher, designated LNO_TB_C02 and LNO_TB_C03. The volume particle size distributions of LNO_TB_C02 are presented in Fig. 4.1. The red and the black curve denote the cumulative distribution and the histogram of the raw powder as received from the manufacturer, while the distributions after milling in a planetary ball are shown in green and blue. The measured particle size distributions are given as volume distributions. To reflect the width of the distribution, the characteristic parameters $d_{10}$, $d_{50}$ and $d_{90}$ are reported, which correspond to the particle sizes given in the cumulative distribution at 10%, 50% and 90%. The unmilled LNO_TB_C02 showed a bimodal particle size distribution with particle sizes between 0.3 and 4.7 µm ($d_{10}$ and $d_{90}$, respectively). According to Rahaman [266], a narrow particle size distribution with particles smaller than 1 µm is recommended if reasonable sintering times and a uniform microstructure are required. Although a broader particle size distribution can result in higher packing densities in green bodies, because smaller particles can easily fill voids between larger ones, it likely results in an irregular microstructure. Also, agglomerated particles could lead to heterogenous packing densities in green bodies, which promotes crack formation during sintering and should therefore be avoided [266]. The applied milling procedure included 6 steps of milling at 900 rpm for 10 min in ethanol as suspension medium and a subsequent cooling down period of 30 min to prevent the buildup of excess pressure in the milling cups. This rather harsh treatment reduced the median particle size ($d_{50}$) from 2.5 to 0.3 µm and provided a monodisperse powder showing a narrow particle size distribution.
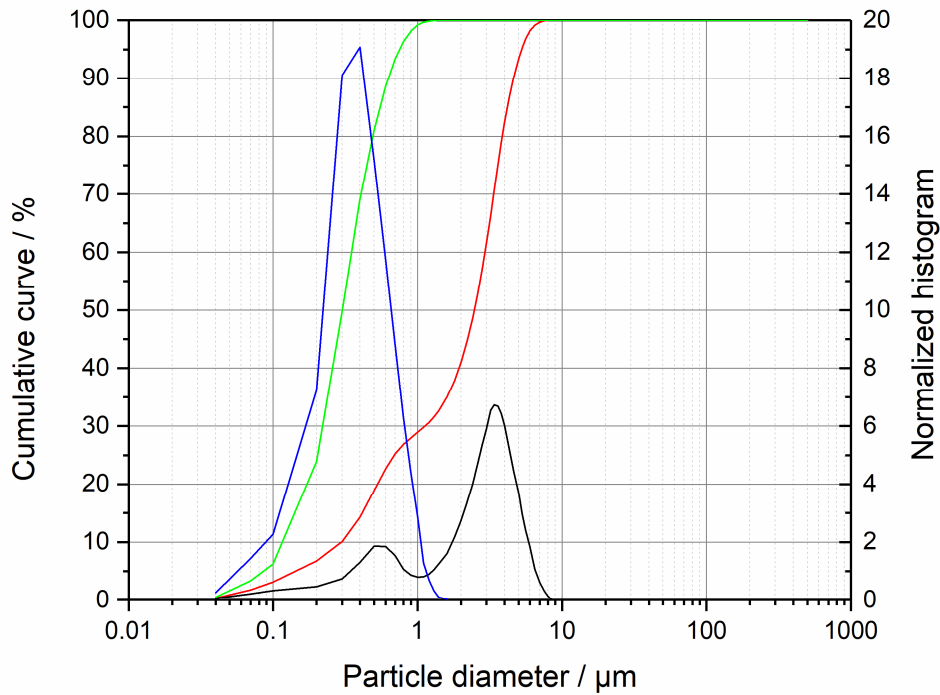
*Fig. 4.1: Cumulative particle size distribution of LNO_TB_C02 as received from the manufacturer (red) and after milling in a planetary mill (green). The corresponding population density distributions are shown in black and blue, respectively.*

Since only small powder quantities could be milled in the planetary mill at a time, the second powder batch (LNO_TB_C03) was ground in a roller bed mill. In addition to its higher milling capacity, this method is also gentler on the milling equipment, as it produces significantly less attrited $ZrO_2$ particles. This results, however, in considerably prolonged milling times. Fig. 4.2 presents the evolution of the characteristic parameters $d_{10}$, $d_{50}$, and $d_{90}$ over time. The milling procedure was stopped after 56 h when a $d_{50}$ of 0.7 µm was achieved. The corresponding cumulative and population density distributions are shown in Fig. 4.3. Similar to LNO_TB_C02, this powder also showed a bimodal distribution in the as-delivered state.

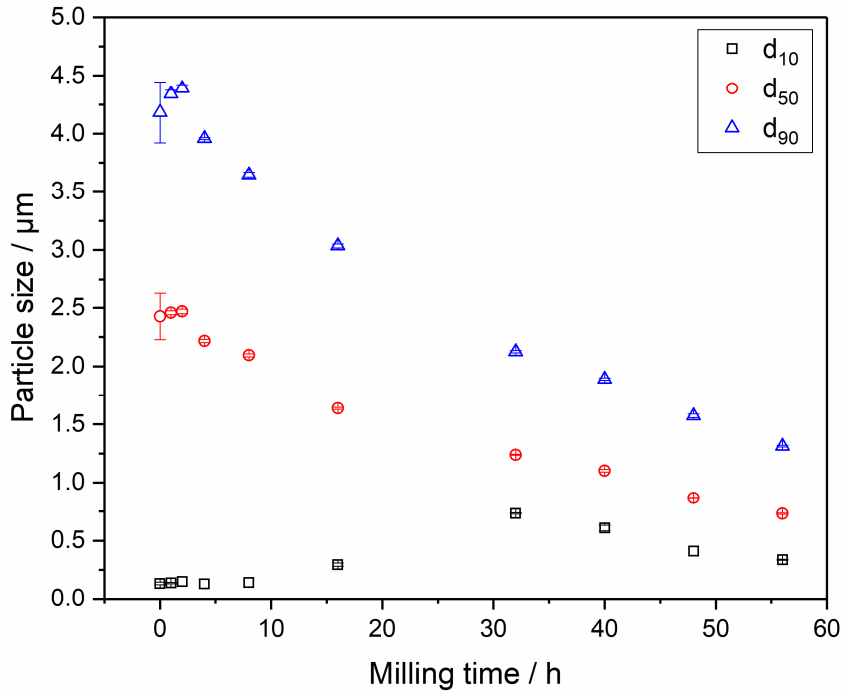*Fig. 4.2: Characteristic distribution parameters $d_{10}$, $d_{50}$, and $d_{90}$ of LNO_TB_C03 as a function of time spend in a roller bed mill.*
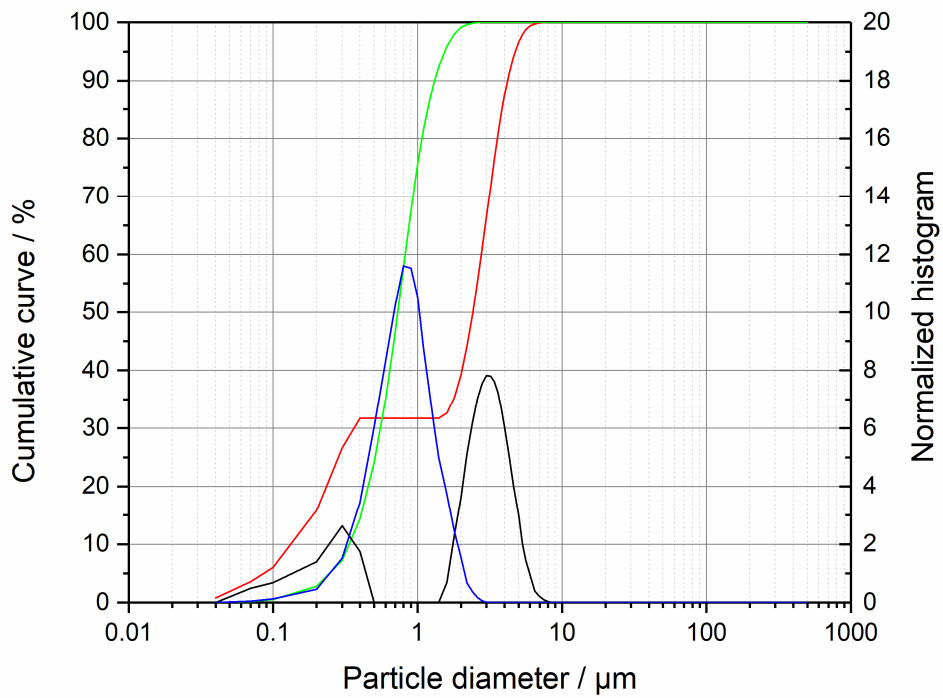


*Fig. 4.3: Cumulative particle size distribution of LNO_TB_C03 as received from the manufacturer (red) and after milling for 56h in a roller bed mill (green). The corresponding population density distributions are shown in black and blue, respectively.*

Fig. 4.4 shows the particle size distribution of the PNO powder batch PNO_MT2 as received from the manufacturer. Since the powder showed a narrow, monodisperse size distribution with a median particle size of 0.4 µm an additional milling step was not deemed necessary.
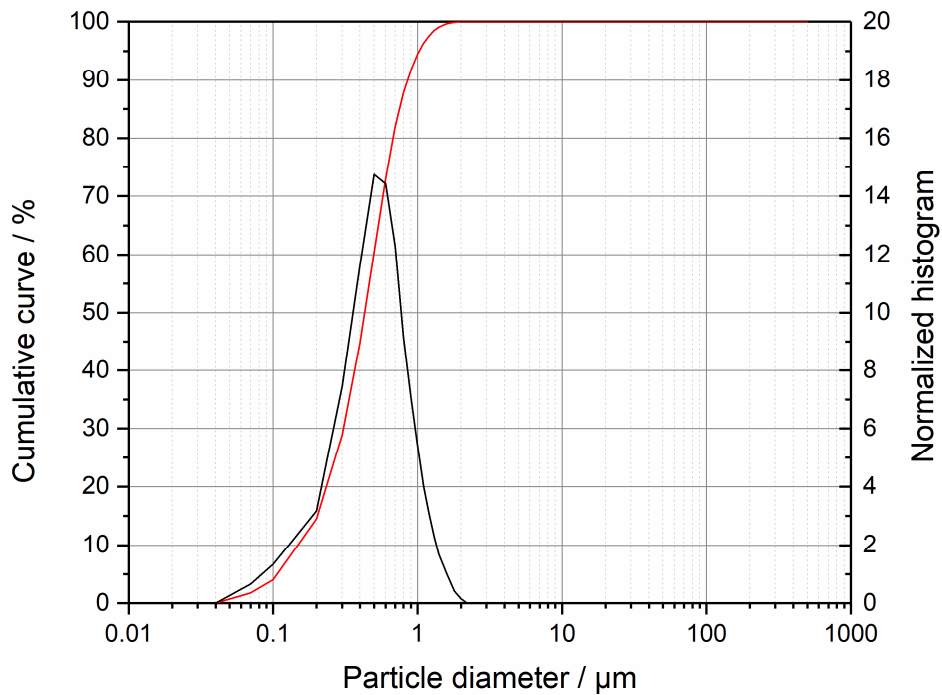


Fig. 4.4: Particle size distribution of PNO as received from the manufacturer. The red line shows the cumulative distribution while the black line denotes the corresponding population density.

### 4.1.2 Crystal structure

To determine the phase composition of the raw materials before the degradation studies room temperature XRD-patterns were recorded. Quantification of the XRD-patterns was realized via Rietveld refinement using the software package Topas [263]. The fitting procedure was carried out until the profile weighted index ($R_{wp}$) was minimized. $R_{wp}$ values were calculated by the fitting software according to [267].

$$R_{wp} = \left[ \frac{\sum_i w_i \, (y_{oi} - y_{ci})^2}{\sum_i w_i \, (y_{oi})^2} \right]^{\frac{1}{2}} \qquad\qquad 4.1$$

Fig. 4.5 and Fig. 4.6 show the measured XRD-pattern of the two milled LNO powder batches, as well as the fit function. The XRD-spectrum confirms the typical $K_2NiF_4$-structure with a minor orthorhombic distortion, which is caused by the tilting of the $NiO_6$ octahedra due to the incorporation of oxygen interstitials [250]. The LNO patterns were refined using a

crystallographic information file from the ICSD data base [249]. Application of the orthorhombic *Fmmm* space group (SG: 69) yielded the lowest $R_{wp}$ values for both LNO batches.
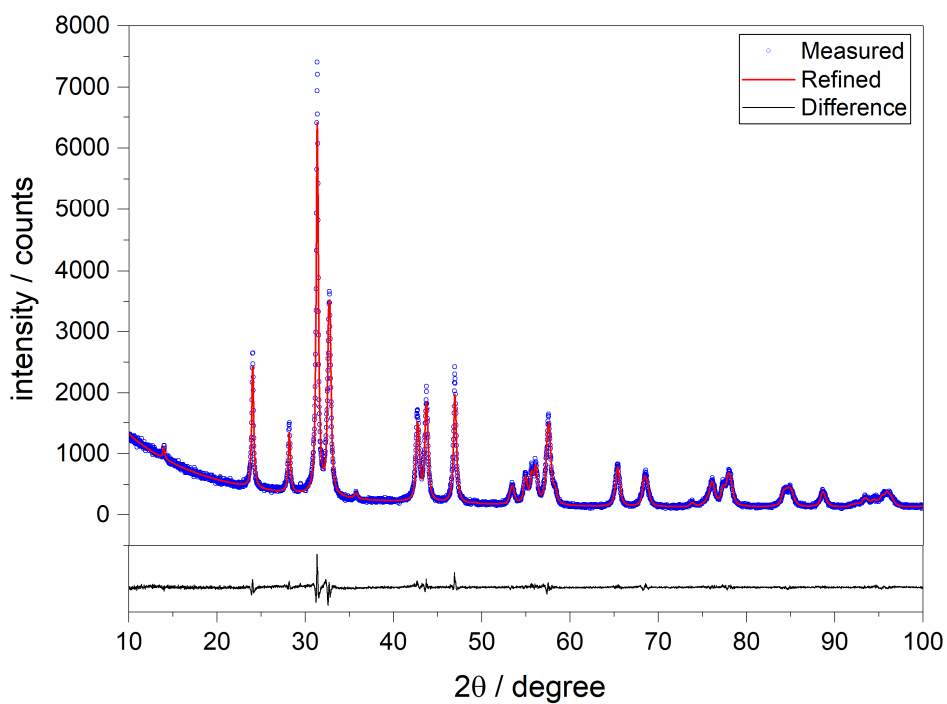


*Fig. 4.5: XRD-pattern of LNO_TB_C02 (blue symbols) and corresponding fit (red line) determined via Rietveld refinement (ICSD 98557).*

*Fig. 4.6: XRD-pattern of LNO powder (LNO_TB_C03), corresponding fit determined via Rietveld refinement (ICSD 98557) and calculated crystal structure.*

The orthorhombic symmetry of the LNO unit cell should result in a separation of the (200) and the (020) reflections at $2\theta \approx 33°$ (see Fig. 4.7). However, this separation was not observed for both LNO samples, most likely due to insufficient resolution of XRD. Furthermore, the refinement indicated that both LNO powder batches were single phase powders.
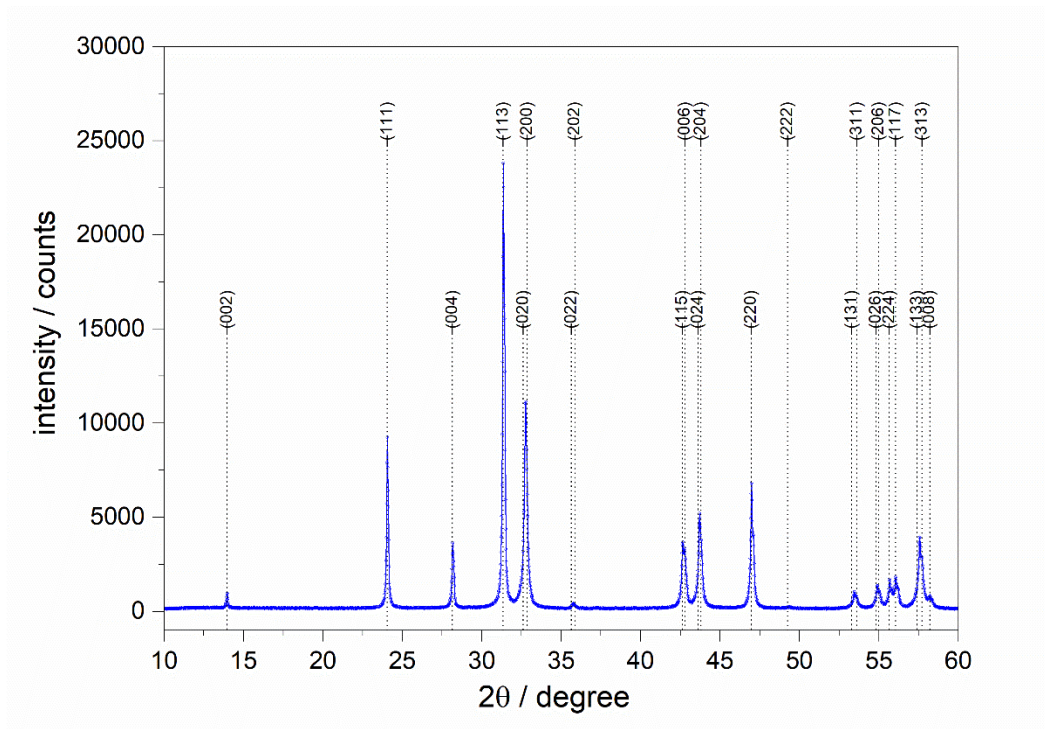
*Fig. 4.7: Indexed XRD-pattern of LNO_TB_C03.*

In contrast to the phase pure LNO powders, XRD-analysis of the purchased PNO powder indicated small amounts of $Pr_6O_{11}$ (1.3 wt-%) and NiO (1.6 wt-%) secondary phases (see Fig. 4.8). The PNO structure was also refined in the orthorhombic space group *Fmmm*, based on structural data by Chung et al. [268]. In the case of PNO, the orthorhombic character of the crystal structure is even more obvious as the aforementioned splitting of the (200) and the (020) peaks is quite pronounced (Fig. 4.9). Table 4.1 provides an overview of the lattice parameters and densities of the three powders as obtained from Rietveld refinements, as well as the $R_{wp}$ values of the resulting fit functions.
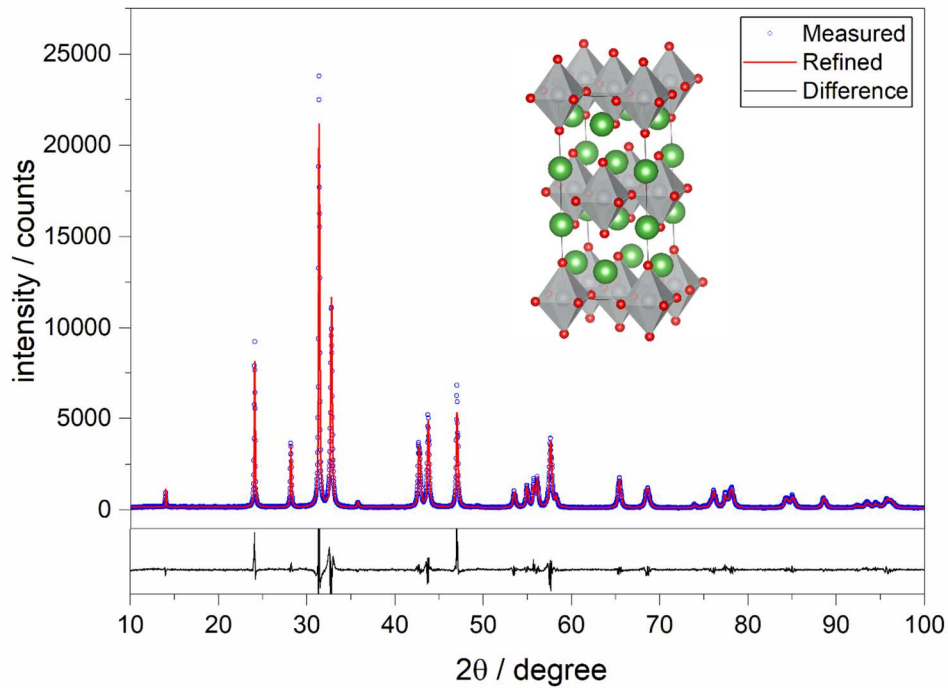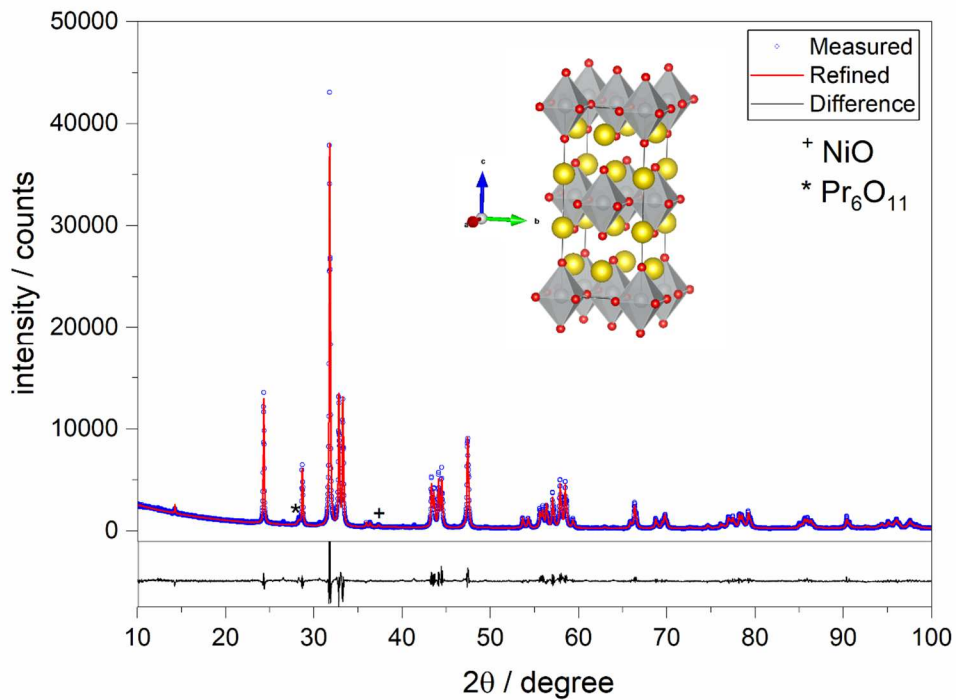
*Fig. 4.8: XRD-pattern of PNO powder (PNO_MT2), corresponding fit determined via Rietveld refinement (ICSD 81577) and calculated crystal structure. The star and cross symbols mark the presence of $Pr_6O_{11}$ and NiO secondary phases, respectively.*



*Fig. 4.9: (a) Indexed XRD-pattern and (b) crystal structure of PNO as calculated from refined data. The star and cross symbols mark the presence of $Pr_6O_{11}$ and NiO secondary phases, respectively.*

*Table 4.1: Comparison of physical properties of the used powders. $R_{wp}$ values were calculated according to eq. 4.1.*

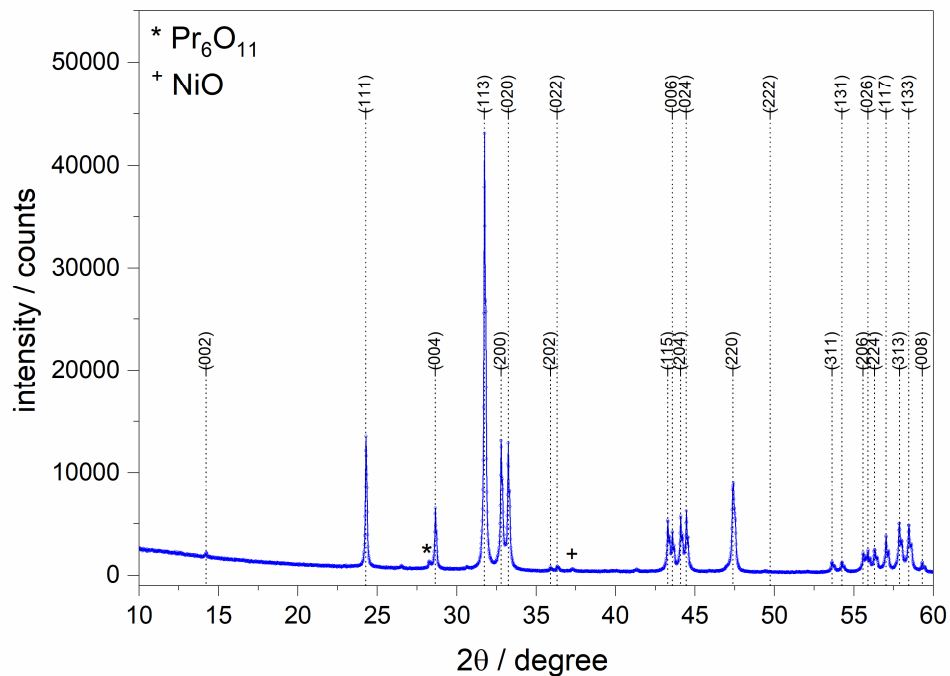| Sample | Lattice parameter Å | | | Density g cm$^{-3}$ | $R_{wp}$ % | Ref. cif |
|--------|-----------|-----------|------------|--------|--------|--------|
| | a | b | c | | | |
| LNO_TB_C02 | 5.4563(3) | 5.4858(3) | 12.6561(5) | 7.06 | 9.8 | [249] |
| LNO_TB_C03 | 5.45850(13) | 5.47172(12) | 12.6659(2) | 7.07 | 7.2 | [249] |
| PNO_MT_2 | 5.45973(7) | 5.38692(7) | 12.45507(18) | 7.34 | 8.3 | [268] |

### 4.1.3 Microstructure and chemical analysis

The microstructure of a sintered, polished and thermally etched LNO_TB_C02 sample is presented in Fig. 4.10. Two SEM images showing the secondary (SE) and the backscattered electron (BSE) signals were simultaneously recorded. While the SE image provides information about the surface topography, the BSE image reveals the presence of secondary phases, since the BSE emission coefficient increases with increasing average atomic number. This way, phases with different chemical composition can easily be discerned in the BSE image [269]. Grains of the same composition can also show slight variation in grey values, due to channeling contrast. Channeling or orientation contrast in the BSE image is caused by the interaction of lattice planes of different orientation in polycrystalline samples. This type of contrast can be easily discerned from Z-contrast by tilting the sample [270]. The LNO_TB_C02 sample shows mainly large grains between 2-10 µm in diameter. The large grain size can be attributed to the long and repeated sintering steps, which were necessary to obtain sintered samples with relative densities above 95%. The large grains of the main phase are surrounded by smaller elongated grains, which show similar grey values in the BSE image. This suggests that the chemical compound that formed the smaller grains has a similar average atomic number as the main phase. However, the BSE image also reveals small, black spots located mostly at triple junction sites. Looking at the SE image, it becomes clear that these spots are grains and not pores, which indicates that these spots are indeed a distinct secondary phase.
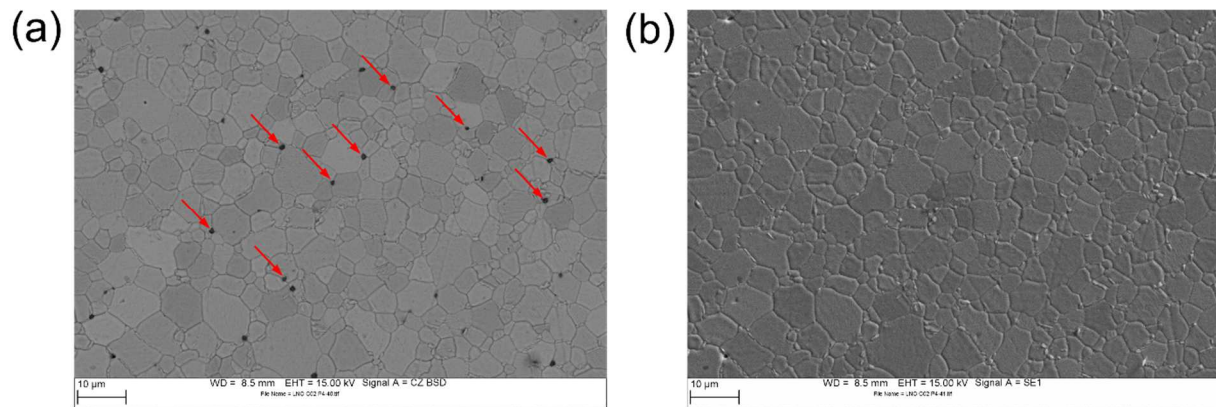
*Fig. 4.10: (a) SEM-BSE and (b) SEM-SE image of sintered, polished and thermally etched LNO_TB_C02. The red arrows mark inclusions of a secondary phase.*

To obtain more information about the chemical composition of the detected secondary phases, another BSE image at higher magnification as well as EDX-spectra were recorded (see Fig. 4.11). The EDX-spectrums of the large grains (spectrum 1) and the surrounding, elongated grains (spectrum 5) appear very similar and correspond to the LNO main phase. As mentioned before, similar grey values of the large and small grains in the BSE image indicate a comparable average Z for both phases. However, the interaction volume of the electron beam within the material is larger than the grain of the secondary phase itself, and thus prevents the exact determination of the actual chemical composition of this phase via EDXS-measurements. Slight variations in the La/Ni ratio between the two phases are a possibility. EDXS-analysis of the dark spots (spectrum 2) shows predominantly Ni and O signals, which indicates a nickel oxide phase. Additional La-signals arise from electron excitation of the surrounding LNO grain due to beam interaction with the material. Nevertheless, the dark spots correspond most likely to NiO. A small inclusion embedded in an LNO grain (spectrum 3) was identified as a silicon-containing phase. Another small grain was shown to contain significant amounts of Zr (spectrum 4), which was most likely introduced into the powder by the harsh milling process using $ZrO_2$ grinding balls.

*Fig. 4.11: Detailed SEM-BSE image of LNO_TB_C02 and EDXS-spot analysis of several different phases.*

Fig. 4.12 presents the SEM-BSE and SEM-SE images of LNO_TB_C03. In general, flat, polished samples provide better material contrast in BSE images [271] and significantly improve the quality of X-ray microanalysis [269]. Thus, a polished, unetched sample was analyzed in addition to the thermally etched sample. In the BSE image of the polished sample (Fig. 4.12a) several dark patches of different grey values embedded in the main phase are visible, indicating the presence of secondary phases. Comparison with the SE-image shows that most of these patches are in fact not pores, which are marked with green arrows in Fig. 4.12b. The thermally etched sample (Fig. 4.12c) showed a coarse but dense microstructure with grain sizes between 2 and 10 μm. At some grain boundaries, crystalline outgrowths were found. In

comparison to the polished sample presented in Fig. 4.12a, there was hardly any material contrast detected, and the only dark spots visible in this image can be attributed to pores. It therefore seems that thermal etching somewhat masks the presence of secondary phases.
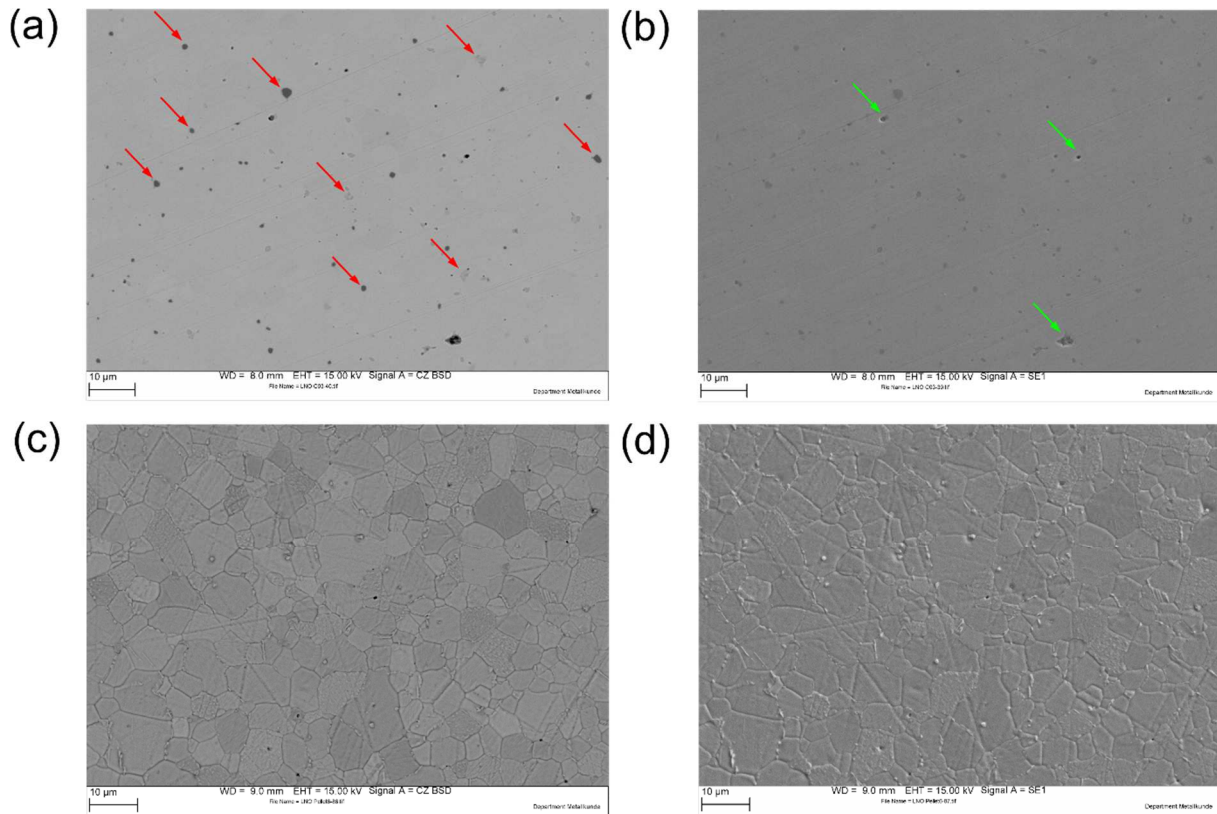


*Fig. 4.12: (a, c) SEM-BSE and (b, d) SEM-SE image of sintered and polished LNO-TB_C03 samples. The samples presented in (c) and (d) were additionally thermally etched. The red and green arrows mark inclusions of secondary phases and pores, respectively.*

A detailed image section of Fig. 4.12a and the corresponding EDXS-analysis are shown in Fig. 4.13. Spectrum 1 reveals the presence of a secondary phase containing Si, Mo, and Zr. Additional La and Ni signals can be ascribed to excitation of the surrounding material. As discussed above, Zr may again have been introduced by ball milling, although the milling process was a lot more gentle in comparison to the one used for the LNO_TB_C02 batch. Mo and Si could have been introduced by evaporated compounds from heating elements in high temperature furnaces, which are often manufactured from SiC or $MoSi_2$. However, as Mo and Si were found deep within the bulk of a sintered sample, both elements must already have been present in the raw powder. The certificate of analysis provided by the manufacturer indeed lists a Si-content of 90 ppm. The Mo content was either not determined or was well below the detection limit of the applied analysis method, which was also not specified in the certificate. Another secondary phase of similar apparent grey value reveals a phase containing La, Si and small amounts of Al. The La/Ni ratio in spectrum 2 is increased in comparison to

spectrum 4, which represents the pure LNO phase. This indicates that La is most likely part of the detected chemical compound, whereas the Ni-signal is derived from the surrounding LNO. The black dots were confirmed to be nickel oxide (spectrum 3).
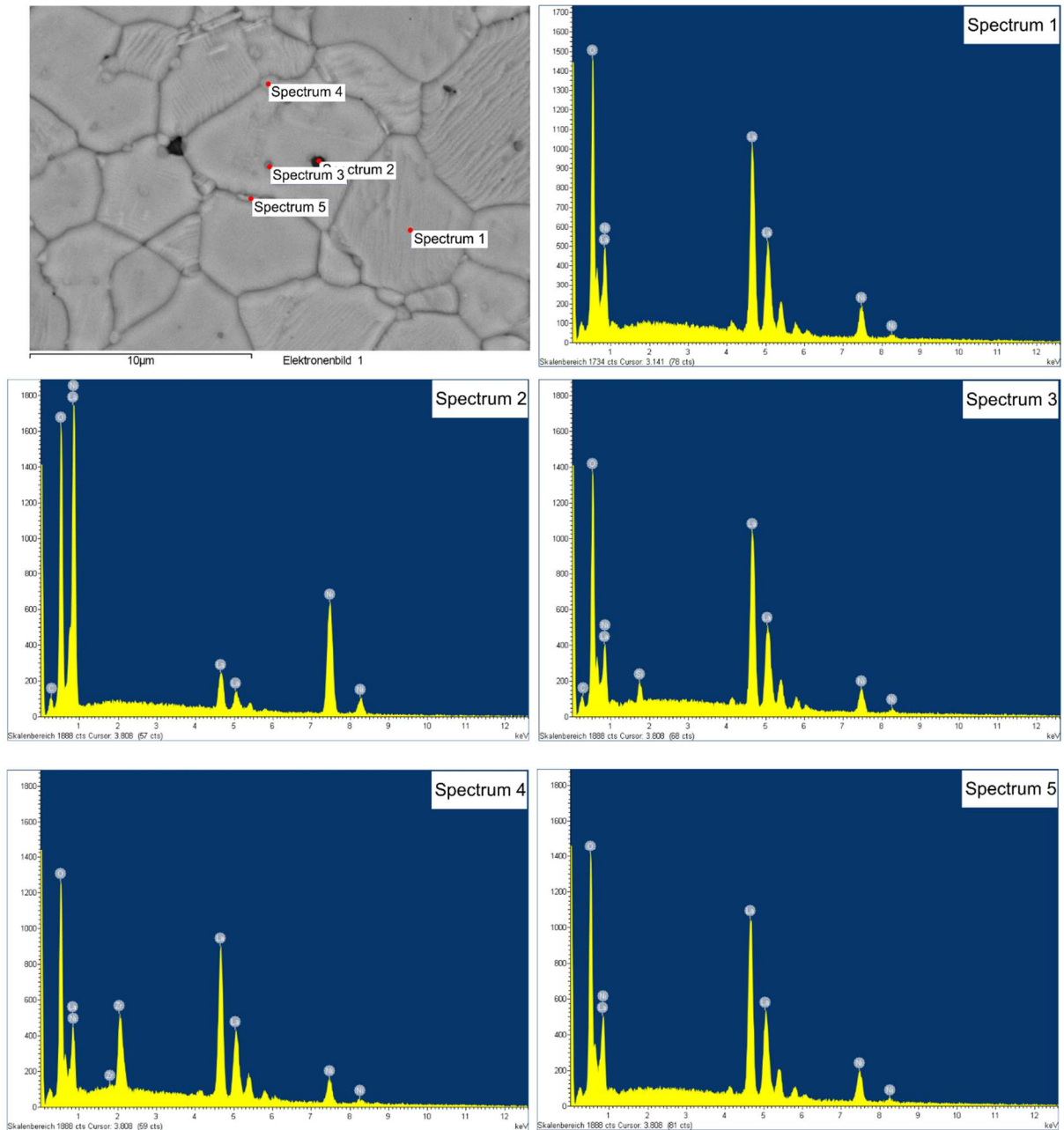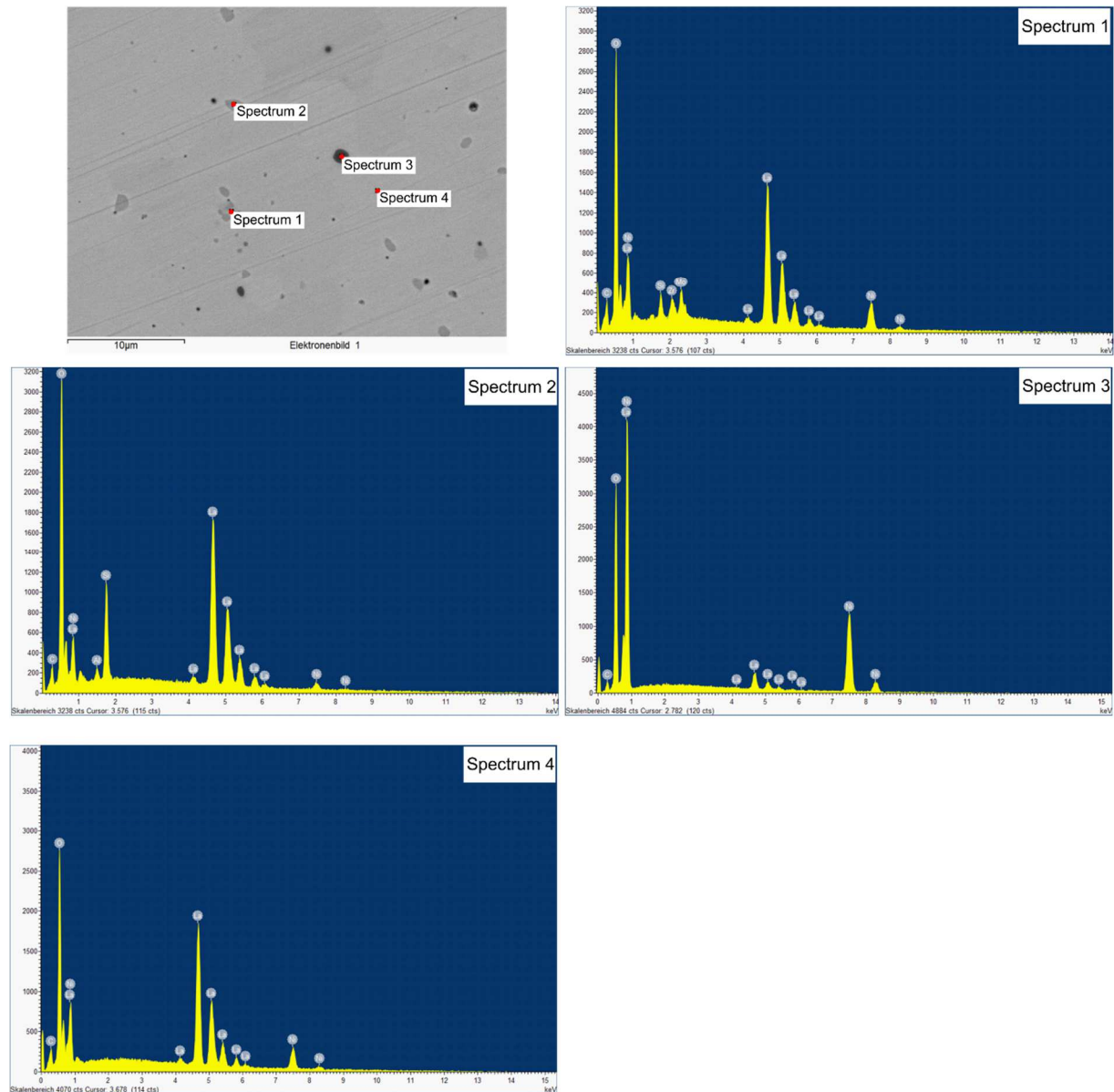


*Fig. 4.13: Detailed SEM-BSE image of LNO_TB_C03 and EDXS-spot analysis of several different phases.*

Fig. 4.14 displays SEM-BSE and SEM-SE micrographs of a polished and thermally etched PNO samples. The polished PNO sample (Fig. 4.14a) reveals numerous, small grains of secondary phases. The corresponding SE-image (Fig. 4.14b) shows that some of the dark spots in the BSE-image actually are pores or pulled put grains of secondary phase (green arrows). The SEM image of the etched sample (Fig. 4.14c and d) show a very uniform and dense microstructure with small grains with diameters between 1 and 4 µm in size. This is consistent with the narrow particle size distribution of the raw powder (Fig. 4.4) and the short sintering time of only 2 h

at 1350°C. Despite the thermal etching, the dark secondary phases are still visible. Nevertheless, it appears that fewer of them are visible compared to the polished sample.
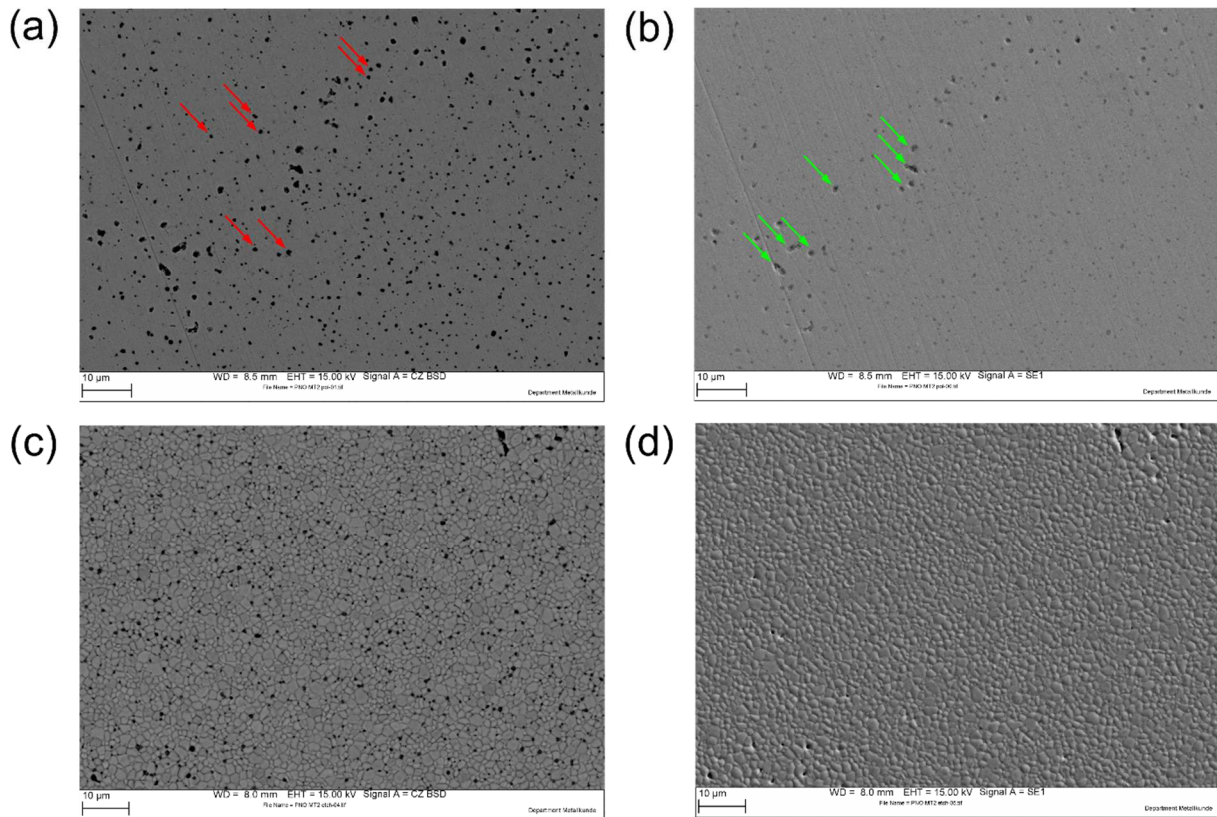


*Fig. 4.14: SEM-BSE (a, c) and SEM-SE (b, d) images of sintered, polished and thermally etched PNO_MT2 samples. Samples (a) and (b) were polished and samples (c) and (d) also thermally etched. The red and green arrows mark inclusions of a secondary phase and grain pull-outs, respectively.*

Fig. 4.15 presents EDXS-spot analyses of three distinct secondary phases detected in a detailed image in BSE-contrast. A phase with medium grey value (spectrum 1) was found to contain Pr, Si, Al, and O, whereas the amount of Ni is clearly reduced in comparison to the PNO main phase (spectrum 3) and comes most likely from the surrounding area. Potential sources for Si and Al are grinding balls, furnace cladding or ceramic crucibles, which could have been used in previous processing steps by the manufacturer. The dark spots consist almost exclusively of Ni and O and can be ascribed to the NiO phase detected in the recorded XRD-pattern (see Fig. 4.8). It is noteworthy that no secondary phases containing Zr were found, which is a strong indication that the Zr impurities detected in both LNO powders were indeed introduced by milling with $ZrO_2$ based grinding materials. The PNO powder, however, was used as delivered by the manufacturer.
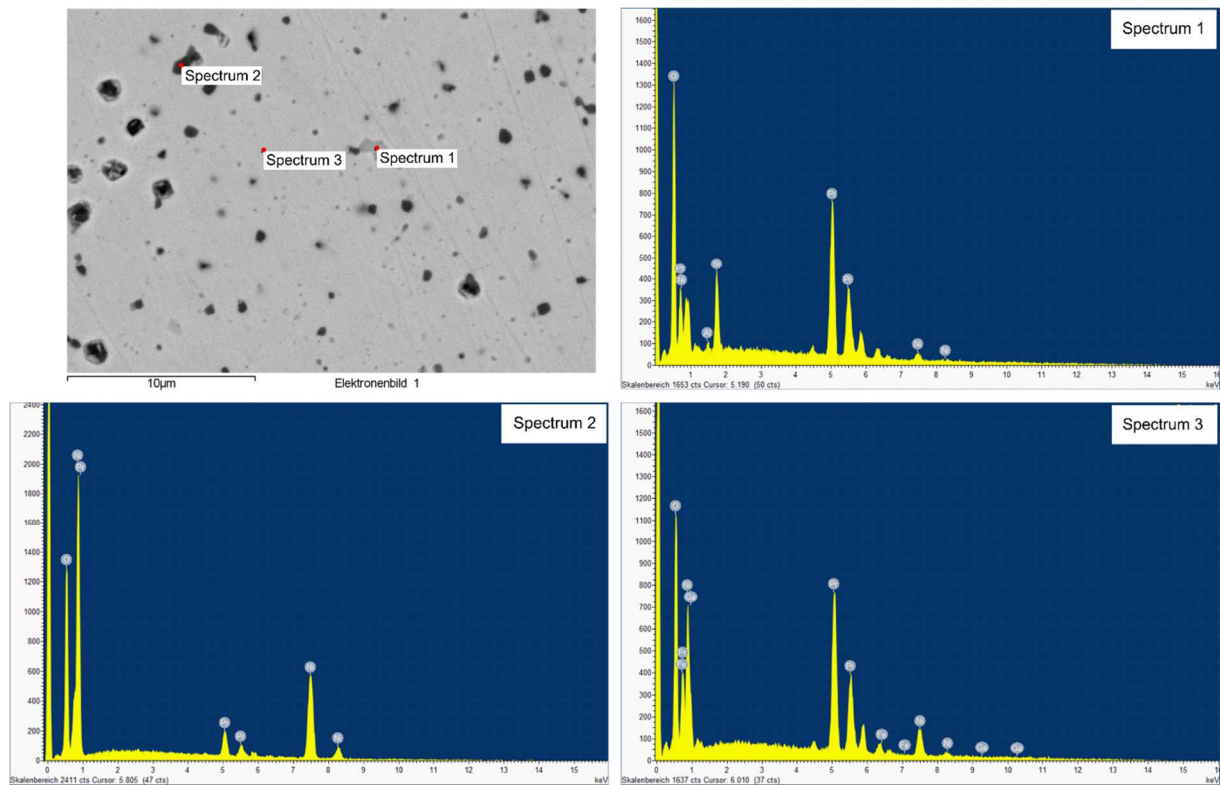
*Fig. 4.15: Detailed SEM-BSE image of PNO_MT2 and EDXS-spot analysis of several different phases.*

## 4.2 Long-term stability of dense La$_2$NiO$_{4+\delta}$ samples against Cr- and Si-poisoning

Two long-term experiments were conducted at temperatures of 700°C and 800°C under the same pO$_2$ and pH$_2$O to assess the long-term stability of LNO against the combined influences of Cr- and Si-contamination, based on the changes in oxygen exchange kinetics over time. Special emphasis was put on the chemical surface exchange coefficient ($k_{chem}$) of oxygen, which is regarded as a sensitive parameter providing information about the chemical and morphological condition of the sample surface. Conductivity relaxation measurements were carried out in both cases for approximately 4000 hours.

Average $k_{chem}$ values of the samples measured in dry atmosphere without Cr, but in the presence of Si, are regarded as representative for the fresh sample. Fig. 4.16 compares mean values based on 10 – 12 measurements at 700°C and 800°C, respectively to values published in the literature. Although there can be significant variation in $k_{chem}$ values published by different groups, depending on the surface quality of the sample (e.g. polishing and presence of contaminants) and experimental conditions (e.g. varying pO$_2$), the values obtained in this study are in good agreement with the published values.

Fig. 4.16: Chemical surface exchange coefficients ($k_{chem}$) of oxygen taken from literature in comparison with data from this work.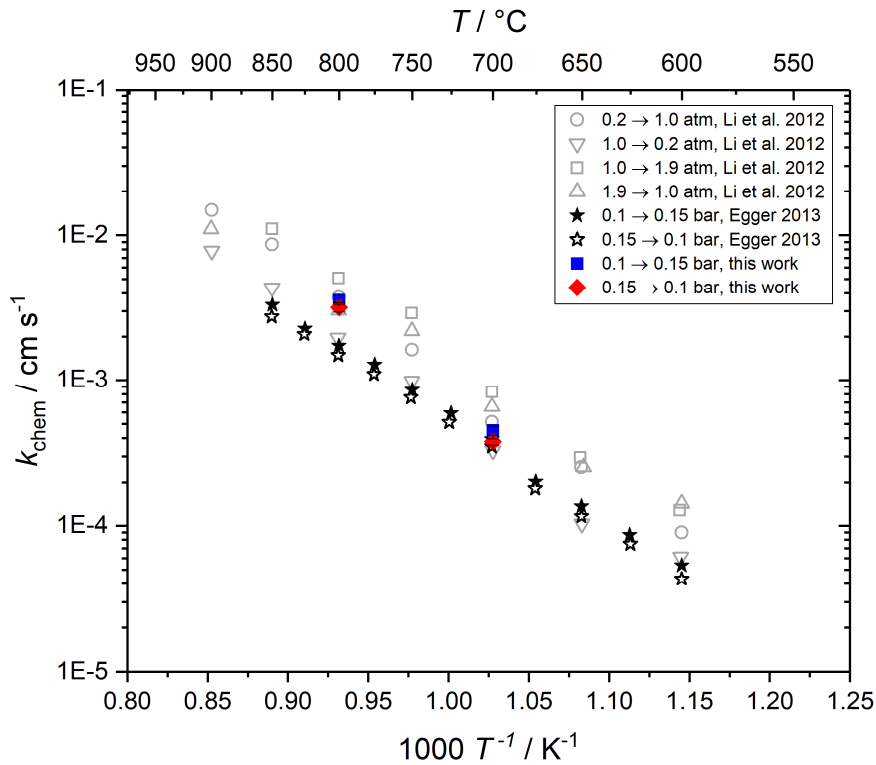 Open grey symbols are taken from Li and Haugsrud [272], black stars from Egger [84]. The blue and red symbols represent mean values of $k_{chem}$ for the oxidation (blue square) and the reduction (red diamond) reaction, calculated based on 10-12 data points measured in dry $O_2/Ar$ mixtures over a period of $13 - 22$ days at 700°C and 800°C, respectively. Image taken from Schrödl et al. [273].

### 4.2.1 Oxygen exchange kinetics at 700°C

The results presented in the following section were published in part in two publications by Schrödl et al. [241,274]. In Fig. 4.17 the temporal evolution of $k_{chem}$ at 700°C and $pO_2 = 0.1$ bar is presented. The first stage of the experiment was used to determine the intrinsic stability of LNO at 700°C in a dry gas stream ($pO_2 = 0.1$ bar). Surprisingly, the already high initial $k_{chem}$ value of $3.6 \times 10^{-4}$ cm s⁻¹ increased within the first 340 h, indicating some sort of surface activation. Due to the systematic deviation between the oxidation and the reduction step, average $k_{chem}$ values were calculated separately for both reaction steps over the course of stage 1 ($4.5 \times 10^{-4}$ cm s⁻¹ for the oxidation and $3.8 \times 10^{-4}$ cm s⁻¹ for the reduction process).

For the next 1180 h the sample was exposed to Cr- and Si-sources under dry conditions reducing $k_{chem}$ by a factor of 2.8. As XPS-analysis later revealed, this slight decrease in the surface activity can be ascribed to small amounts of Cr on the sample surface. The sharp kink in the $k_{chem}$ curve at the end of stage 2 at round 1390 h can be attributed to cooling the sample down to room temperature in order to remove the first ancillary sample for chemical and morphological analysis and subsequent reheating to 700°C. For the next experimental period,

the test gas was moderately humidified (30% r.h.) by pumping the gas stream through a water filled washing bottle, which was kept at 6°C in a thermostat before it entered the reactor. This led to rapid decrease of $k_{chem}$ by a factor of 40, pointing to significant chemical changes on the sample surface. It should be noted that at the end of this stage the sample was again cooled down to room temperature to remove the second ancillary LNO piece. This time no change in $k_{chem}$ was observed after reheating to 700°C. A further increase in humidity to 60% r.h. (stage 4) did not increase the degradation rate any further. That is not surprising considering the partial pressure of the most abundant, volatile Cr-species, chromic acid ($H_2CrO_4$) only changes from $5.4 \times 10^{-8}$ bar to $1.1 \times 10^{-7}$ bar, and the partial pressure of the dominant volatile Si-species, $H_4SiO_4$, increases from $3.1 \times 10^{-11}$ bar (30%), $1.3 \times 10^{-10}$ bar when humidity is raised from 30% r.h. to 60% r.h. (calculated using FactSage v.6.4 [275] based on data from Ebbinghaus [276] and Jacobson et al. [236]), assuming that volatile Cr- and Si-species are involved in the degradation of LNO. The total decrease of $k_{chem}$ over the course of the experiment of almost 3800 h amounted to a factor 230.
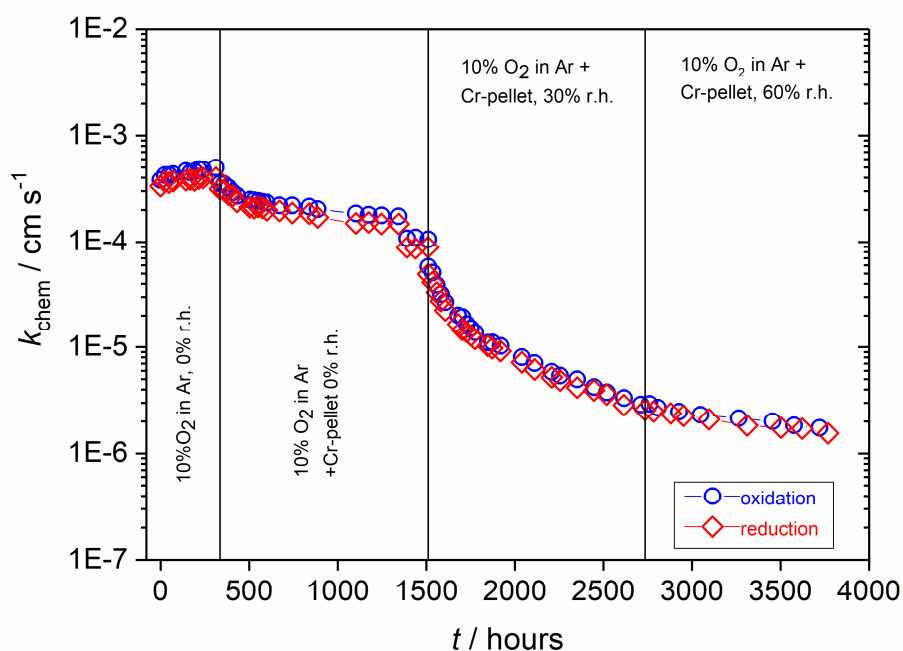


Fig. 4.17: Chemical surface exchange coefficient ($k_{chem}$) of oxygen of LNO as a function of time at 700°C and $pO_2$ = 0.1 bar (Schrödl et al. [241]).

Due to the sample geometry (vdP) it was not possible to determine $k_{chem}$ and $D_{chem}$ simultaneously from the measured data. VdP sample geometry can be applied for conductivity relaxation measurements, however, the diffusion must be limited to the direction perpendicular to the surface of the slab [277]. This can either be achieved by actively blocking some faces of the sample with an oxygen tight material (gold) or by limiting the sample

thickness, as for a diameter-to-thickness ratio of 10:1 or higher the contribution of in-plane diffusion paths is negligible [278].

Additionally, the electronic conductivity of LNO was measured between the conductivity relaxation measurements (Fig. 4.18), which remained between 80-84 S cm$^{-1}$ for the duration of the degradation experiment. This suggests that the bulk of the tested sample, as well as the gold contacts remained intact and that the degradation processes mainly affected the surface of LNO, which is indeed the case as will be discussed in later sections.
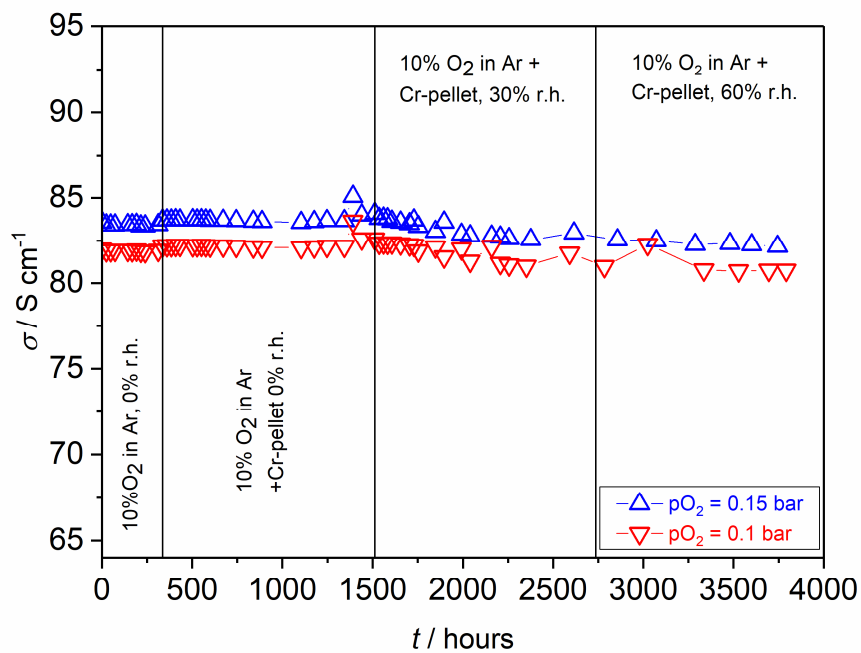


*Fig. 4.18: Electronic conductivity σ of LNO at 700°C and pO₂ = 0.1 bar (Schrödl et al. [241]).*

### 4.2.2 Chemical and morphological analyses of the 700°C sample

The morphological changes caused by the progressive degradation of LNO were investigated using atomic force microscopy (AFM). In comparison to SEM images, AFM provides better lateral resolution as well as height information, which allows the quantification of the surface roughness. This advantage was used to track the formation of a degradation layer on the sample surface. Fig. 4.19 presents large AFM surface scans (10×10 μm$^2$) of LNO at different stages of the experiment. The corresponding values of the root mean square surface roughness $\sigma_{rms}$ and the lateral correlation length are listed in Table 4.2.

The undegraded, polished sample depicted in Fig. 4.19a shows a very smooth surface, which is also indicated by the small $\sigma_{rms}$ and ξ. The only evident surface features are fine grooves left over by the polishing process.
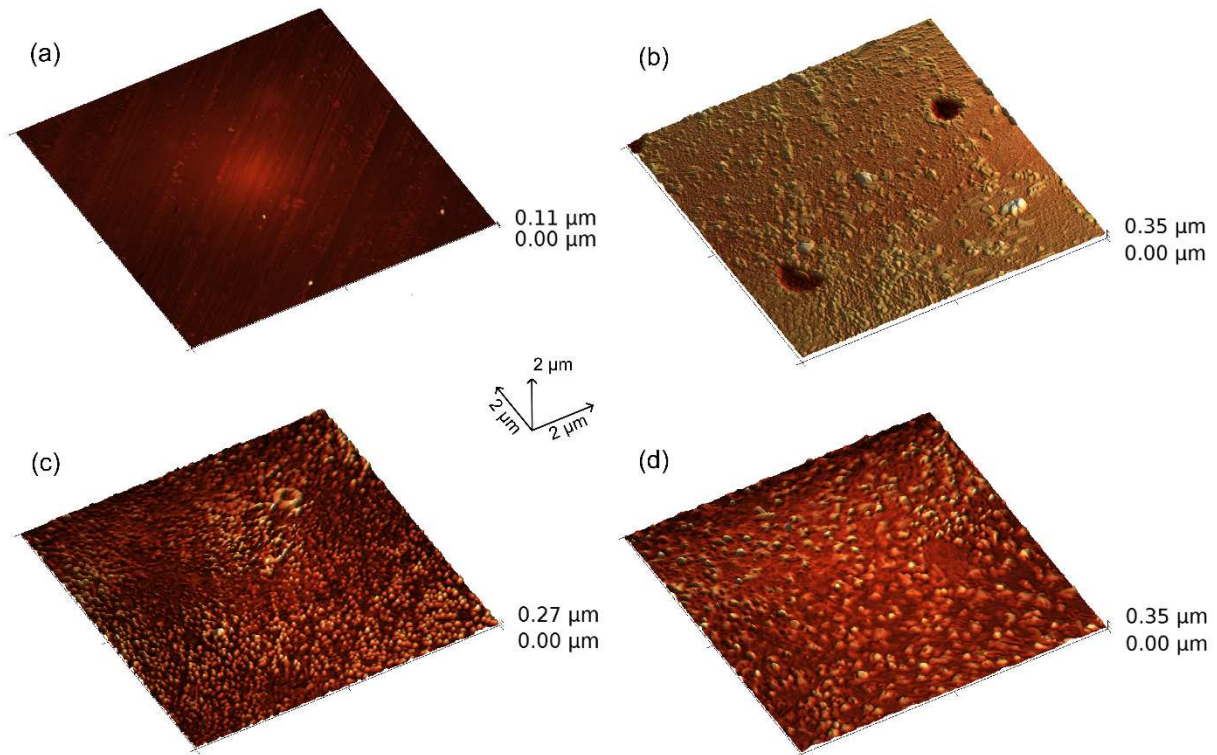
*Fig. 4.19: 10x10 µm² AFM surface images of LNO at different experimental stages in a three-dimensional, illuminated presentation with (a) the freshly polished sample, (b) after 1000 h in dry atmosphere with Cr and Si present, (c) after an additional 1000 h in the presence of Cr and Si at moderate humidity (30% r.h.) and (d) after yet another 1000 h with Cr and Si in strongly humidified atmosphere (60 % r.h.). Image taken from Schrödl et al. [241].*

After 1000 h under the influence Cr and Si in dry test gas, a slight increase in $\sigma_{rms}$ and $\xi$ by a factor of 6 and 1.5, respectively, suggest the formation of small structures on the surface, which are indeed visible in Fig. 4.19b. Fine, rod-like crystallites are spread across the sample surface. In some areas cavities of approximately 1 µm in diameter have formed, which are also surrounded by crystallites.

*Table 4.2: Root mean square surface roughness $\sigma_{rms}$ and lateral correlation length $\xi$ of LNO at 700°C and different stages of the experiment.*

| Stage | Treatment | $\sigma_{rms}$ / nm | $\xi$ / nm | Image size / µm2 |
|---|---|---|---|---|
| 0 | Polished | 3 | 60 | 1×1 |
| 2 | + 1000 hours Cr/Si, dry | 18 | 96 | 1×1 |
| 3 | + 1000 hours Cr/Si, 30% r.h. | 34 | 88 | 10×10 |
| 4 | + 1000 hours Cr/Si, 60% r.h. | 32 | 141 | 10×10 |

After stage 3 – treatment in 30% r.h. with Cr- and Si present – the surface is densely covered in roundly shaped crystallites featuring a diameter of 50 – 300 nm. Accordingly, an increase in surface roughness and a decrease in lateral correlation length is observed, indicating an

increase in crystallite height and number. As is indicated by $\sigma_{rms}$ and ξ elevating the humidity levels in the reactor to 60% r.h. leads to an enlargement of the crystalline grains, rather than growth in height, as is also indicated by $\sigma_{rms}$ and ξ.
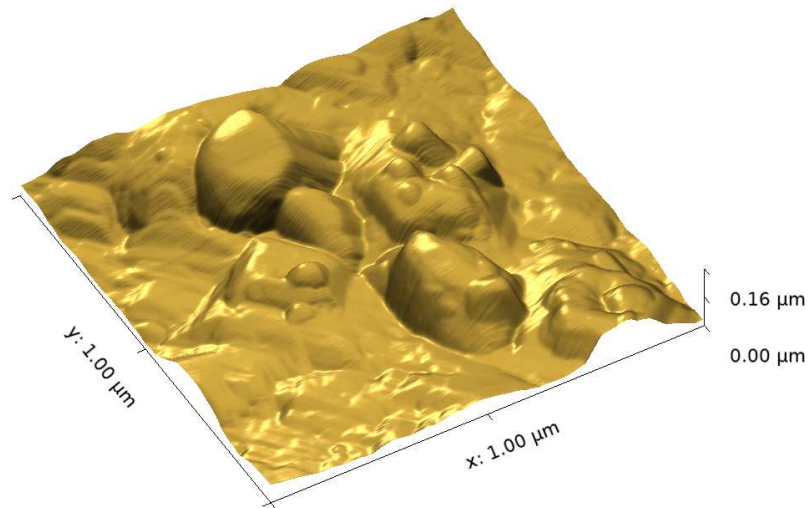


*Fig. 4.20: Detailed 3D AFM image (1×1 µm$^2$) of small crystallite, protruding from the LNO surface after approximately 3800 h in dry and humid atmospheres in the presence of a Cr- and a Si-source (taken from Schrödl et al. [241]).*

Fig. 4.20 shows a detailed view of some surface features, which present themselves as irregularly shaped structures. The absence of crystalline structures with clearly defined facets might be hinting at the presence of multiple secondary phases, as opposed to one main degradation phase. The sample surface of the most degraded sample - which was exposed to all four subsequent steps of environmental conditions – was further investigated using high-resolution scanning electron microscopy (Fig. 4.21).
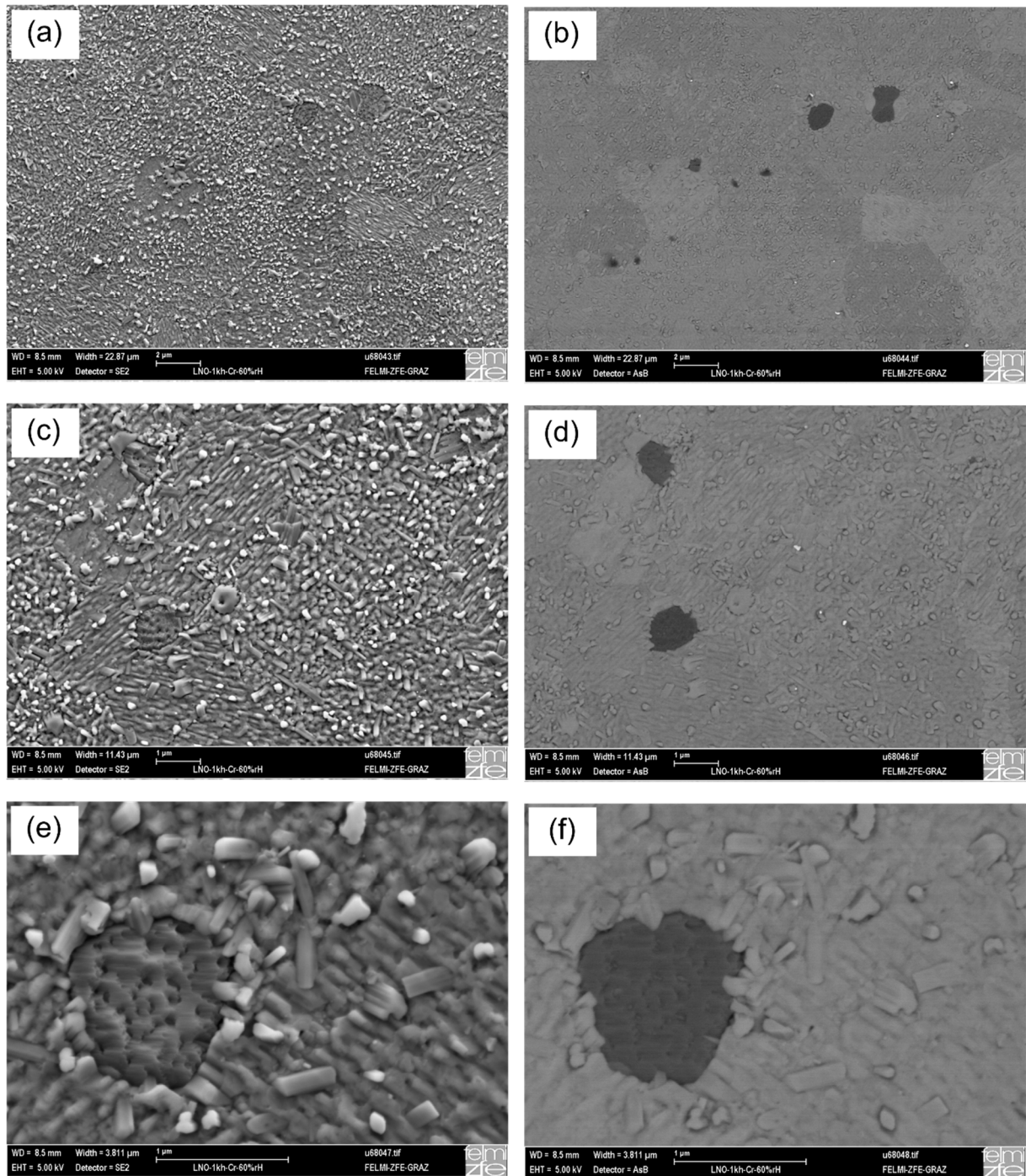
*Fig. 4.21: High resolution SEM images of the surface of the main sample, which was exposed to all four subsequent experimental stages. Images a, c and e were recorded in secondary electron mode, images b, d and f in backscattered electron mode.*

Images taken with the secondary electron detector provide a clearer representation of the surface morphology than those acquired by AFM but lack the additional height information. As has been shown by AFM analysis, the sample surface is almost completely covered with deposited material and features elongated, square-edged crystallites (Fig. 4.21a, c, and e). The orientation of these crystallites seems to be somewhat correlated with the LNO grain structure

underneath the crystals. Dark, round patches visible in the BSE-images (Fig. 4.21b, d, and f) were identified as NiO secondary phases by EDXS-spot analysis.

To obtain more information about the lateral distribution of Cr and Si on the degraded main sample, EDXS-elemental distribution maps were recorded (see Fig. 4.22). In addition to the investigated contaminants, La-, Ni-, and O-distributions were also determined to gain insight into the chemical composition of the formed secondary phases. In the backscattered electron (BSE) image (Fig. 4.22, top left) the grain structure is distinctly visible due to channeling contrast, which is caused by a difference in crystal orientation, i.e. crystallite orientations featuring lattice planes with a large number of atoms backscatter electrons with a higher probability than orientations with less occupied lattice planes. The large surface structures in the bottom section of the image turned out to be particles deposited on top of the surface. Small, roundly shaped dots in the BSE-image, which correlate with bright spots in the Ni-map, were identified by EDXS as NiO inclusions. NiO has also been discovered in a freshly sintered sample (see Fig. 4.10 and Fig. 4.11), which was prepared from the same LNO pellet as the main sample. It is conceivable that the NiO is formed during the initial sintering step or is the result of Ni-excess in the raw powder. However, room temperature X-ray diffraction measurements of the powder used as a raw material did not confirm the presence of NiO (Fig. 4.5). La as well as O are spread evenly across the sample surface. The distribution of Cr could not be determined reliably by EDXS due to the strong overlaps of the Cr-L line (0.573 keV) with the O-K line (0.525 keV) and the Cr-K-line (5.410 keV) with the La-L line (5.372 keV). Since also a WDXS-area analysis did not provide any evidence of Cr-contamination it is reasonable to assume that only a very small amount of Cr was deposited, even under humid conditions. Si-species on the other hand were clearly identified by EDXS and found to be dispersed across the entire surface, as well as accumulated in insular patches.
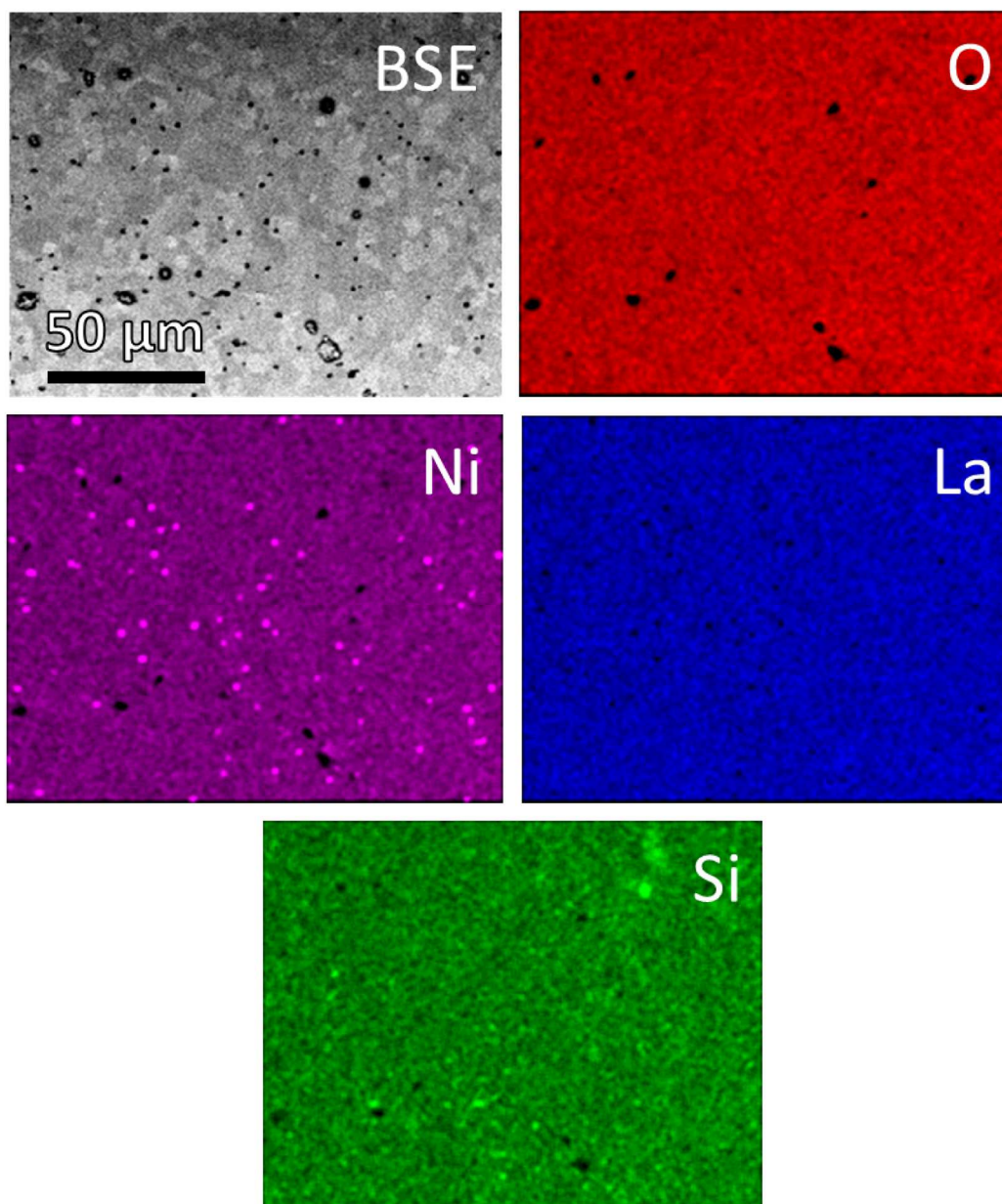
*Fig. 4.22: SEM-BSE image and corresponding SEM-EDXS-elemental distribution maps of the main LNO sample after all four subsequent stages of the degradation experiment (taken from Schrödl et al. [241]).*

In addition to the lateral elemental distribution, depth profiles of La, Ni, O, and Cr were acquired using X-ray photoelectron spectroscopy (XPS) in combination with $Ar^+$-sputtering. In Fig. 4.23, the XPS-depth profiles recorded on a freshly polished sample (a), after 1000 h in dry atmosphere (10% $Ar/O_2$) in the presence of Cr and Si (b), after additional 1000 h in 30% r.h. with Cr and Si present (c) and after additional 1000 h in strongly humidified test gas (60% r.h.) are presented. As a complementary technique to SEM-EDXS-mapping, XPS proved to be useful for the detection of small amounts of Cr, but not for Si, due to overlapping signals with Bi and Cd contaminants. Fig. 4.23a shows the profiles of La, Ni, and O of the as-prepared, polished sample prior to the degradation experiment. The profiles were recorded until a stable

composition was reached. Deviations from the nominal LNO composition are most likely caused by preferential sputtering of lighter elements. However, XPS-depth profiling still delivers useful information about general trends with respect to changes in elemental composition. The steep decline of the profiles within the first few nm were attributed to adsorbed species like hydroxyl and hydrate compounds. In addition to a surface contamination with carbon, which is not shown here for reasons of clarity, small amounts of Bi and Cd (<3 at.%) were found on all degraded samples. These elements were likely introduced to the system via the gold paste used for the electrical contacts on the main sample. Bi was indeed detected via SEM-EDXS-analysis in the unfired gold paste. Fig. 4.23b confirms the presence of small amounts of Cr, which could explain the earlier mentioned decline in $k_{chem}$ during this stage of the experiment. Further examination of the data reveals increased levels of La within the topmost 40 nm, indicating La-segregation and therefore possibly the formation of compounds containing La and Cr.
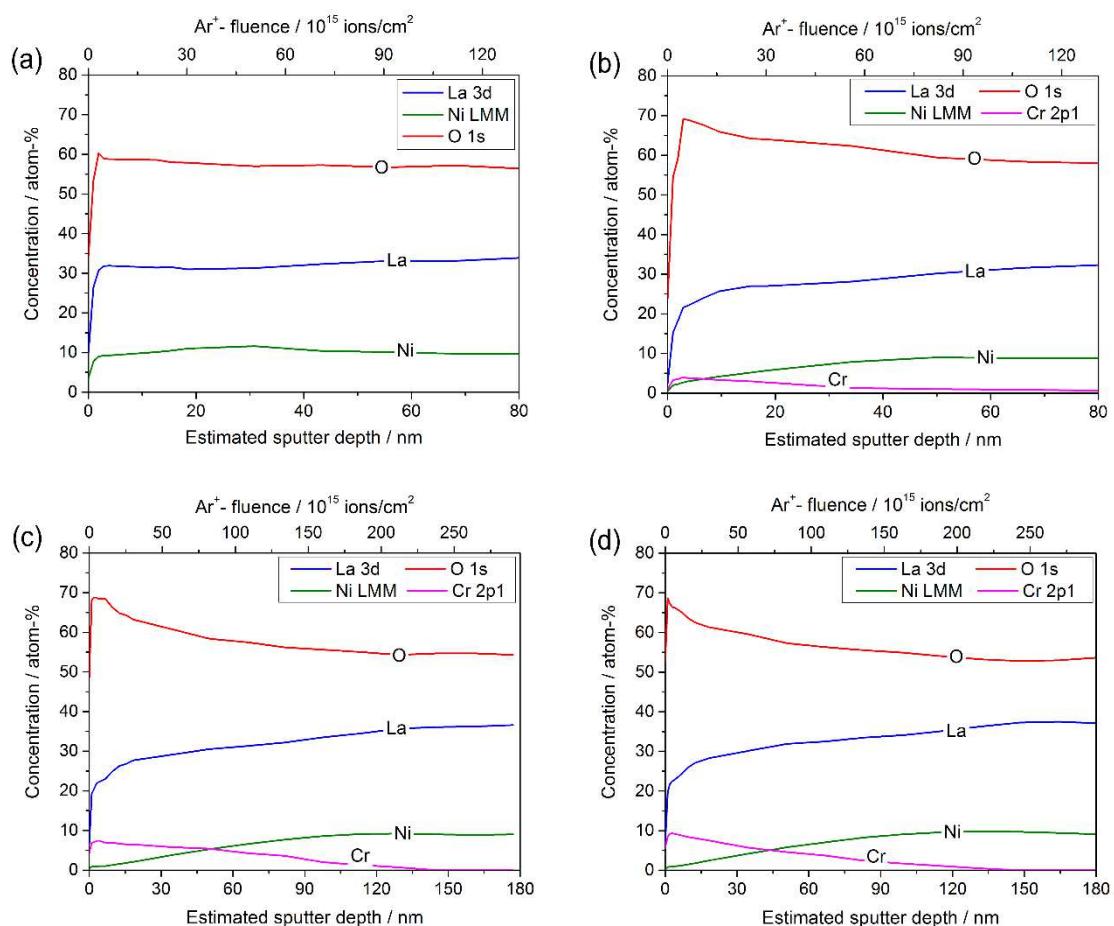


Fig. 4.23: XPS-elemental depth profiles of La, Ni, O and deposited Cr-impurities of (a) the undegraded, polished sample, (b) after approximately 1000 h in dry atmosphere at 700°C in the presence of Cr and Si, (c) after an additional 1000 h in 30% r.h. with Cr and Si present and (d) after another 1000 h in 60% r.h. with a Cr-and a Si-source present (taken from Schrödl et al [241]).

The segregation of A-site cations in LNO was demonstrated in degradation experiments on La$_2$NiO$_{4+\delta}$ single crystals via HRTEM by Gauquelin et al. [279], on polycrystalline ceramic samples using Low-Energy Ion Scattering (LEIS) by Druce et al. [280,281] and on La$_{1.67}$Sr$_{0.33}$NiO$_4$ single crystals by Burriel et al. [282]. Introducing humidity to the gas stream (Fig. 4.23c) leads – as expected – to an enrichment of Cr on the sample surface, as well as an increased thickness of the degraded surface layer. Associated with the increased Cr-concentration is a depletion of Ni, which further indicates the assumed formation of La-chromate. After additional 1000 h in even higher humidity (Fig. 4.23d) the surface levels of Cr have increased further, however, the layer thickness of the degradation layer seems unchanged. This is in good agreement with the observed coarsening of the surface crystallites depicted in Fig. 4.19d and the fact that no strong decline of $k_{chem}$ was detected at elevated humidity levels (see Fig. 4.17).

To determine the composition of the secondary phases formed by degradation processes the main sample was investigated by analytical TEM. A STEM-HAADF image of the prepared lamella is presented in Fig. 4.24. The ring-shaped HAADF detector allows for the angle-dependent detection of strongly scattered electrons, which provides information about the mean atomic number of the elements in the sample. Elements with low atomic number scatter electrons to smaller angles and therefore produce less intensity, i.e. they appear darker than elements with higher atomic number. The image shows large LNO grains of 2-4 µm in diameter, intermixed with secondary phases, which appear dark in the image. These phases were identified as NiO and Zr- or Si-containing compounds, which were already present as impurities in the raw powder. The degradation layer is a small zone of approximately 100 – 150 nm under the Pt-layer. A large round grain of La-silicate was detected in the middle of the degradation layer. A detailed view of this phase in combination with an EDXS-line profile is presented in Fig. 4.25. The EDXS-profile across the secondary phase indicates that it is comprised of La, Si, O, and small amounts of Al, but completely depleted of Ni. The round shape and the size of the Si-phase suggest that it is a Si-rich inclusion, most likely formed during sintering from segregating impurities that were present in the powder, but at concentrations below the detection limit of XRD. However, analysis of the sintered, undegraded sample also showed that Si-Al phases were present after sintering (see Fig. 4.11). Si and Zr- phases in ceramic materials are often the result of the attrition of Si$_3$N$_4$ or ZrO$_2$ milling balls during ball milling procedures [193,283].
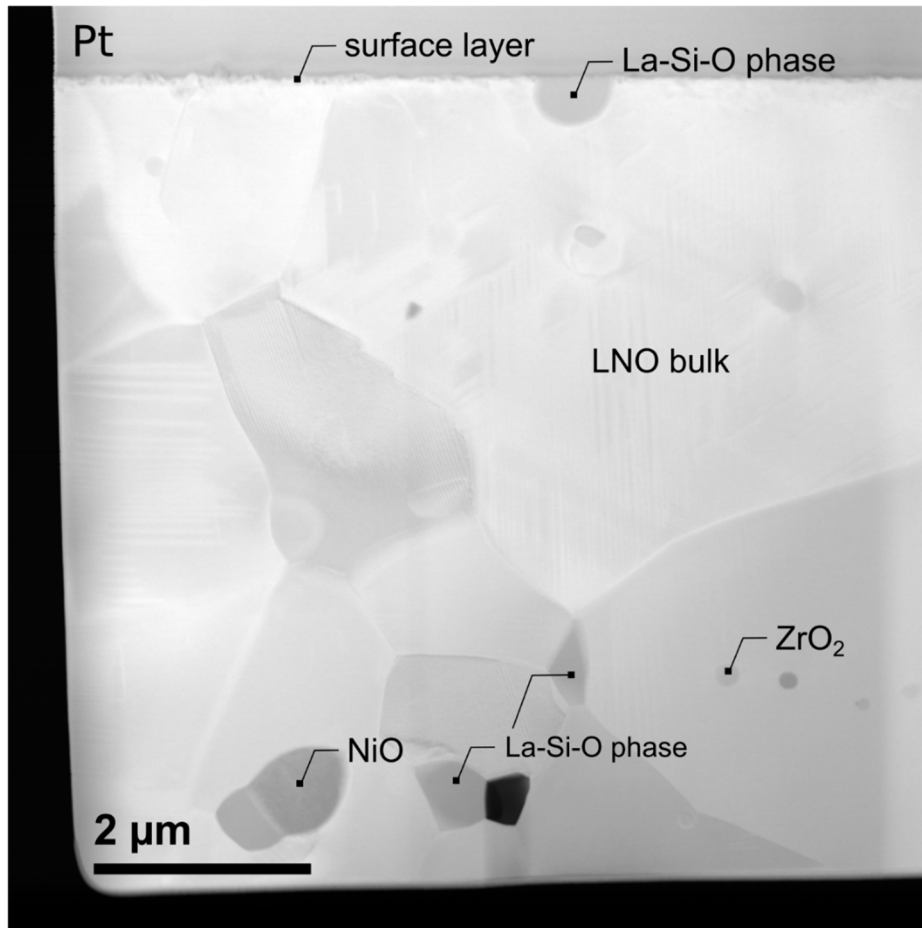
*Fig. 4.24: TEM lamella of a degraded LNO sample after stage 4 of the degradation experiment. The sample was exposed to a Cr- and Si-source at 700°C for more than 3000 h in dry and humid atmospheres.*
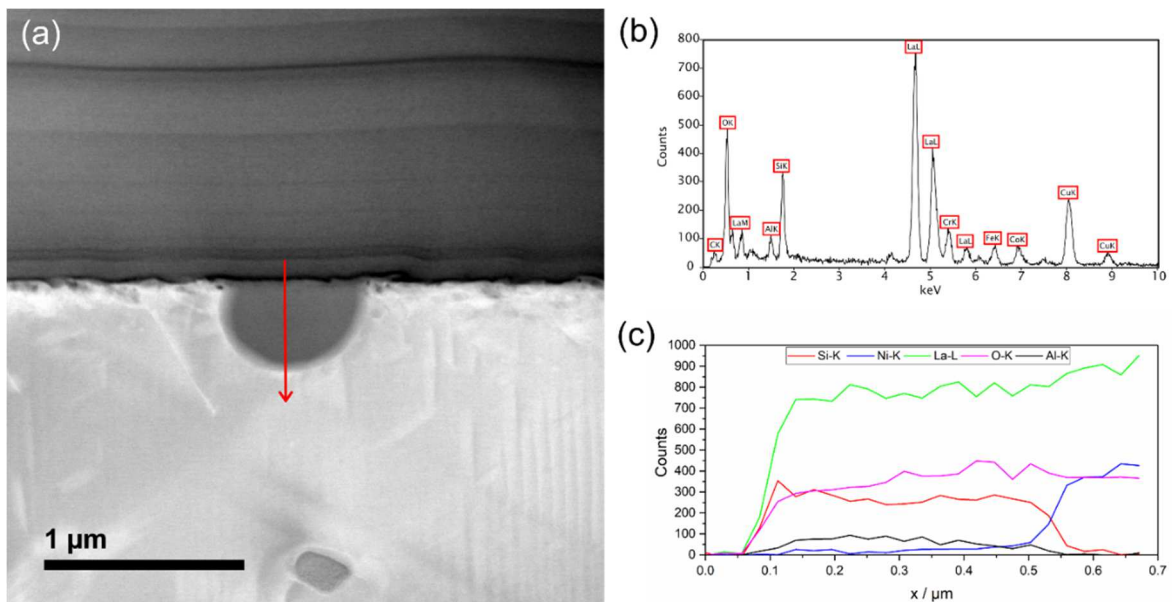


*Fig. 4.25: Detailed cross-section view of (a) the embedded Si-containing phase, (b) EDX-spectrum and (c) EDXS-line profile along the red arrow.*

Considering that a lot of these Si- and Zr-containing phases are deeply embedded in LNO grains it is reasonable to assume that they are not the result of surface degradation processes.

Fig. 4.26 presents a cross-section view of the layer of nanocrystalline material deposited on top of LNO, which is depicted from the top in the SEM images in Fig. 4.21. The distinctly faceted crystal on top is mainly composed of La, Si, and O, as well as of small amounts of Cd according to EDXS-analysis (Fig. 4.26b). Cd-impurities were most likely introduced by the used gold paste, as elements like Cd and Bi are often used as bonding or fluxing agents in contacting pastes [220,284-286]. Post-test SEM-EDXS and XRF analysis of the applied gold paste indeed revealed the presence of significant amounts of Bi and traces of Cd. The pronounced Pt-peaks are caused by the protective coating, which is applied during FIB preparation, in which the crystal is embedded. Fe and Co signals are typically the result of interactions of the electron beam with parts of the microscope column and the Cu-signal can be ascribed to the copper grid, which is used to mount the sample.
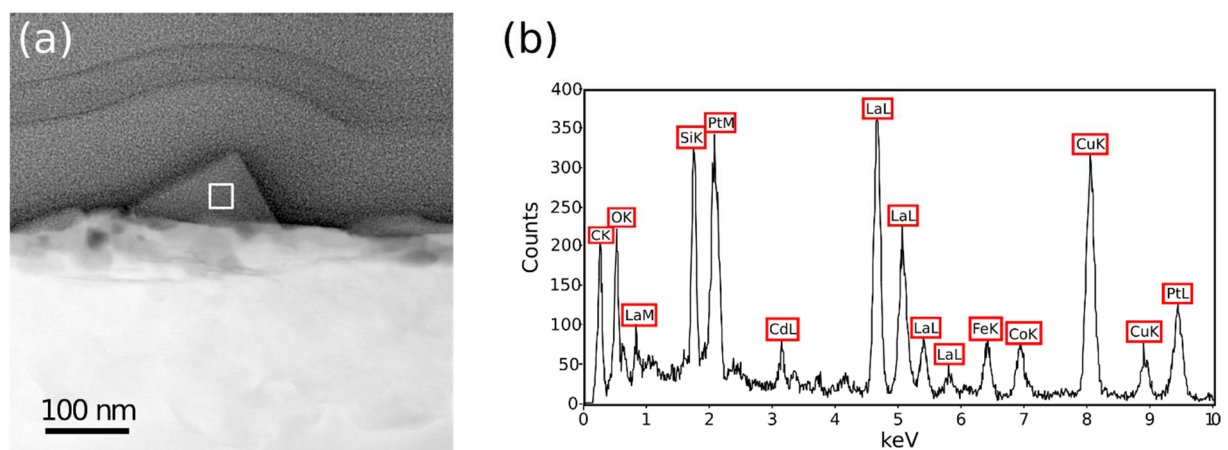


*Fig. 4.26: (a) STEM-HAADF cross-section image of the degraded surface of LNO and (b) the corresponding EDXS-analysis of the region marked with a white square (taken from Schrödl et al. [274]).*

The different grey-values of the 50 – 100 nm surface layer below the faceted Cd-containing crystal in the HAADF-image (Fig. 4.26) are caused by a difference in material density rather than distinct chemical composition. This is supported by EDXS-spot analysis in 3 different areas of the degradation layer (Fig. 4.27), which revealed differences in the concentrations of Cr and Si in areas with similar grey values. The detection of Cr-impurities via EDXS-analysis proved to be challenging due to the superposition of the Cr $K_{\alpha1/\alpha2}$ and the La $L_{\beta1/\beta2}$ X-ray emission lines. While the Cr – concentration is high enough at site A for the Cr-signal to be clearly discerned (see Fig. 4.27a) - as indicated by the Cr $K_{\alpha1/\alpha2}$ signal in Fig. 4.27b – it is below the detection limit at site B and C. In this case, the highly sensitive EEL spectroscopy is far better suited to detect small amounts of Cr, provided that the sample lamella is thin enough. Indeed, the presence of Cr was clearly proven by EELS at site B (Fig. 4.27c). The bright spots visible in the

upper part of the image were caused by prolonged exposure to the electron beam. Imaging of a different part of the near-surface zone revealed a mostly constant thickness of the degradation layer, apart from a cavity of approximately 200 nm in diameter, which appears to be filled with material (a). The roundly shaped structure in the bottom left corner of the image is another Zr-O inclusion. EDXS- and EELS-elemental distribution maps showed that Si is deposited in patches on top of a layer containing Cr (b). La and O seem to be present in both the Si- and Cr-deposits, which suggests the formation of La-silicate and La-chromate phases.
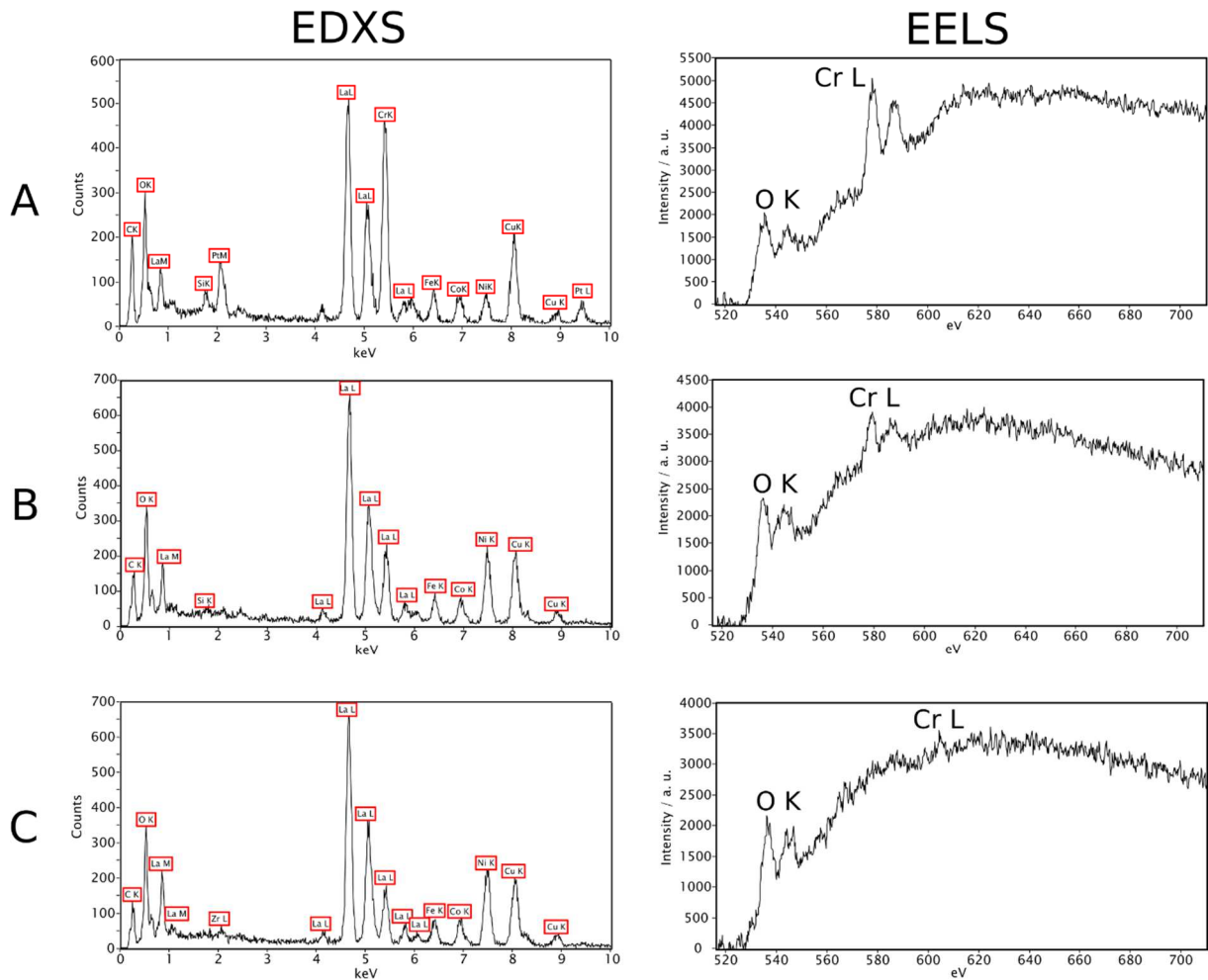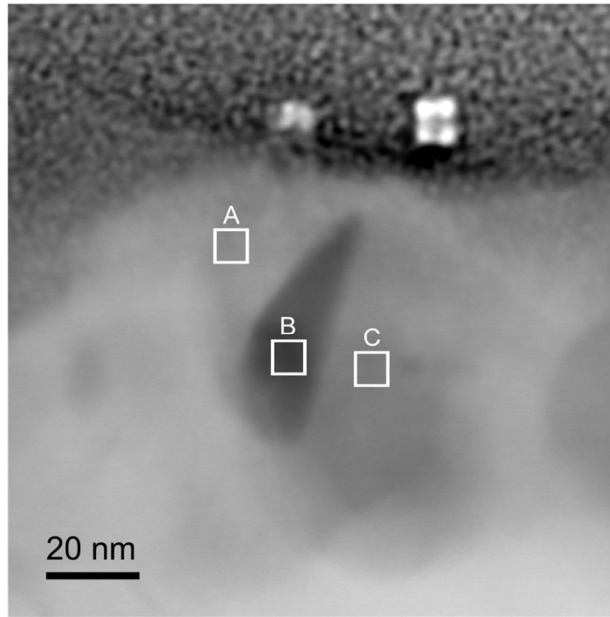
Fig. 4.27: STEM-HAADF cross-section image of the decomposed surface layer of LNO, EDXS- and EELS-analysis of 3 different areas marked with A, B and C (taken from Schrödl et al. [274]).

Ni is found predominantly in areas depleted of Cr. This is in good agreement with the measured XPS-depth profiles (Fig. 4.23), which also showed opposite trends in the concentrations of Ni and Cr. The chemical composition of the La-chromate and La-silicate phases could not be determined using EDXS due to the nanocrystalline nature of the degradation layer.

The so far presented findings suggest a degradation mechanism induced by the segregation of La to the surface during long-term treatment at 700°C in dry $O_2$/Ar atmosphere. The La-depleted layer underneath the La-enriched surface layer contains presumably a mixture of different Ni-rich Ruddlesden-Popper phases ($La_{n+1}Ni_nO_{3n+1}$) or potentially the end member of the series, $LaNiO_3$ ($n=\infty$). The surface segregation of A-site cations [280,282,287-289] and the formation of these Ruddlesden-Popper type nickelates [279] have been reported in the literature. Čebašek et al. found that the diffusion of A-site cations in LNO is dominated by bulk diffusion processes [290,291]. Volatile Si- and Cr-species are transported to the surface via the gas-phase especially under humid conditions where they react to La-chromate and La-silicate phases. The continuous decrease in Cr-concentration from surface to bulk and the corresponding increase in Ni-content might suggest the formation of a $La(Cr, Ni)O_3$ perovskite phase where Cr is partly substituted by Ni at the B-site in the $ABO_3$ structure [292].
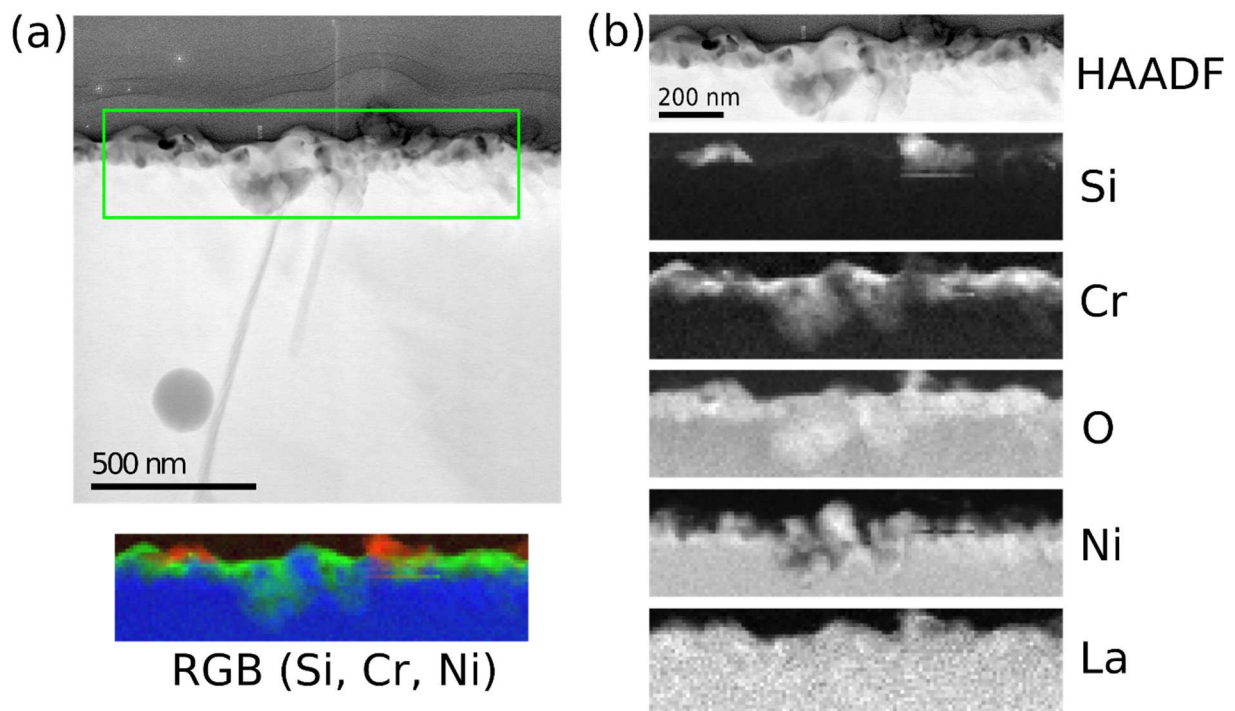


*Fig. 4.28: (a, top) STEM-cross section image of the degraded LNO sample, (a, bottom) colored image of the area marked with the green rectangle and showing the distribution of Si, Cr, and Ni in red, green and blue, respectively. (b) STEM-HAADF image and corresponding elemental distribution maps from the zone marked in (a). The Si-, La-, O-, and Ni-distribution maps were generated using EDXS and the Cr-map using EELS (taken from Schrödl et al. [274]).*

### 4.2.3 Oxygen exchange kinetics at 800°C

To establish a clearer picture about the chemical changes in LNO due to the prolonged exposure to Cr and Si, a second long-term study on a dense LNO sample was conducted for approximately 4000 h. Parts of the results of this study have already been published in several publications [273,293,294]. The oxygen exchange kinetics was determined via dc-conductivity relaxation measurements on a bar-shaped sample in linear four-point geometry at 800°C, which is a frequently required operating temperature for SOFCs. The chosen sample geometry allowed for the simultaneous measurement of both, $k_{chem}$ and $D_{chem}$, which are plotted as a function of time in Fig. 4.29 and Fig. 4.30, respectively. Again, oxidation steps are presented in blue and reduction steps are shown in red symbols. Abrupt changes in $pO_2$ were carried out between 0.1 and 0.15 bar. Additionally, the electrical conductivity of the sample was measured between oxidation and reduction steps to determine changes in the bulk material and electrical contacts. Since all measurements were carried out in a quartz glass reactor a Si-source was always present.
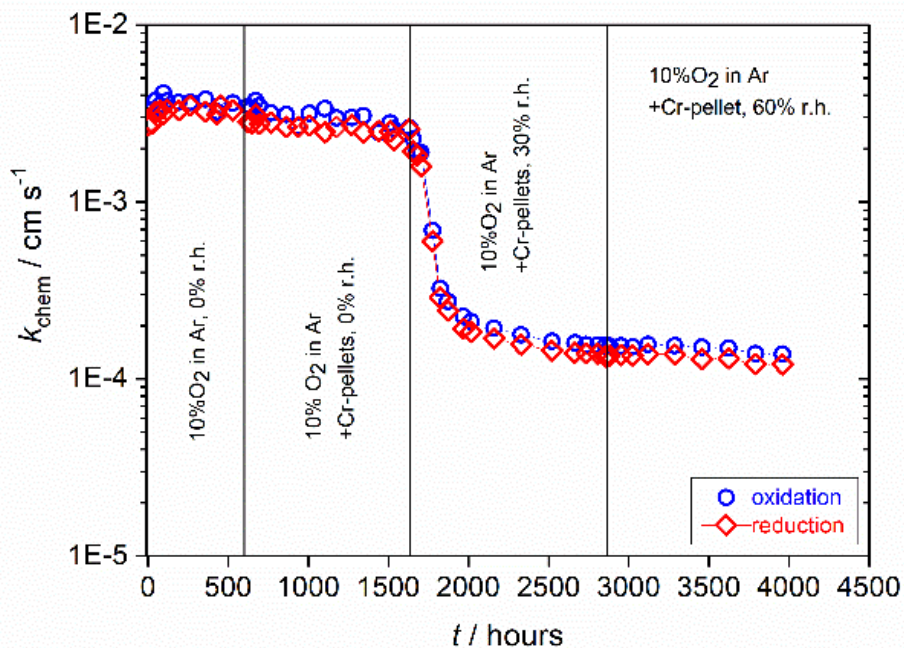


*Fig. 4.29: Chemical surface exchange coefficient $k_{chem}$ of oxygen at 800°C and $pO_2$ = 0.1 bar as a function of time (taken from [273]).*

For the first 600 h LNO was kept at 800°C in dry atmosphere and without the presence of a Cr-source. Under these conditions, LNO exhibits excellent intrinsic stability as $k_{chem}$ and $D_{chem}$

remained stable at values of $3.4 \times 10^{-3}$ cm s$^{-1}$ and $1.5 \times 10^{-4}$ cm$^2$ s$^{-1}$ (average of oxidation and reduction steps), respectively.

To fix a broken contact the sample had to be cooled down to room temperature and subsequently reheated to 800°C. This did not affect the kinetic parameters in any way. After 600 h a Cr-source was placed near the sample and the CR measurements were continued for approximately 1000 h. During this time period $k_{chem}$ was slightly reduced by a factor of 1.3, indicating subtle chemical changes at the sample surface. A similar, but more pronounced effect was observed for the LNO sample tested at 700°C (see Fig. 4.17), which could be explained by the formation of small Cr-containing crystallites on the sample surface. Humidification of the test gas (30% r.h.) resulted in a steep decrease of $k_{chem}$ by a factor of 18. Consequently, $D_{chem}$ could no longer be determined from the measured conductivity curves (see Fig. 4.30). This suggests that the oxygen exchange reaction changed from a mixed-controlled into a surface-controlled process, which indicates significant chemical alterations of the sample surface, slowing the oxygen reduction reaction down. The most likely explanation for this is the accelerated deposition of impurity phases, which is caused by the enhanced gas phase transport of volatile Cr-species ($CrO_2(OH)_2$) and the formation of volatile Si-compounds ($H_4SiO_4$) under humid conditions [236,276]. After 1000 hours under moderately humid conditions with a Cr- and a Si-source the surface exchange coefficient had stabilized at a value of $1.4 \times 10^{-4}$ cm s$^{-1}$. Another increase in humidity to 60% r.h. for a period of 1000 h lead only to a slight decrease in $k_{chem}$. Given that at 800°C the partial pressure of the most abundant Cr-vapor species ($CrO_2(OH)_2$) only increases from $1.9 \times 10^{-8}$ bar at 30% r.h. to $3.9 \times 10^{-8}$ bar at 60% r.h. this is hardly surprising [219]. The electrical conductivity of the sample (Fig. 4.31) was fairly constant at values between 67 and 73 S cm$^{-1}$ for the entire duration of the experiment, which suggests that the bulk of the LNO sample remained unaffected by degradation processes. Compared to the long-term degradation experiment at 700°C, where a decrease in $k_{chem}$ by a factor of 230 was observed (see section 4.2), LNO seems to be much less affected by the Cr/Si-degradation at 800°C, since $k_{chem}$ decreased at 800°C by only a factor of 25 under otherwise similar experimental conditions. It should be noted that these experiments did not allow for the determination of humidity effects on LNO, due to the fact that all measurements were conducted in a quartz glass reactor, which acted as constant Si-source.
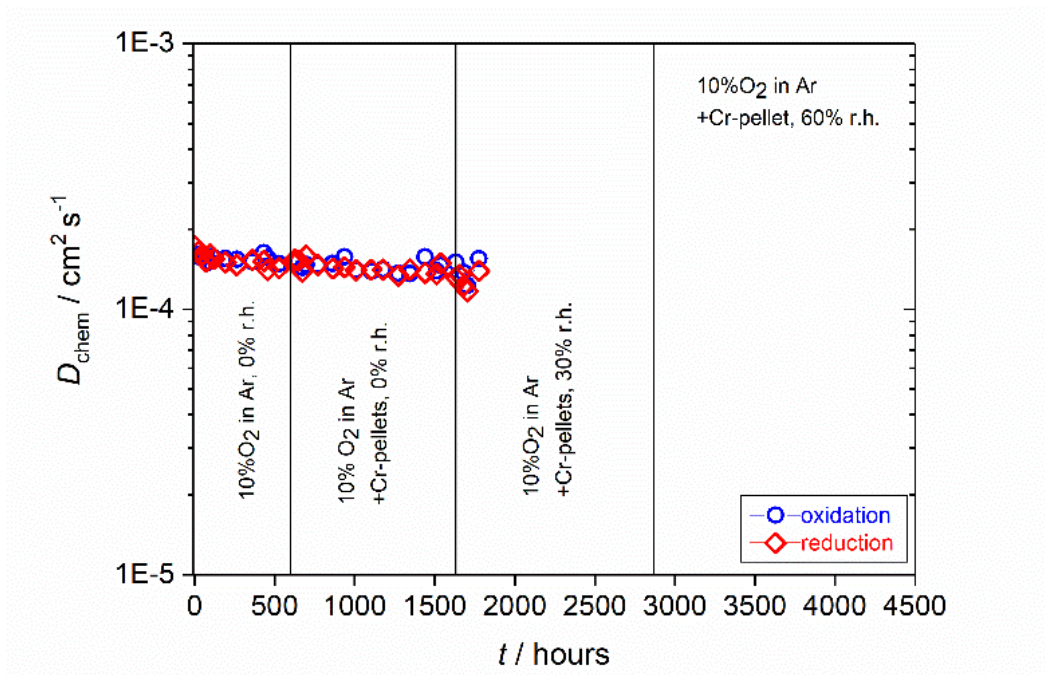
Fig. 4.30: Chemical diffusion coefficient $D_{chem}$ of oxygen at 800°C and $pO_2$ = 0.1 bar as a function of time (taken from Schrödl et al. [273]).
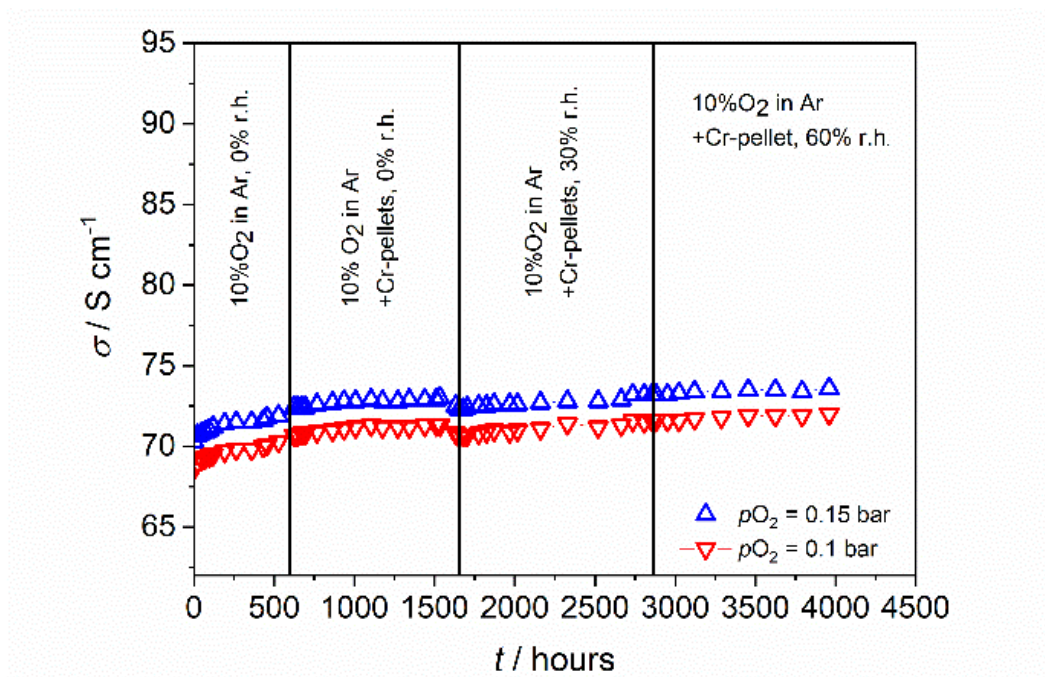


Fig. 4.31: Electrical conductivity σ of LNO at 800°C and $p(O_2)$ = 0.1 bar as a function of time (taken from Schrödl et al. [273]).

## 4.2.4 Chemical and morphological analyses of the 800°C sample

To examine the effects of Cr- and Si-deposition under dry and humid conditions on polycrystalline LNO surfaces, AFM and SEM-EDXS-analyses were performed on additional LNO samples, which were placed in the reactor together with the main sample and removed at different stages of the experiment. Fig. 4.32 displays 2D-AFM images of a freshly polished (a), a sample treated for 600 h under dry and Cr-free conditions and 1000 h with Cr (b), a sample kept for additional 1000 h in 30% r. h. close to a Cr- and a Si-source (c) and the main sample, which remained in the reactor for another 1000 h in even higher humidity (60% r.h.) (d). In comparison to the fresh surface, which is - aside from some scoring due to polishing – smooth, the surface roughness significantly increased during annealing in dry atmosphere and in the presence of Cr. Similarly, increased surface roughness was described by Gauquelin et al., who observed elongated surface features on single crystal LNO surfaces after annealing in dry, synthetic air for 13 days at 1000°C [279].
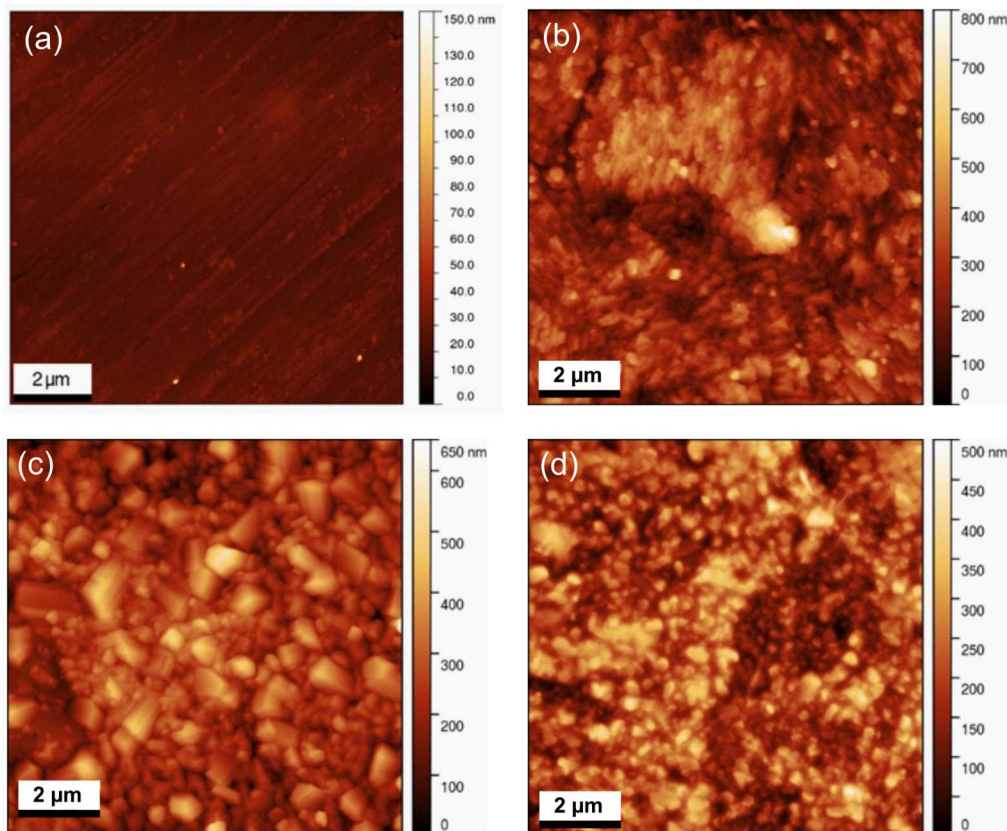


*Fig. 4.32: 2D-AFM images of LNO surfaces at different stages of Cr-/Si-poisoning at 800°C in 10% $O_2$/Ar atmosphere. Fresh sample (a), after 600 h without Cr and additional 1000 h in dry atmosphere in the presence of a Cr-source (b), after additional 1000 h at 30% r.h. with Cr (c) and after another 1000 h at 60% r.h. with Cr (d). A Si-source was present at all stages of the experiment (Image size: $10 \times 10 \ \mu m^2$). Image was taken from [294].*

The crystallites are small with diameters between 100 and 200 nm and are arranged in insular patches across the surface with deep gaps in between. Humidification of the test gas leads to an increase in number as well as in the size in of the crystallites in the presence of Cr and Si (Fig. 4.32c). During this stage of the experiment a significant drop in $k_{chem}$ was recorded, which would likely lead to serious performance degradation of an LNO cathode in an SOFC. While the surface in Fig. 4.32b, which depicts the surface morphological changes caused by Cr- and Si-poisoning under dry conditions, is only partially covered by fine crystallites, the surface of the sample depicted in Fig. 4.32c is blocked by a thick layer of larger crystals. Increasing humidity levels to 60% r.h. results in the deposition of finer material on top of an already thick, blocking layer (d). This deposition, however, does not contribute much to the total coverage of the sample surface, and thus should not lead to another pronounced drop of $k_{chem}$, which was indeed the case (see Fig. 4.29).

Complementary SEM-BSE images of the same samples are displayed in Fig. 4.33. EDX-spectra of the LNO surface were recorded for each sample. The polished and thermally etched sample presented in Fig. 4.33a reveals 5 to 10 µm large grains. EDXS-analysis of the sample surface confirmed a La:Ni cation ratio of 2:1 indicating $La_2NiO_4$, but found no impurities. As already established in section 4.1.3 analysis of a polished sample of the same ceramic pellet, however, shows small NiO secondary phases at the grain boundaries of LNO grains (see Fig. 4.13). On the surface of the sample exposed to Cr/Si-sources for a period of 1000 hours in dry atmospheres (Fig. 4.33b), large LNO grains covered in smaller crystallites are visible. Small patches of darker grey value are located in between the larger grains, which were identified as Zr- und Si-containing phases by EDXS. These phases were also found in the raw powder used to produce this sintered sample (Fig. 4.13). Furthermore, Si-volatilization from the quartz glass reactor can be excluded as a source of Si-compounds found on the sample, since Si and $SiO_2$ do not form volatile gas species in $O_2$/Ar under dry conditions [236]. It is noteworthy that no Cr-containing phases were confirmed. However, small amounts of Bi were detected in regions with fine crystallites, which originate from the gold paste used for contacting the sample. These contaminants do not seem to have a significant influence on the oxygen exchange kinetics. In Fig. 4.33c and Fig. 4.33d sample surfaces exposed to $O_2$/Ar gas streams with 30% and 60% r.h. in the presence of a Cr-source are displayed. Both samples feature a dense surface coverage with fine crystallites, which was already demonstrated in the AFM images. Qualitative analysis using EDXS revealed small amounts of Cr, Si, and Bi at several different sites on the surface. In addition, EDXS-elemental distribution maps of the main sample, which had been exposed to all mentioned conditions, were recorded.
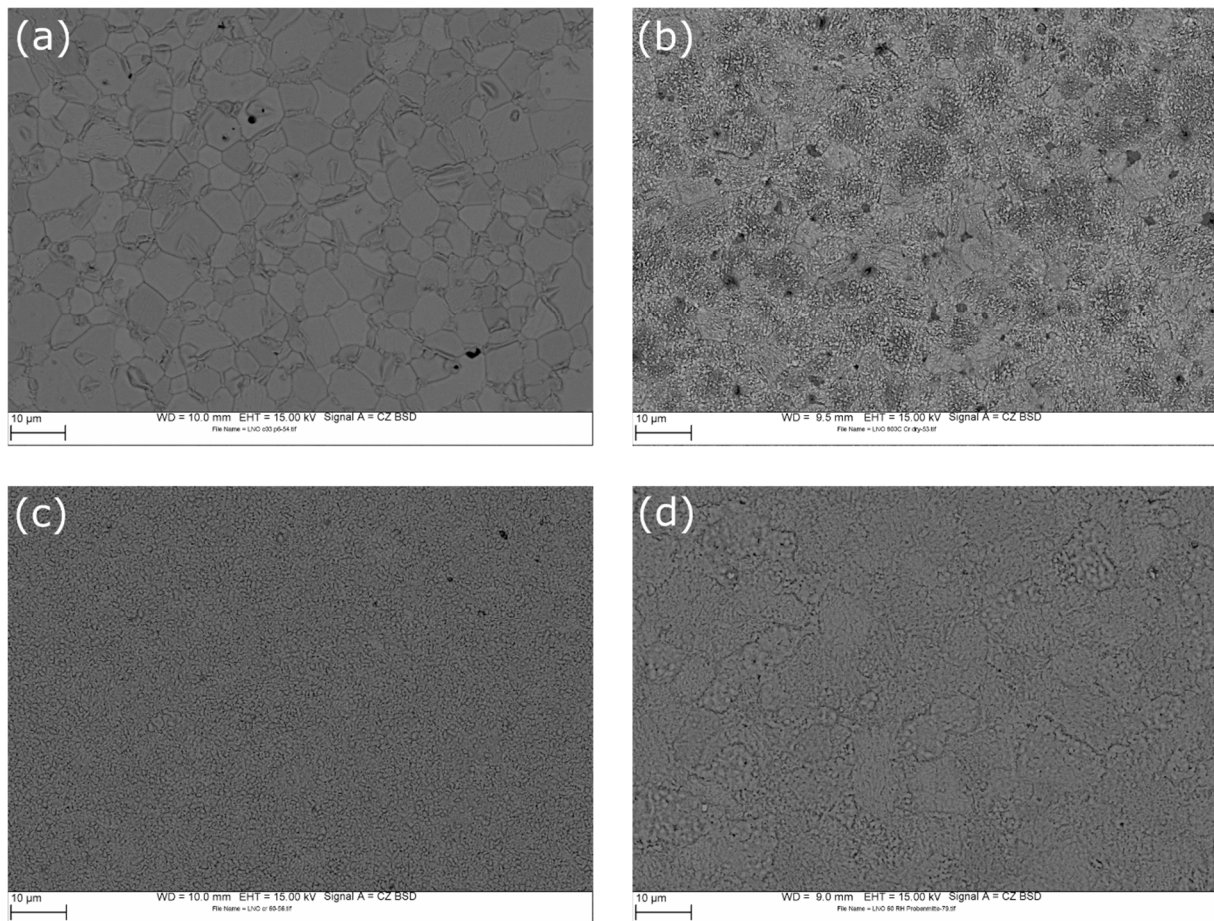
*Fig. 4.33: SEM-BSE images of (a) a polished and thermally etched LNO sample, (b) after 600 h without Cr and additional 1000 h in dry atmosphere in the presence of a Cr-source, (c) after additional 1000 h at 30% r.h. with Cr and (d) after another 1000 h at 60% r.h. with Cr (taken from Schrödl et al. [273]).*

Aside from these localized inhomogeneities, La as well as O seem to be evenly distributed across the surface. Looking at the Cr- and Si-distributions it appears that Cr and Si are deposited in distinct patches. Regions of high Cr-concentration, which appear bright in the Cr-map, correspond to dark areas in the Si-map and vice versa, which indicates the presence of Cr- and Si-containing secondary phases. Both of these phases also contain La and O, however Ni seems to be only present in Cr-rich, but not in Si-rich areas. Furthermore, Bi was detected predominantly in areas of high Cr-concentration.
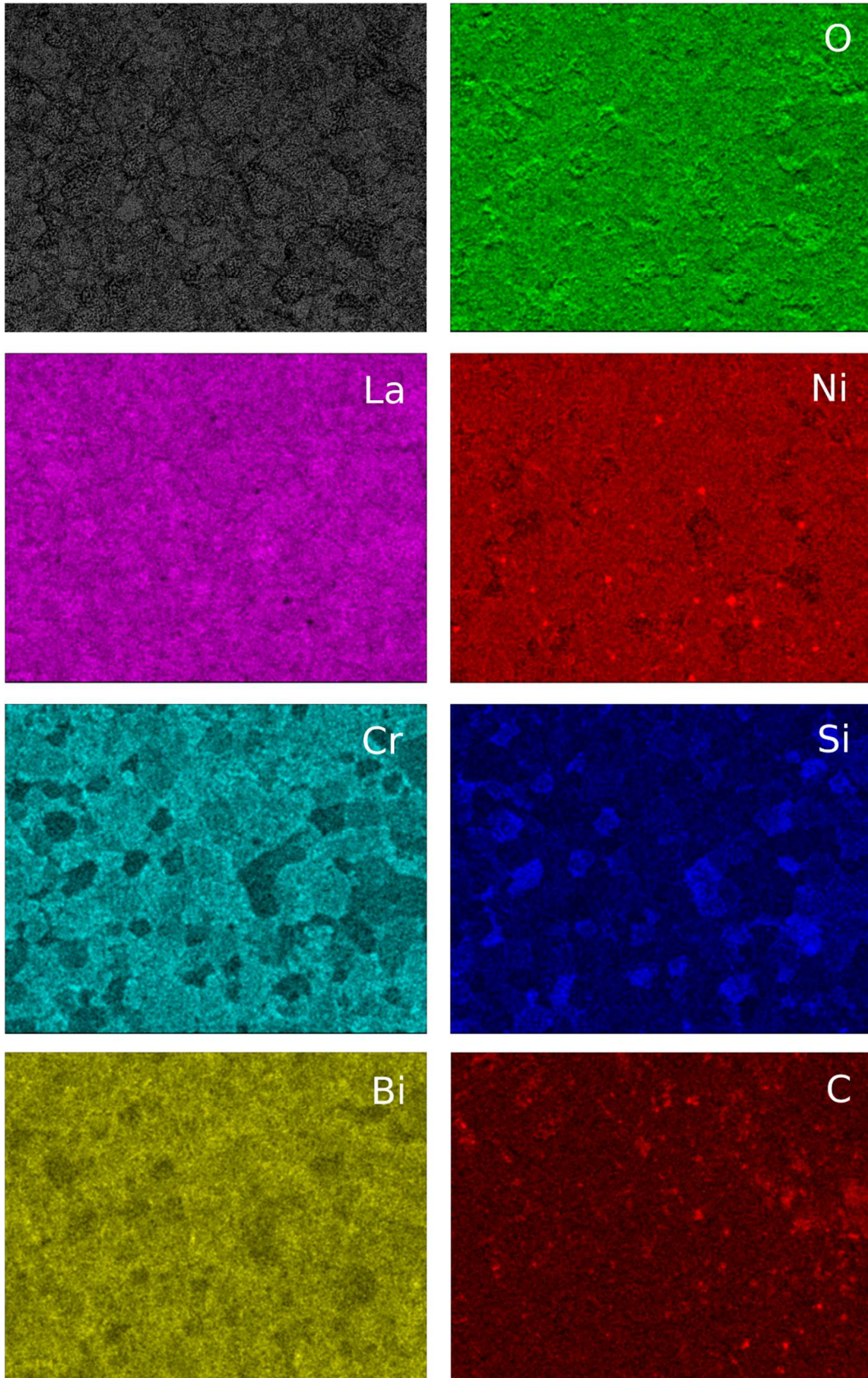
*Fig. 4.34: Post-test SEM image (top left) and SEM-EDXS-elemental distribution maps of the main LNO sample after all stages of the degradation experiment (image width: 108.54 µm). Image taken from Schrödl et al. [273].*

At this point it should be mentioned that the separation of La-, Cr-, and O-signals in EDX-spectra is not straightforward, due to an overlap of the Cr-K$_\alpha$ peak (5.410 keV) with the La-L$_\beta$ peak (5.372 keV) and the overlap of the Cr-L$_\alpha$ peak (0.573 keV) and the O-K$_\alpha$ peak (0.525 keV). Therefore, it is possible that a part of the La-signal may have been attributed to the Cr-map whereas a part of the Cr-signal could be included in the O-map. However, STEM results of Cr- and Si-poisoned LNO presented in section 4.2.2, which confirmed the formation of La-chromate and La-silicate phases are in good agreement with the present results.

In addition, XPS-elemental depth profiling was conducted on the same samples removed at different stages during the long-term study (Fig. 4.35). The sample surface was sputtered off until constant concentrations for La, Ni, and O were obtained. After each sputter session, XP-spectra were recorded.
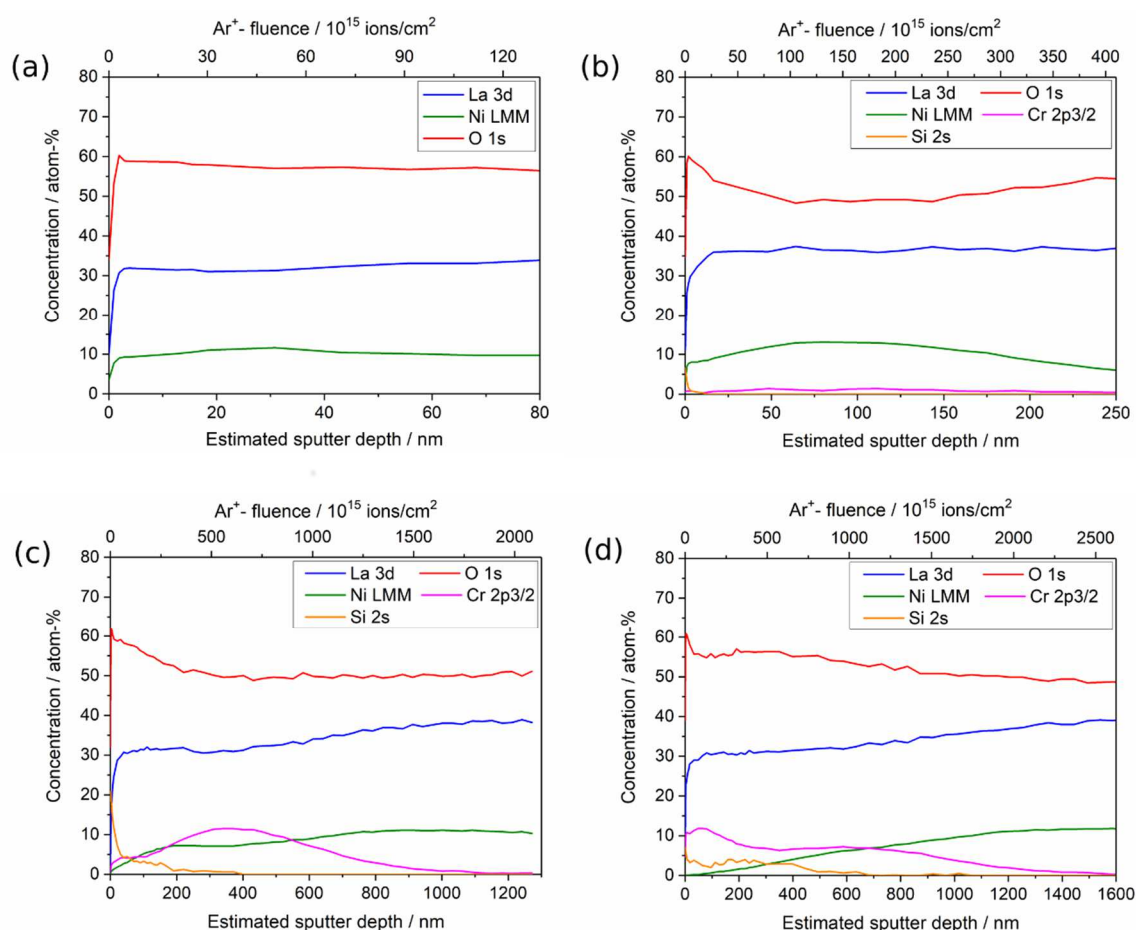


*Fig. 4.35: XPS-elemental depth profiles of La, Ni, O, Cr, and Si of (a) the fresh, undegraded sample, (b) after 600 h without Cr and additional 1000 h in dry atmosphere in the presence of a Cr-source, (c) after additional 1000 h at 30% r.h. with Cr and (d) after another 1000 h at 60% r.h. with Cr.*

Fig. 4.35a presents the XPS-depth profile of a fresh, undegraded sample. Apart from the steep profile slopes close to the surface, which can be attributed to high levels of carbon on the sample surface, the depth distribution of La, Ni, and O is uniform. These carbon compounds,

which were also detected in the elemental distribution maps, could have been introduced during sample preparation or during storage in ambient air [295]. In Fig. 4.35b, which displays the sample treated for 1600 h in dry $O_2$/Ar with Cr and Si present, an increase of the La:Ni ratio within the first 15 nm from the surface is visible. This is followed by a zone with higher Ni content, which suggests a segregation of La towards the surface. Surface segregation of La has been reported in the literature by several authors [280,289,296,297]. Interestingly, small amounts of Cr and Si were found, which were not detected in the EDXS-analysis, because the amounts of impurities were below the detection limit of the method. XPS, however, has a much higher sensitivity for the detection of Cr and Si. The presence of both of these elements could be responsible for the slight decrease of $k_{chem}$ in dry atmospheres (see Fig. 4.29).

Fig. 4.35c shows that after additional 1000 hours in moderately humidified atmosphere (30% r.h.) an approximately 800 nm thick layer of decomposed LNO is formed, which is indicated by a stabilization of the La, Ni, and O concentrations at a constant value. It should be noted that small amounts of Cr are still present beyond the 800 nm mark, which could be the result of Cr-diffusion into the bulk material. Compared to the bulk composition, the degradation layer features an increased La:Ni ratio. The maximum amount of Cr is found at depths of approximately 400 nm. High concentrations of Si-species were found within the first 50 nm of the degradation layer but could be detected up to 400 nm from the sample surface. After another 1000 hours in strongly humidified $O_2$/Ar atmosphere (60% r.h.) (Fig. 4.35d), the thickness of the degradation layer increased by approximately 200 nm, which did not cause a significant decline in oxygen surface exchange rates (see section 4.2.3). This is not surprising considering that the material was not deposited as a dense layer – as the recorded AFM and SEM images revealed – but rather as small crystalline structures on top of an older degradation layer. Therefore, it is conceivable that although additional material was deposited at higher humidity enough active surface was left for a decent oxygen reduction rate. Nevertheless, over the course of 1000 h a slight decline of $k_{chem}$ is noticeable (see Fig. 4.29). Interestingly, the degradation layer appears to be almost completely devoid of Ni while the Cr-profile indicates a Cr-accumulation within the first 200 nm, followed by a broad plateau. Si-compounds were found predominantly at the surface and interspersed with Cr-rich regions up to depths of 600 nm within the near-surface degradation zone. Fig. 4.36 shows the sequence of XP-spectra of signals, which were selected for the quantification of Cr ($2p_{3/2}$), Si (2s) and Bi (4f) during XPS-depth profiling of the main LNO sample. The hatched areas indicate the range of measured binding energies of Cr-, Si-, and Bi-oxides with different oxidation states, which were obtained from the NIST X-ray Photoelectron Spectroscopy data base [298]. The recorded XP-spectra of the Cr $2p_{3/2}$ region (Fig. 4.36, left) indicate the presence of Cr(III) oxide compounds, however, signals of Cr(VI) species (e.g. chromate $CrO_4^{2-}$ or dichromate $Cr_2O_7^{2-}$) were not detected. The second peak emerging at lower binding energies at increased

sputtering depth, corresponds to metallic Cr. It is highly unlikely that Cr was deposited in metallic form at the applied experimental conditions (800°C, $pO_2$ = 0.2 bar). Therefore, the peak is probably an artifact caused by prolonged $Ar^+$ ion bombardment during the sputtering process, which has been described in the literature for Cr [299,300] and other transition metals [58,295,301-303]. Additionally, the only other elements with similar binding energies as metallic Cr – Ag ($3p_{3/2}$) and Te ($3d_{5/2}$) – have not been detected by other analytical methods employed in this work and are not present in any of the materials used in the experimental setup. Signals corresponding to Si(IV)-oxides were identified (Fig. 4.36, right), which point to the formation of a lanthanum silicate phase. This is further supported by the results of SEM-EDXS-analysis of Si-containing secondary phases. Bismuth signals, which can be discerned in the surface scan (Fig. 4.36, right), quickly disappear after the first few sputtering steps, suggesting a very thin surface layer of Bi. No metallic silicon was detected.
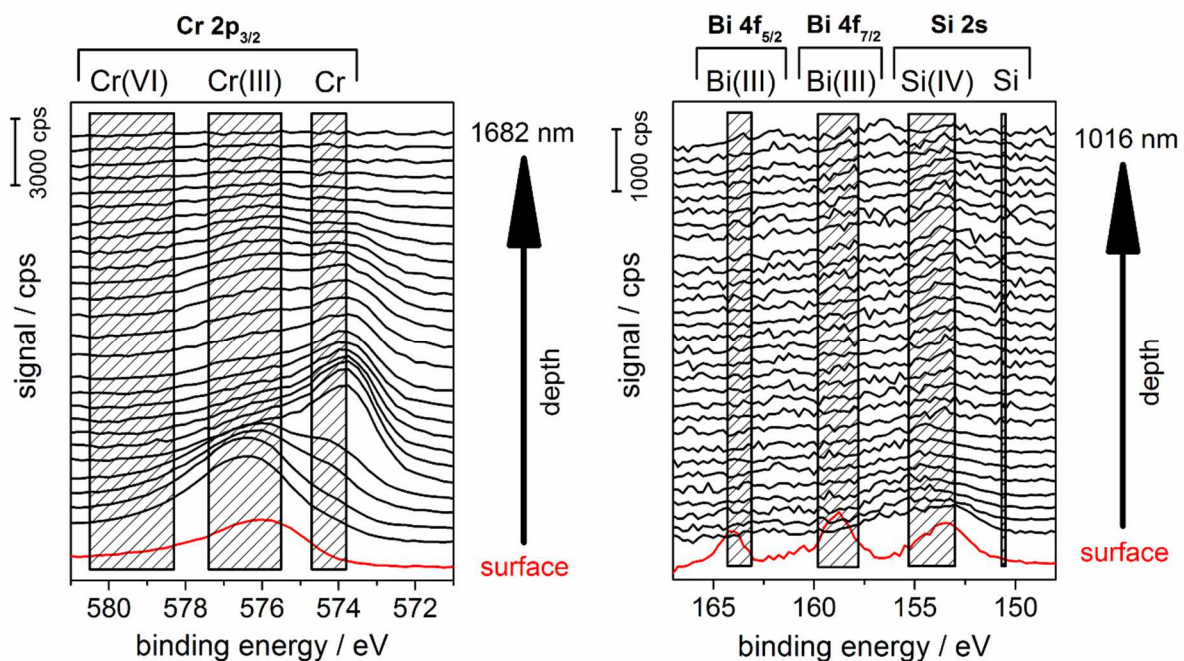


Fig. 4.36: Sequence of XPS-spectra recorded during depth profiling of the main LNO sample, which was subjected to all 4 stages of the degradation experiment. The spectra of the immediate surface are shown in red (taken from [273]).

It should be mentioned that the interpretation of data determined by XPS-depth profiling on rough samples is not as straightforward as on smooth, evenly layered ones. The material accumulated over time is not neatly deposited in flat layers of even thickness, but rather stacked in piles and clusters. Ion sputtering not only removes accumulations of matter but leads to considerable intermixing of the sputtered deposits. Therefore, the elemental depth profiles do not represent the precise distribution of elements within the surface layer. Nevertheless, the method allows the determination of an average thickness of the

decomposed near-surface zone. A second challenge arises due to the deposition of more than one type of contaminant at varying rates depending on the environmental conditions. Judging from the XPS-profiles of the sample analyzed after the first humidity stage (Fig. 4.35c) it seems that the topmost reaction layer is composed of a Si-compound on top of a Cr-containing phase. In theory, the higher volatility of $CrO_3$ in dry atmospheres in comparison to $SiO_2$ should lead to preferential Cr-deposition in the early stages of the degradation study (dry atmospheres), whereas Si is deposited as soon as humidity is added to the gas stream. The XPS-depth profiles recorded after exposition to 60% r.h. (Fig. 4.35d), however, do not support this case.

To identify the actual chemical composition of the various phases detected in SEM-EDXS-analyses a FIB lamella of the main LNO sample was prepared. A STEM-HAADF cross section image of the decomposition layer and the bulk phase underneath is presented in Fig. 4.37.
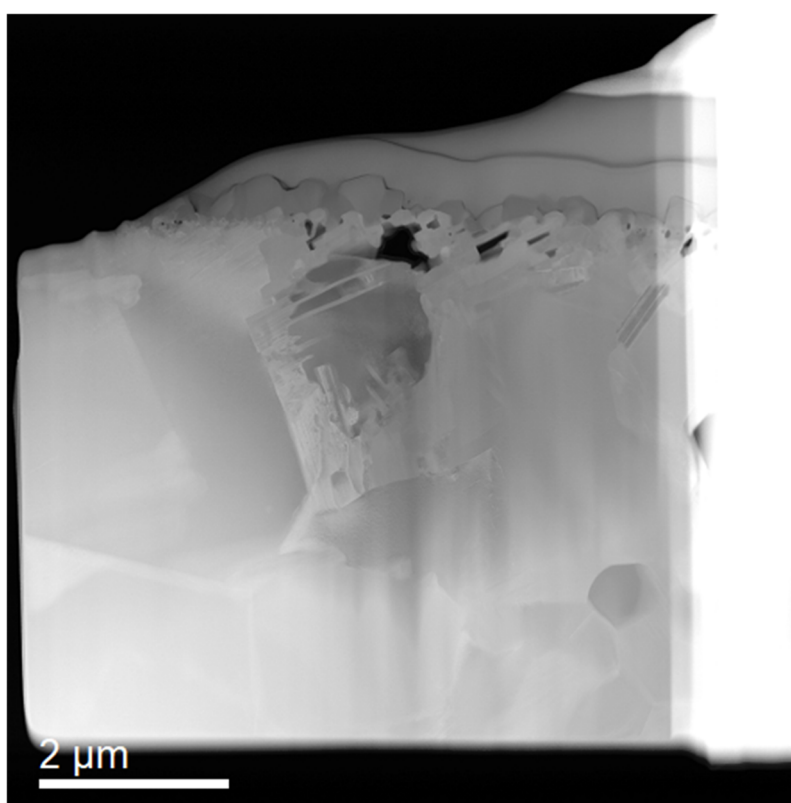


*Fig. 4.37: STEM-HAADF cross section image of the prepared FIB lamella.*

The image features an approximately 1 μm thick near-surface degradation zone containing secondary phases with different composition, as indicated by the HAADF Z-contrast. EDXS-analysis of region 1 in Fig. 4.38a, confirms the presence of La, Si, and O. Complementary electron energy loss spectroscopy (EELS) measurements found no evidence of Ni or Cr within this layer. The smaller, brighter appearing structures below the topmost layer (region 2) were identified as La-Cr-Ni-oxide. However, the small size of the features did not allow for a reliable

determination of the actual chemical composition of this phase using EDXS. In region 3 a dark round inclusion is visible, which was identified as NiO by EDXS and EELS. Judging from the size of the inclusion and its round shape it is most likely one of the NiO inclusions, which can be discerned in the elemental distribution map of Ni (see Fig. 4.22). NiO grains in similar size were also found in a fresh sample, which suggests that this inclusion is not caused by secondary phase formation during the degradation process. The EDX-spectrum of the bulk composition (region 4) is depicted in Fig. 4.38b for reference.
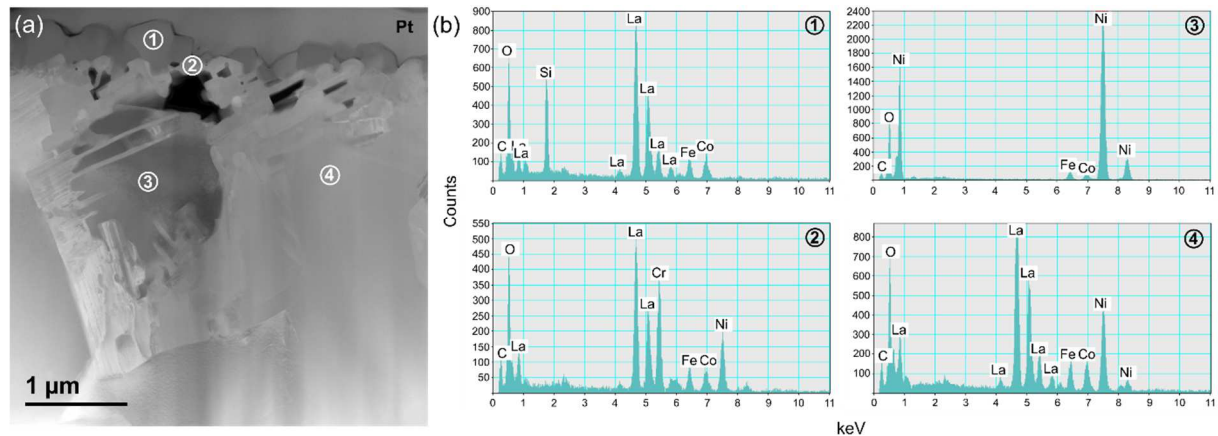


*Fig. 4.38: Post-test STEM-HAADF image of (a) the degraded near-surface zone of LNO after degradation at 800°C in 60% r.h. and (b) EDX-spectra of the detected secondary phases marked with numbers in image (a). Peaks of Fe and Co are caused by the interior lining of the microscope column (taken from Schrödl et al. [273]).*

Fig. 4.39 depicts a detailed image of the decomposed near-surface zone. Corresponding EDXS-elemental distribution maps of Cr, Si, Ni, and La of a region marked with a white rectangle show a Cr-containing crystallite with a layer of Si-containing deposit on top. According to the La-distribution map both the Cr-rich and the Si-rich layers contain La. The elemental maps reveal high Cr-levels and an almost complete depletion of Ni on top of the crystal. The Cr- and Ni-concentrations appear to be inversely related. The Ni-distribution map further indicates that the highest concentrations of Ni are located near the bulk phase. No evidence of Ni was found in the Si-rich phase. Based on the recorded elemental maps a pseudo-colored image showing Si in blue, Ni in green, and Cr in red was generated. The orange hue in the middle of the crystallite illustrates a zone containing Cr and Ni.
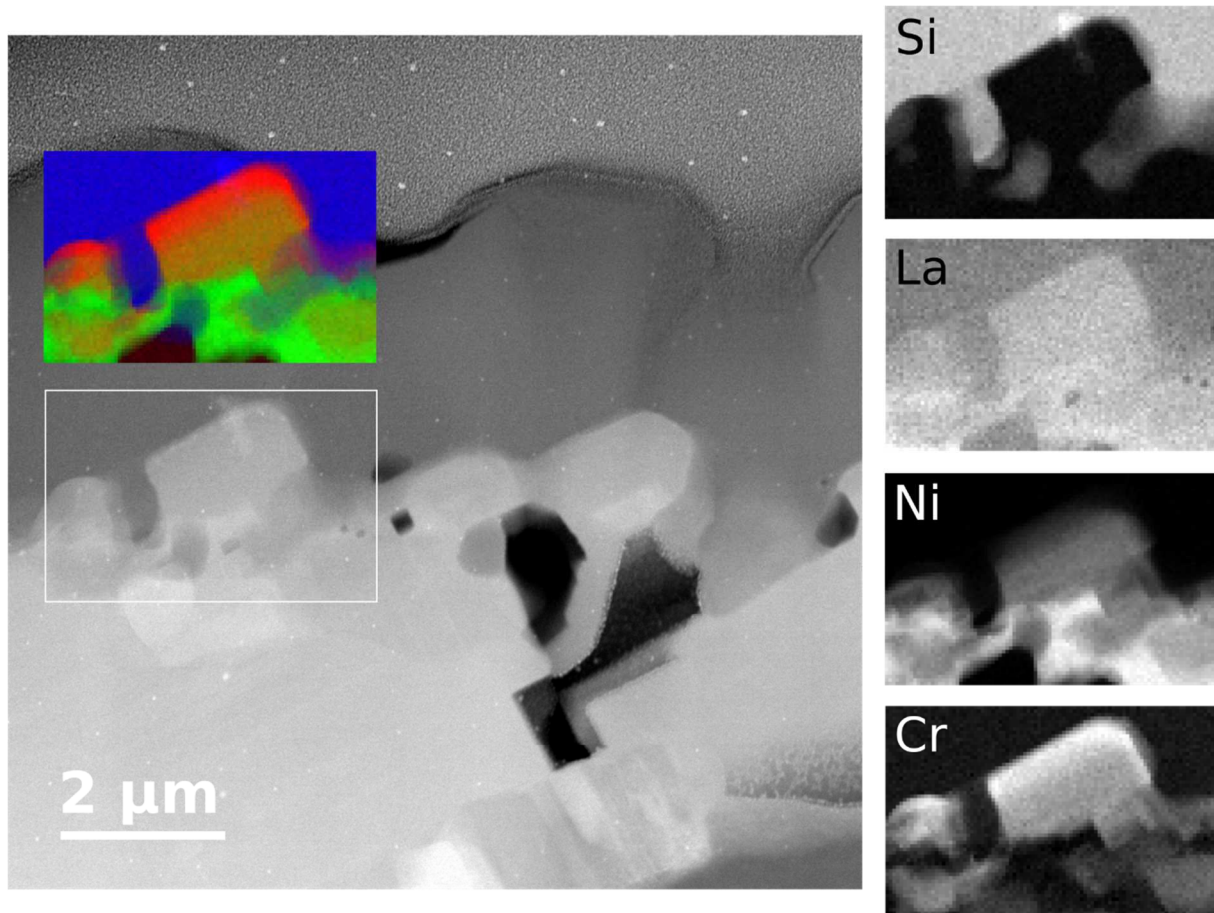
*Fig. 4.39: Detailed view of the degraded near-surface region of LNO after degradation at 800°C in 60% r.h. and corresponding EDXS-elemental maps of the area marked with the white rectangle.*

The compositions of the La-Si-O and La-Cr-Ni-O secondary phases were obtained in HR-STEM mode (Fig. 4.40 and Fig. 4.41). A high-resolution image of the area marked by a white circle in Fig. 4.40a was recorded (Fig. 4.40b). The bright white dots as well as the triangularly shaped structures in the crystal lattice correspond to columns of La-atoms. The fainter dots between the La-triads are alternately stacked La- and Si-atoms. Individual columns of Si or O atoms were too faint to detect in in the high-resolution image. By comparing an HAADF-simulation (white rectangle in Fig. 4.40b) of this compound with the acquired high-resolution image, the phase was identified as a silicon oxyapatite of the composition $La_{9.33}(SiO_4)_6O_2$ with space group $P6_3/m$ (176). Additionally, a comparison of a calculated Fast Fourier Transformation (FFT) based on the HR-STEM image with the simulated diffraction pattern of $La_{9.33}(SiO_4)_6O_2$ in [2 -1 -1 3] zone axis also confirms this result. Interestingly, this material has been investigated as electrolyte material for intermediate-temperature solid oxide fuel cells [304,305] due to the fact that its ionic conductivity is comparable to that of YSZ (10-20 mS cm$^{-1}$ at 800°C [306].

*Fig. 4.40: (a) STEM-HAADF cross-sectional image of the degraded LNO surface layer with a white circle marking the analyzed region within a Si-enriched secondary phase, (b) HR-STEM-HAADF image of the marked area with a superimposed HAADF-simulation (white rectangle), (c) FFT-image of the selected area and (d) simulated diffraction pattern of $La_{9.33}(SiO_4)_6O_2$ in [2 -1 -1 3] zone axis. The red arrows a and b indicate the diffraction planes (-1 0 1) and (0 1 0), respectively (taken from Schrödl et al. [273]).*

The Cr-containing phase depicted in Fig. 4.41a could also be identified by a similar comparison. A HR-STEM image of the area marked with a black circle was recorded. The white dots in the HR-STEM image of the area marked with a black circle (Fig. 4.41b) illustrate columns of La-atoms, while Cr, Ni, and O are not visible in the image. The calculated FFT image (Fig. 4.41c) corresponds to the simulated diffraction pattern of a La(Cr,Ni)O$_3$ perovskite with space group *Pnma* (62) (Fig. 4.41d). The presence of Cr and Ni in this part of the degradation layer was already suggested by results from EDXS- and EELS-analysis. Complementary EDXS-line scans across such a crystal show a decrease in Cr-concentration while the Ni-content increases (Fig. 4.42). This result suggests the presence of a $LaCr_{1-x}Ni_xO_3$ phase which, according to literature, forms a complete solid solution on the perovskite B-site [307].
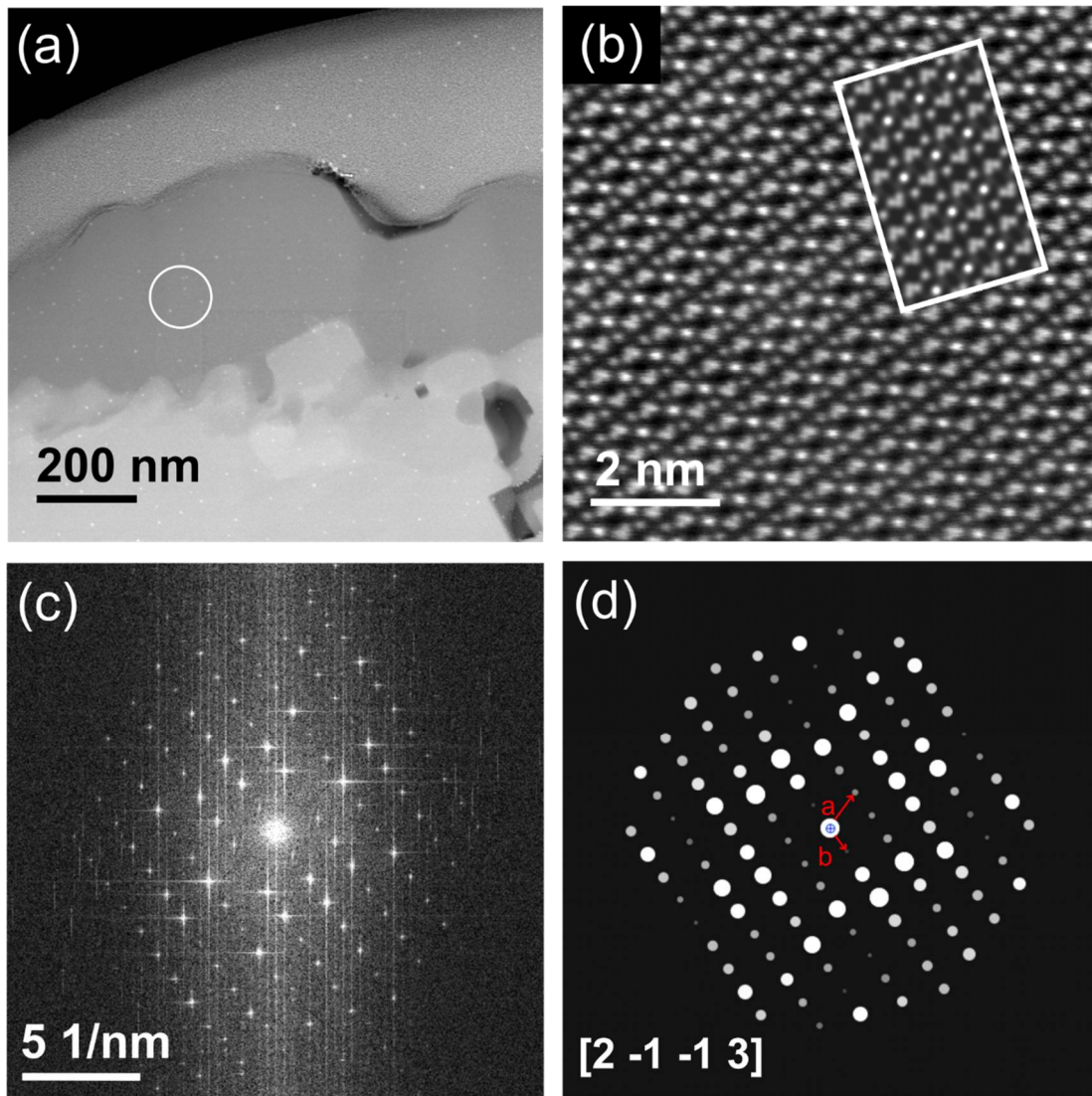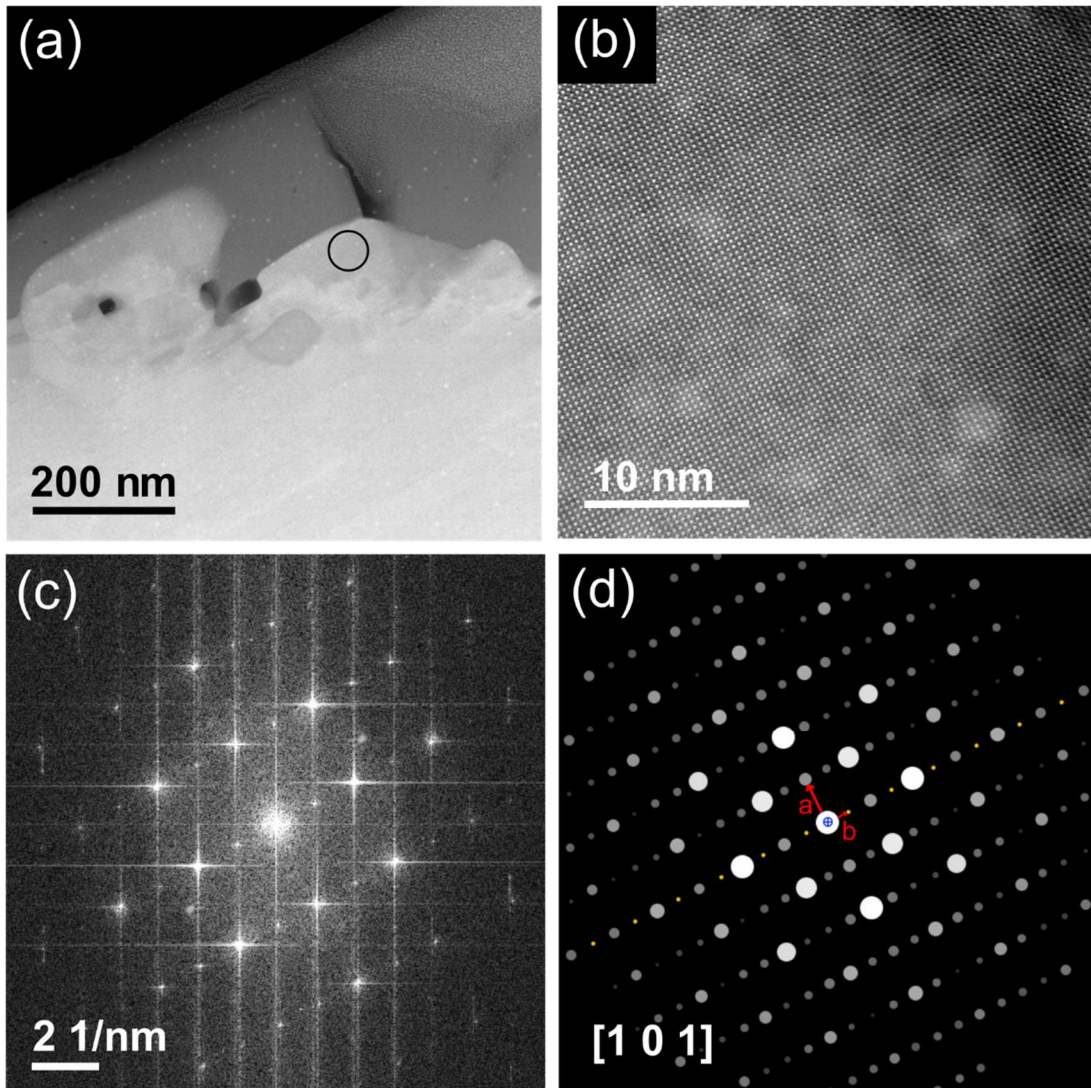
*Fig. 4.41: (a) STEM-HAADF cross-sectional image of the degraded LNO surface layer with a black circle marking a region within a Cr-rich deposit, (b) HR-STEM-HAADF image of the marked area, (c) FFT-image of the selected area and (d) simulated diffraction pattern of a perovskite structure in space group Pnma. The red arrows a and b designate the diffraction planes (1 0 -1) and (0 -1 0), respectively (taken from Schrödl et al [273]).*
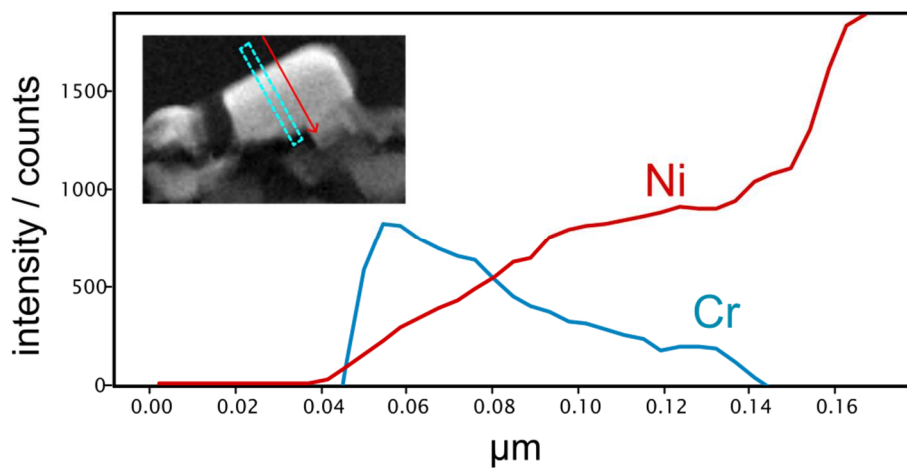


*Fig. 4.42: EDXS-line scan across a Cr-rich crystallite in direction of red arrow. The Cr-line profile is depicted in blue, the Ni-profile in red.*

One of the parent compounds of this series – $LaCrO_3$ – is a *p*-type electronic conductor which was used for interconnector plates in high-temperature SOFCs for many years [6]. However, the electrical conductivity of $LaCrO_3$ is quite low (0.96 S cm$^{-1}$ at 800°C in air [308]) compared to that of LNO. Lee et al. [194] observed the formation of $LaCrO_3$ in reactivity studies when they annealed powders of LNO and $Cr_2O_3$ at 1000°C for 24 h in air. Based on the so far obtained results it is difficult to conclude whether the $LaCr_{1-x}Ni_xO_3$ phases were formed by Cr-diffusion into a $LaNiO_3$ phase, or Ni-diffusion into a $LaCrO_3$ secondary phase. However, LNO is known to expel $La_2O_3$ from its structure, thus creating higher-order, Ni-rich Ruddlesden-Popper phases when annealed in dry or humid atmospheres [279]. It is conceivable both processes happen at the same time. $La_2O_3$ could react directly with Cr-species and form $LaCrO_3$, which could be the driving force for further decomposition of the Ruddlesden-Popper phase into $LaNiO_3$.

A closer inspection of the bulk phase directly below the degraded surface zone (see Fig. 4.43a) revealed stacking anomalies in the LNO phase. A HRTEM image of these stacking faults presented in Fig. 4.43b shows monolayers of the n=3 member of the $La_{n+1}Ni_nO_{3n+1}$ Ruddlesden-Popper series (Fig. 4.43c) embedded in regular (n=1) LNO layers. The formation of these monolayers is probably the result of the continuous La-segregation to the sample surface, which also has been reported in the literature [279]. This further supports the earlier proposed degradation mechanism.
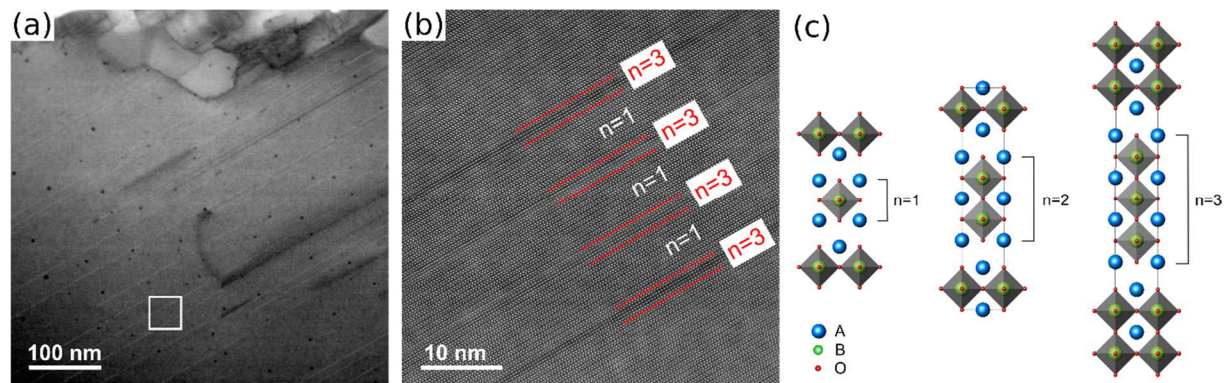


*Fig. 4.43: (a) STEM-HAADF image of the LNO bulk phase below the decomposed surface region after degradation at 800°C in 60% r.h., (b) HR-STEM-HAADF image of the selected area with red lines indicating the boundaries between the $La_2NiO_{4+\delta}$ main phase (n=1) and $La_4Ni_3O_{10}$-type interlayers and (c) crystal structure of the first three orders of Ruddlesden-Popper phases $A_{n+1}B_nO_{3n+1}$ (n=1, 2, 3). Image taken from Schrödl et al. [273].*

The post-test analysis of the degraded LNO sample revealed that LNO decomposes into secondary phases with some degree of ionic or electronic conductivity. This could explain the fact, that significant activity for the oxygen exchange reaction is still retained, despite the strong composition of the sample surface.

## 4.3  Long-term stability of La₂NiO₄₊δ – air electrodes against Cr-poisoning at 800°C under current load

This section describes long-term degradation experiments on symmetrical LNO cells at 800°C for a duration of more than 2000 h. Measurements were conducted in an $Al_2O_3$ tube reactor which allowed the examination of the effects of Cr-poisoning on LNO electrodes. By staying consistent in terms of electrode polarity, both fuel cell (SOFC) and electrolyzer (SOEC) mode were investigated in a single cell test. This allows the direct comparison of the effects of polarization on degradation processes under identical environmental conditions. The long-term stability experiment was carried out in 3 subsequent stages at 800°C and 20%$O_2$ in Ar. The results of this study were in part published in [309].

### 4.3.1  Determination of electrode sintering parameters

In order to optimize the sintering parameters for LNO electrodes a layer was screen printed on a dense and polished GDC substrate. The screen-printed layer was dried in a drying oven for 1h at 100°C to remove the organic solvent. Then, the sample was dry cut into four quarters by means of a diamond wire saw. Three of the four samples were sintered at temperatures between 1000°C and 1200°C for 2 h with heating and cooling rates of 5 and 2 K min$^{-1}$, respectively. The last sample was kept as a reference to illustrate the particle size and shape. The sintered samples were mounted on an aluminum SEM sample holder using double-sided adhesive copper tape and contacted with silver paste. The microstructure of the electrode layers was assessed via SEM-images recorded in SE mode. Fig. 4.44a displays an SEM-image of the raw, unsintered electrode layer, which features very large and fine particles. It should be noted, that it was not the intended goal of this experiment to optimize the microstructure to achieve a low ASR. Thus, LNO_TB_C03 powder was used in its unmilled state, which explains the coarse microstructure. Sintering at 1000°C for 2 h (Fig. 4.44b) resulted in some connectivity between the small particles, while the larger ones remained unconnected. This is hardly surprising considering the lower sinter activity of large particles. The samples sintered at 1100°C and 1200°C both displayed sinter bonds between large and fine grains (Fig. 4.44c and Fig. 4.44d). However, only the LNO layer sintered at 1200°C showed sufficient adhesion to the electrolyte substrate, which was tested via a scoth-tape test. Furthermore, the microstructure of the layer sintered at 1200°C (Fig. 4.44d) exhibits are more mechanically stable network of connected grains and pores.
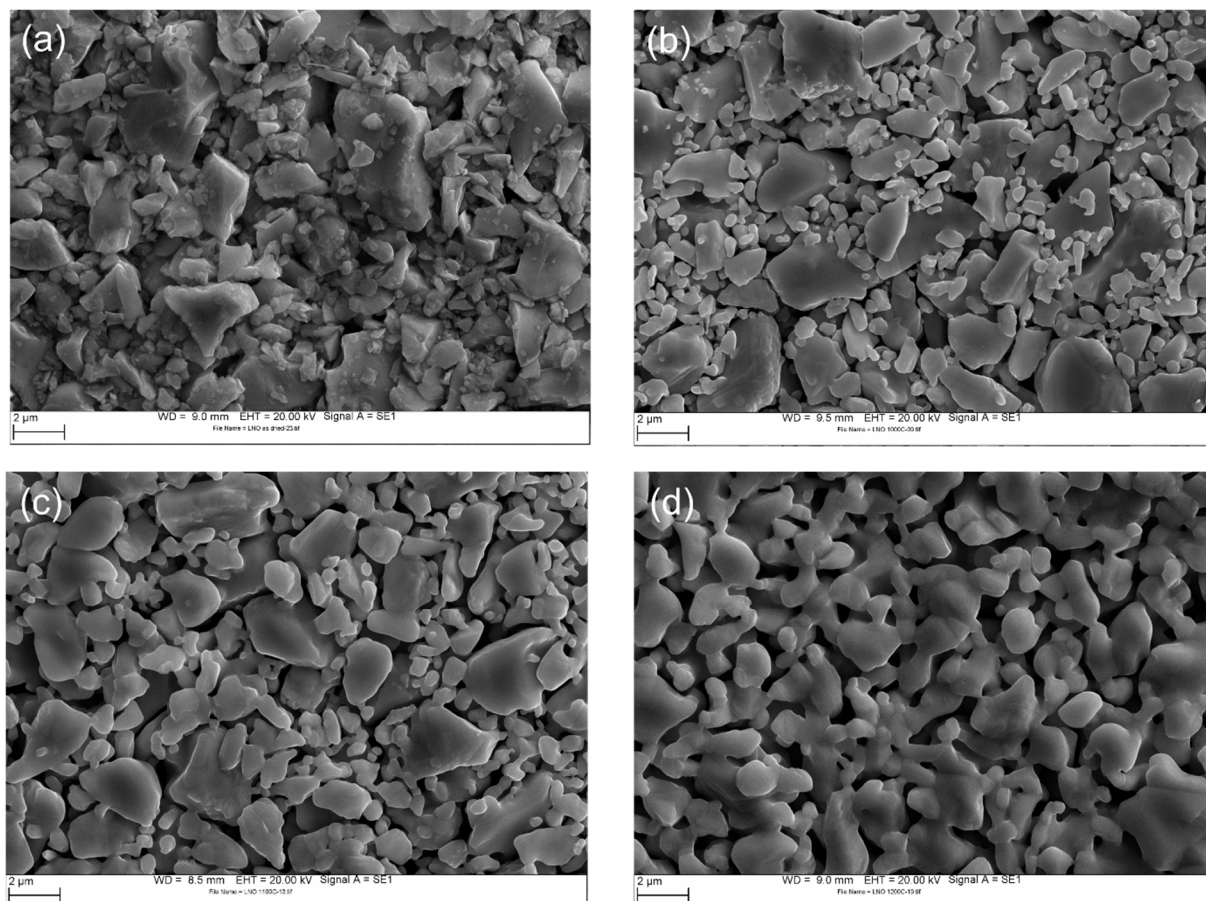
*Fig. 4.44: Topographical SEM-images of (a) an unsintered and (b), (c) and (d) screen-printed LNO electrode layers sintered at 1000°C, 1100°C and 1200°C for 2 h, respectively.*

### 4.3.2 Reactivity of LNO with GDC

Chemical reactions, which form electrically insulating phases at the interface between the electrode and electrolyte are a common occurrence, especially during sintering, when the electrode is subjected to the highest temperatures during operation. These phases often form small crystalline deposits or layers at the immediate interface, which can be imaged and analyzed in the TEM. However, the small dimensions and random orientation of crystallites of such phases often impede the determination of their chemical composition. Therefore, an XRD-study on powder mixtures, containing 50 wt-% of $La_2NiO_{4+\delta}$ (LNO) and $Ce_{0.9}Gd_{0.1}O_{2-\delta}$ (GDC) was conducted. The powders were premixed for 24h in a roller bed mill using $ZrO_2$ grinding balls in ethanol as milling medium. After that the powder was separated from the milling balls and dried.
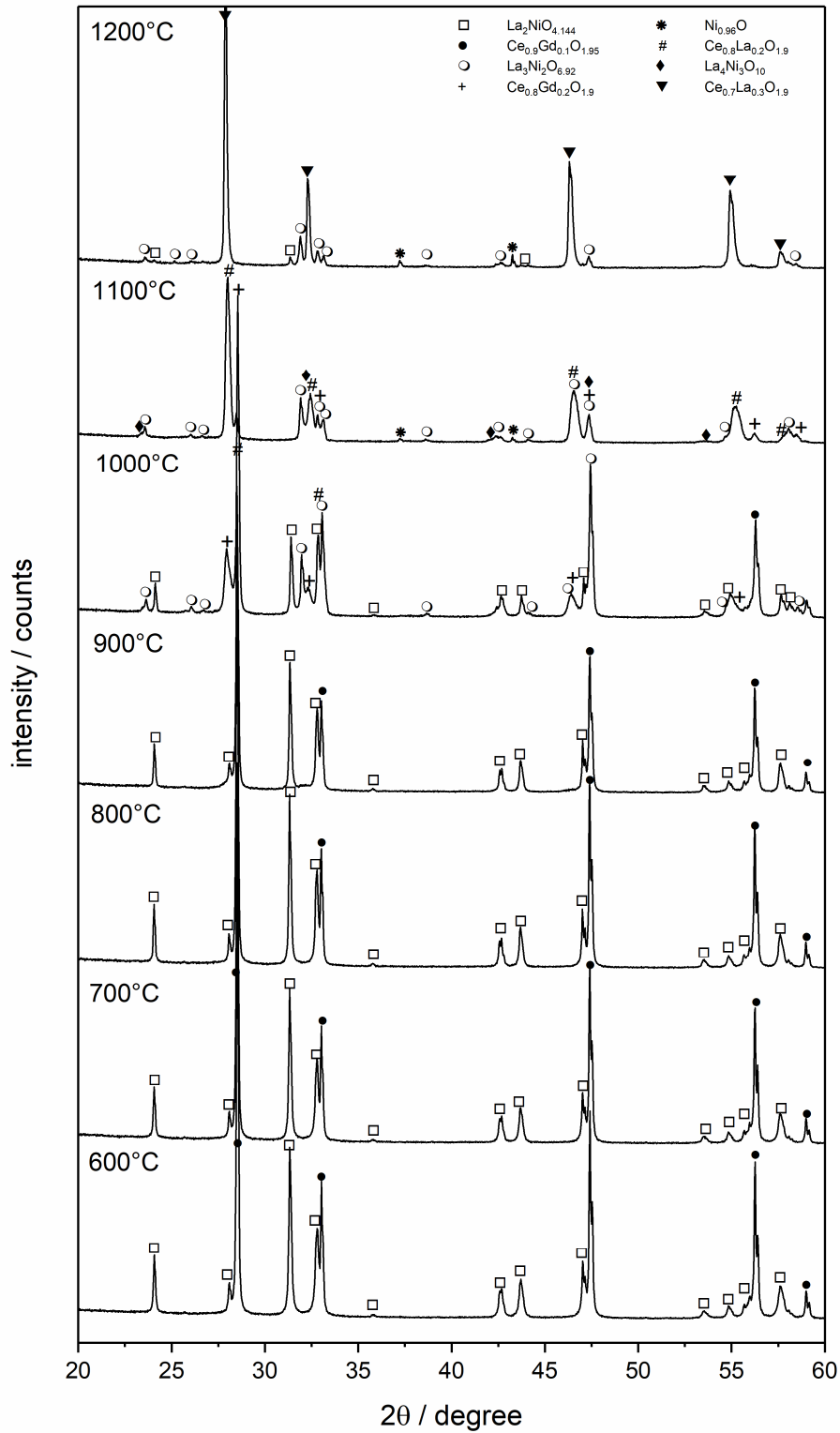
*Fig. 4.45: Room temperature XRD-patterns of 50 wt-% LNO/GDC powder mixtures annealed at temperatures between 600 and 1200°C for 6 h.*

For the reaction tests powder samples of 2 g were annealed in an alumina crucible for six hours at temperatures between 600°C and 1200°C. Subsequently, room temperature XRD-

powder patterns of the annealed samples were recorded covering a 2θ range between 10° and 100°. Quantification of the XRD-patterns was realized using Rietveld refinement.

For reasons of clarity only a detailed view (20° ≤ 2θ ≤ 60°) of the XRD-data is presented in Fig. 4.45. Signals marked with the same symbols correspond to the same phase. Fig. 4.46 displays the weight percentage of each detected phase. Between 600°C and 900°C only signals corresponding to $La_2NiO_4$ and $Ce_{0.9}Gd_{0.1}O_2$ were detected. At 1000°C additional peaks of the higher-order Ruddlesden-Popper phases $La_3Ni_2O_7$ and $La_4Ni_3O_{10}$, as well as signals corresponding to La-substituted ceria phase were found, which suggests a substantial diffusion of into the ceria structure. As a result, the relative amount of Gd in the remaining ceria phase increased and the pattern of $Ce_{0.8}Gd_{0.2}O_2$ gave a better match. It should be mentioned that the exact stoichiometry of isostructural phases (e.g. $Ce_{1-x}Gd_xO_2$) cannot be determined using XRD, unless a significant peak shift from one composition to the next is observed. At 1100°C the LNO phase was completely decomposed and peaks corresponding to a NiO phase emerged. The $Ce_{0.8}Gd_{0.2}O_2$ phase has mostly been converted to a $Ce_{1-x}La_xO_2$ phase and the amount of $La_3Ni_2O_7$ increased in comparison to $La_4Ni_3O_{10}$. At 1200°C, only $La_3Ni_2O_7$, $Ce_{1-x}La_xO_2$ and small amounts of NiO and LNO are present, which indicates the decomposition of $La_4Ni_3O_{10}$ into LNO and NiO. No evidence of GDC was found.
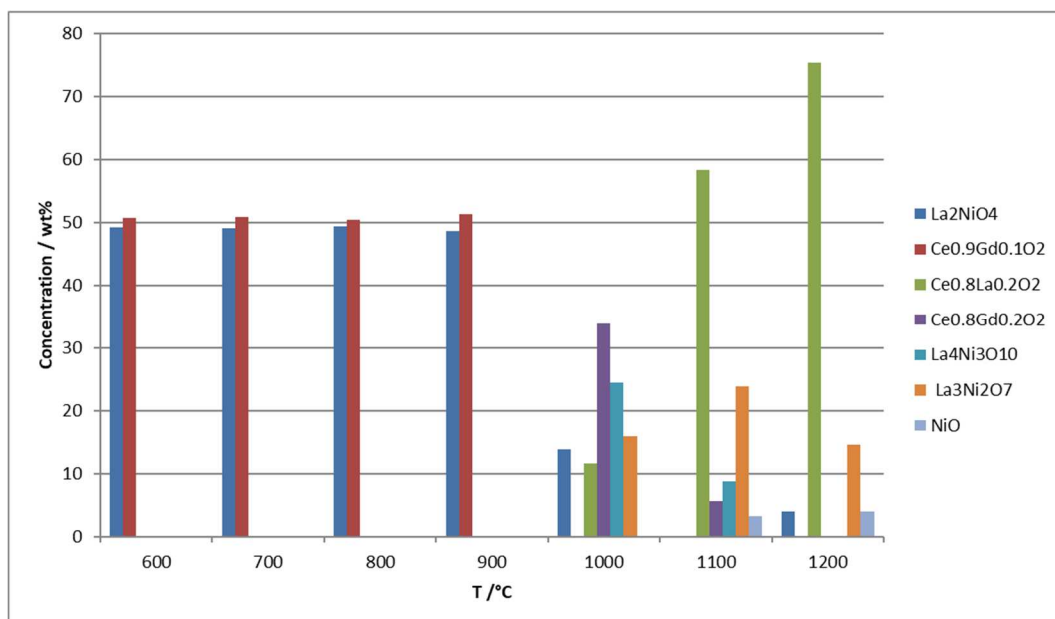


*Fig. 4.46: Concentrations of detected chemical compounds in weight percent as determined by Rietveld refinement.*

### 4.3.3 Electrochemical properties

Fig. 4.47 presents electrochemical impedance spectra of the LNO SOEC anode (a) and the SOFC cathode (b) under open-circuit voltage conditions. The area specific resistance (ASR) of each electrode can be determined from the real axis intercepts of the impedance curves. The initial ASR value of the SOEC anode is in good agreement with the ASR of the SOFC cathode (0.16 $\Omega$ cm$^2$). Impedance curves denoted in black correspond to stage 1 of the degradation experiment. During the first 168 h, no current load was applied and thus, also no I-V-curves were recorded. The sample was kept in dry test gas (20% $O_2$ in Ar) and no Cr-source was present to determine the intrinsic degradation of the electrodes. After that, the cell was subjected to a low electric current of 110 mA cm$^{-2}$ between the OCV EIS-measurements. This procedure simulates SOFC operation on the cathode, where molecular oxygen is reduced and incorporated into the electrode, and SOEC operation on the anode where oxide ions are re-oxidized released as oxygen gas. Additionally, I-V-curves were recorded to determine the ASR at higher working voltages. Currents were kept at low levels because earlier investigations had shown that higher currents lead to the delamination of the LNO SOFC cathode. A sudden jump in the ASR of both electrodes during stage 2 was caused by a setup change which required a cool-down and reheating of the cell to 800°C. After 1000 h under minor current load, a Cr-source was placed close to the cell and the test gas was humidified to 30% r.h., where 100% corresponds to the equilibrium vapor pressure at of $H_2O$ at 25°C. Cr-poisoning under dry conditions was not investigated because only minor Cr-deposition was found on dense samples at 800°C in dry atmospheres (see section 4.2.3).
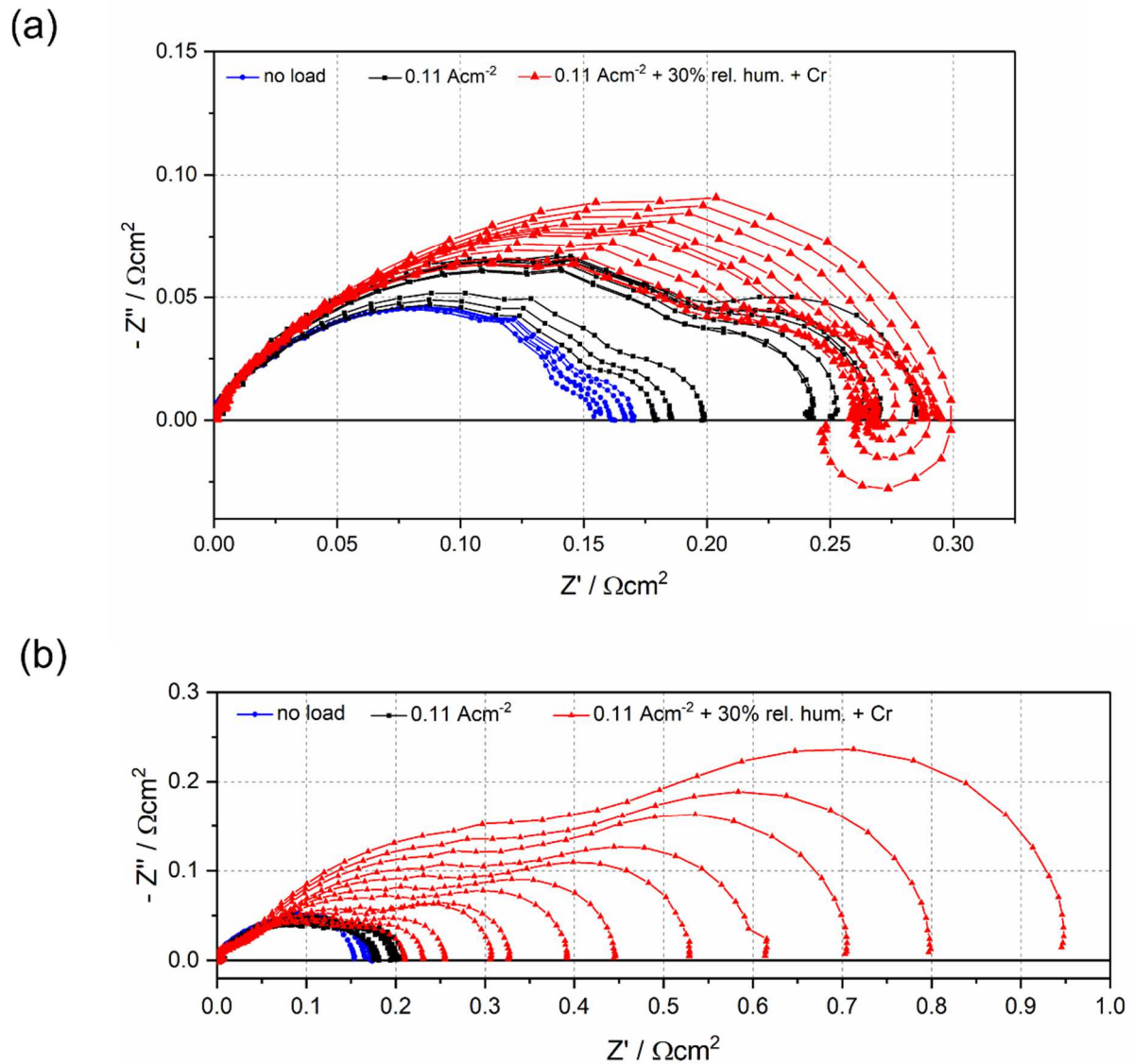
Fig. 4.47: OCV electrochemical impedance spectra of the LNO SOEC anode (a) and the SOFC cathode (b) at 800°C. The impedance spectra have been corrected for the inductance of the test setup as well as the resistance of the electrolyte. Different stages of the degradation experiment are color coded.

However, as soon as humidity and a Cr-source are introduced the ASR of the SOFC cathode increased rapidly, in comparison to the ASR of the SOEC anode. Furthermore, the SOEC anode developed inductive loops in the low frequency range, which can be caused by improper placement of the reference electrode (RE) or by differences in polarization resistances ($R_p$) or time constants ($\tau$) between working (WE) and counter electrode (CE) [310]. To avoid the misinterpretation of EIS-distortions caused by the RE, the cell impedance was also measured in 2-electrode configuration (Fig. 4.48). The EIS-spectra of the cell show no distortions, but also a significant degradation of the cell ASR.
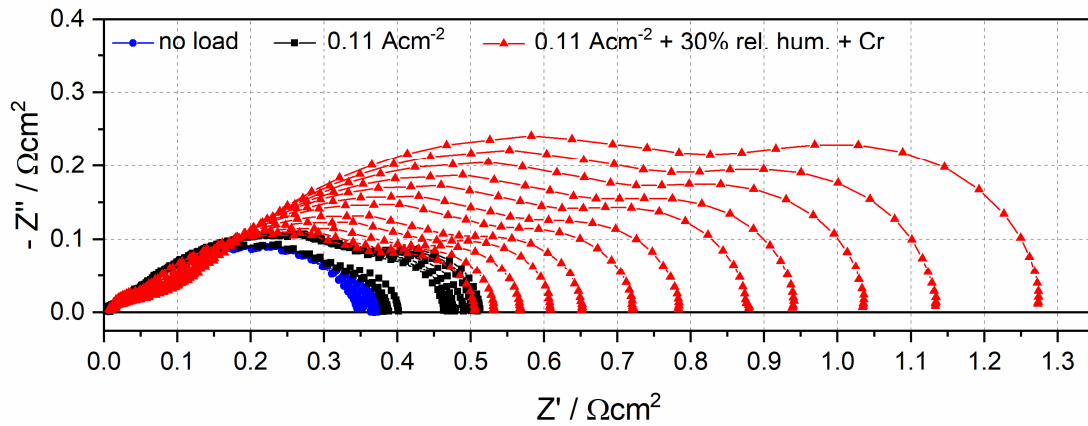
*Fig. 4.48: OCV impedance spectra of the symmetrical LNO-GDC-LNO cell. The contributions of the inductance of the test setup and the electrolyte resistance have already been subtracted. Black curves denote measurements conducted without Cr, humidity or load. Blue curves correspond to measurements without the presence of Cr or humidity, but current load of 110 mA cm$^{-2}$. Red curves show measurements conducted under the influence of current load, Cr and H$_2$O. Taken from [309].*

Fig. 4.49 shows the separated resistance contributions of the SOEC anode and the SOFC cathode over time, which are split into a series resistance (R$_s$) corresponding to the ohmic resistance of electrolyte and a polarization resistance (R$_p$) of the electrode layer. During the first two stages of the experiment - under dry and Cr-free conditions with and without any applied current load - a slight increase in the ASR of both electrodes was detected. This minor increase might be caused by La-segregation towards the LNO surface, which was observed on dense samples annealed under dry conditions (see section 4.2.4). As soon as the cell is subjected to humidity in the presence of a Cr-source, the ASR of the SOFC cathode rises to 0.96 Ω cm$^2$. The SOEC anode, however, is significantly less affected in comparison, showing a final ASR value of 0.30 Ω cm$^2$. These trends are further supported by the I-V-measurements (Fig. 4.50).
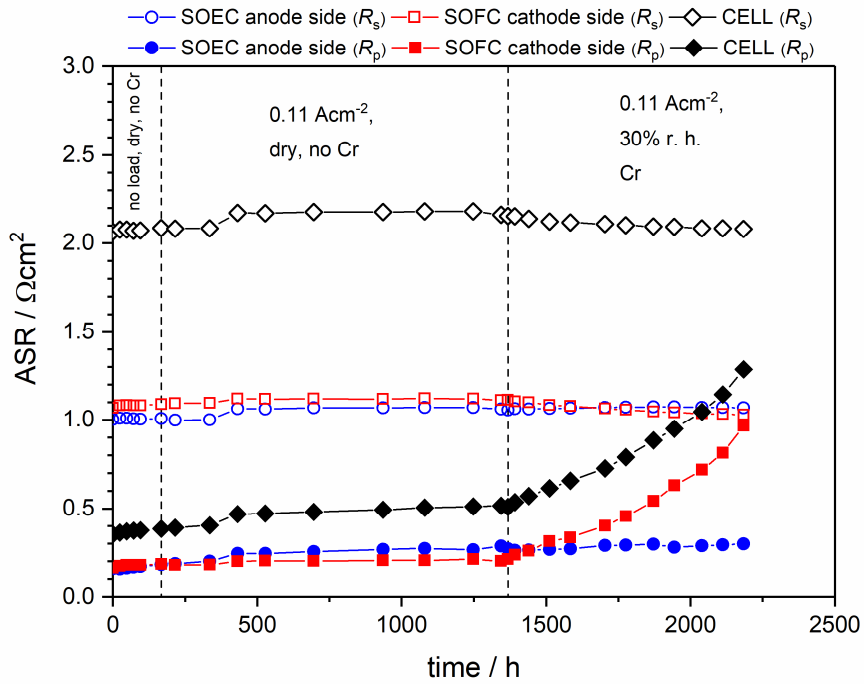
*Fig. 4.49: Evolution of the area specific resistance (ASR) of the SOEC anode (blue), the SOFC cathode (red) and the cell (black) over time. $R_s$ and $R_p$ denote the series resistance, mainly the ohmic resistance across the electrolyte and the polarization resistance of the electrodes. Taken from [309].*
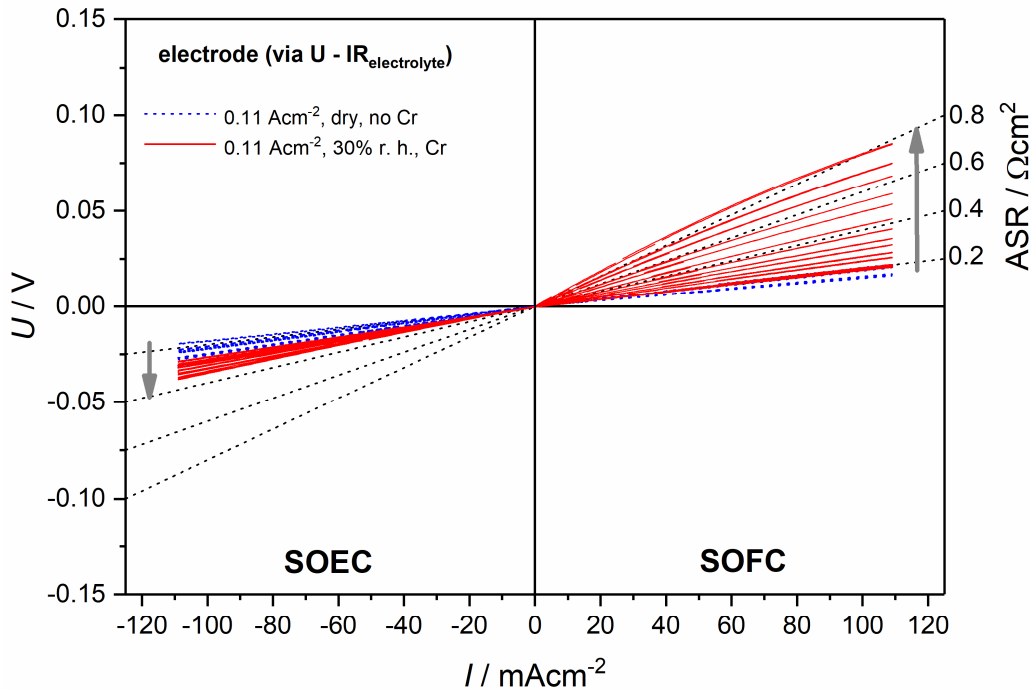


*Fig. 4.50: I-V-characteristics of the SOEC anode (blue) and the SOFC cathode (red). Black curves refer to half of the I-V-curve of the symmetrical cell. Taken from [309].*

### 4.3.4   Post-test analysis

Two additional dense and polished samples – control sample 1 and 2 - were placed near the symmetrical LNO cell, which were removed for chemical and microstructural analysis at after stage 2 (before the addition of Cr) and at the end of the experiment to complement the analyses performed on the LNO electrodes. Fig. 4.51 shows SEM micrographs of control sample 1 (a) and 2 (b) recorded in BSE mode. Dark and light grey patches, which correlate with the LNO grain structure underneath are clearly visible in both images, due to Z-contrast. EDXS-analyses revealed that the light grey areas on both samples are covered in a layer of platinum. The surface of control sample 2 also contained small amounts of Cr, which barely registered in the recorded EDX-spectra.
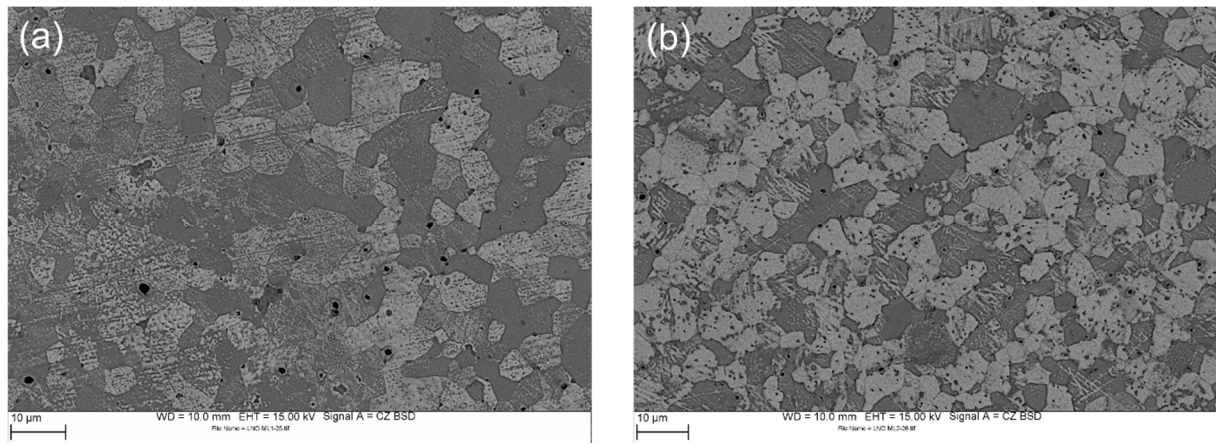


*Fig. 4.51: SEM-BSE images of control sample 1 (a) and 2 (b).*

Fig. 4.52 shows cross section SEM-images of the SOEC anode and the SOFC cathode. Both electrodes show a layer thickness of 12 μm. The LNO grains are well attached to each other in both electrodes, but the adhesion to the electrolyte seems to be poor. This apparent delamination could be the result of the performed degradation experiment. However, the obvious gaps between the electrode layer and the electrolyte could also have been caused by the sample preparation. After completion of the long-term stability test, the cell was cut in multiple pieces for post-test analysis by means of a diamond wire saw. The applied mechanical strain could be responsible for the poor connectivity of the LNO grains to the electrolyte. In any case, it is implausible that the observed ASR increase of the SOFC cathode is caused by electrode delamination, because both electrodes exhibit this poor connectivity to a similar degree.
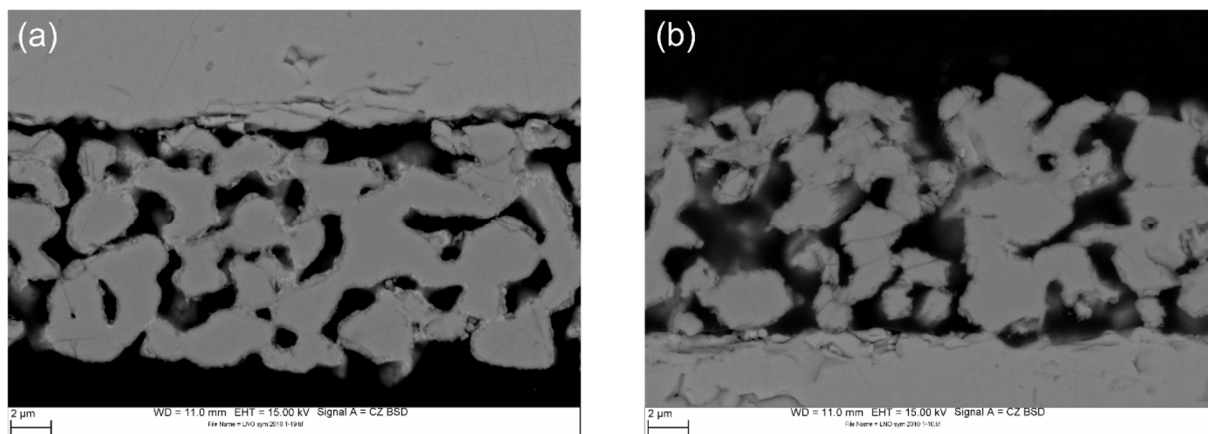
*Fig. 4.52: SEM-BSE cross section image of the LNO SOEC anode (left) and the SOFC cathode (right). Image taken from [309].*

Upon close inspection of the SOEC anode a light grey secondary phase around the circumference of the LNO grains can be perceived. EDXS-spot analysis on multiple sites confirmed that the phase contains Pt. No evidence of Cr was found on the anode. The SOFC cathode, however, does not possess a Pt-layer, but small amounts of Cr near the electrode surface, which are almost undetectable in the BSE-contrast. To determine the extent of the Cr-contamination, EDXS-elemental mappings of both electrode layers were recorded (Fig. 4.53). No deviations of the main constituents (La, Ni, and O) were found. The elemental distribution maps were created by deconvolution of the La $L_{\beta2}$ and Cr $K_{\alpha1,2}$ peaks. To verify the findings of the EDXS-analysis, WDX-spectra were recorded at several spots on both electrodes (see Fig. 4.54 and Fig. 4.55). Clear signs of Cr-poisoning where found on both electrodes, however the SOFC cathode seems to be affected to a much higher degree.
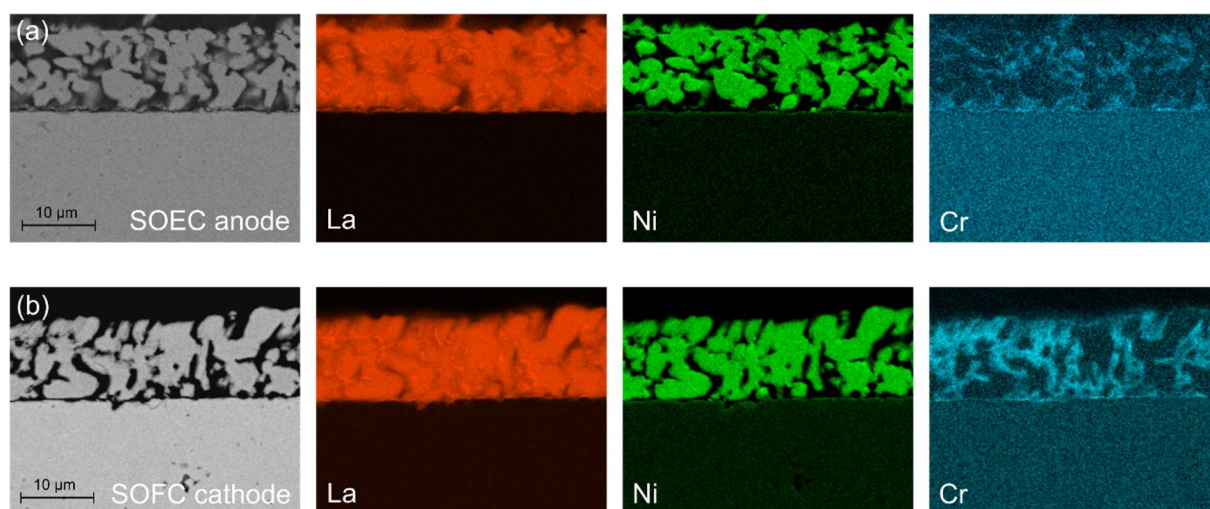


*Fig. 4.53: SEM-BSE image of the SOEC anode (a) and the SOFC cathode (b), with the corresponding elemental distribution maps of La, Ni and Cr. The La- and the Ni-map were recorded using EDXS, whereas the Cr-map was determined using WDXS-analysis.*

The recorded WDX-spectra allow for a clear distinction between the La $L_{\beta2}$ and the Cr $K_{\alpha}$ peaks, which confirms the presence of Cr-deposit on the surface of LNO grains. No significant amount of Cr was found inside the cross-cut LNO grains, which substantiates the initially assumed gas phase transport of volatile Cr-species. Furthermore, the WDX-spectra in Fig. 4.54 and Fig. 4.55 depict a distinct difference between the La/Cr ratios of the SOEC anode and the SOFC cathode indicating a more severe Cr-contamination on the SOFC cathode.
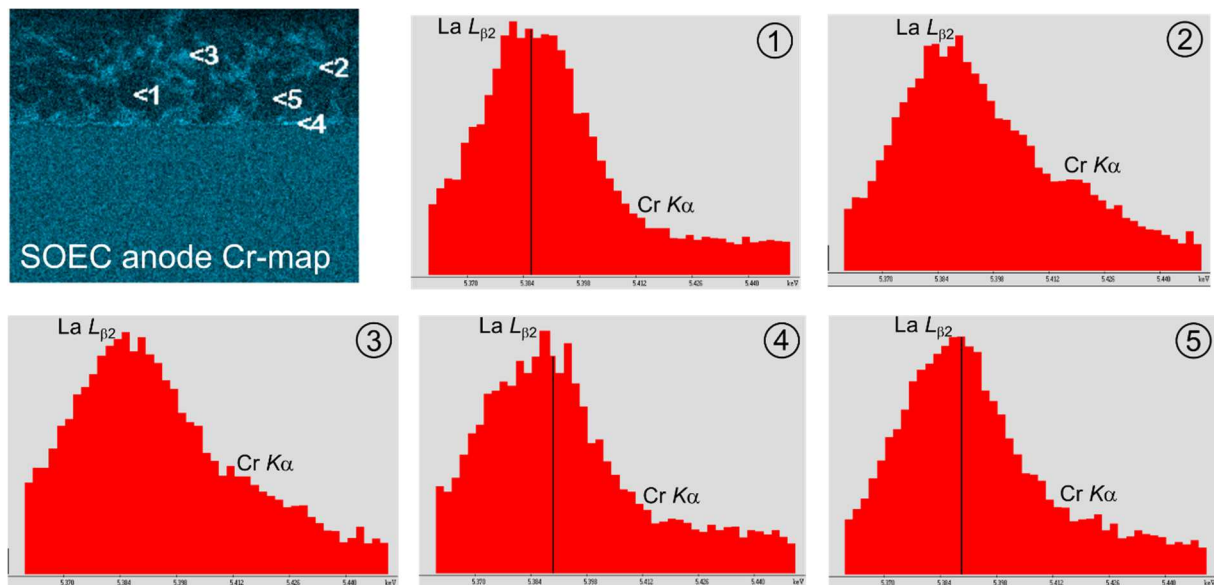


Fig. 4.54: Cr EDXS-elemental map of the SOEC anode and complementary WDXs-spot analyses.
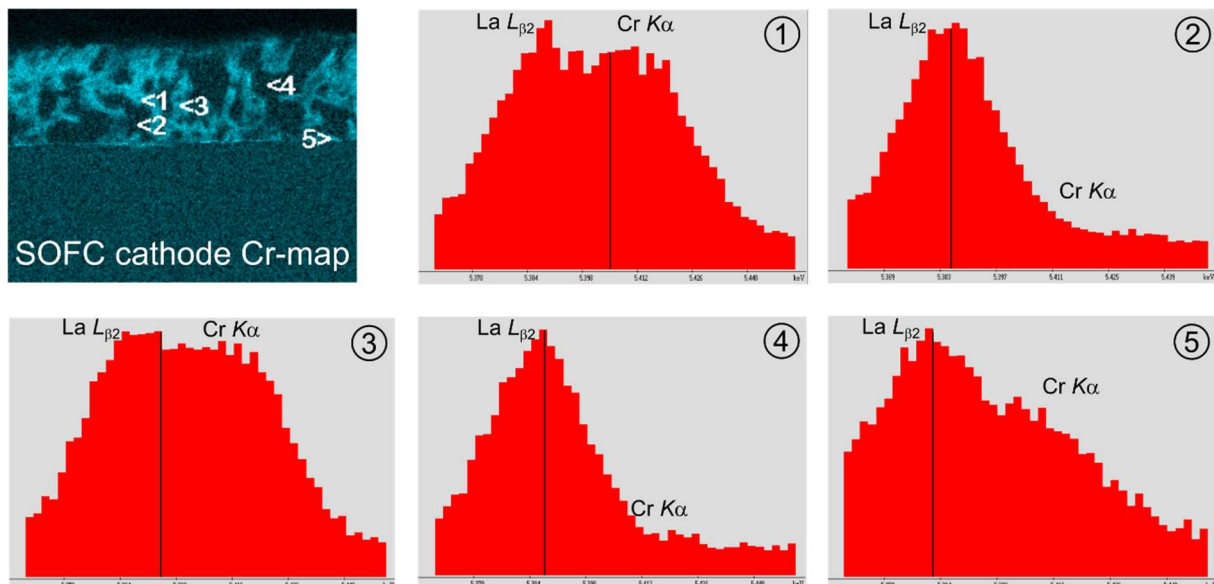


Fig. 4.55: Cr EDXS-elemental map of the SOFC cathode and complementary WDXs-spot analyses.

Based on the results obtained so far, the most likely explanation for the strong performance deterioration of the SOFC cathode seems to be higher levels of Cr deposited on the SOFC

cathode in comparison to the SOEC anode. Several reasons for the higher sensitivity to Cr-poisoning of the SOFC cathode have been proposed. The anodic polarization might protect the SOEC anode electrochemically from reductive deposition of gaseous Cr(VI)-species to Cr(III)- compounds [176,187,311]. Also, the direction of oxygen flow in the electrode might play a role. In SOFC cathode the oxygen flow is directed into the pore structure, therefore also promoting the gas phase transport of volatile impurity species, whereas the oxygen flow out of the pores somewhat impedes the Cr-inward diffusion [312]. At this point, it should also be mentioned that the design of the used sample holder might also contribute to the difference in Cr-deposition. The cells were placed horizontally in the sample holder, with one electrode facing upwards (SOFC cathode) and one downwards (SOEC anode). The Cr-source was placed at the same level as the electrolyte substrate and as close as possible to the mounted cell, to ensure a symmetrical gas phase transport of Cr towards both electrodes. Nevertheless, gas transport to the downward facing electrode could have been partially constricted, which, in this case, coincides with lower levels of Cr found on the SOEC anode.

### 4.3.5  Discussion of Cr-poisoning without current load

In an attempt to separate the effects of current load and geometrical constraints, a second cell was annealed for 1000 h at 800°C in humid (30% r.h.) atmosphere in the presence of a Cr-source. Like the main sample, the cell consisted of a GDC electrolyte substrate, screen printed with one layer of LNO paste on each side sintered at 1200°C for 2 h. However, the cell was prepared without Pt-reference electrode or Au-grid-contacts, because no electrochemical measurements were conducted. After 1000 h under Cr-poisoning conditions, the sample cell was analyzed using SEM-EDXS. Fig. 4.56 shows SEM-BSE cross section images of the upward facing electrode (top) and the downward facing electrode (bottom) and the corresponding EDXS-elemental distribution maps of La, Ni, O, and Cr. La and O seem to be homogeneously distributed across both electrodes. In the Ni-map some Ni-accumulations are visible on both electrodes. Clear signs of Cr-poisoning were found on top and bottom electrode (see Cr-EDXS-map). The effect, however, seems to be more pronounced for the top electrode. This seems to suggest that the observed differences in Cr-deposition may be, at least in part, caused by the asymmetric design of the sample holder.
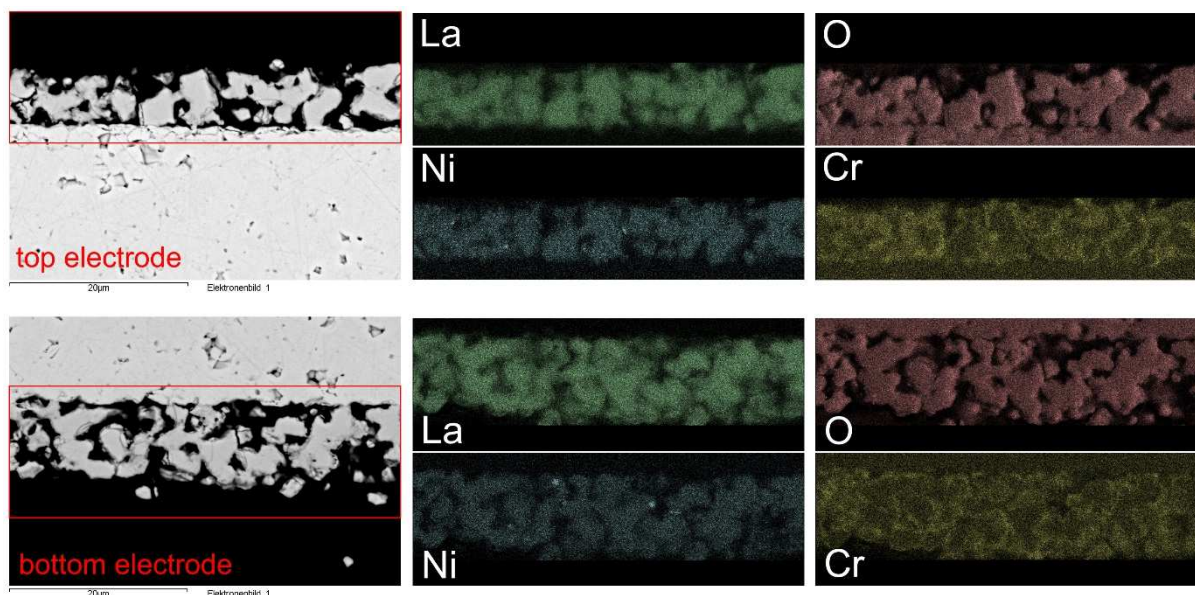
*Fig. 4.56: SEM-BSE images of the LNO up-facing electrode (top) and the down-facing electrode (bottom) of a symmetrical cell annealed for 1000 h at 800°C in 20%O₂/Ar at 30% r.h. without current load. The corresponding elemental distribution maps pf La, Ni, O, and Cr were generated using EDX-spectra.*

## 4.4 Long-term stability of $La_2NiO_{4+\delta}$ - $Ce_{0.9}Gd_{0.1}O_{2-\delta}$ – composite air electrodes against Cr-poisoning at 800°C under current load

To gain a better understanding of the effects of high current loads on Cr-deposition under anodic and cathodic polarization, a long-term study on an LNO/GDC composite cell was conducted. In earlier tests, rapid delamination of the SOFC cathode during I-V-characterization was observed for LNO cells. One way to improve electrode adhesion is the application of composite electrodes made from the electrode and the electrolyte material. In a pre-study, LNO/GDC composite electrode layers were applied to a GDC electrolyte substrate and subjected to current loads of up to 2 A cm⁻². No electrode delamination was observed under anodic or cathodic polarization. For the long-term Cr-poisoning study, electrodes with two functional layers were applied. The top layer consisted of pure LNO with coarse microstructure to provide sufficient electronic conductivity and the layer directly in contact with the electrolyte consisted of a 50 wt-% LNO/GDC composite layer with fine microstructure, to avoid delamination issues. Due to the substantial Pt-contamination observed in the Cr-poisoning study of LNO, the reference electrode was replaced by a porous LNO electrode, contacted with a gold wire around the circumference of the button cell. Pt-wires used to contact the working and the counter electrodes were also replaced by Au-contacts.

## 4.4.1 Determination of electrode sintering parameters

A screen-printed layer of LNO/GDC composite paste on GDC was dried and quartered using a diamond wire saw. The resulting samples were sintered at temperatures between 1200°C and 1300°C with heating and cooling rates of 5 and 2 K min$^{-1}$ to produce properly adhered electrode layers. SEM-BSE images of the thus obtained electrode layers are displayed in Fig. 4.57. To produce a uniform microstructure finely milled powders of LNO and GDC had been mixed. Fig. 4.57a shows the electrode layer obtained at 1200°C. The microstructure seems mechanically stable, showing good intergranular connectivity. The BSE-contrast reveals the presence of several dark secondary phases, which were identified as NiO using EDXS. This is not surprising since La-diffusion into ceria has already been found in the reactivity study (see section 4.3.2), as well as in post-test analyses of LNO electrode-electrolyte interfaces.
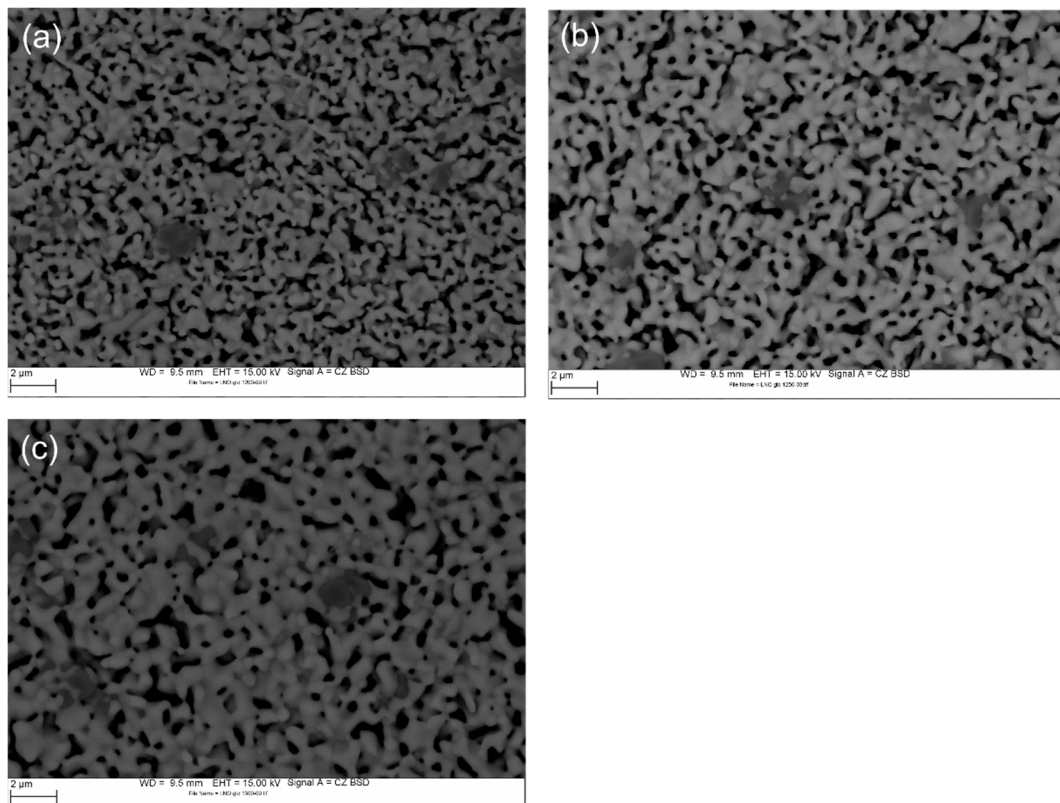


*Fig. 4.57: SEM-BSE-images of screen-printed LNO/GDC composite electrode layers sintered at (a) 1200°C, (b) 1250°C and (c) 1300° for 2 h.*

The microstructure of the layer sintered at 1250°C looks less uniform, due the aggregation smaller particles, which lead to the formation of elongated pores. At 1300°C, the microstructure of the electrode layer already appears too dense (Fig. 4.57c). Application of the scotch-tape test to check the electrode adhesion showed, that a minimum temperature of 1250°C is necessary to obtain sufficient adhesion of the electrode to the electrolyte.

### 4.4.2 Electrochemical properties

Fig. 4.58 presents the OCV impedance spectra of the LNO_LNO/GDC-composite electrodes in electrolyzer (a) and fuel cell mode (b). Contributions of the series resistance of the electrolyte and the inductance of the measurement setup have already been subtracted from the curves. Both electrodes showed initial ASRs of approximately 0.3 $\Omega$ cm$^2$, which is almost twice as high as for the pure LNO electrode. During stage 1 of the experiment, where no electrical current between the EIS-measurement was applied, the ASR of the SOEC anode and the SOFC cathode remained remarkably constant. Results from 2-electrode EIS-measurement (Fig. 4.59) are in good agreement with the sum of the SOEC and the SOFC contributions, indicating a properly functioning reference electrode.
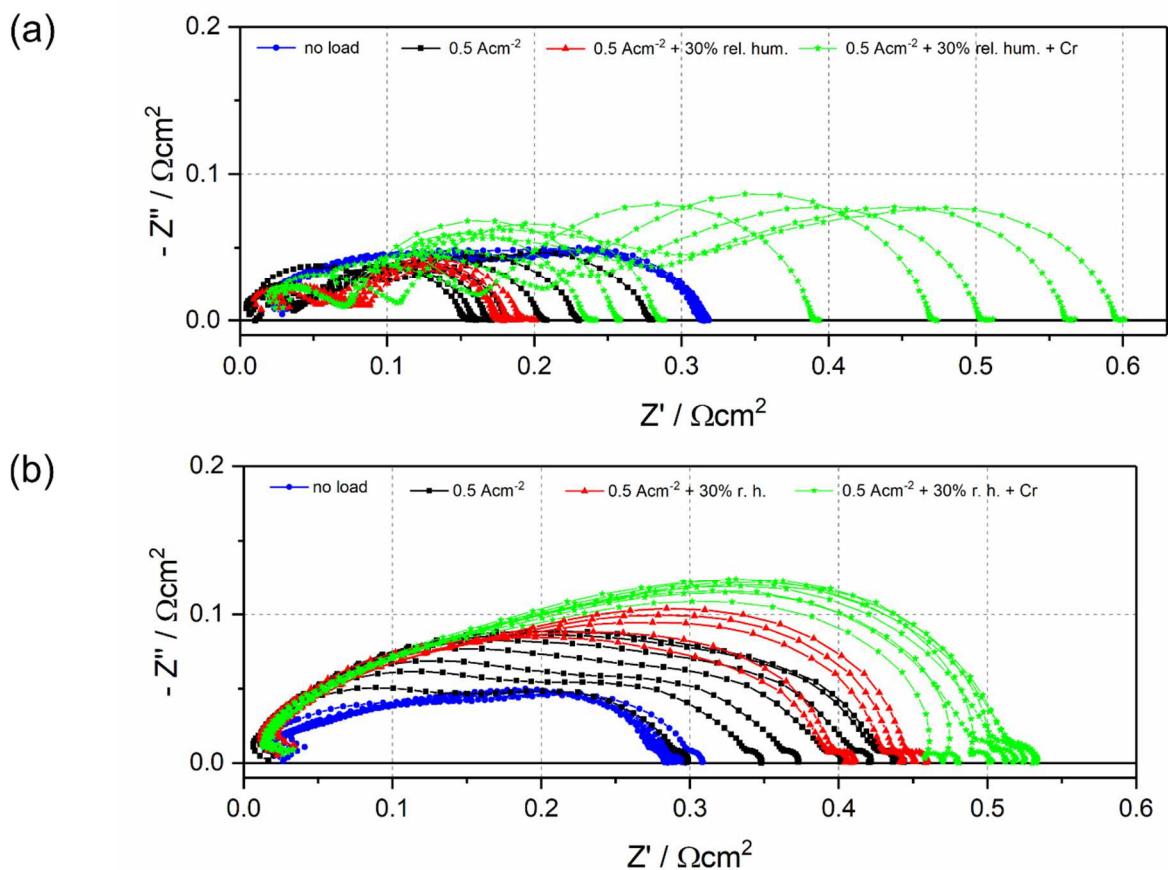


Fig. 4.58: OCV electrochemical impedance spectra of the LNO/LNOGDC SOEC anode (a) and the SOFC cathode (b) at 800°C and 0.5 Acm$^{-2}$. The impedance spectra have been corrected for the inductance of the test setup as well as the resistance of the electrolyte.
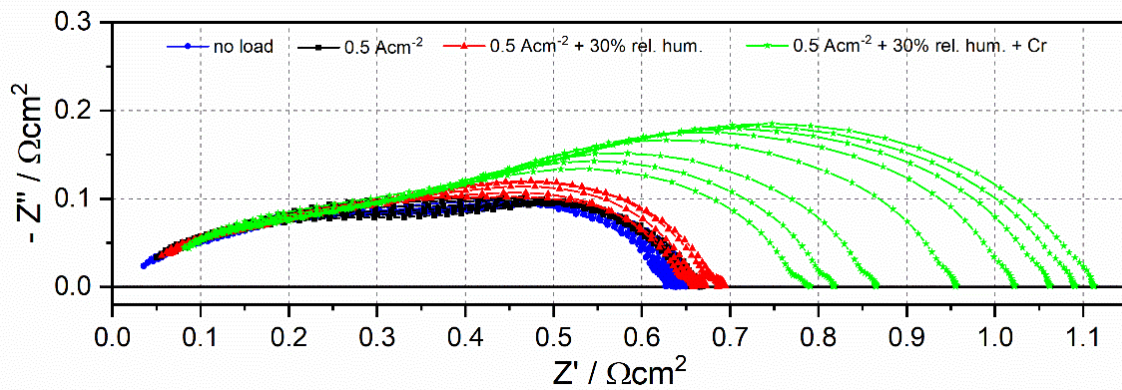
*Fig. 4.59: OCV impedance spectra of the symmetrical LNO/GDC composite cell at 800°C and 0.5 Acm⁻². The contributions of the inductance of the test setup and the resistance of the electrolyte have already been subtracted.*

The contributions of each electrode, the series resistance attributed to the electrolyte and the cell impedance measurements are presented in Fig. 4.60 as a function of time and under different experimental conditions. During stage 2 of the degradation experiment a constant current load of 500 mA cm⁻² was applied to the cell between the OCV EIS-measurements. The sample cell was still measured under dry and Cr-free conditions. With the start of stage 2, also IV-curves were recorded in the same time intervals (Fig. 4.61). As soon as a current was drawn through the cell, the ASR of the SOEC anode dropped, whereas the resistance contribution of the SOFC cathode increased. Usually, an increase in electrode ASR suggests that degradation phenomena are occurring at the electrode. However, it seems that the ASR drop of the SOEC anode and the ASR increase of the SOFC cathode amount to the same difference in resistance. A closer look at the cell impedance data indeed reveals a constant ASR measured in 2-electrode configuration. This indicates that the change in ASR is most likely an artifact caused by the reference electrode. Apart from this initial change, the ASR remained constant over the entire duration of stage 2.
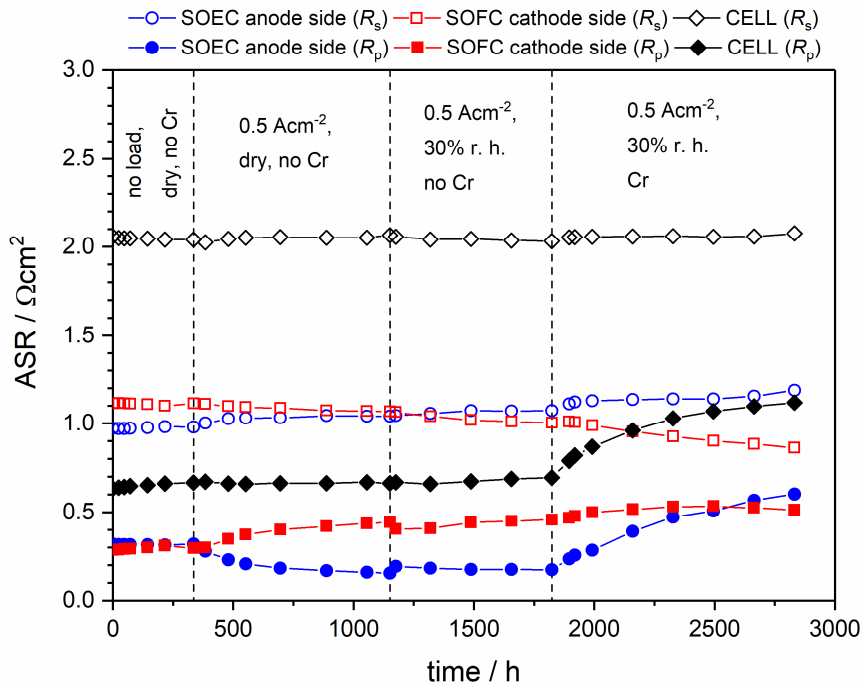
*Fig. 4.60: Area specific resistance (ASR) of the LNO/GDC composite SOEC anode (blue), SOFC cathode (red) and the symmetrical cell (black) vs. time. Rs and Rp refer to the series and polarization resistance, respectively.*

To determine whether humidity has a detrimental influence on the electrode performance or not, the test gas was humidified to 30% r.h. based on the equilibrium water vapor pressure at 25°C, while still applying the same current load. Apart from a slight kink in the ASR curve at the beginning of stage 3, the ASRs of both electrodes remained almost constant over the course of 650 h. It can therefore be concluded that humidity in the absence of easily vaporized Si and Cr-compounds has no significant influence on electrode performance and thus no substantial effect on the oxygen exchange reaction at the LNO surface. At the beginning of stage 4 a Cr-source was placed close to the sample. Measurements were continued in humid test gas and the same current load was employed in between measurement cycles. Once the cell was exposed to humidity and chromium at the same time, the ASR of the SOEC anode increased steadily, whereas the ASR of the SOFC cathode remained the same for the entire duration of 940 h. Additionally, the corresponding I-V-data mirror this trend (Fig. 4.61). The measured I-V-curves show no hysteresis or strong curvature. Interestingly, Cr-poisoning under realistic current load seems to have the opposite effect on composite electrodes, when compared to pure LNO electrodes. However, it is somewhat unclear whether the observed effect is simply the result of the increased polarization or of different material properties of the composite electrode.

115
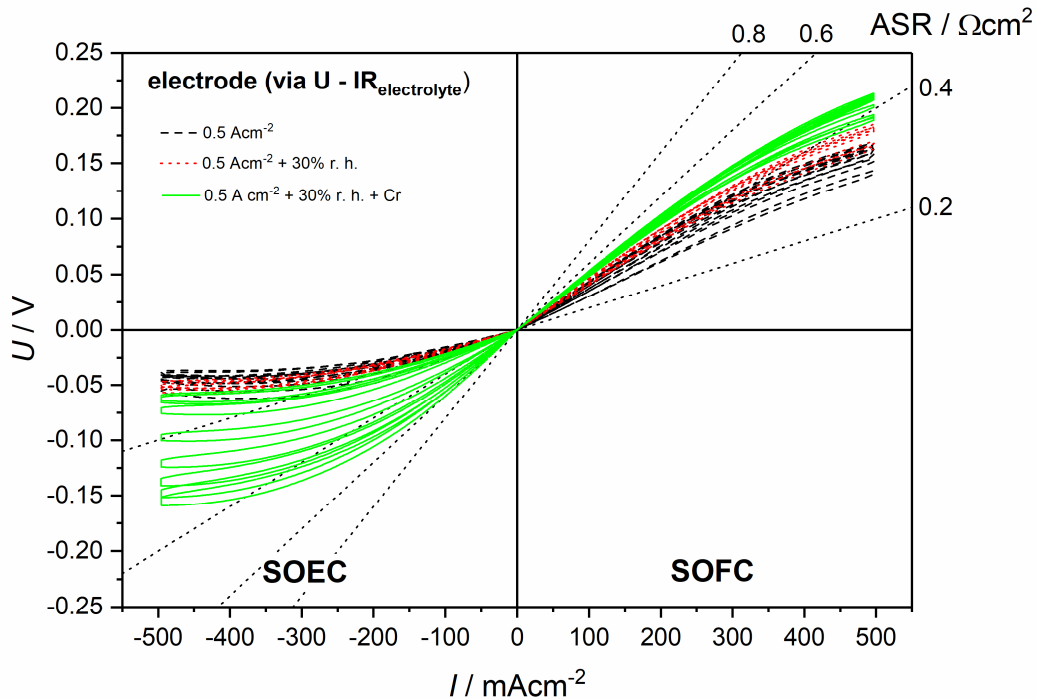
*Fig. 4.61: I-V-curves of the LNO/GDC composite SOEC anode (left) and SOFC cathode (right) layers at 800°C under different conditions. The black curves correspond to the I-V-curve of the cell divided by 2. The series resistance contribution of the electrolyte has already been subtracted.*

### 4.4.3 Post-test analysis

To identify the cause of the performance degradation of the SOEC anode, SEM-EDXS-analysis were performed. A cross-section view of both electrode layers is presented in Fig. 4.62. Both electrodes exhibit a uniform layer thickness of 13 μm. The SOEC anode (top) shows a dense microstructure in the composite layer, as well as dark specks in the LNO current collector. EDX-spot analysis confirmed Cr-rich phases, which are almost depleted of Ni within the composite layer. The dark spots in the LNO layer, however, correspond mostly to sulphur impurities. Cr-levels, however, are almost beneath the detection limit of EDX. On the SOFC cathode (Fig. 4.62, bottom), Cr was not detectable via EDXS-spot analysis. The composite layer is partly decomposed into NiO and La-doped ceria phases. Remaining LNO phases show no sign of Cr-poisoning. La-diffusion into ceria grains was found on both electrodes. Despite the seemingly poor connection between the composite layer and the GDC electrolyte, no electrode delamination was observed.
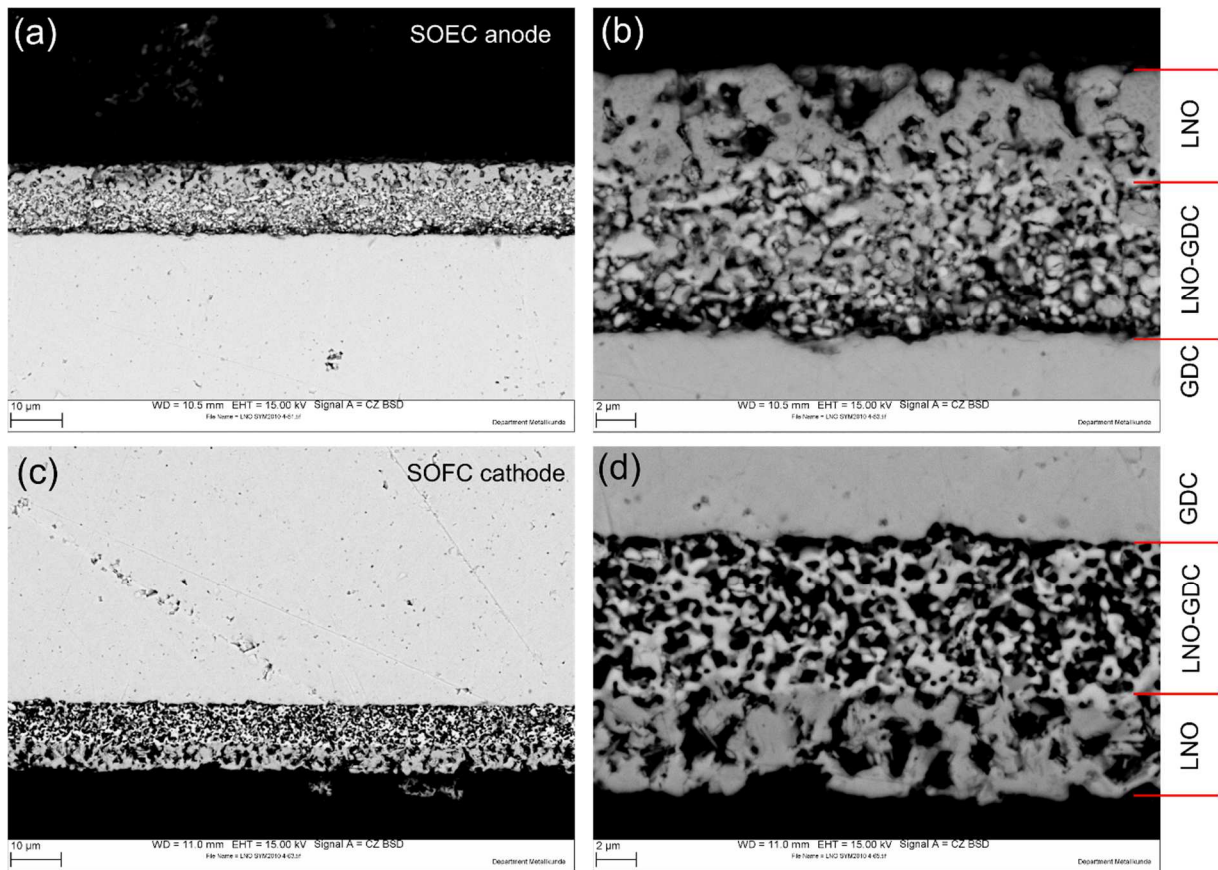
*Fig. 4.62: SEM-BSE cross section images of the LNO/GDC composite SOEC anode (a, b) and SOFC cathode (c, d) in 1000x (left) and 4000x magnification (right).*

To obtain a clearer picture about the extent of the Cr-deposition, EDXS-elemental distribution maps of both electrodes were recorded. Fig. 4.63 shows a SEM-BSE image and corresponding maps of O, Cr, Ni, La, and Ce. The Cr-map reveals that Cr is present in the LNO current collector, as well as in the composite layer. La is concentrated mostly in the LNO current collector, apart from some accumulations in the composite layer. These La-accumulations correspond with the Cr-accumulations in the Cr-map. The Ni-map shows some larger Ni-grains in the composite layer, which are caused by the partly decomposition of LNO in the presence of GDC at high temperatures. Oxygen is distributed rather homogeneously in both functional layers.
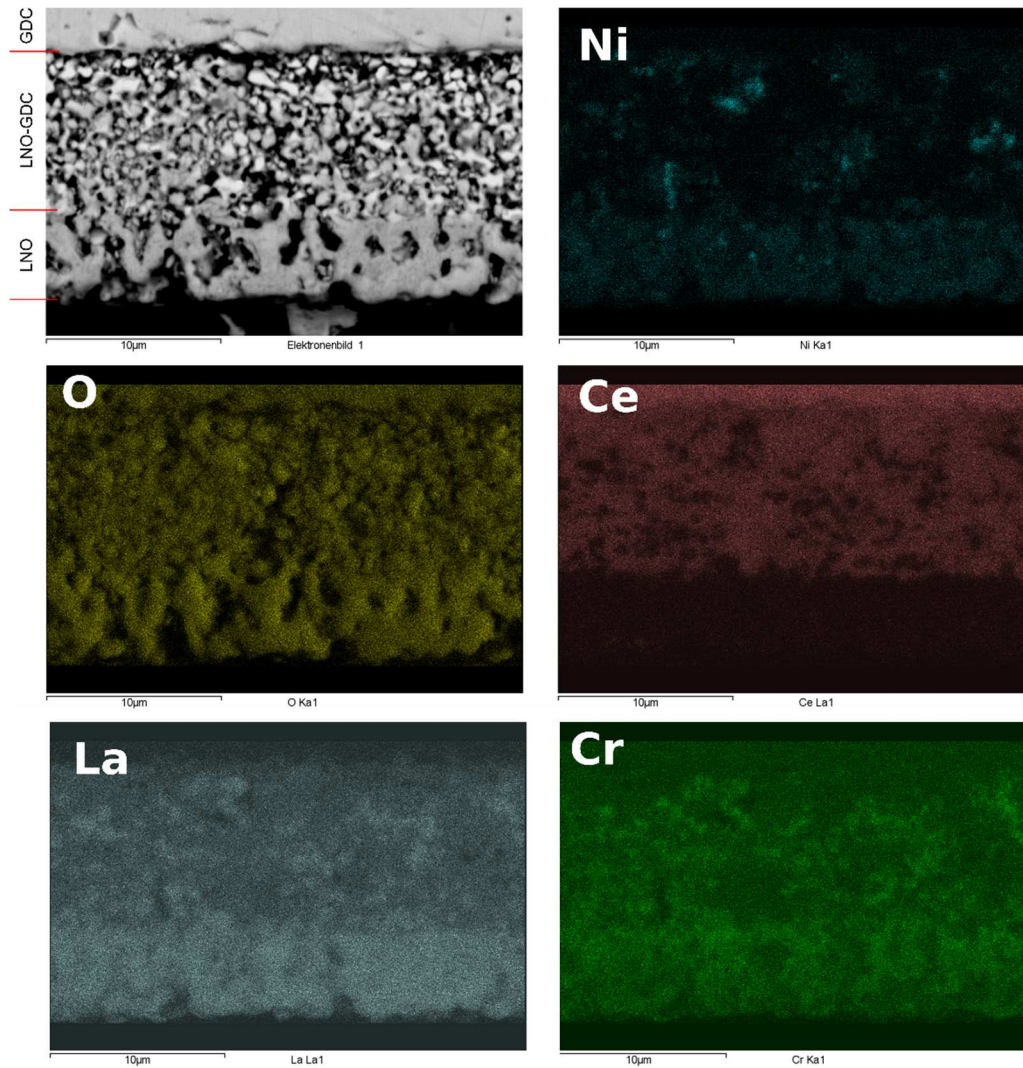
*Fig. 4.63: Post-test SEM-BSE image of the degraded LNO/GDC composite SOEC anode and corresponding EDXS-elemental maps.*

Fig. 4.64 depicts a SEM-BSE image of the SOFC cathode and corresponding maps of O, Ni, La, and Ce. Cr-levels were below the detection limit of EDXS. Apart from the absence of Cr, the elemental distribution within the SOFC layer is similar to the SOEC anode.
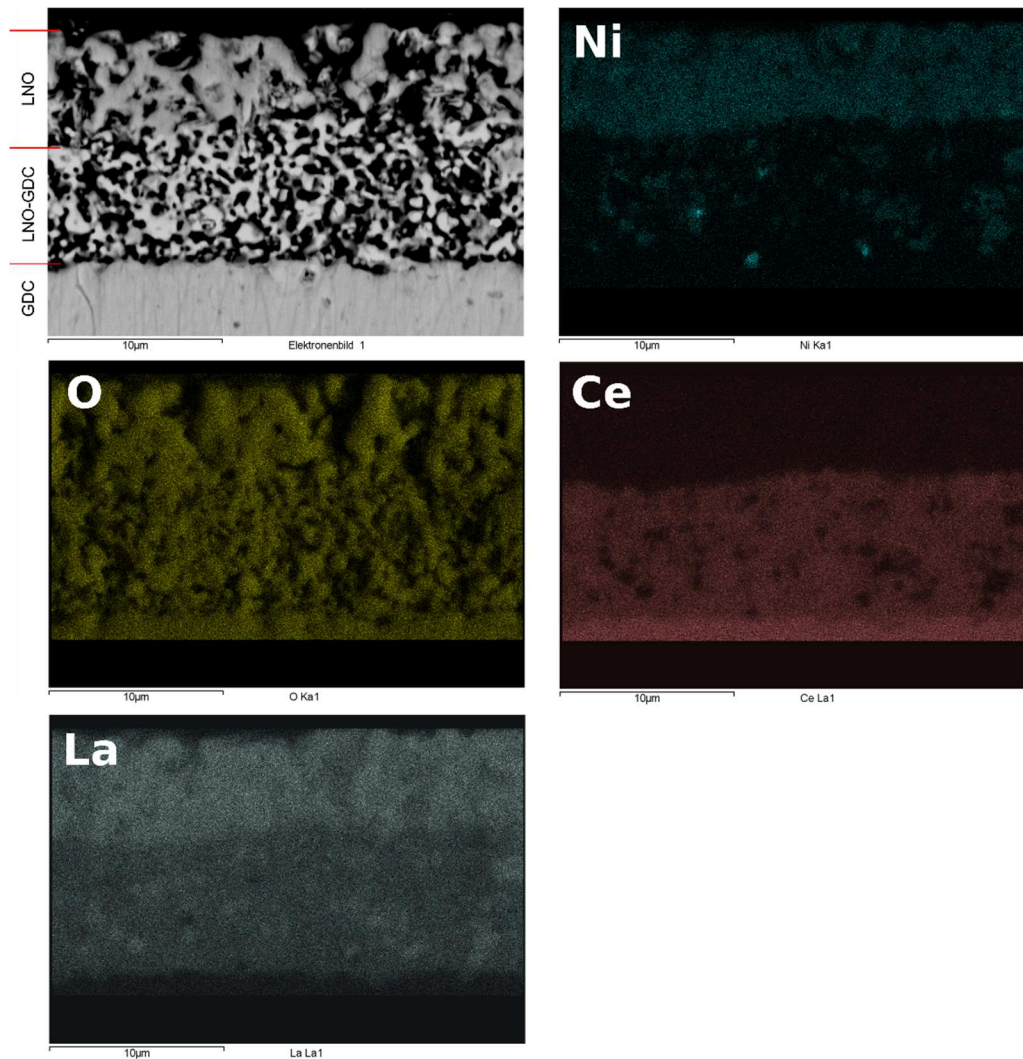
*Fig. 4.64: Post-test SEM-BSE image of the degraded LNO/GDC composite SOFC cathode and corresponding elemental distribution maps.*

Again, a pronounced electrode performance degradation is correlated with the presence of Cr. However, it remains unclear why Cr was predominantly deposited on the SOEC anode. As already mentioned in section 4.3.5, the horizontal placement of the cell in the sample mount might also influence the amount of deposited Cr-species. It is possible, that the top electrode– in this case, the SOEC anode - is exposed to higher gas flow rates and thus higher Cr-levels than the bottom electrode.

### 4.4.4   Discussion of Cr-poisoning without current load

To determine the influence of the asymmetry of the sample holder, an identical cell (but without reference electrode and contacting grids) was constructed and annealed for 1000 h at 800°C in a humid gas stream in the presence of a Cr-source. Post-test analysis of cross

sections of the bottom and top electrode are presented in Fig. 4.65 and Fig. 4.66, respectively. The Cr-maps show that Cr-impurities were deposited on both electrodes at similar levels.
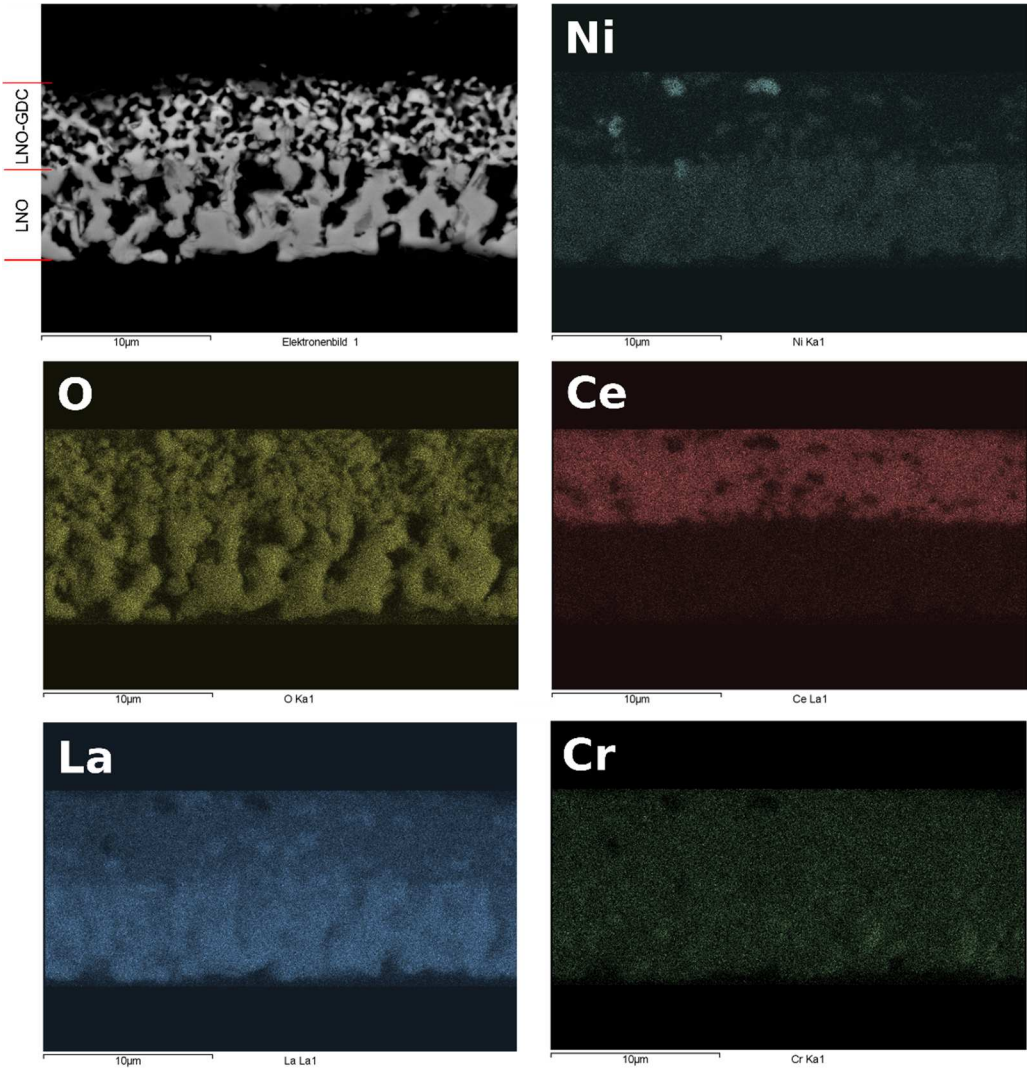


*Fig. 4.65: SEM-BSE cross section image of the bottom electrode of an LNO/GDC composite cell annealed at 800°C in 20% $O_2$ in Ar and 30% r.h. for 1000 h without current load, as well as correspond EDXS-elemental distribution maps.*
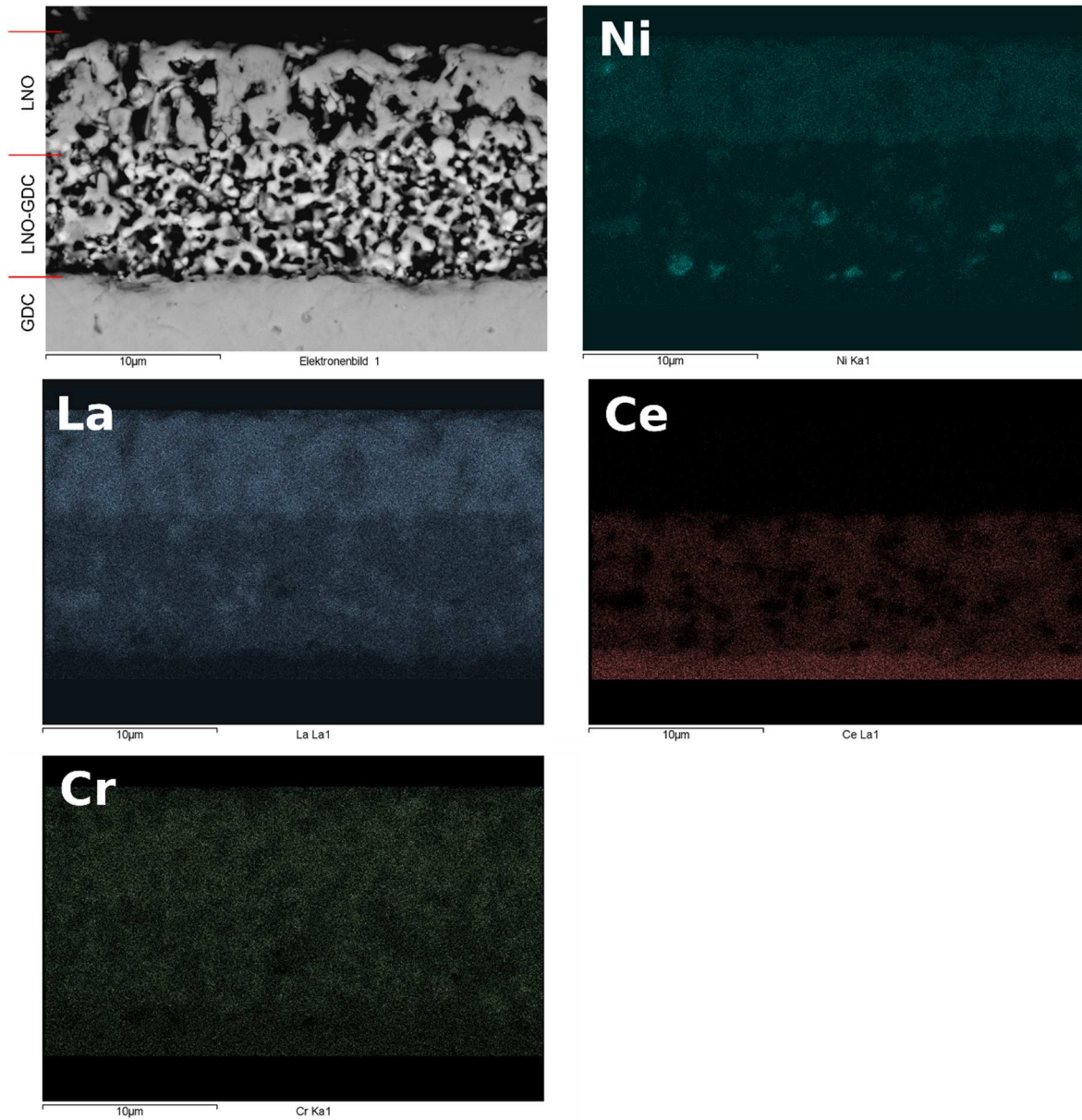
*Fig. 4.66: SEM-BSE cross section image of the top electrode of an LNO/GDC composite cell annealed at 800°C in 20% $O_2$ in Ar and 30% r.h. for 1000 h without current load, as well as correspond EDXS-elemental distribution maps.*

## 4.5 Long-term stability of $Pr_2NiO_{4+\delta}$ – air electrodes against Cr-poisoning at 800°C under current load

The third long-term Cr-poisoning experiment was conducted on a symmetrical PNO-GDC button cell. To the best of the author's knowledge only $La_2NiO_4$ and $Nd_2NiO_4$ have so far been investigated as SOFC electrode material with respect to Cr-induced degradation. The lack of data on the long-term stability of PNO is probably owed to the phase instability of PNO in the temperature range of 700°C – 1000°C. The decomposition of the electrode material during operation could have serious implications concerning conductivity and electrode adhesion at the electrode-electrolyte interface. However, PNO might be less prone to chemical reactions with Cr. For the long-term Cr-poisoning study, electrodes with four layers of PNO paste were screen-printed for each electrode. A Pt-reference electrode was used to separate the resistance contributions of the SOEC anode and the SOFC cathode. The experimental stages were identical to the ones in the Cr-poisoning study of LNO-electrodes.

### 4.5.1 Determination of electrode sintering parameters

A screen-printed PNO layer on GDC was dried and cut into 4 pieces. The electrode sintering temperature was varied between 1100°C and 1200°C. SEM-BSE surface micrographs of the sintered electrode layers are depicted in Fig. 4.67. The electrode layer sintered at 1100°C (Fig. 4.67a) exhibits a highly uniform and mechanically stable microstructure. The fine PNO grains show good intergranular connectivity and the pore size distribution is homogeneous. The electrode layers sintered at 1150°C and 1200°C (Fig. 4.67b and c) show a coarsened microstructure and significantly reduced electrode surface in comparison to the layer sintered at 1100°C. Since all three layers demonstrated excellent adhesion to the GDC electrolyte in a scotch-tape-test, 1100°C was chosen as the appropriate sintering temperature.
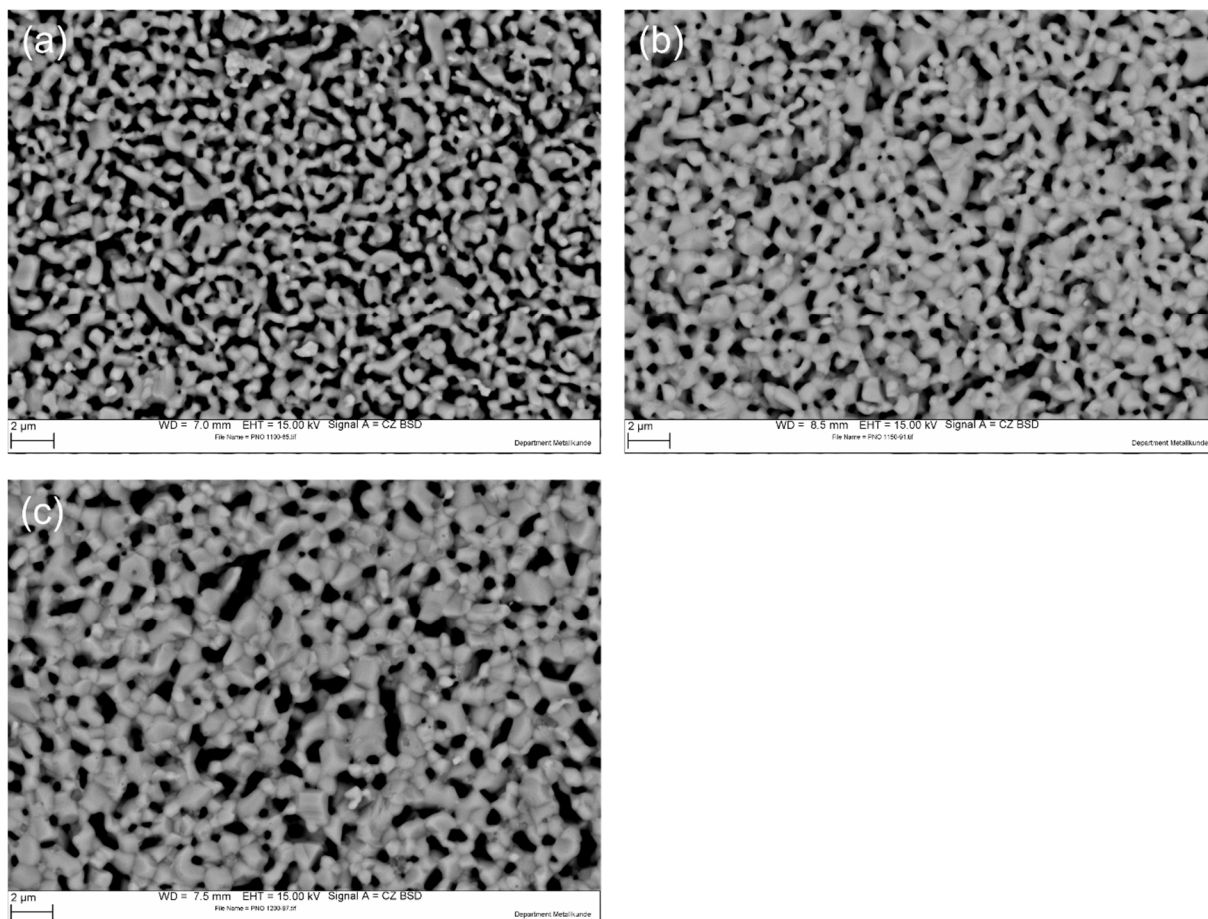
*Fig. 4.67: SEM-BSE images of screen-printed PNO electrode layers sintered at (a) 1100°C, (b) 1150°C and (c) 1200°C for 2 h.*

### 4.5.2 Reactivity of PNO with GDC

To determine the reaction products between a PNO electrode and the GDC electrolyte, fine powders of both materials were mixed in a weight ratio of 1/1 in a roller bed mill for 24 h. The resulting composite powder was then annealed in an alumina crucible at temperatures between 600°C and 1200°C for 6h. Room temperature XRD-patterns of the annealed samples were recorded covering a 2θ range between 10° and 100°. Quantification of the XRD-patterns was realized using Rietveld refinement.

Fig. 4.68 presents a detailed view of the XRD-patterns (20° ≤ 2θ ≤ 60°). Signals marked with the same symbols correspond to the same phase. The results of the quantification are depicted in Fig. 4.69. After annealing at 600°C, only signals corresponding to PNO and GDC were detected. At 700°C, a $PrNiO_3$ perovskite phase emerges, due to the partial decomposition of PNO. With increasing temperature more of the PNO phase decomposes into the corresponding perovskite structure and Pr-oxide.
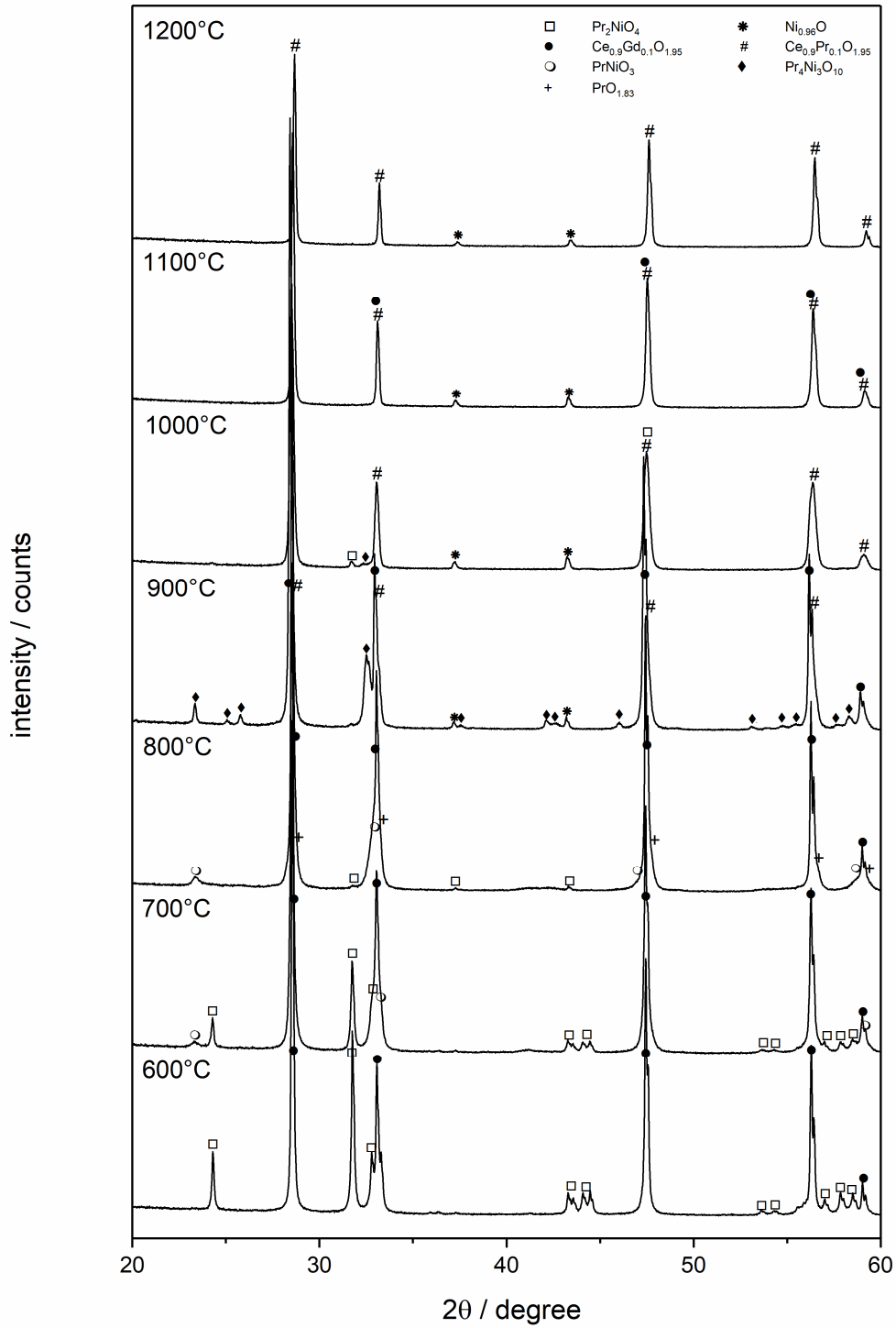
*Fig. 4.68: Room temperature XRD-patterns of 50 wt-% PNO/GDC powder mixtures annealed at temperatures between 600 and 1200°C.*
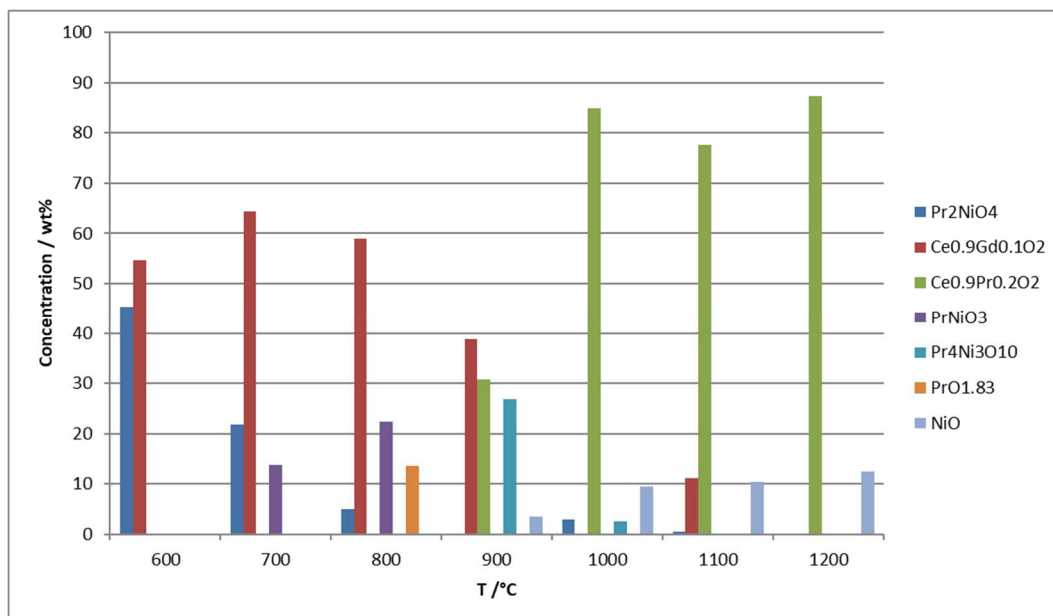
*Fig. 4.69: Concentrations of detected chemical compounds in weight percent in PNO/GDC powder mixtures after annealing for 6 h at the specified temperature as determined by Rietveld refinement.*

The first chemical reactions with the electrolyte material occur at 900°C, due to Pr-diffusion into GDC, forming a $Ce_{1-x}Pr_xO_2$ compound of unknown stoichiometry. Additionally, $Pr_4Ni_3O_{10}$ (PNO43), the n=3 member of the PNO RP-series and small amounts of NiO are present. At 1000°C PNO43 partly reforms into PNO and NiO. Increasing the temperature by 100°C to 1100°C produces mostly Pr-doped ceria, but small amounts of NiO, GDC and LNO are also present. At 1200°C, the most common sintering temperature for nickelate-based electrode, only $Ce_{1-x}Pr_xO_2$ and NiO were detected.

### 4.5.3   Electrochemical properties

In Fig. 4.70 the OCV impedance spectra of the PNO SOEC anode (a) and SOFC cathode (b) at 800°C are depicted. The inductance of the sample mount has already been subtracted from the curves. The initial ASRs of both electrodes amounted to approximately 0.1 Ω cm², which is slightly lower than in comparison to an LNO electrode. In the first part of the experiment (stage 1), the intrinsic stability of the electrodes was tested. During this time, no current load was applied, and all measurements were conducted under dry, Cr-free and OCV-conditions. After an initial increase, the ASR of both electrodes remained remarkably constant. Cell impedance measurements conducted in 2-electrode configuration (Fig. 4.71) are in good agreement with the sum of the SOEC and the SOFC contributions.
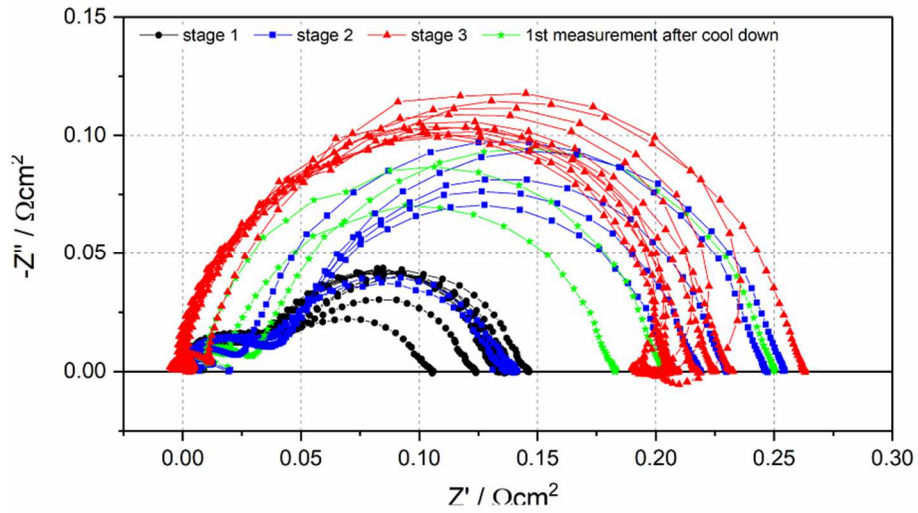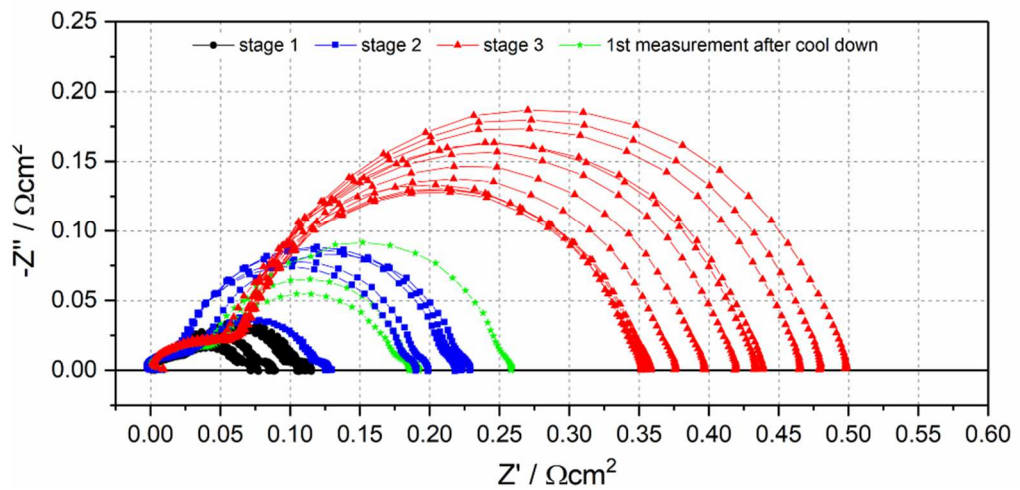
*Fig. 4.70: OCV electrochemical impedance spectra of the PNO SOEC anode (a) and the SOFC cathode (b) at 800°C. The inductance of the measurement setup and the electrolyte resistance have already been subtracted. Black curves denote measurements conducted without Cr, humidity or load. Blue curves correspond to measurements without the presence of Cr or humidity, but current load of 110 mA cm^-2. Red curves show measurements conducted under the influence of current load, Cr and 30% r.h..*
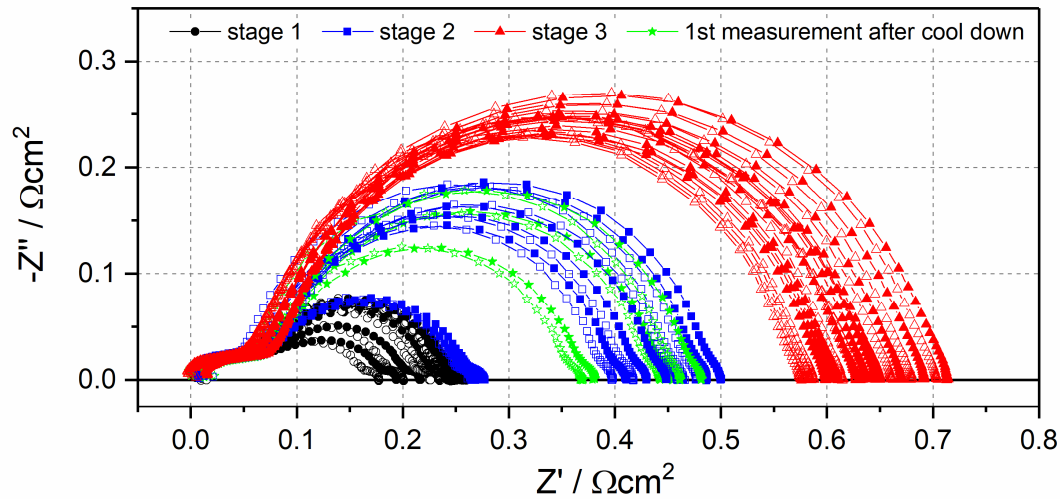
*Fig. 4.71: OCV impedance spectra of the symmetrical PNO-GDC-PNO cell. The contributions of the inductance of the test setup and the electrolyte resistance have already been subtracted. Black curves denote measurements conducted without Cr, humidity or load. Blue curves correspond to measurements without the presence of Cr or humidity, but current load of 110 mA cm$^{-2}$. Red curves show measurements conducted under the influence of current load, Cr and 30% r.h..*

The series and polarization resistances of the SOEC anode and SOFC cathode are presented in Fig. 4.72 vs. time. Abrupt increases in ASR are caused by cooling-heating cycles due to a setup change. For the duration of stage 2 of the degradation experiment a constant current load of 110 mA cm$^{-2}$ was drawn through the cell between the OCV EIS-measurements. EIS and I-V-measurements were still conducted under dry and Cr-free conditions. A strong increase in ASR of both electrodes at the beginning of stage 2 was caused by a furnace malfunction. The applied current load did not seem to influence the ASR in a negative fashion. However, as soon as humidity and Cr were introduced to the system (stage 3), the ASR of the SOFC cathode increased at a slow, but steady rate, whereas the ASR of the SOEC anode remained at a constant value of 0.2 Ω cm$^2$. A similar trend can be observed in the recorded I-V-curves (Fig. 4.73). The resistances obtained from the slopes of the I-V-curves are also in good agreement with resistances determined from impedance measurements.
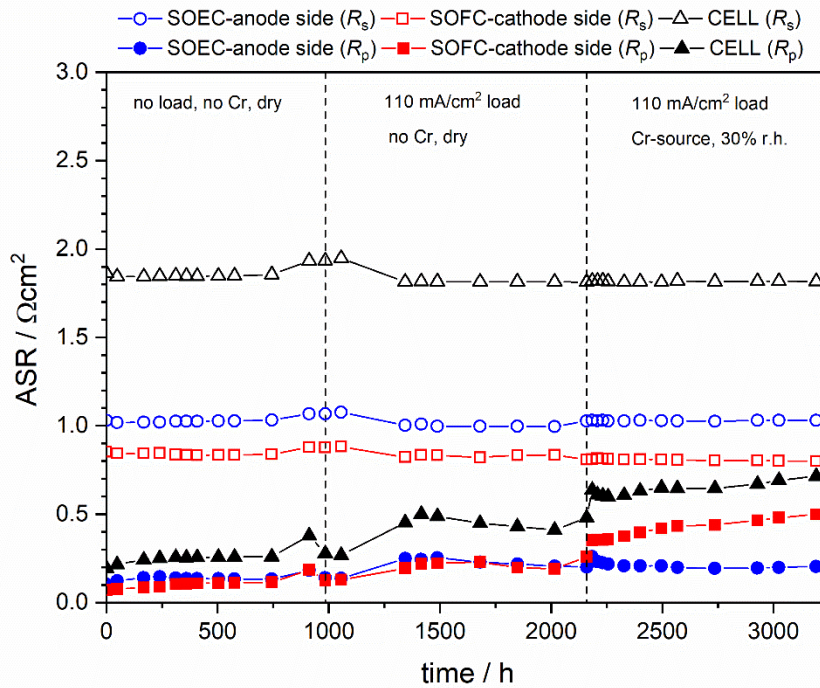
Fig. 4.72: Area specific resistance (ASR) of the PNO SOEC anode (blue), SOFC cathode (red) and the symmetrical cell (black) vs. time. $R_s$ and $R_p$ refer to the series and polarization resistance, respectively.
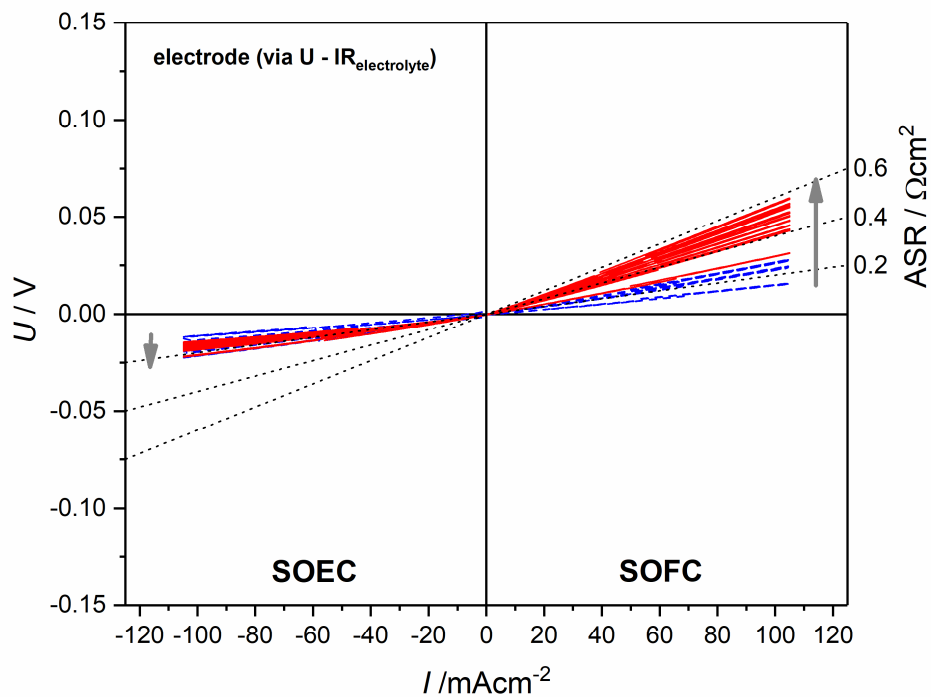


Fig. 4.73: I-V-characteristics of the PNO SOEC anode (left) and the SOFC cathode (right). Blue I-V-curves refer to measurements conducted under dry, Cr-free conditions but with 110 mA cm$^{-2}$ current load, whereas red curves correspond to measurements conducted in 30% r.h. with Cr and a current load of 110 mA cm$^{-2}$.

Based on the so far obtained results, the degradation behavior of PNO and LNO electrodes appears to be very similar. Furthermore, PNO electrodes seem to be less affected by Cr-poisoning than LNO-base electrodes under identical experimental conditions. However, it should be noted that the thickness and the surface area of the PNO electrodes were significantly higher in comparison to the investigated LNO electrodes. Therefore, a direct comparison of the results obtained for PNO and LNO electrodes is not recommended.

### 4.5.4 Post-test analysis

Two control samples placed near the symmetrical PNO cell were removed for chemical and microstructural analysis after stage 2 (before the addition of Cr) and at the end of the experiment. Fig. 4.74 shows SEM-BSE micrographs of control sample 1 (a) and 2 (b). The surface of both control samples is covered by a layer of fine crystallites. However, the second control sample, which was subjected to humid atmospheres, shows a second layer of even finer crystallites. Similar crystallization phenomena were observed in AFM images of LNO control samples, annealed at 800°C in 30% r.h. with a Cr- and a Si-source present (see Fig. 4.32c). EDXS-area analysis revealed the presence of Pt and Si-, but not Cr-species. It is probable that volatile Pt- and Si-compounds released from wiring or contact pastes were transferred to the control samples, blocking any sites for Cr-deposition.
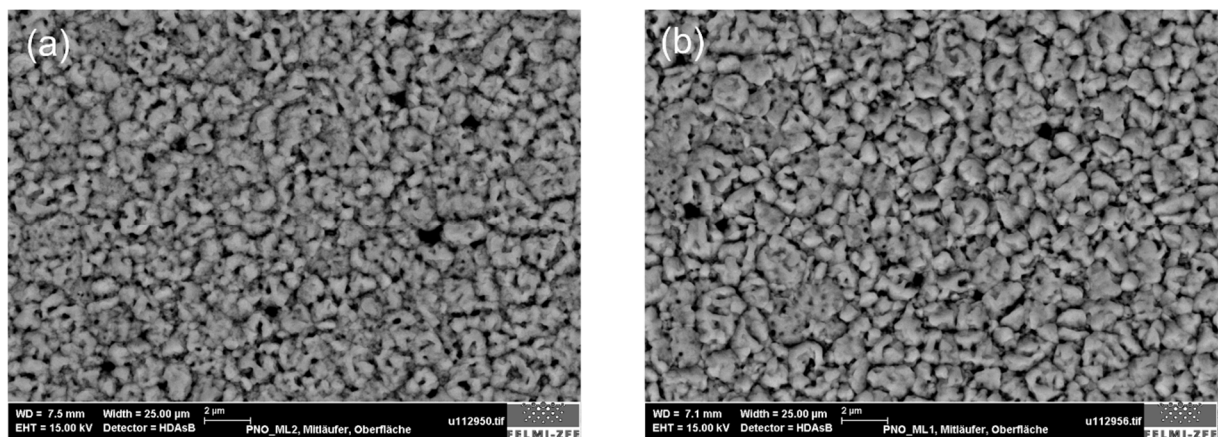


*Fig. 4.74: Post-test SEM-BSE images of control sample 1 (a) and 2 (b).*

Fig. 4.75 and Fig. 4.76 display SEM-BSE cross section images of the PNO SOEC anode and SOFC cathode, as well as EDX-spectra of selected areas. The layer thickness of the electrode is in both cases approximately 30 μm. Both electrodes adhere well to the electrolyte and no signs of delamination have been detected. EDX-area analysis reveal only the main components of electrode and electrolyte and Cr-deposition was not confirmed.
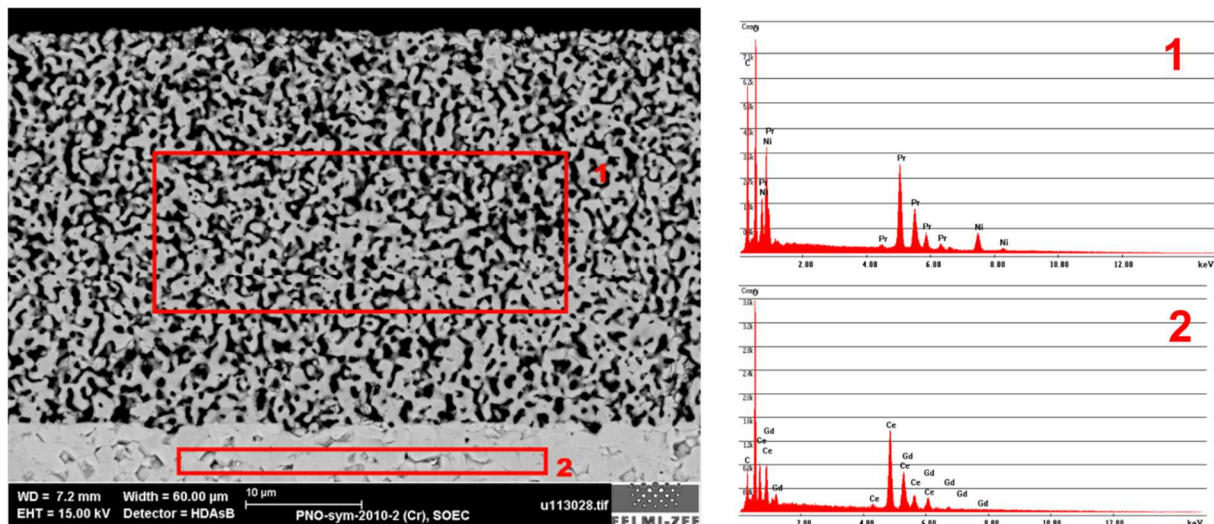
*Fig. 4.75: Post-test SEM-BSE cross section image of the degraded PNO SOEC anode and corresponding EDXS-area analysis.*
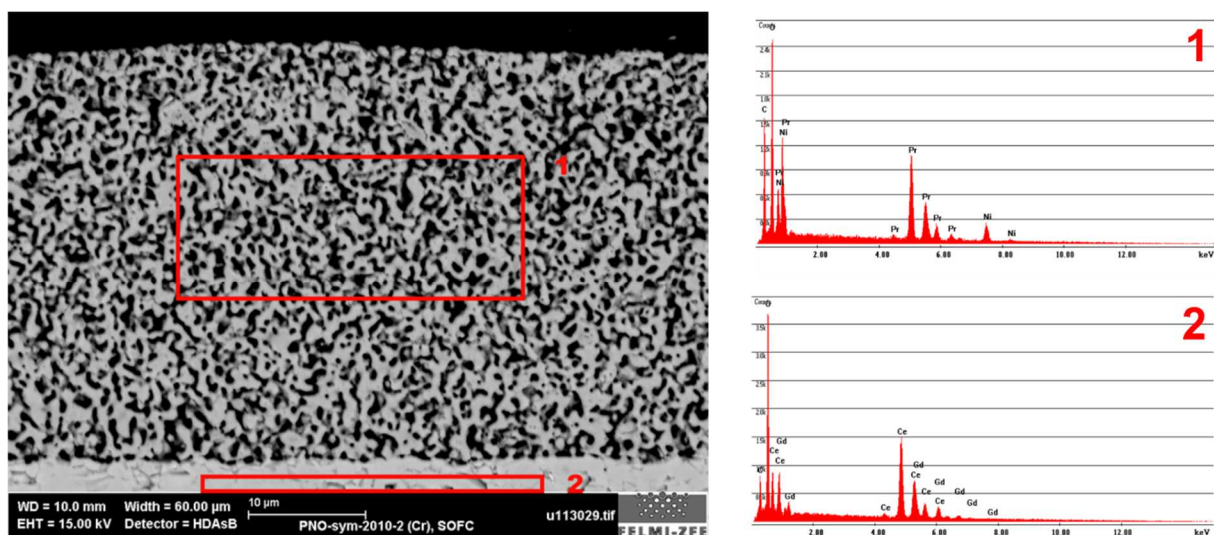


*Fig. 4.76: Post-test SEM-BSE cross section image of the degraded SOFC cathode and corresponding EDXS-area analysis.*

To determine the reason for the observed increase in ASR on the SOFC cathode side, EDXS-elemental mappings of both electrodes were recorded. Cr-maps were generated from WDXS-measurements because Cr-levels were below the detection limit of EDXS. Fig. 4.77 shows a SEM-BSE image and the corresponding elemental maps of Pr, Ni, Cr, Ce and Gd. The Ni-map shows some NiO grains, which were formed during electrode sintering. The Pr, Ce and Gd maps do not display any irregularities. The Cr map demonstrates that Cr levels on the SOEC anode are almost below the detection limit of WDXS. However, taking a closer look at the Cr map of the SOFC cathode (Fig. 4.78), Cr-deposits are clearly visible, which are mostly concentrated in the upper part of the electrode. Similar to the observed degradation behavior of LNO and LNO/GDC composite electrodes, the performance deterioration of one PNO

130

electrode is correlated with the presence of Cr-compounds. Furthermore, the Cr-deposition on the SOFC cathode of the PNO cells proves that the aforementioned gas transport restrictions to the bottom electrode, might not apply after all with this experiment, as the upward facing electrode was the SOEC anode.
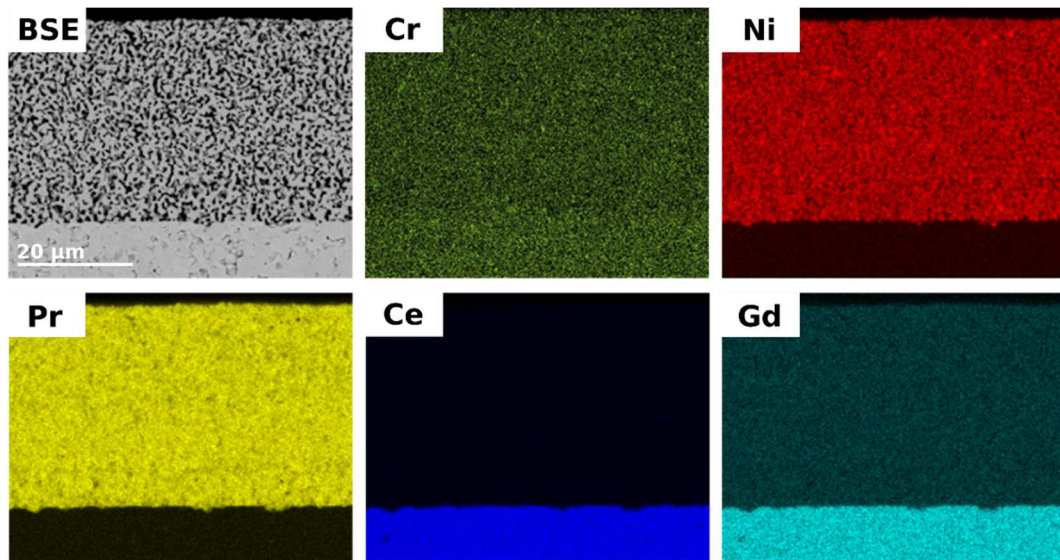


*Fig. 4.77: Post-test SEM-BSE image of the PNO SOEC anode and corresponding elemental distribution maps.*
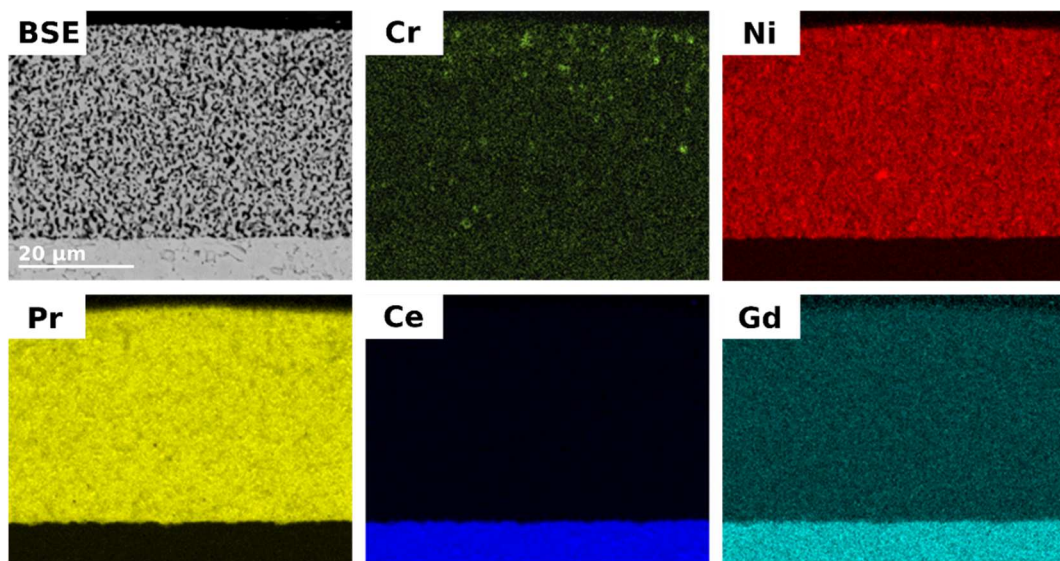


*Fig. 4.78: Post-test SEM-BSE image of the PNO SOFC cathode and corresponding elemental distribution maps.*

In order to determine the chemical composition of the detected Cr-species, extensive TEM investigations were performed. Since the Cr-contamination was negligible on the SOEC anode, FIB lamellae were cut from the SOFC cathode near the surface and at the electrode-electrolyte interface. In Fig. 4.79a a STEM-HAADF image of the near-surface zone of the SOFC cathode is depicted. The Z-contrast in the HAADF image indicates a heterogenous distribution of

elements and thus the presence of several secondary phases. However, for proper interpretation of elemental distribution maps, the sample thickness should also be considered, especially if porous structures are analyzed. Therefore, a relative thickness map (t/λ-map) was recorded using the EEL spectrometer (see Fig. 4.79b). It depicts the ratio between the absolute thickness of the sample (t) and the inelastic mean free path of the electrons (λ) through the sample. A change in color indicates thus indicates a change in sample thickness or material. The thickest parts of the lamella are indicated in white, whereas holes appear black. The polymer resin used to embed the cell (Caldofix) appears blue in between the denser PNO grains. The thinnest areas (blue-green) on the right side of the FIB lamella were used for further EELS analysis.
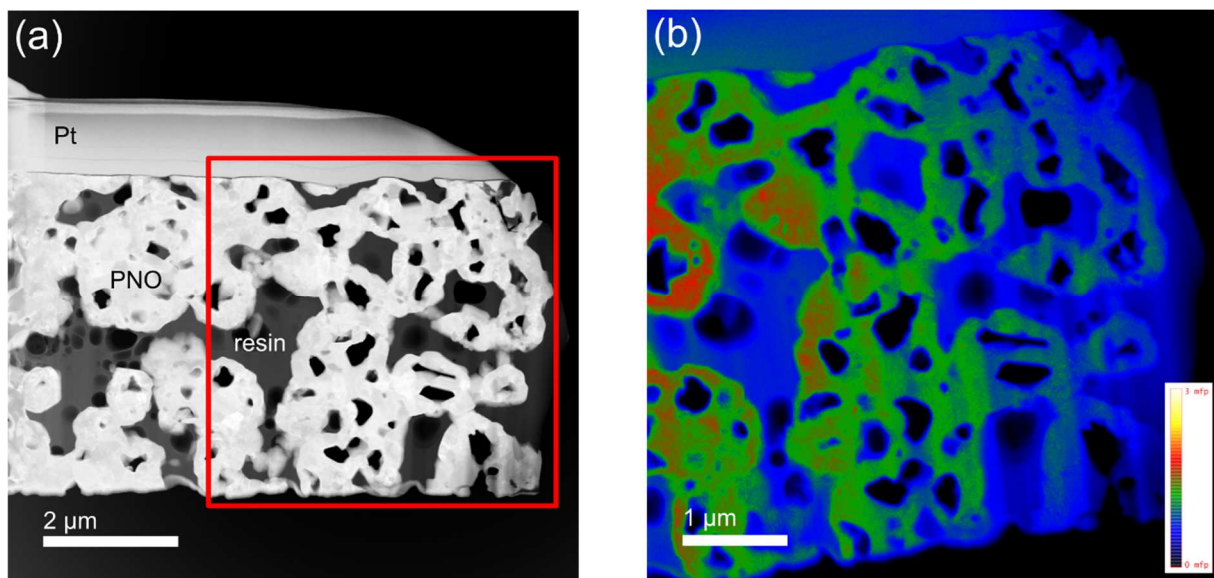


Fig. 4.79: Post-test STEM-HAADF image of a FIB lamella cut from the near-surface zone of the SOFC cathode (a) and t/λ-map of area marked with the red square (b).

Fig. 4.80 provides a detailed view of the porous PNO-electrode structure, with corresponding EELS elemental maps of Pr, Ni, O, and Cr. The part of the lamella that was analyzed exhibits a homogenous thickness. The Pr-map reveals Pr-accumulations in the vicinity of pores, which indicates the exsolution of $Pr_xO_y$, potentially leaving higher-order Ruddlesden-Popper-structures behind.

Interestingly, the Cr-deposits depicted in the Cr-map are not found in the same place as the Pr-accumulations, which is surprising considering the comparatively high reactivity of LaO-phases with Cr found on dense LNO-samples (see section 4.2.4). A complementary EEL spectrum of the area marked with the red arrow, which shows a Cr-L edge is depicted for comparison. Ni seems to be distributed rather homogeneously with the exception of a single

isolated NiO grain. According to the Cr-map, O-concentrations are elevated at sites with high Cr and Pr-content.
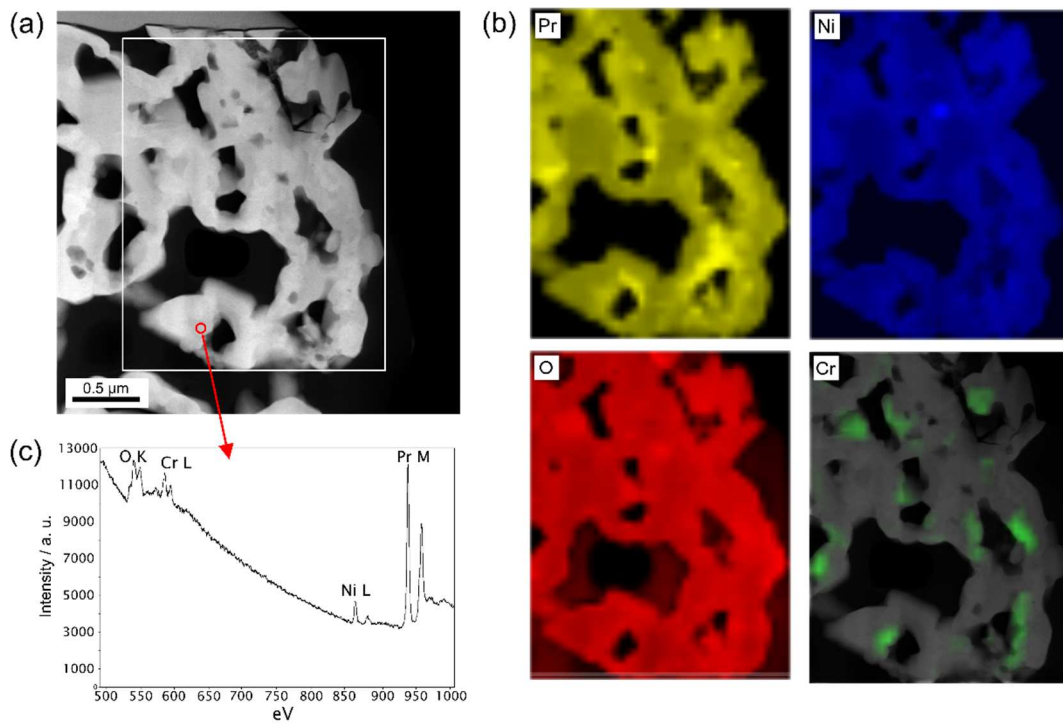


*Fig. 4.80: Detailed view of the porous SOFC cathode (a), corresponding EELS elemental maps of Pr, Ni, O, and Cr (b) and EEL spectrum of the area marked with red arrow (c).*

Further investigation of the electrode structure (see Fig. 4.81) using EDXS-spot analysis in 12 distinct sites confirmed the presence of several compounds with varying chemical composition.
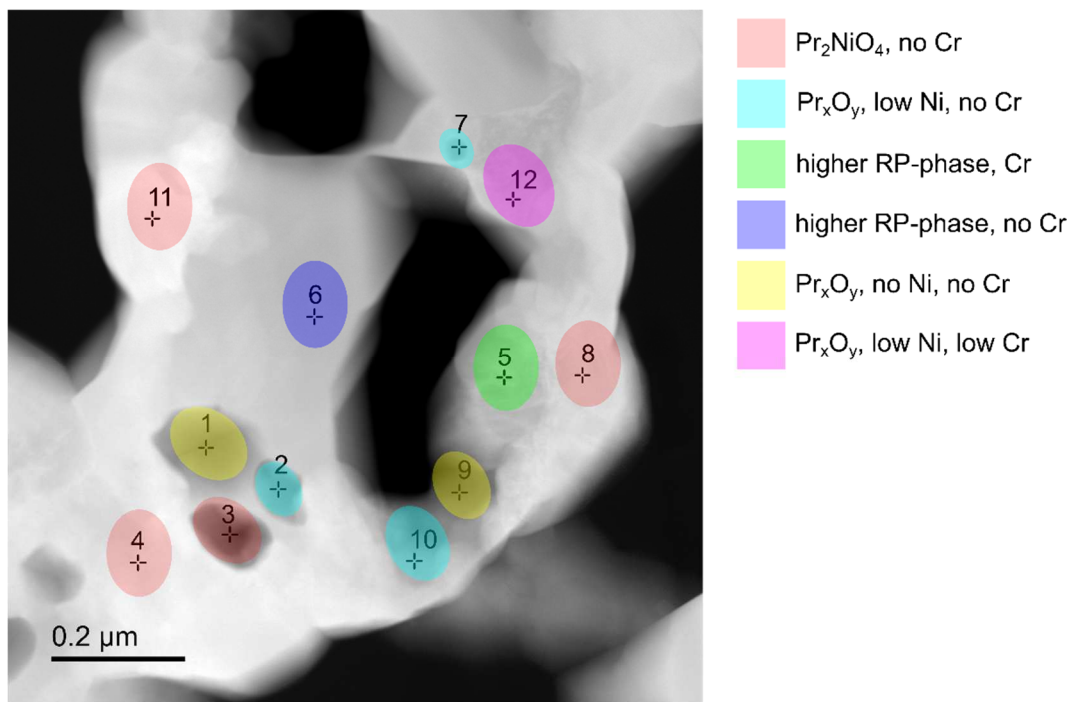
Fig. 4.81: STEM-HAADF image of PNO grains within the SOFC cathode structure. Numbers mark the spots analyzed with EDXS and colors correspond to chemically similar sites according to EDXS.

Table 4.3: Quantification of EDXS-spot analyses conducted on the sample depicted in Fig. 4.81.

| Site | EDXS-quantification in at-% | | | | | | | |
|------|------|------|------|------|------|------|------|-------|
|      | Pr   | Ni   | O    | Cr   | Pt   | Ir   | Si   | Pr/Ni |
| 1    | 35.3 | 0.67 | 63.0 | 0.0  | 0.56 | 0.21 | 0.17 | 52.7  |
| 2    | 40.0 | 3.0  | 53.0 | 0.0  | 3.4  | 0.23 | 0.31 | 13.3  |
| 3    | 22.8 | 9.9  | 56.4 | 0.0  | 10.0 | 0.11 | 0.68 | 2.3   |
| 4    | 29.3 | 13.3 | 41.2 | 0.0  | 15.2 | 0.05 | 0.94 | 2.2   |
| 5    | 26.3 | 15.4 | 53.2 | 3.2  | 1.2  | 0.17 | 0.47 | 1.7   |
| 6    | 28.4 | 17.3 | 53.9 | 0.0  | 0.11 | 0.2  | 0.12 | 1.6   |
| 7    | 35.5 | 7.3  | 56.4 | 0.0  | 0.32 | 0.25 | 0.13 | 4.9   |
| 8    | 25.7 | 10.7 | 48.2 | 0.0  | 14.6 | 0.0  | 0.8  | 2.4   |
| 9    | 48.8 | 0.36 | 48.6 | 0.0  | 0.38 | 0.5  | 1.2  | 135   |
| 10   | 41.6 | 2.3  | 54.5 | 0.0  | 0.23 | 0.35 | 1.1  | 18    |
| 11   | 26.4 | 11.4 | 46.9 | 0.0  | 14.7 | 0.0  | 0.62 | 2.3   |
| 12   | 35.1 | 9.1  | 53.5 | 0.54 | 1.1  | 0.24 | 0.4  | 3.8   |

The results of the EDXS-quantification are summed up in Table 4.3. At this point it should be noted that quantification of EDX-spectra under optimal conditions (i.e. on a flat, polished

sample) allows for an analytical accuracy of 1-2% at best [269]. It is therefore reasonable to assume that EDX-measurements on porous, heterogenous structures, e.g. screen-printed electrode layers, are even less accurate. Additionally, absorption effects within the sample, e.g. absorption of low energy O-K X-rays, may influence the results. Thus, deviations from the nominal composition of chemical compounds should be expected with EDXS-measurements.

In addition to the expected elements Pr, Ni, and O several contaminants were detected. In addition to Cr, small amounts of Pt and traces of Ir and Si were identified via EDXS-analysis. Sites 3, 4, 8, and 11 feature substantial quantities of Pt (10-15 at-%), which were most likely caused by deposition of volatile Pt-species released from the used Pt-wires or contacting paste. Redeposition of the Pt applied during FIB preparation as cause for the Pt-contamination was ruled out. At the same time the Pr/Ni ratio (between 2 and 3) at the aforementioned sites suggests the presence of $Pr_2NiO_4$. Small deposits of Cr were found only in site 5 and 12. The low Pr/Ni ratio (<2) at site 5 indicates the decomposition of PNO in at least one higher RP-phase, whereas site 12 appears to be mostly Pr-oxide of unknown composition with small amounts of Ni. EDXS-analysis of site 6 also points to the formation of a higher RP-phase, albeit without any Cr present. The remaining sites (1, 2, and 10) are most likely also Pr-oxide of unknown composition with varying amounts of Ni based on the measured Pr/Ni ratio.
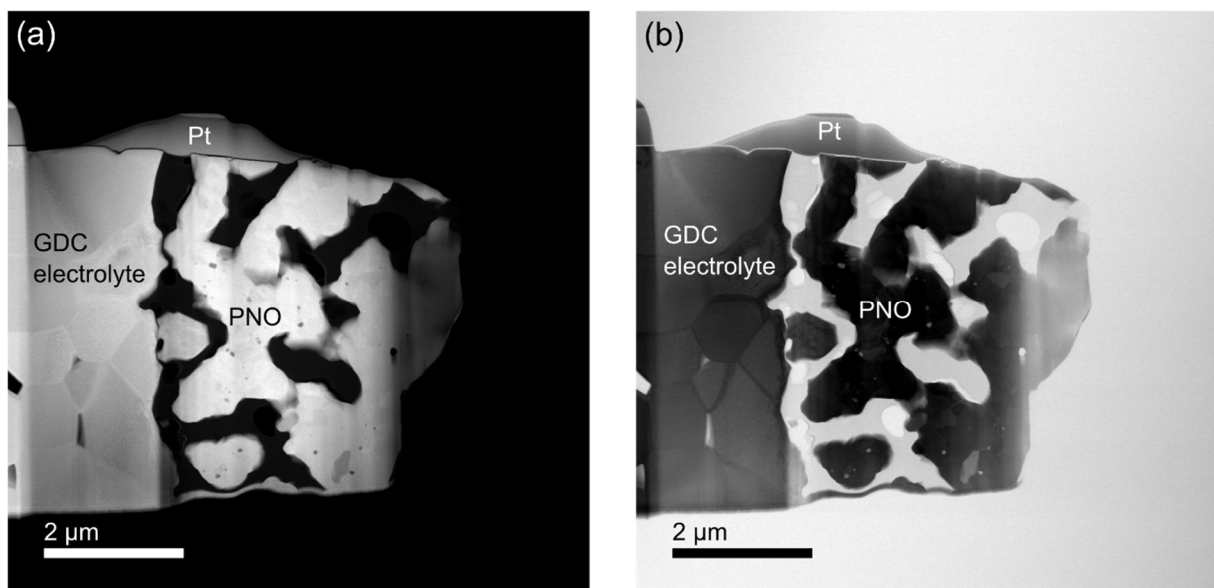


*Fig. 4.82: Post-test STEM-HAADF image of a FIB lamella cut from the SOFC cathode – electrolyte interface (a) and corresponding BF image (b).*

To study the decomposition and chemical reactions at the electrode-electrolyte interface a second FIB lamella was prepared. Fig. 4.82 depicts a STEM-HAADF (a) and a complementary bright field image (b) of the second lamella, which provides additional information about the density of the imaged material. The Pt layer shown on top of the lamella is a protective coating

applied during sample preparation. In Fig. 4.83a detailed view of the PNO-microstructure near the electrode – electrolyte interface is depicted. EDXS-spot analyses were conducted at the marked sites, which are supplemented by EELS elemental maps of Pr, Ni, and O (Fig. 4.83b). The distributions of Pr, Ni, and O are comparable to the ones found on the first analyzed lamella (Fig. 4.81) with distinct patches of Pr, which correlated with increased O-content. A large NiO inclusion is clearly visible in the Ni-distribution map, as well as in the HAADF contrast (site 1).
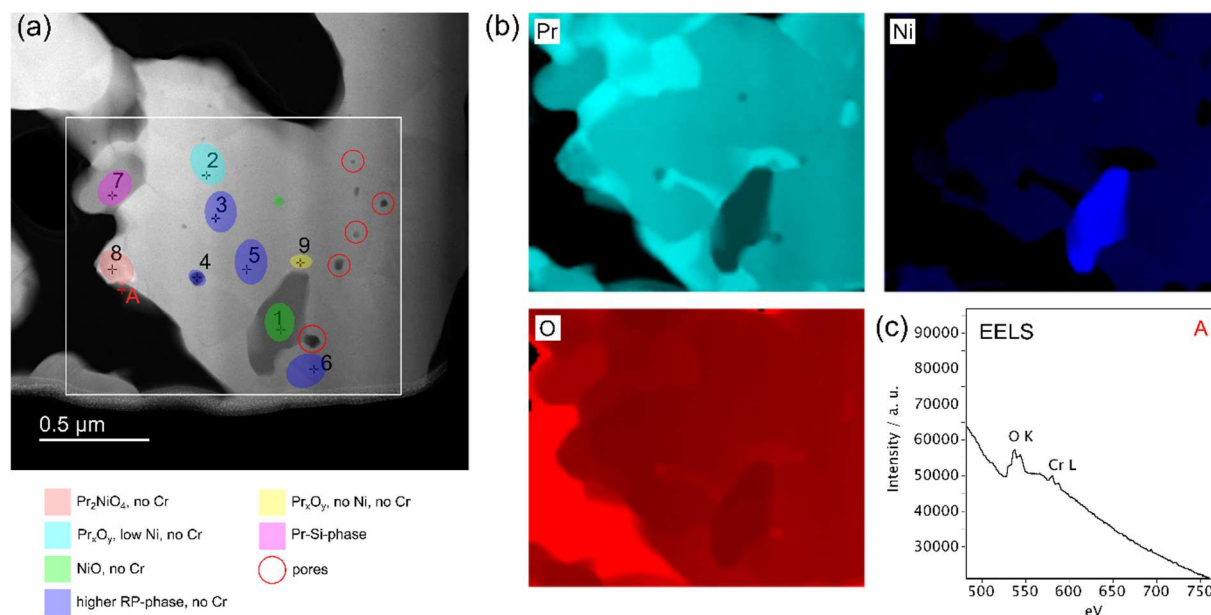


*Fig. 4.83: STEM-HAADF image of PNO grains within the SOFC cathode structure near the electrode-electrolyte interface (a), EELS elemental maps of Pr, Ni, and O from the area marked with the white rectangle (b), and an EEL spectrum recorded at the spot marked with a red A (c). Numbers mark the spots analyzed with EDXS and colors correspond to chemically similar sites according to EDXS.*

The quantification of the EDXS-spot analysis suggests the presence of higher-order RP-phases at the sites 3, 4, 5, and 6 (Pr/Ni ratio of 1.5 – 1.8) and Pr-oxide exclusions at sites 2, and 9. Remarkably, a sizable amount of Si was detected at site 7 in combination with large amounts of Pr and O and negligible quantities of Ni, which indicates the formation of a Pr-silicate phase. Based on earlier results (data not published), it is most likely a Pr-oxyapatite phase. Very small amounts of Cr were detected using EELS (Fig. 4.83c) at the site marked with a red A in Fig. 4.83a.

*Table 4.4: Quantification of EDXS-spot analyses conducted on the sample depicted in Fig. 4.83.*

| Site | EDXS-quantification in at-% | | | | | | |
|------|------|------|------|------|------|------|-------|
|      | Pr   | Ni   | O    | Cr   | Ce   | Si   | Pr/Ni |
| 1    | 0.13 | 42.8 | 55.3 | -    | -    | 1.8  | 0.003 |
| 2    | 34.7 | 2.7  | 61.8 | -    | -    | 0.74 | 13    |
| 3    | 27.2 | 15.4 | 57.2 | -    | -    | 0.25 | 1.8   |
| 4    | 21.8 | 13.5 | 63.7 | -    | -    | 0.98 | 1.6   |
| 5    | 25.2 | 15.3 | 59   | -    | -    | 0.23 | 1.6   |
| 6    | 22.7 | 14.7 | 60.6 | -    | -    | 2.0  | 1.5   |
| 7    | 23.6 | 0.47 | 61.7 | -    | -    | 14.2 | 50    |
| 8    | 24.3 | 11.1 | 63.3 | -    | -    | 1.3  | 2.2   |
| 9    | 32.7 | 0.53 | 63   | -    | 2.9  | 0.88 | 62    |

Special attention was paid to the striped grain below the NiO inclusion, which is depicted in Fig. 4.84a. A high-resolution image of the area selected with the red square was recorded (b). As suspected, the enhanced image revealed that the stripes were indeed stacked layers of atoms. Due to the comparatively low mass of the Ni atoms in contrast to the Pr-atoms, only the Pr-atoms can be clearly discerned in the recorded high-resolution image. Comparison of an FFT image (Fig. 4.84c) of the area marked with the white rectangle in Fig. 4.84b with diffraction patterns of Pr-Ni-O compounds showed that the grain is comprised mostly of $Pr_4Ni_3O_{10}$ (third order RP-phase) in zone axis [3 1 0] with stacking faults in between. A corresponding HAADF simulation of $Pr_4Ni_3O_{10}$ (red rectangle in Fig. 4.84e), which perfectly matches the detected stacking of atom layers, further confirms the presence of $Pr_4Ni_3O_{10}$ phase. To illustrate the stacking order of Pr- and Ni-atoms in $Pr_4Ni_3O_{10}$, a model of the crystal structure oriented in the same way is provided in Fig. 4.84f. For reasons of clarity the oxygen atoms were omitted from the picture. Both, the simulated HAADF and diffraction pattern were generated with the software package JEMS [265]. The crystal structure of $Pr_4Ni_3O_{10}$ with was created using VESTA [243].
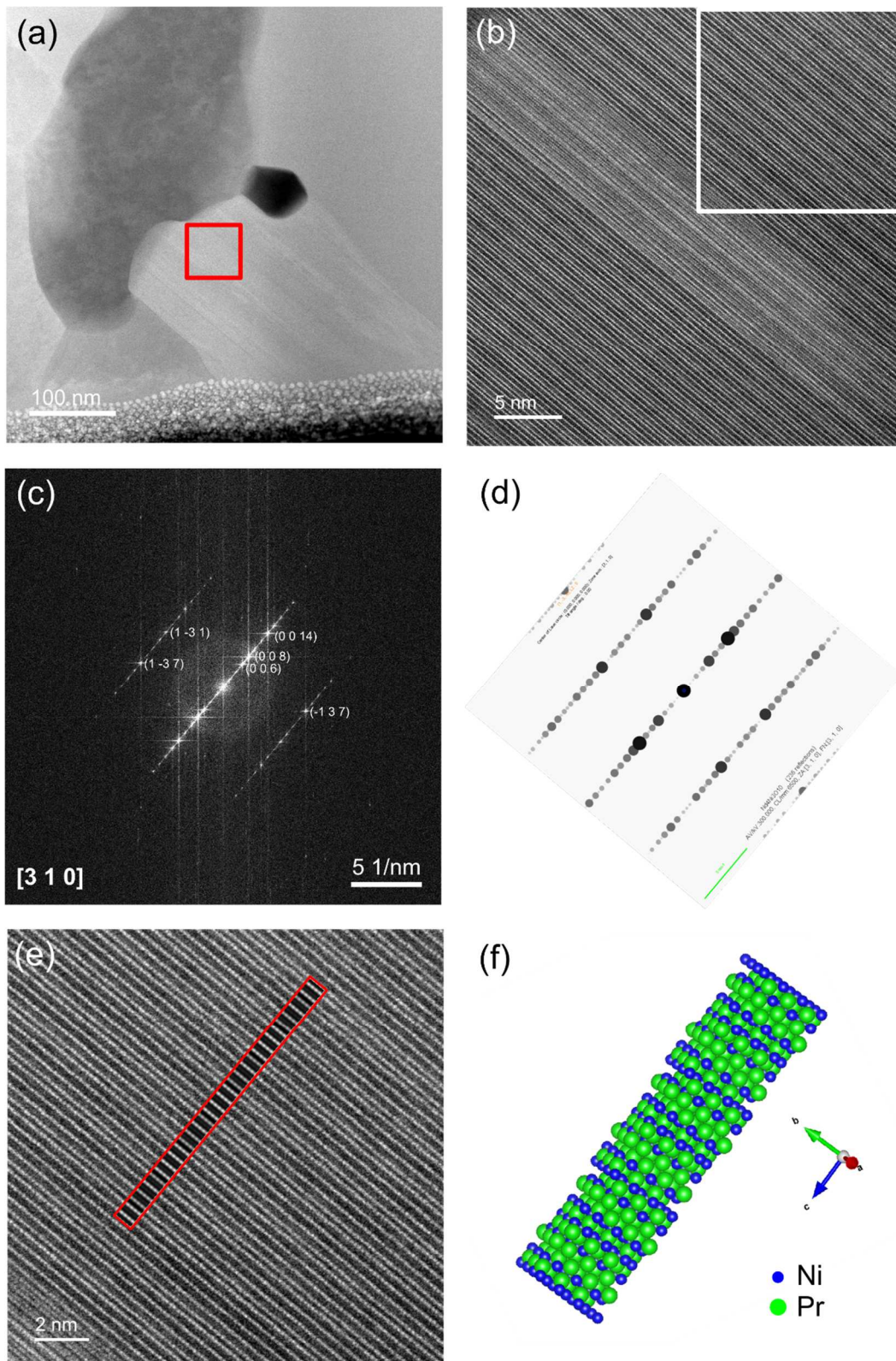
Fig. 4.84: Detailed image of a striped grain next to a NiO inclusion (a), HR-STEM image of area selected within the red square (b), FFT image of area marked with a white square (c), simulated diffraction pattern of $Pr_4Ni_3O_{10}$ in space group P 21/a (d), enhanced HR-STEM image of stacked atom layers with a superimposed HAADF-image simulation of $Pr_4Ni_3O_{10}$ in [3 1 0] orientation (e) and crystal structure of $Pr_4Ni_3O_{10}$ in the same orientation.

In addition, the immediate interface between electrode and the electrolyte was more closely inspected. Fig. 4.85a depicts a STEM-HAADF cross section image of a PNO grain in direct contact with the GDC electrolyte. The varying grey values in the HAADF image suggest the presence of several different chemical phases. The area marked with the white rectangle was analyzed using EDXS. The resulting elemental distribution maps of Ni, Pr, O, and Cr are presented in Fig. 4.85b. The complementary relative thickness map, depicted in Fig. 4.85c, reveals a non-uniform thickness of the PNO grain, which has to be taken into account when interpreting the elemental distribution maps.
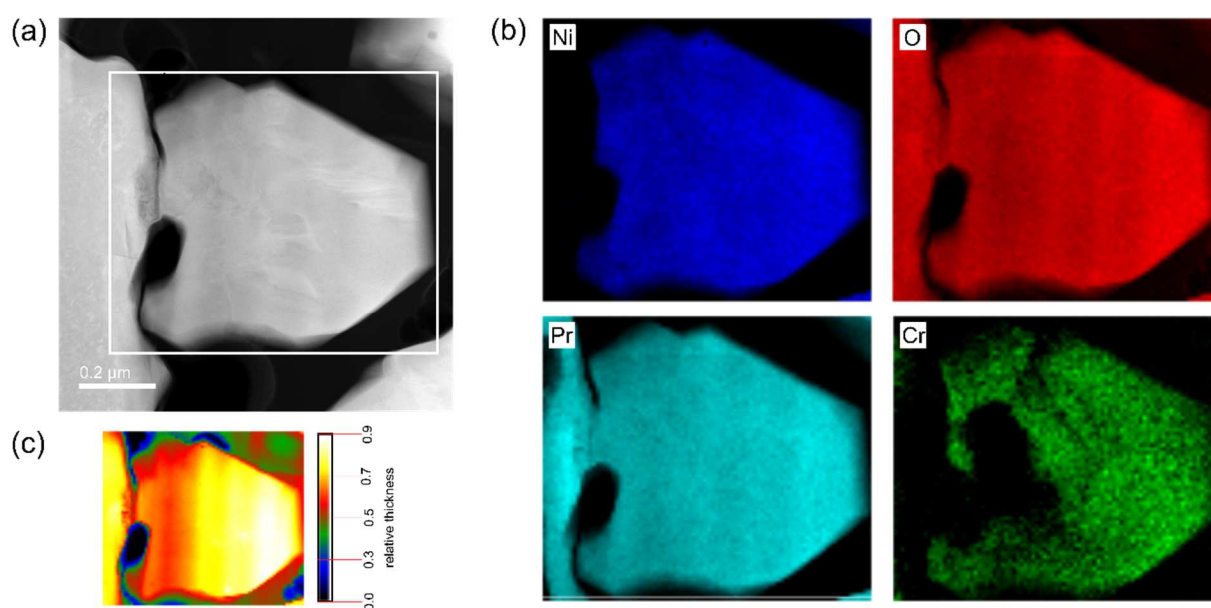


*Fig. 4.85: STEM-HAADF image of a PNO grain at the immediate electrolyte interface (a), the corresponding EDXS-elemental maps of Ni, O, Pr, and Cr (b) and EEL thickness map (c) of the area marked with the white rectangle.*

Surprisingly, Pr, Ni, and O seem to be homogeneously distributed over the entire PNO grain, which is rather unexpected considering Pr-distribution in the grains that have been analyzed so far. This suggests that the PNO grain in composed of only one chemical compound. High-resolution images of different areas on the PNO grain also show the same atomic arrangement and orientation, further confirming that the PNO grain is comprised of one single crystallographic phase (data not shown). Unfortunately, the unfavorable orientation of the crystal did not allow for the determination of the crystal structure via FFT analysis.

Furthermore, the Pr-map clearly indicates the diffusion of Pr into the electrolyte material. The boundary between PNO and GDC grain can clearly be discerned where the Ni distribution abruptly ends. Cr was found to be spread on almost the entire PNO grain instead of small insular patches at the boundary of the grain. EDXS-spot analysis at several different sites across the PNO grain show a similar Pr/Ni ratio independent of Cr-contamination (data not

shown). This suggests that Cr is deposited as thin oxide layer on top of the PNO surface and not part of the PNO crystal structure, i.e. substituting Ni.
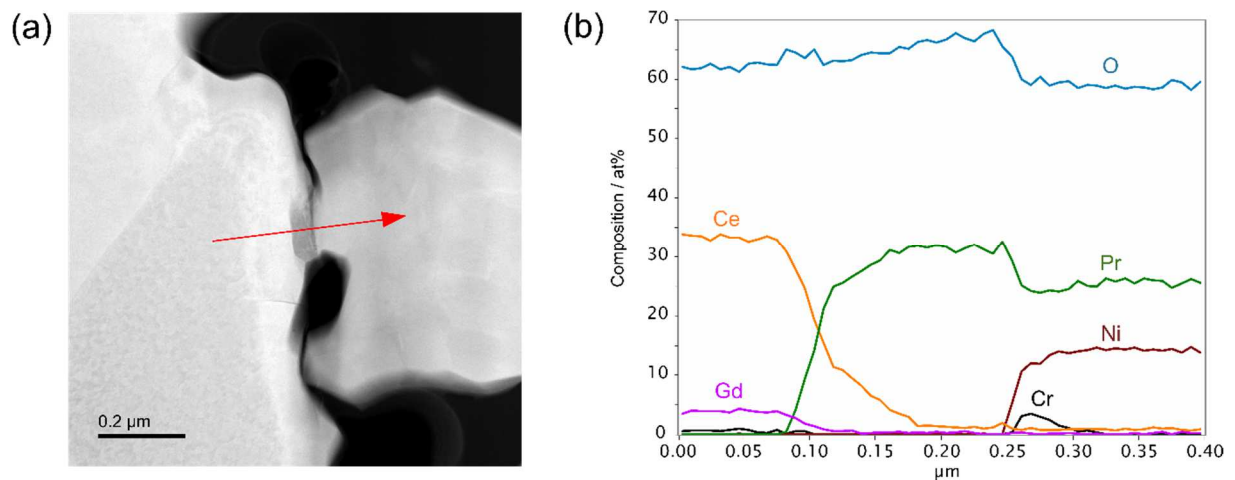


*Fig. 4.86: STEM-HAADF image of a PNO grain at the immediate electrolyte interface (a) and quantified EDXS-line scan along the red arrow (b).*

Close attention was also paid to the contacting interface between the PNO SOFC cathode and the GDC electrolyte (Fig. 4.86). EDXS-line scan performed across the interface showed a cation interdiffusion zone of approximately 170 nm, where Pr diffused into GDC while Ni remains in the PNO phase. Pr-doped ceria is a predominantly ionic conductor with slightly lower conductivity in comparison to GDC [313,314]. As indicated by the dark grey region in the HAADF-image and the EDXS-line scan (Fig. 4.86a and b), a pure Pr-oxide zone is located between the PNO grain and GDC electrolyte. The line scan also shows small amounts of Cr in the vicinity of the PNO-Pr-oxide interface.

In summary, the TEM investigation found several different chemical compounds in the SOFC cathode structure. Sufficient evidence was found that PNO decomposed into Pr-oxide and higher-order RP-phases during conducted the long-term measurements at 800°C. However, considering all the data collected, there is no indication that Cr actually reacted with any of the present phases, but rather is deposited as Cr-oxide layer on top of the PNO grains. While the covering of the active surface of the cathode material leads to a reduction in oxygen exchange activity it would seem that Pr-Ni-O compounds do not readily react with Cr under the applied experimental conditions. It can therefore be concluded that PNO is more stable under SOFC operating conditions than LNO.

# 5 Summary and conclusions

In this work the long-term stability of $K_2NiF_4$-type rare earth nickelates against chromium and silicon poisoning was tested under experimental conditions similar to real operating conditions in intermediate temperature SOFCs. Based on the available literature it was assumed that unsubstituted rare earth nickelates show better stability against Cr-poisoning than alkaline earth metal substituted perovskites. Therefore, $La_2NiO_{4+\delta}$ and $Pr_2NiO_{4+\delta}$ - despite its tendency towards decomposition - were chosen as most promising compounds in terms of oxygen exchange kinetics for this investigation. Conductivity relaxation measurements on dense ceramic samples and cell tests on symmetrical half cells with porous electrodes were successfully employed to monitor degradation processes caused by volatile contaminants in the gas phase.

The oxygen exchange kinetics was determined using the conductivity relaxation technique in linear four-point and van der Pauw geometry. Since the initial stages of poisoning phenomena take place at the sample surface, special emphasis was put on the chemical surface exchange coefficient of oxygen as a surface sensitive parameter providing reliable information about the condition of the active sample surface. The phase decomposition of $La_2NiO_{4+\delta}$ was studied on the basis of densely sintered and polished ceramic samples exposed to volatile Cr- and Si-species at 700°C and 800°C for more than 3000 hours under dry and humid conditions. The long-term experiments consisted of 4 subsequent stages to separately determine the influence of different humidity levels in the presence of contaminants: (i) dry test gas without Cr and with Si, (ii) dry test gas in the presence of a Cr- and a Si-source, (iii) moderately humidified (30% r. h.) atmosphere with Cr and Si and (iv) strongly humidified atmosphere (60% r. h.) with Cr and Si. To determine chemical and morphological changes due to poisoning effects, samples were analyzed at different stages of the experiment using AFM, SEM, XPS and TEM.

LNO exhibits excellent stability under dry conditions even in the presence of a Cr- and a Si-source. However, the results suggest that the oxygen exchange kinetics is strongly influenced by humidity. The chemical surface exchange coefficient $k_{chem}$ is reduced by a factor of 230 and 25 at 700°C and 800°C, respectively, indicating a decreased activity for the oxygen exchange reaction. Based on the obtained $k_{chem}$ values it can be concluded that at 800°C LNO is less prone to Cr-/Si-poisoning than at 700°C. Analysis of the sample surface, however, revealed a much more pronounced surface decomposition of LNO at 800°C. The segregation of La-species, which serve as a nucleation site for volatile Cr- and Si- compounds, leads to the formation Si- and Cr-rich phases, which were identified using HR-STEM as $La_{9.33}(SiO_4)_6O_2$ and $La(Cr, Ni)O_3$. Although the decomposed layer was found to be thicker on the sample at 800°C,

the oxygen exchange kinetics seems to be less influenced, which indicates that the effect of the material decomposition is somewhat compensated by the faster oxygen exchange kinetics at higher temperatures.

In the second part of the study, three different rare earth nickelate based electrode materials were tested in the presence of a Cr-source: a $La_2NiO_{4+\delta}$ (LNO) electrode, a $La_2NiO_{4+\delta}$-$Ce_{0.9}Gd_{0.1}O_{2-\delta}$ (LNO-GDC) composite electrode and a $Pr_2NiO_{4+\delta}$ (PNO) electrode. Long-term cell tests were conducted over a period of more than 3000 hours. The electrode performance was assessed via electrochemical impedance spectroscopy and current-voltage characterization of the symmetrical cells in a three-electrode configuration. The area specific resistance, which was extracted from impedance spectra, was monitored over time. The cells were subjected to a constant current load between measurements at 800°C in a 20% $O_2$/Ar atmosphere to simulate cell operation. A reference electrode was used to separate the area specific resistance of the cell into the contributions of the SOEC anode and the SOFC cathode, which allowed for the simultaneous study of Cr-poisoning under anodic and cathodic polarization. Similar to the tests on dense samples, the cells were exposed to different levels of humidity with and without a Cr-source. Post-test analyses of the cells were performed after the final stage of the degradation experiment using SEM and TEM.

The electrode performance remained quite stable with only a minor increase in the ASR of both electrodes under dry and Cr-free operation. However, the introduction of humidity to the gas stream in the presence of a Cr-source resulted in a strong ASR increase of the SOFC cathode. The ASR of the SOEC anode, however, seems to be comparatively less affected. Post-test analysis uncovered larger amounts of Cr on the SOFC cathode, which could be the cause of the measured performance degradation. The same correlation was found for pure PNO electrodes in the long-term study under identical operating conditions. A cell test performed on LNO-GDC composite electrodes under higher current densities also showed a strong correlation between deposited amounts of Cr and electrode performance degradation. In this case, however, a degradation of the SOEC anode was observed. The reasons for the opposing behavior are not yet understood. It is conceivable that Cr-poisoning mechanisms in LNO-composite electrodes generally deviate from those in pure LNO electrodes or are simply a result of the increased current density.

In conclusion, the conductivity relaxation study of dense samples provided valuable insights into the destructive effects of Cr- and Si-poisoning on the oxygen exchange kinetics of LNO. The obtained results suggest that due to delamination issues under high cathodic polarization, pure LNO electrodes might not be suitable as SOFC cathodes. However, LNO might be a promising anode material for SOECs. Application of LNO as composite material with GDC seems to significantly improve electrode adhesion, even at high current densities.

142

Furthermore, LNO composite electrodes demonstrate superior long-term stability under Cr-poisoning conditions in comparison to pure LNO electrodes. Cr-deposition tests with and without current load suggest that electrode polarization has a strong influence on Cr-deposition. Despite the decomposition of $Pr_2NiO_{4+\delta}$ into $Pr_4Ni_3O_{10+\delta}$ and $Pr_6O_{11}$ shows excellent performance with regards to adhesion to the electrolyte and susceptibility to Cr.

# 6 References

[1] H. Ibrahim, A. Ilinca, J. Perron, Renewable and Sustainable Energy Reviews 12 (2008) 1221-1250.

[2] P.G. Grimes, IEEE Aerospace and Electronic Systems Magazine 15 (2000) 7-10.

[3] P. Kurzweil in: J. Garche (Eds.), *Encyclopedia of Electrochemical Power Sources*, Elsevier, 2009, p. 579-595.

[4] R. O'Hayre, S.-W. Cha, W.G. Colella, F.B. Prinz, *Fuel Cell Fundamentals*, 3rd edition, John Wiley & Sons, Inc., Hoboken, New Jersey, 2016.

[5] K.-D. Kreuer in: K.-D. Kreuer (Eds.), *Fuel Cells: Selected Entries from the Encyclopedia of Sustainability Science and Technology*, Springer New York, 2013, p. 1-7.

[6] T.S. Zhao, N. Meng (Eds.), Solid oxide fuel cells: From materials to system modeling, RSC Publishing, Cambridge, UK, 2013.

[7] S.C. Singhal in: J.T.S. Irvine, P. Connor (Eds.), *Solid Oxide Fuels Cells: Facts and Figures: Past Present and Future Perspectives for SOFC Technologies*, Springer London, 2013, p. 1-23.

[8] E.J. Naimaster, A.K. Sleiti, Energy and Buildings 61 (2013) 153-160.

[9] M. Suzuki, S. Iwata, K. Higaki, S. Inoue, T. Shigehisa, I. Miyachi, H. Nakabayashi, K. Shimazu, ECS Trans. 25 (2009) 143-147.

[10] A. Mai, B. Iwanschitz, J.A. Schuler, R. Denzler, V. Nerlich, A. Schuler, ECS Trans. 57 (2013) 73-80.

[11] J. Lawrence, M. Boltze, J. Power Sources 154 (2006) 479-488.

[12] P. Lamp, J. Tachtler, O. Finkenwirth, S. Mukerjee, S. Shaffer, Fuel Cells 3 (2003) 146-152.

[13] J. Rechberger, A. Kaupert, J. Hagerskans, L. Blum, Transportation Research Procedia 14 (2016) 3676-3685.

[14] S.C. Singhal, K. Kendall in: S.C. Singhal, K. Kendall (Eds.), *High Temperature and Solid Oxide Fuel Cells*, Elsevier Science, 2003, p. 1-22.

[15] Z. Shao, M.O. Tadé in: Z. Shao, M.O. Tadé (Eds.), *Intermediate-Temperature Solid Oxide Fuel Cells: Materials and Applications*, Springer Berlin Heidelberg, 2016, p. 177-198.

[16] Z. Yang, K.S. Weil, D.M. Paxton, J.W. Stevenson, J. Electrochem. Soc. 150 (2003) A1188-A1201.

[17] V.V. Kharton, F.M.B. Marques, A. Atkinson, Solid State Ionics 174 (2004) 135-149.

[18] O. Yamamoto, Y. Arati, Y. Takeda, N. Imanishi, Y. Mizutani, M. Kawai, Y. Nakamura, Solid State Ionics 79 (1995) 137-142.

[19] S.P.S. Badwal, Solid State Ionics 52 (1992) 23-32.

[20] M.A. Borik, S.I. Bredikhin, V.T. Bublik, A.V. Kulebyakin, I.E. Kuritsyna, E.E. Lomonova, P.O. Milovich, V.A. Myzina, V.V. Osiko, P.A. Ryabochkina, N.Y. Tabachkova, J. Am. Ceram. Soc. 100 (2017) 5536-5547.

[21] Y. Arachi, H. Sakai, O. Yamamoto, Y. Takeda, N. Imanishai, Solid State Ionics 121 (1999) 133-139.

[22]   A. Mitterdorfer, L.J. Gauckler, Solid State Ionics 111 (1998) 185-218.

[23]   G.C. Kostogloudis, G. Tsiniarakis, C. Ftikos, Solid State Ionics 135 (2000) 529-535.

[24]   J.-M. Bassat, D. Mesguich, C. Ferchaud, Y. Zhang-Steenwinkel, F. Van Berkel, C. Aymonier, J. Watkins, J.-C. Grenier, ECS Trans. 35 (2011) 1945-1954.

[25]   A. Tsoga, A. Gupta, A. Naoumidis, P. Nikolopoulos, Acta Materialia 48 (2000) 4709-4714.

[26]   H. Yahiro, K. Eguchi, H. Arai, Solid State Ionics 36 (1989) 71-75.

[27]   K. Huang, M. Feng, J.B. Goodenough, C. Milliken, J. Electrochem. Soc. 144 (1997) 3620-3624.

[28]   K. Huang, M. Feng, J.B. Goodenough, M. Schmerling, J. Electrochem. Soc. 143 (1996) 3630-3636.

[29]   B. Shri Prakash, S. Senthil Kumar, S.T. Aruna, Renewable and Sustainable Energy Reviews 36 (2014) 149-179.

[30]   S.P.S. Shaikh, A. Muchtar, M.R. Somalu, Renewable and Sustainable Energy Reviews 51 (2015) 1-8.

[31]   L. Holzer, B. Iwanschitz, T. Hocker, B. Münch, M. Prestat, D. Wiedenmann, U. Vogt, P. Holtappels, J. Sfeir, A. Mai, T. Graule, J. Power Sources 196 (2011) 1279-1294.

[32]   T. Klemensø, C.C. Appel, M. Mogensen, Electrochem. Solid-State Lett. 9 (2006) A403-A407.

[33]   B. Stoeckl, V. Subotić, M. Preininger, H. Schroettner, C. Hochenauer, Electrochim. Acta 275 (2018) 256-264.

[34]   S. Kavurucu Schubert, M. Kusnezoff, A. Michaelis, S.I. Bredikhin, J. Power Sources 217 (2012) 364-372.

[35]   M. Gong, X. Liu, J. Trembly, C. Johnson, J. Power Sources 168 (2007) 289-298.

[36]   K. Haga, S. Adachi, Y. Shiratori, K. Itoh, K. Sasaki, Solid State Ionics 179 (2008) 1427-1431.

[37]   A. Weber, B. Sauer, A.C. Müller, D. Herbstritt, E. Ivers-Tiffée, Solid State Ionics 152-153 (2002) 543-550.

[38]   X. Li, H. Zhao, N. Xu, X. Zhou, C. Zhang, N. Chen, Int. J. Hydrogen Energy 34 (2009) 6407-6414.

[39]   Z. Du, H. Zhao, X. Zhou, Z. Xie, C. Zhang, Int. J. Hydrogen Energy 38 (2013) 1068-1073.

[40]   M.C. Tucker, G.Y. Lau, C.P. Jacobson, S.J. Visco, L.C. De Jonghe, J. Power Sources 195 (2010) 3119-3123.

[41]   M.A. Buccheri, J.M. Hill, Fuel Cells 14 (2014) 162-170.

[42]   S.-I. Lee, J.M. Vohs, R.J. Gorte, J. Electrochem. Soc. 151 (2004) A1319-A1323.

[43]   T. Takeguchi, R. Kikuchi, T. Yano, K. Eguchi, K. Murata, Catal. Today 84 (2003) 217-222.

[44]   C. Sun, R. Hui, J. Roller, J. Solid State Electrochem. 14 (2010) 1125-1144.

[45]   J. Mizusaki, Y. Yonemura, H. Kamata, K. Ohyama, N. Mori, H. Takai, H. Tagawa, M. Dokiya, K. Naraya, T. Sasamoto, H. Inaba, T. Hashimoto, Solid State Ionics 132 (2000) 167-180.

[46]   T. Suzuki, M. Awano, P. Jasinski, V. Petrovsky, H.U. Anderson, Solid State Ionics 177 (2006) 2071-2074.

[47] T. Kenjo, M. Nishiya, Solid State Ionics 57 (1992) 295-302.

[48] A. Chen, G. Bourne, K. Siebein, R. DeHoff, E. Wachsman, K. Jones, J. Am. Ceram. Soc. 91 (2008) 2670-2675.

[49] A. Hessler-Wyser, Z. Wuillemin, J.A. Schuler, A. Faes, J. Van herle, J. Mater. Sci. 46 (2011) 4532-4539.

[50] G. Chen, Y. Gao, Y. Luo, R. Guo, Ceramics International 43 (2017) 1304-1309.

[51] Y.J. Leng, S.H. Chan, K.A. Khor, S.P. Jiang, Journal of Applied Electrochemistry 34 (2004) 409-415.

[52] Y. Leng, S.H. Chan, Q. Liu, Int. J. Hydrogen Energy 33 (2008) 3808-3817.

[53] H. Yokokawa in: T. Ishihara (Eds.), *Perovskite Oxide for Solid Oxide Fuel Cells*, Springer US, 2009, p. 17-43.

[54] Z. Shao, M.O. Tadé in: Z. Shao, M.O. Tadé (Eds.), *Intermediate-Temperature Solid Oxide Fuel Cells: Materials and Applications*, Springer Berlin Heidelberg, 2016, p. 59-126.

[55] F.M. Figueiredo, J.A. Labrincha, J.R. Frade, F.M.B. Marques, Solid State Ionics 101–103, Part 1 (1997) 343-349.

[56] M. Kubicek, G.M. Rupp, S. Huber, A. Penn, A.K. Opitz, J. Bernardi, M. Stöger-Pollach, H. Hutter, J. Fleig, Phys. Chem. Chem. Phys. 16 (2014) 2715-2726.

[57] Y. Orikasa, E.J. Crumlin, S. Sako, K. Amezawa, T. Uruga, M.D. Biegalski, H.M. Christen, Y. Uchimoto, Y. Shao-Horn, ECS Electrochemistry Letters 3 (2014) F23-F26.

[58] E. Bucher, W. Sitte, F. Klauser, E. Bertel, Solid State Ionics 191 (2011) 61-67.

[59] S.P. Simner, M.D. Anderson, M.H. Engelhard, J.W. Stevenson, Electrochem. Solid-State Lett. 9 (2006) A478-A481.

[60] E. Bucher, W. Sitte, Solid State Ionics 173 (2004) 23-28.

[61] W. Preis, E. Bucher, W. Sitte, Solid State Ionics 175 (2004) 393-397.

[62] S.P. Simner, J.P. Shelton, M.D. Anderson, J.W. Stevenson, Solid State Ionics 161 (2003) 11-18.

[63] M.D. Anderson, J.W. Stevenson, S.P. Simner, J. Power Sources 129 (2004) 188-192.

[64] Y. Cheng, T.-S. Oh, R. Wilson, R.J. Gorte, J.M. Vohs, J. Electrochem. Soc. 164 (2017) F525-F529.

[65] S.A. Muhammed Ali, M. Anwar, N.A. Baharuddin, M.R. Somalu, A. Muchtar, J. Solid State Electrochem. 22 (2018) 263-273.

[66] V. Dusastre, J.A. Kilner, Solid State Ionics 126 (1999) 163-174.

[67] F. Si, G. Zhang, K. Huang, J. Electrochem. Soc. 163 (2016) F626-F628.

[68] C. Gao, Y. Liu, K. Xi, S. Jiao, R.I. Tomov, R.V. Kumar, Electrochim. Acta 246 (2017) 148-155.

[69] E. Bucher, A. Egger, M. Yang, W. Sitte, F. Klauser, E. Bertel, Proc. 9th European Solid Oxide Fuel Cell Forum, 2010, p. 7/11-18.

[70] E. Bucher, W. Sitte, Solid State Ionics 192 (2011) 480-482.

[71] E. Bucher, M. Yang, W. Sitte, J. Electrochem. Soc. 159 (2012) B592-B596.

[72] Z. Pan, Q. Liu, L. Zhang, X. Zhang, S.H. Chan, J. Electrochem. Soc. 162 (2015) F1316-F1323.

[73] H. Wang, S.A. Barnett, ECS Trans. 78 (2017) 905-913.

[74]  E. Boehm, J.M. Bassat, P. Dordor, F. Mauvy, J.C. Grenier, P. Stevens, Solid State Ionics 176 (2005) 2717-2725.

[75]  L.P. Sun, Q. Li, H. Zhao, L.H. Huo, J.C. Grenier, J. Power Sources 183 (2008) 43-48.

[76]  A. Chroneos, D. Parfitt, J.A. Kilner, R.W. Grimes, J. Mater. Chem. 20 (2010) 266–270.

[77]  R.J. Woolley, S.J. Skinner, Solid State Ionics 255 (2014) 1-5.

[78]  M. Ferkhi, A. Ringuedé, A. Khaled, L. Zerroual, M. Cassir, Electrochim. Acta 75 (2012) 80-87.

[79]  M. Rieu, R. Sayers, M.A. Laguna-Bercero, S.J. Skinner, P. Lenormand, F. Ansart, J. Electrochem. Soc. 157 (2010) B477-B480.

[80]  D. Pérez-Coll, A. Aguadero, Fuel Cells 11 (2011) 91-101.

[81]  H. Luebbe, J. Van Herle, H. Hofmann, P. Bowen, U. Aschauer, A. Schuler, F. Snijkers, H.J. Schindler, U. Vogt, C. Lalanne, Solid State Ionics 180 (2009) 805-811.

[82]  J. Wan, J.B. Goodenough, J.H. Zhu, Solid State Ionics 178 (2007) 281-286.

[83]  C. Ferchaud, J.-C. Grenier, Y. Zhang-Steenwinkel, M.M.A. van Tuel, F.P.F. van Berkel, J.-M. Bassat, J. Power Sources 196 (2011) 1872-1879.

[84]  A. Egger, *Rare earth nickelates as cathodes for solid oxide fuel cells*, PhD thesis, University of Leoben, Austria, Department of General, Analytical and Physical Chemistry, 2013.

[85]  A. Montenegro-Hernández, J. Vega-Castillo, L. Mogni, A. Caneiro, Int. J. Hydrogen Energy 36 (2011) 15704-15714.

[86]  P. Odier, C. Allançon, J.M. Bassat, J. Solid State Chem. 153 (2000) 381-385.

[87]  V.V. Kharton, A.V. Kovalevsky, M. Avdeev, E.V. Tsipis, M.V. Patrakeev, A.A. Yaremchenko, E.N. Naumovich, J.R. Frade, Chem. Mater. 19 (2007) 2027-2033.

[88]  V. Vibhu, A. Rougier, J.-C. Grenier, J.M. Bassat, ECS Trans. 57 (2013) 2093-2100.

[89]  A. Montenegro-Hernández, L. Mogni, A. Caneiro, Int. J. Hydrogen Energy 35 (2010) 6031-6036.

[90]  A. Montenegro-Hernández, L. Mogni, A. Caneiro, Int. J. Hydrogen Energy 37 (2012) 18290-18301.

[91]  A. Hauch, S.D. Ebbesen, S.H. Jensen, M. Mogensen, J. Mater. Chem. 18 (2008) 2331-2340.

[92]  A. Godula-Jopek (Eds.), Hydrogen Production: Electrolysis, Wiley-VCH, Weinheim, Germany, 2015.

[93]  Y. Wang, T. Liu, L. Lei, F. Chen, Fuel Processing Technology 161 (2017) 248-258.

[94]  Y.A. Daza, J.N. Kuhn, RSC Advances 6 (2016) 49675-49691.

[95]  B. Yu, W. Zhang, J. Xu, J. Chen, X. Luo, K. Stephan, Int. J. Hydrogen Energy 37 (2012) 12074-12080.

[96]  M. Ni, M.K.H. Leung, D.Y.C. Leung, Int. J. Hydrogen Energy 33 (2008) 2337-2354.

[97]  K.J. Lee, J.W. Seo, J.S. Yoon, H.J. Hwang, ECS Trans. 57 (2013) 3255-3260.

[98]  K.J. Lee, M.J. Lee, S.h. Park, H.J. Hwang, J. Korean Ceram. Soc 53 (2016) 489-493.

[99]  T. Ishihara, AIP Conference Proceedings 1877 (2017) 020001.

[100] T.H. Shin, J.-H. Myung, M. Verbraeken, G. Kim, J.T.S. Irvine, Faraday Discussions 182 (2015) 227-239.

[101] K. Chen, S.P. Jiang, J. Electrochem. Soc. 163 (2016) F3070-F3083.

[102] E. Lay-Grindler, J. Laurencin, J. Villanova, I. Kieffer, F. Usseglio-Viretta, T. Le Bihan, P. Bleuet, A. Mansuy, G. Delette, ECS Trans. 57 (2013) 3177-3187.

[103] S.J. Kim, K.J. Kim, G.M. Choi, Int. J. Hydrogen Energy 40 (2015) 9032-9038.

[104] C. Jin, C. Yang, F. Zhao, D. Cui, F. Chen, Int. J. Hydrogen Energy 36 (2011) 3340-3346.

[105] X. Yue, J.T.S. Irvine, Solid State Ionics 225 (2012) 131-135.

[106] X.L. Yue, J.T.S. Irvine, Electrochem. Solid-State Lett. 15 (2012) B31-B34.

[107] R. Xing, Y. Wang, S. Liu, C. Jin, J. Power Sources 208 (2012) 276-281.

[108] S.-E. Yoon, S.-H. Song, J. Choi, J.-Y. Ahn, B.-K. Kim, J.-S. Park, Int. J. Hydrogen Energy 39 (2014) 5497-5504.

[109] Y. Wang, T. Liu, S. Fang, F. Chen, J. Power Sources 305 (2016) 240-248.

[110] J. Li, C. Zhong, X. Meng, H. Wu, H. Nie, Z. Zhan, S. Wang, Fuel Cells 14 (2014) 1046-1049.

[111] Y. Wang, J. Xu, X. Meng, T. Liu, F. Chen, Electrochemistry Communications 79 (2017) 63-67.

[112] K. Xie, Y. Zhang, G. Meng, J.T.S. Irvine, Energy Environ. Sci. 4 (2011) 2218-2222.

[113] D. Grientschnig, W. Sitte, Z. Phys. Chem. 168 (1990) 143-159.

[114] G.J. Dudley, B.C.H. Steele, J. Solid State Chem. 31 (1980) 233-247.

[115] L.J. van der Pauw, Philips Res. Rep. 13 (1958) 1-9.

[116] H. Dünwald, C. Wagner, Z. Physik. Chem. B 24 (1934) 53-58.

[117] H.J.M. Bouwmeester, H. Kruidhof, A.J. Burggraaf, Solid State Ionics 72 (1994) 185-194.

[118] M.W. den Otter, H.J.M. Bouwmeester, B.A. Boukamp, H. Verweij, J. Electrochem. Soc. 148 (2001) J1-J6.

[119] X.D. Zhou, S.C. Singhal in: J. Garche (Eds.), *Encyclopedia of Electrochemical Power Sources*, Elsevier, 2009, p. 1-16.

[120] D.D. Macdonald, Electrochim. Acta 51 (2006) 1376-1388.

[121] E. Barsoukov, J.R. Macdonald, *Impedance Spectroscopy: Theory, Experiment, and Applications*, John Wiley & Sons, Inc., Hoboken, New Jersey, 2005.

[122] V.F. Lvovich, *Impedance Spectroscopy: Applications to Electrochemical and Dielectric Phenomena*, John Wiley & Sons, Inc., Hoboken, New Jersey, 2012.

[123] M.E. Orazem, N. Pébère, B. Tribollet, J. Electrochem. Soc. 153 (2006) B129-B136.

[124] A. Lasia, Journal of Electroanalytical Chemistry 397 (1995) 27-33.

[125] T. Pajkossy, Solid State Ionics 176 (2005) 1997-2003.

[126] T. Pajkossy, T. Wandlowski, D.M. Kolb, Journal of Electroanalytical Chemistry 414 (1996) 209-220.

[127] M.R. Shoar Abouzari, F. Berkemeier, G. Schmitz, D. Wilmer, Solid State Ionics 180 (2009) 922-927.

[128] B. Emmanuel, Journal of Electroanalytical Chemistry 624 (2008) 14-20.

[129] J.R. Macdonald, Solid State Ionics 13 (1984) 147-149.

[130] A. Lasia in: A. Lasia (Eds.), *Electrochemical Impedance Spectroscopy and its Applications*, Springer New York, 2014, p. 85-125.

[131] A. Bieberle-Hütter, M. Søgaard, H.L. Tuller, Solid State Ionics 177 (2006) 1969-1975.

[132] J. Fleig, Solid State Ionics 150 (2002) 181-193.

[133] S.R. Taylor, E. Gileadi, CORROSION 51 (1995) 664-671.

[134] E. Warburg, Annalen der Physik 303 (1899) 493-499.

[135] ZView®, © Scribner Associates Inc. (http://www.scribner.com/).

[136] B.A. Boukamp, H.J.M. Bouwmeester, Solid State Ionics 157 (2003) 29-33.

[137] H. Gerischer, Zeitschrift fuer physikalische Chemie, Stoechiometrie und Verwandtschaftslehre 198 (1951) 286-313.

[138] S.B. Adler, J.A. Lane, B.C.H. Steele, J. Electrochem. Soc. 143 (1996) 3554-3564.

[139] H. Yokokawa, H. Tu, B. Iwanschitz, A. Mai, J. Power Sources 182 (2008) 400-412.

[140] A. Aphale, C. Liang, B. Hu, P. Singh in: N.P. Brandon, E. Ruiz-Trejo, P. Boldrin (Eds.), *Solid Oxide Fuel Cell Lifetime and Reliability*, Academic Press, 2017, p. 101-119.

[141] N.H. Menzler, A. Mai, D. Stöver in: W. Vielstich, H. Yokokawa, H.A. Gasteiger (Eds.), *Handbook of Fuel Cells - Fundamentals, Technology and Applications*, John Wiley & Sons, Ltd., 2009, p. 566-578.

[142] Y.L. Liu, K. Thydén, M. Chen, A. Hagen, Solid State Ionics 206 (2012) 97-103.

[143] M.V. Ananyev, A.S. Farlenkov, V.A. Eremin, E.K. Kurumchin, Int. J. Hydrogen Energy 43 (2018) 951-959.

[144] M. Shah, P.W. Voorhees, S.A. Barnett, Solid State Ionics 187 (2011) 64-67.

[145] D. Yan, L. Liang, J. Yang, T. Zhang, J. Pu, B. Chi, J. Li, Energy 125 (2017) 663-670.

[146] T. Komatsu, Y. Yoshida, K. Watanabe, R. Chiba, H. Taguchi, H. Orui, H. Arai, J. Power Sources 195 (2010) 5601-5605.

[147] J. Kim, H.-I. Ji, H.P. Dasari, D. Shin, H. Song, J.-H. Lee, B.-K. Kim, H.-J. Je, H.-W. Lee, K.J. Yoon, Int. J. Hydrogen Energy 38 (2013) 1225-1235.

[148] N. Ni, S.J. Cooper, R. Williams, N. Kemen, D.W. McComb, S.J. Skinner, ACS Applied Materials & Interfaces 8 (2016) 17360-17370.

[149] L.C. Baqué, A.L. Soldati, E. Teixeira-Neto, H.E. Troiani, A. Schreiber, A.C. Serquis, J. Power Sources 337 (2017) 166-172.

[150] L. Zhao, J. Drennan, C. Kong, S. Amarasinghe, S.P. Jiang, J. Mater. Chem. A 2 (2014) 11114-11123.

[151] H. Ding, A.V. Virkar, M. Liu, F. Liu, Phys. Chem. Chem. Phys. 2013 (2013) 489.

[152] P. Hjalmarsson, M. Søgaard, M. Mogensen, Solid State Ionics 179 (2008) 1422-1426.

[153] J. Laurencin, M. Hubert, D.F. Sanchez, S. Pylypko, M. Morales, A. Morata, B. Morel, D. Montinaro, F. Lefebvre-Joud, E. Siebert, Electrochim. Acta 241 (2017) 459-476.

[154] W. Wang, S.P. Jiang, J. Solid State Electrochem. 8 (2004) 914-922.

[155] A. Mai, M. Becker, W. Assenmacher, F. Tietz, D. Hathiramani, E. Ivers-Tiffee, D. Stöver, W. Mader, Solid State Ionics 177 (2006) 1965-1968.

[156] M.Z. Khan, M.T. Mehran, R.-H. Song, J.-W. Lee, S.-B. Lee, T.-H. Lim, S.-J. Park, Ceramics International 42 (2016) 6978-6984.

[157] A. Mai, V.A.C. Haanappel, F. Tietz, D. Stöver, Solid State Ionics 177 (2006) 2103-2107.

[158] H.-J. Choi, Y.-H. Na, D.-W. Seo, S.-K. Woo, S.-D. Kim, Ceramics International 42 (2016) 545-550.

[159] F. Wang, M.E. Brito, K. Yamaji, D.-H. Cho, M. Nishi, H. Kishimoto, T. Horita, H. Yokokawa, Solid State Ionics 262 (2014) 454-459.

[160] J. Malzbender, P. Batfalsky, R. Vaßen, V. Shemet, F. Tietz, J. Power Sources 201 (2012) 196-203.

[161] F. Tietz, D. Sebold, A. Brisse, J. Schefold, J. Power Sources 223 (2013) 129-135.

[162] A. Mahmoud, M. Al Daroukh, M. Lipinska-Chwalek, M. Luysberg, F. Tietz, R.P. Hermann, Solid State Ionics 312 (2017) 38-43.

[163] K. Park, S. Yu, J. Bae, H. Kim, Y. Ko, Int. J. Hydrogen Energy 35 (2010) 8670-8677.

[164] S. Li, H. Tu, L. Yu, M.T. Anwar, Electrochim. Acta 212 (2016) 303-312.

[165] M.Z. Khan, R.-H. Song, S.-B. Lee, J.-W. Lee, T.-H. Lim, S.-J. Park, Int. J. Hydrogen Energy 39 (2014) 20799-20805.

[166] J. Schefold, A. Brisse, H. Poepke, Int. J. Hydrogen Energy 42 (2017) 13415-13426.

[167] M. Keane, V. Atul, S. Prabhakar, Proc. Advances in Solid Oxide Fuel Cells VII, edited by N.P. Bansal, P. Singh, (2011) p. 183-191.

[168] K. Chen, S.P. Jiang, Int. J. Hydrogen Energy 36 (2011) 10541-10549.

[169] M.A. Laguna-Bercero, R. Campana, A. Larrea, J.A. Kilner, V.M. Orera, J. Power Sources 196 (2011) 8942-8947.

[170] T. Daio, P. Mitra, S.M. Lyth, K. Sasaki, Int. J. Hydrogen Energy 41 (2016) 12214-12221.

[171] E. Bucher, C. Gspan, W. Sitte, Solid State Ionics 272 (2015) 112-120.

[172] J. Xie, Y.-W. Ju, T. Ishihara, Solid State Ionics 249-250 (2013) 177-183.

[173] C.C. Wang, K. Chen, T. Jiang, Y. Yang, Y. Song, H. Meng, S.P. Jiang, B. Lin, Electrochim. Acta 269 (2018) 188-195.

[174] T. Kushi, Int. J. Hydrogen Energy 42 (2017) 9396-9405.

[175] E.N. Naumovich, K. Zakharchuk, S. Obrębowski, A. Yaremchenko, Int. J. Hydrogen Energy 42 (2017) 29443-29453.

[176] K. Hilpert, D. Das, M. Miller, D.H. Peck, R. R. Weiss, J. Electrochem. Soc. 143 (1996) 3642-3647.

[177] H. Yokokawa, T. Horita, N. Sakai, K. Yamaji, M.E. Brito, Y.P. Xiong, H. Kishimoto, Solid State Ionics 177 (2006) 3193-3198.

[178] Y. Zhen, A.I.Y. Tok, F.Y.C. Boey, S.P. Jiang, Electrochem. Solid-State Lett. 11 (2008) B42-B46.

[179] S.P. Jiang, J.P. Zhang, L. Apateanu, K. Foger, J. Electrochem. Soc. 147 (2000) 4013-4022 .

[180] S.P. Jiang, Journal of Applied Electrochemistry 31 (2001) 181-192.

[181] S.P. Jiang, J.P. Zhang, X.G. Zheng, J. Eur. Ceram. Soc. 22 (2002) 361-373.

[182] T. Komatsu, H. Arai, R. Chiba, K. Nozawa, M. Arakawa, K. Sato, Electrochem. Solid-State Lett. 9 (2006) A9-A12.

[183] T. Komatsu, R. Chiba, H. Arai, K. Sato, J. Power Sources 176 (2008) 132-137.

[184] E. Park, S. Taniguchi, T. Daio, J.-T. Chou, K. Sasaki, Solid State Ionics 262 (2014) 421-427.

[185] W. Guan, L. Jin, W. Wu, Y. Zheng, G. Wang, W.G. Wang, J. Power Sources 245 (2014) 119-128.

[186] Y. Matsuzaki, I. Yasuda, Solid State Ionics 132 (2000) 271-278.

[187] Y. Matsuzaki, I. Yasuda, J. Electrochem. Soc. 148 (2001) A126-A131.

[188] S.P. Jiang, J.P. Zhang, K. Foger, J. Electrochem. Soc. 148 (2001) C447-C455.

[189] E. Konysheva, J. Mertens, H. Penkalla, L. Singheiser, K. Hilpert, J. Electrochem. Soc. 154 (2007) B1252-B1264.

[190] B.J. Ingram, T.A. Cruse, M. Krumpelt, J. Electrochem. Soc. 154 (2007) B1200-B1205.

[191] M. Yang, E. Bucher, W. Sitte, J. Power Sources 196 (2011) 7313-7317.

[192] J.A. Schuler, H. Lübbe, A. Hessler-Wyser, J. Van Herle, J. Power Sources 213 (2012) 223-228.

[193] J.A. Schuler, H. Lübbe, A. Hessler-Wyser, J. Van Herle, Proc. Proc. of the 15$^{th}$ European Solid Oxide Fuel Cell Forum, 2011, p. B0503.

[194] S.-N. Lee, A. Atkinson, J. Kilner, ECS Trans. 57 (2013) 605-613.

[195] M. de Ridder, A.G.J. Vervoort, R.G. van Welzenis, H.H. Brongersma, Solid State Ionics 156 (2003) 255-262.

[196] M. de Ridder, R.G. van Welzenis, A.W. Denier van der Gon, H.H. Brongersma, S. Wulff, W.F. Chu, W. Weppner, J. Appl. Phys. 92 (2002) 3056-3064.

[197] M. Mogensen, K.V. Jensen, M.J. Jørgensen, S. Primdahl, Solid State Ionics 150 (2002) 123-129.

[198] J.A. Schuler, Z. Wuillemin, A. Hessler-Wyser, J. Van herle, Electrochem. Solid-State Lett. 14 (2011) B20-B22.

[199] J.-M. Bae, B.C.H. Steele, Solid State Ionics 106 (1998) 247-253.

[200] M. Aoki, Y.-M. Chiang, I. Kosacki, L.J.-R. Lee, H. Tuller, Y. Liu, J. Am. Ceram. Soc. 79 (1996) 1169-1180.

[201] J.H. Lee, Monatsh. Chem. 140 (2009) 1081-1094.

[202] T. Carvalho, E. Antunes, J. Calado, F.M. Figueiredo, J.R. Frade, Solid State Ionics 225 (2012) 484-487.

[203] J.L. Hertz, A. Rothschild, H.L. Tuller, J. Electroceram. 22 (2009) 428-435.

[204] J.A. Lane, J.L. Neff, G.M. Christie, Solid State Ionics 177 (2006) 1911-1915.

[205] P. Jasinski, V. Petrovsky, T. Suzuki, H.U. Anderson, J. Electrochem. Soc. 152 (2005) J27-J32.

[206] B.C.H. Steele, Solid State Ionics 129 (2000) 95-110.

[207] M.J. Verkerk, B.J. Middelhuis, A.J. Burggraaf, Solid State Ionics 6 (1982) 159-170.

[208] S.P.S. Badwal, J. Drennan, J. Mater. Sci. 22 (1987) 3231-3239.

[209] J.H. Lee, T. Mori, J.G. Li, T. Ikegami, M. Komatsu, H. Haneda, J. Electrochem. Soc. 147 (2000) 2822-2829.

[210] J.-H. Lee, T. Mori, J.-G. Li, T. Ikegami, M. Komatsu, H. Haneda, J. Am. Ceram. Soc. 83 (2000) 1273-1275.

[211] M.A. Laguna-Bercero, H. Luebbe, J. Silva, J. Van herle, Fuel Cells 15 (2015) 98-104.

[212] W.M. Harris, J.J. Lombardo, M.B. DeGostin, G.J. Nelson, H. Luebbe, J.A. Schuler, J. Van herle, J.C. Andrews, Y. Liu, P. Pianetta, Y.-C. Karen Chen, J. Wang, W.K.S. Chiu, Solid State Ionics 237 (2013) 16-21.

[213] Y. Liu, X. Zhu, M. Li, W. Li, W. Yang, J. Membr. Sci. 492 (2015) 173-180.

[214] E.J. Opila, J. Am. Ceram. Soc. 86 (2003) 1238-1248.

[215] E.J. Opila, J.L. Smialek, R.C. Robinson, D.S. Fox, N.S. Jacobson, J. Am. Ceram. Soc. 82 (1999) 1826-1834.

[216] E. Sooby Wood, S.S. Parker, A.T. Nelson, S.A. Maloy, J. Am. Ceram. Soc. 99 (2016) 1412-1419.

[217] I. Kaus, K. Wiik, M. Dahle, M. Brustad, S. Aasland, J. Eur. Ceram. Soc. 27 (2007) 4509-4514.

[218] D. Schlehuber, E. Wessel, L. Singheiser, T. Markus, J. Membr. Sci. 351 (2010) 16-20.

[219] E. Bucher, C. Gspan, T. Höschen, F. Hofer, W. Sitte, Solid State Ionics 299 (2017) 26-31.

[220] D. Ortolino, A. Engelbrecht, H. Lauterbach, M. Bräu, J. Kita, R. Moos, Journal of Ceramic Science and Technology 5 (2014) 317-326.

[221] N.M. Davey, R.J. Seymour, Platinum Metals Review 29 (1985) 2.

[222] Z. Liu, D.D.L. Chung, Journal of Electronic Packaging 123 (2000) 64-69.

[223] T.H. L., Gold Bulletin 8 (1975) 13-15.

[224] M.M. Viitanen, R.G. v. Welzenis, H.H. Brongersma, F.P.F. van Berkel, Solid State Ionics 150 (2002) 223-228.

[225] T. Horita, H. Kishimoto, K. Yamaji, M.E. Brito, Y. Xiong, H. Yokokawa, Y. Hori, I. Miyachi, J. Power Sources 193 (2009) 194-198.

[226] P.S. Gentile, S.W. Sofie, C.F. Key, R.J. Smith, International Journal of Applied Ceramic Technology 9 (2012) 1035-1048.

[227] J.A. Schuler, C. Gehrig, Z. Wuillemin, A.J. Schuler, J. Wochele, C. Ludwig, A. Hessler-Wyser, J. Van herle, J. Power Sources 196 (2011) 7225-7231.

[228] F. Smeacetto, M. Salvo, M. Santarelli, P. Leone, G.A. Ortigoza-Villalba, A. Lanzini, L.C. Ajitdoss, M. Ferraris, Int. J. Hydrogen Energy 38 (2013) 588-596.

[229] Y.-S. Chou, E.C. Thomsen, J.P. Choi, J.W. Stevenson, J. Power Sources 197 (2012) 154-160.

[230] B. Karmakar in: B. Karmakar (Eds.), *Functional Glasses and Glass-Ceramics*, Butterworth-Heinemann, 2017, p. 281-293.

[231] M.K. Mahapatra, K. Lu, Materials Science and Engineering: R: Reports 67 (2010) 65-85.

[232] G. Rinaldi, S. Diethelm, P. Burdet, E. Oveisi, J. Van herle, D. Montinaro, Q. Fu, A. Brisse, Proc. 12th European SOFC & SOE Forum, edited by Luzern, Switzerland (2016) p. A0802.

[233] E.J. Opila, D.S. Fox, N.S. Jacobson, J. Am. Ceram. Soc. 80 (1997) 1009-1012.

[234] E. Bucher, W. Preis, W. Sitte, C. Gspan, F. Hofer, Proc. 10th European Solid Oxide Fuel Cell Forum, 2012, p. B0543-B0552.

[235] E.J. Opila, N.S. Jacobson, D.L. Myers, E.H. Copland, JOM 58 (2006) 22-28.

[236] N.S. Jacobson, E.J. Opila, D.L. Myers, E.H. Copland, J. Chem. Thermodyn. 37 (2005) 1130-1137.

[237] Z. Wuillemin, A. Nakajo, A. Müller, A.J. Schuler, S. Diethelm, J. Van Herle, D. Favrat, Proc. 11th Intern. Symp. Solid Oxide Fuel Cells (SOFC-XI), 2009, p. 457-466.

[238] A.J. Schuler, Z. Wuillemin, A. Hessler-Wyser, J. Van Herle, Proc. 11th Intern. Symp. Solid Oxide Fuel Cells (SOFC-XI) 2009, p. 2845-2852.

[239]   E. Bucher, C. Gspan, F. Hofer, W. Sitte, Solid State Ionics 230 (2013) 7-11.

[240]   M. Perz, E. Bucher, C. Gspan, J. Waldhäusl, F. Hofer, W. Sitte, Solid State Ionics 288 (2016) 22-27.

[241]   N. Schrödl, E. Bucher, A. Egger, P. Kreiml, C. Teichert, T. Höschen, W. Sitte, Solid State Ionics 276 (2015) 62-71.

[242]   D. Balz, K. Plieth, Z. Elektrochem. 59 (1955) 545-551.

[243]   K. Momma and F. Izumi, J. Appl. Crystallogr. 44 (2011) 1272-1276.

[244]   V.M. Goldschmidt, Berichte Der Deutschen Chemischen Gesellschaft 14 (1926) 477-485.

[245]   R.J.D. Tilley, *Perovskites: Structure-Property Relationships*, John Wiley & Sons, Ltd, Chichester, UK, 2016.

[246]   K.K. Singh, P. Ganguly, J.B. Goodenough, J. Solid State Chem. 52 (1984) 254-273.

[247]   M. Greenblatt, Current Opinion in Solid State & Materials Science 2 (1997) 174-183.

[248]   A. Mehta, P.J. Heaney, Physical Review B 49 (1994) 563.

[249]   S.J. Skinner, Solid State Sci. 5 (2003) 419-426.

[250]   J.D. Jorgensen, B. Dabrowski, S. Pei, D.R. Richards, D.G. Hinks, Physical Review B 40 (1989) 2187.

[251]   T. Kajitani, Y. Kitagaki, K. Hiraga, S. Hosoya, T. Fukuda, Y. Yamaguchi, S. Wada, S. Sugai, Y. Morii, K. Fuchizaki, S. Funahashi, Physica C: Superconductivity 185-189, Part 1 (1991) 579-580.

[252]   J. Rodriguez-Carvajal, M.T. Fernandez-Diaz, J.L. Martinez, J. Phys.-Condens. Matter 3 (1991) 3215.

[253]   M.T. Fernandez-Diaz, J.L. Martinez, J. Rodriguez-Carvajal, Solid State Ionics 63-65 (1993) 902-906.

[254]   A. Demourgues, A. Wattiaux, J.C. Grenier, M. Pouchard, J.L. Soubeyroux, J.M. Dance, P. Hagenmuller, J. Solid State Chem. 105 (1993) 458-468.

[255]   S.N. Ruddlesden, P. Popper, Acta Crystallogr. 11 (1958) 54-55.

[256]   S.N. Ruddlesden, P. Popper, Acta Crystallogr. 10 (1957) 538-539.

[257]   V. Vibhu, A. Rougier, C. Nicollet, A. Flura, J.-C. Grenier, J.-M. Bassat, Solid State Ionics 278 (2015) 32-37.

[258]   V. Vibhu, A. Rougier, C. Nicollet, A. Flura, S. Fourcade, N. Penin, J.-C. Grenier, J.-M. Bassat, J. Power Sources 317 (2016) 184-193.

[259]   M.A. Yatoo, A. Aguadero, S.J. Skinner, APL Materials 7 (2018) 013204.

[260]   V. Vibhu, J.-M. Bassat, A. Flura, C. Nicollet, J.-C. Grenier, A. Rougier, ECS Trans. 68 (2015) 825-835.

[261]   R.J. Woolley, S.J. Skinner, J. Power Sources 243 (2013) 790-795.

[262]   J.D. Sullivan, D.J. Buttrey, D.E. Cox, J. Hriljac, J. Solid State Chem. 94 (1991) 337-351.

[263]   Bruker AXS Topas V5, General profile and structure analysis software for powder diffraction data, User's manual, 2014, Karlsruhe, Germany.

[264]   W.D. Kingery, H.K. Bowen, D.R. Uhlmann, *Introduction to Ceramics*, second ed., John Wiley & Sons, New York, 1976.

[265]   P.A. Stadelmann, Ultramicroscopy 21 (1987) 131-145.

[266] M.N. Rahaman, *Ceramics processing and sintering*, Second Edition, CRC Press, Boca Raton, London, New York, 2003.

[267] H. Krischner, B. Koppelhuber-Bitschnau, *Röntgenstrukturanalyse und Rietveldmethode. Eine Einführung. 5. neubearbeitete Auflage*, Springer Fachmedien Wiesbaden, 1994.

[268] Y.K. Chung, Y.-U. Kwon, S.H. Byeon, Bulletin of the Korean Chemical Society 16 (1995) 120-125.

[269] J.I. Goldstein, D.E. Newbury, P. Echlin, D.C. Joy, C.E. Lyman, E. Lifshin, L. Sawyer, J.R. Michael, *Scanning electron microscopy and X-ray microanalysis*, third edition, Springer Science and Business Media, LLC, New York, 2003.

[270] L. Reimer, *Scanning Electron Microscopy*, Springer, Berlin-Heidelberg, 1998.

[271] G.E. Lloyd, Mineral. Mag. 51 (1987) 3-19.

[272] Z. Li, R. Haugsrud, Solid State Ionics 206 (2012) 67-71.

[273] N. Schrödl, A. Egger, C. Gspan, T. Höschen, F. Hofer, W. Sitte, Solid State Ionics 322 (2018) 44-53.

[274] N. Schrödl, E. Bucher, C. Gspan, A. Egger, C. Ganser, C. Teichert, F. Hofer, W. Sitte, Solid State Ionics 288 (2016) 14-21.

[275] FactSage© 6.4, thermodynamic software package, © 1976-2013 Thermfact and GTT Technologies.

[276] B.B. Ebbinghaus, Combust. Flame 93 (1993) 119-137.

[277] W. Preis, M. Holzinger, W. Sitte, Monatsh. Chem. 132 (2001) 499-508.

[278] W. Preis, Solid State Ionics 316 (2018) 118-124.

[279] N. Gauquelin, T.E. Weirich, M. Ceretti, W. Paulus, M. Schroeder, Monatsh. Chem. 140 (2009) 1095-1102.

[280] J. Druce, H. Téllez, M. Burriel, M.D. Sharp, L.J. Fawcett, S.N. Cook, D.S. McPhail, T. Ishihara, H.H. Brongersma, J.A. Kilner, Energy Environ. Sci. 7 (2014) 3593–3599.

[281] J. Druce, T. Ishihara, J. Kilner, Solid State Ionics 262 (2014) 893-896.

[282] M. Burriel, S. Wilkins, J.P. Hill, M.A. Muñoz-Márquez, H.H. Brongersma, J.A. Kilner, M.P. Ryan, S.J. Skinner, Energy Environ. Sci. 7 (2014) 311-316.

[283] M.A. Gülgün, R. Voytovych, I. Maclaren, M. Rühle, R.M. Cannon, Interface Science 10 (2002) 99-110.

[284] T.J. Rabbow, N. Junker, M. Schneider, A. Michaelis, Materialwissenschaft und Werkstofftechnik 42 (2011) 777-783.

[285] T. Maeder, International Materials Reviews 58 (2013) 3-40.

[286] D. Kim, H. Kim, J. Am. Ceram. Soc. 96 (2013) 774-780.

[287] A. Egger, W. Sitte, F. Klauser, E. Bertel, J. Electrochem. Soc. 157 (2010) B1537-B1541.

[288] A. Egger, W. Sitte, Proc. 10th European Solid Oxide Fuel Cell Forum, 2012, p. B05104-B05114.

[289] J. Choisnet, N. Abadzhieva, P. Stefanov, D. Klissurski, J.M. Bassat, V. Rives, L. Minchev, J. Chem. Soc. - Faraday Trans. 90 (1994) 1987-1991.

[290] N. Čebašek, R. Haugsrud, Z. Li, T. Norby, J. Am. Ceram. Soc. 96 (2013) 598-605.

[291] N. Čebašek, R. Haugsrud, T. Norby, Solid State Ionics 231 (2013) 74-80.

[292] J. Yang, Acta Crystallogr. B 64 (2008) 281-286.

[293] A. Egger, N. Schrödl, W. Sitte, Faraday Discussions 182 (2015) 379-391.

[294] A. Egger, N. Schrödl, W. Sitte, ECS Trans. 68(1) (2015) 3345-3358.

[295] E. Bucher, W. Sitte, F. Klauser, E. Bertel, Solid State Ionics 208 (2012) 43-51.

[296] T. Akbay, A. Staykov, J. Druce, H. Tellez, T. Ishihara, J.A. Kilner, J. Mater. Chem. A 4 (2016) 13113-13124.

[297] G. Amow, P.S. Whitfield, I.J. Davidson, R.P. Hammond, C.N. Munnings, S.J. Skinner, Ceramics International 30 (2004) 1635-1639.

[298] NIST X-ray Photoelectron Spectroscopy Database, NIST Standard Reference Database Number 20, Gaithersburg MD, 20899 (2000), 10.18434/T4T88K, Feb. 2018.

[299] J.F. Weaver, H.A.E. Hagelin-Weaver, G.B. Hoflund, G.N. Salaita, Applied Surface Science 252 (2006) 7895-7903.

[300] S. Suzuki, M. Oku, Y. Waseda, Surf. Interface Anal. 25 (1997) 161-166.

[301] T.J. Chuang, C.R. Brundle, K. Wandelt, Thin Solid Films 53 (1978) 19-27.

[302] S. Suzuki, K. Sugiyama, Y. Waseda, Journal of Surface Analysis 9 (2002) 455-458.

[303] S. Hashimoto, C. Tanaka, A. Murata, T. Sakurada, Journal of Surface Analysis 13 (2006) 14-18.

[304] X.G. Cao, S.P. Jiang, Int. J. Hydrogen Energy 41 (2016) 1203-1212.

[305] D. Marrero-López, M.C. Martín-Sedeño, J. Peña-Martínez, J.C. Ruiz-Morales, P. Núñez, M.A.G. Aranda, J.R. Ramos-Barrado, J. Power Sources 195 (2010) 2496-2506.

[306] S. Nakayama, M. Sakamoto, J. Eur. Ceram. Soc. 18 (1998) 1413-1418.

[307] J. Yang, Acta Crystallogr. B 64 (2008) 281-286.

[308] S.P. Jiang, L. Liu, K.P. Ong, P. Wu, J. Li, J. Pu, J. Power Sources 176 (2008) 82-89.

[309] A. Egger, N. Schrödl, C. Gspan, W. Sitte, Solid State Ionics 299 (2017) 18-25.

[310] M. Cimenti, V.I. Birss, J.M. Hill, Fuel Cells 7 (2007) 377-391.

[311] S.P.S. Badwal, R. Deller, K. Foger, Y. Ramprakash, J.P. Zhang, Solid State Ionics 99 (1997) 297-310.

[312] M.S. Sohal, J.E. O'Brien, C.M. Stoots, V.I. Sharma, B. Yildiz, A. Virkar, J. Fuel Cell Sci. Technol. 9 (2012) 011017/1-9.

[313] S.R. Bishop, T.S. Stefanik, H.L. Tuller, Phys. Chem. Chem. Phys. 13 (2011) 10165-10173.

[314] C. Lenser, F. Gunkel, Y.J. Sohn, N.H. Menzler, Solid State Ionics 314 (2018) 204-211.

# 7 Appendix

The following publications, which originated within the scope of this thesis with myself as first author, are attached in this appendix.

N. Schrödl, E. Bucher, A. Egger, P. Kreiml, C. Teichert, T. Höschen, W. Sitte, Long-term stability of the IT-SOFC cathode materials $La_{0.6}Sr_{0.4}CoO_{3-\delta}$ and $La_2NiO_{4+\delta}$ against combined chromium and silicon poisoning, Solid State Ionics 276 (2015) 62-71.

N. Schrödl, E. Bucher, C. Gspan, A. Egger, C. Ganser, C. Teichert, F. Hofer, W. Sitte, Phase decomposition in the chromium- and silicon-poisoned IT-SOFC cathode materials $La_{0.6}Sr_{0.4}CoO_{3-\delta}$ and $La_2NiO_{4+\delta}$ , Solid State Ionics 288 (2016) 14-21.

N. Schrödl, A. Egger, C. Gspan, T. Höschen, F. Hofer, W. Sitte, Phase decomposition of $La_2NiO_{4+\delta}$ under Cr- and Si-poisoning conditions, Solid State Ionics 322 (2018) 44-53.

The following publications with myself as co-author have additionally been published during the work on my thesis.

A. Egger, N. Schrödl, W. Sitte, Evaluation of oxide ceramics as anodes for SOECs, Faraday Discussions 182 (2015) 379-391.

A. Egger, N. Schrödl, W. Sitte, Evaluation of $La_2NiO_4$ as Anode Material for Solid Oxide Electrolyser Cells, ECS Trans. 68(1) (2015) 3345-3358.

A. Egger, N. Schrödl, C. Gspan, W. Sitte, $La_2NiO_{4+\delta}$ as electrode material for solid oxide fuel cells and electrolyzer cells, Solid State Ionics 299 (2017) 18-25.

C. Berger, E. Bucher, A. Egger, A.T. Strasser, N. Schrödl, C. Gspan, J. Hofer, W. Sitte, Synthesis and characterization of the novel $K_2NiF_4$-type oxide $Pr_2Ni_{0.9}Co_{0.1}O_{4+\delta}$, Solid State Ionics 316 (2018) 93-101.
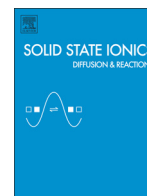
# Long-term stability of the IT-SOFC cathode materials $La_{0.6}Sr_{0.4}CoO_{3-\delta}$ and $La_2NiO_{4+\delta}$ against combined chromium and silicon poisoning

Nina Schrödl [a], Edith Bucher [a,*], Andreas Egger [a], Patrice Kreiml [b], Christian Teichert [b], Till Höschen [c], Werner Sitte [a]

[a] Chair of Physical Chemistry, Montanuniversitaet Leoben, Franz-Josef-Straße 18, A-8700 Leoben, Austria
[b] Institute of Physics, Montanuniversitaet Leoben, Franz-Josef-Straße 18, A-8700 Leoben, Austria
[c] Max Planck Institute for Plasma Physics, EURATOM Association, Boltzmannstraße 2, D-85748 Garching, Germany

## ARTICLE INFO

## ABSTRACT

Long-term degradation effects of combined Cr- and Si-poisoning for the promising intermediate temperature solid oxide fuel cell (IT-SOFC) cathode materials $La_{0.6}Sr_{0.4}CoO_{3-\delta}$ (LSC) and $La_2NiO_{4+\delta}$ (LNO) were investigated at 700 °C in dry and humid atmospheres for subsequent periods of 1000 h by using dc-conductivity relaxation measurements. Changes in the chemical composition and morphology of the contaminated sample surfaces were studied by X-ray photoelectron spectroscopy (XPS), scanning electron microscopy (SEM) with energy and wavelength dispersive X-ray analysis and by atomic force microscopy (AFM). Upon exposure to dry and humid gas flows containing Cr- and Si-species both materials exhibit a strong decrease of the chemical surface exchange coefficient of oxygen by a factor of 110 and 40 for $La_{0.6}Sr_{0.4}CoO_{3-\delta}$ and $La_2NiO_{4+\delta}$, respectively, which can be attributed to the formation of Cr-containing crystallites on the degraded sample surfaces. AFM-measurements reveal faceted crystallites of lateral extensions of up to 2 μm and heights of up to 500 nm on the surface of $La_{0.6}Sr_{0.4}CoO_{3-\delta}$. XPS-analyses confirm the presence of high levels of Cr and Sr in these crystals, indicating the decomposition of the perovskite phase through $SrCrO_4$-formation. The significantly smaller crystallites that are found on the surface of $La_2NiO_{4+\delta}$ also contain Cr, as well as elevated levels of La. For both compounds, silicon is found to spread in small patches across the entire sample surface, as determined by EDXS elemental mapping analysis.

© 2015 Elsevier B.V. All rights reserved.

## 1. Introduction

Solid oxide fuel cells (SOFCs) are high-temperature devices which enable highly-efficient and low-noise conversion of chemical to electrical energy. Due to the high operating temperatures of more than 600 °C, SOFCs can utilize a wide variety of fuels ($H_2$, $CH_4$, diesel reformate, biogas, etc.) without the need for expensive noble metals as catalysts for electrode activation or pre-reforming. Although the SOFC-technology has reached a high level of maturity with respect to performance and efficiency, long-term degradation remains one of the main technical barriers to market entry. Lifetimes of 5000–10,000 h for mobile applications and 45,000–100,000 h for stationary use are often cited as necessary requirements for successful commercialization [1].

Many degradation phenomena take place at the cathode and its interface to the electrolyte. A well-known mode of degradation is chromium poisoning of the cathode by gas phase transport of volatile Cr-species

released from metallic interconnects or balance-of-plant (BOP) components [2]. In the case of interconnects, protective layers – either applied as a thin coating or developed in-situ through high-temperature scale formation – are used as a countermeasure but cannot completely suppress the emission of Cr-species into the gas phase [3,4]. Similar degradation issues may be caused by a poisoning of the cathode by silicon species released into the gas stream from silicate-based glass sealing materials or heat-resistant alloys used in BOP-components [5–10].

Cathode poisoning by Cr- and Si-species strongly depends on the level of humidity in the oxidant owing to enhanced gas transport rates for both elements. This effect can be rationalized by thermodynamic considerations through the comparatively high equilibrium partial pressures of Si- and Cr-oxyhydrates. The presence of humidity in the gas stream is an essential pre-requisite for Si-transport at SOFC-operating temperatures, since volatilities of $SiO_2$ and SiO are very low at temperatures below 1000 °C while the more volatile di-hydrate $H_4SiO_4$ is the primary gaseous Si-species under oxidizing conditions [11, 12]. Chromium has relevant partial pressures in its highest (hexavalent) oxidation state, $CrO_3$ being the dominant gas species in dry and oxidizing conditions while the corresponding mono-hydrate $H_2CrO_4$ is more volatile in humid atmospheres [13,14].

* Corresponding author at: Chair of Physical Chemistry; Montanuniversitaet Leoben; Franz-Josef-Straße 18; A-8700 Leoben; Austria. Tel.:+43 3842 402 4813; fax: +43 3842 402 4802.
*E-mail address:* edith.bucher@unileoben.ac.at (E. Bucher).

Degradation mechanisms of Cr- and Si-poisoning proceed by deposition of Cr- and Si-species at the triple phase boundaries as well as on the cathode surface in the electroactive region of the electrode, thus blocking active sites for the oxygen reduction reaction. Moreover, the deposited layers are often found to react with the underlying cathode material, forming electrically insulating reaction products and changing the local composition of the surface region [15–17].

On this latter point, Sr appears to play an important role, since it is used as a substituent in many cathode materials and has often been observed in reaction phases such as Sr-silicates [18–20] and $SrCrO_4$ [2,21]. Judging from thermodynamic stabilities, calcium and barium are expected to have a similar tendency towards chromate formation [22]. Thus, it appears to be worthwhile to investigate alkaline earth-free cathode materials with regard to their resistance to Cr- and Si-poisoning.

In the present work, a comparative study of the long-term effects of Cr- and Si-poisoning on the stability of the highly active Sr-containing perovskite compound $La_{0.6}Sr_{0.4}CoO_{3-\delta}$ (LSC) and the promising Sr-free material $La_2NiO_{4+\delta}$ (LNO) was conducted. In the course of the degradation experiment, the samples were exposed to increasingly harsh conditions with respect to humidity and Si/Cr-content in the atmosphere.

Since it is evident that poisoning phenomena will proceed from the material surface, degradation processes were characterized on the basis of the temporal evolution of the chemical surface exchange coefficient of oxygen ($k_{chem}$), which is considered as a representative parameter reflecting the state of the cathode surface. In addition to being a fundamental quantity to characterize the performance of mixed ionic-electronically conducting compounds for SOFC and membrane applications [23,24], $k_{chem}$ is known to be very sensitive to surface modifications and can thus be used to continuously monitor in-situ the progress of surface degradation over extended periods of time.

To gain more insight into the type of surface modification and degradation mechanism, samples at different stages in the degradation process were analyzed by employing various techniques. EDXS-elemental mappings from scanning electron microscopy (SEM) provided large-area information on the lateral distribution of constituents and contaminants on the surface. Particular topographical features of the surface were investigated in detail by atomic force microscopy (AFM) and elemental depth profiles of the surface zone were obtained by X-ray photoelectron spectroscopy (XPS) combined with Ar-sputtering.

## 2. Experimental

### 2.1. Sample preparation

Commercial powders of LSC (EMPA, Dübendorf, Switzerland) and LNO (Treibacher Industrie AG, Althofen, Austria) were isostatically pressed into cylindrical pellets at 250 MPa and 200 MPa, respectively. To obtain tablets with relative densities of above 95%, LSC was sintered once for a period of 10 h at 1200 °C in air and LNO twice for a period of 10 h at 1350 °C in air with heating and cooling rates of 2 K min$^{-1}$. Thin slices of approximately $6 \times 6$ mm$^2$ cross section were cut from the sintered pellets with a diamond wire saw. The slabs were ground with a diamond grinding disk and polished by means of polymer-embedded diamond lapping films with 30, 6 and 1 μm particle size to a final thickness of 519 μm and 412 μm for LSC and LNO, respectively. Gold wires were attached to the corners of the square samples to establish electrical contacts by using gold paste (Metalor).

### 2.2. Electrical conductivity relaxation measurements

To investigate the oxygen exchange kinetics, four-point dc-conductivity relaxation experiments were conducted at 700 °C in van der Pauw electrode configuration [25]. Oxidation and reduction steps were applied by changing the oxygen partial pressure in the vicinity of the sample abruptly between $1.0 \times 10^{-1} \leq p(O_2)/bar \leq 1.5 \times 10^{-1}$

by using dry and humidified $O_2$–Ar gas mixtures at a constant flow rate of 2 dm$^3$ h$^{-1}$. The humidification of the test gases was realized by passing the gas streams through washing bottles which were filled with deionized water and placed into a thermostat. The thermostat was set to 6 °C and 17 °C to achieve relative humidities (r.h.) of 30% and 60%, respectively, where 100% corresponds to the equilibrium vapor pressure of $H_2O$ at 25 °C. A constant current of 200–400 mA was applied to the samples and the voltage response was recorded as a function of time. The chemical surface exchange coefficient $k_{chem}$ and the chemical diffusion coefficient $D_{chem}$ of oxygen were obtained from the conductivity relaxation data by using non-linear regression of the corresponding solutions of the diffusion equation [26]. The effects of chromium poisoning were simulated by placing chromium pellets upstream close to the specimen, thus exposing the sample to chromia-containing gas flows. A more detailed description of the experimental procedure is given elsewhere [27]. The experiments were performed in a quartz glass reactor which served as a constant silicon source in humid atmospheres. In addition to the electronically contacted sample (main sample) used for the conductivity relaxation measurements, two smaller pieces of the same material were placed in the reactor and therefore exposed to the same conditions as the main sample. The first one of these samples was removed after approximately 1300–1500 h in dry atmosphere and the second one after additional 1000 h in humidified atmosphere with 30% r.h. for surface analysis. At the end of the experiment, after 1000 additional hours in 60% r.h., the main sample was removed and analyzed.

### 2.3. Atomic force microscopy

Topographic images were recorded with an Asylum Research MFP-3D atomic force microscope (AFM), equipped with a planar closed loop scanner. The AFM was operated in tapping mode at a set-point-to-free amplitude ratio of 0.8. Olympus OMCL-AC160TS silicon probes with a typical spring constant of $k = 42$ N m$^{-1}$ were used to scan the surface of the samples. The probes featured a tetrahedral tip with an opening angle of approximately 35° and a nominal tip radius of 7 nm. The obtained AFM images have undergone step line correction and flattening to eliminate possible sources of errors for roughness analysis like oblique sample mounting. The root mean square (rms) surface roughness $\sigma_{rms}$ is a measure for the vertical surface roughness which describes the root mean square deviations of the height level of the analyzed surface from the average height level and was calculated from topographical data according to

$$\sigma_{rms} = \sqrt{\frac{1}{N^2} \sum_{i=1}^{N} \sum_{j=1}^{N} [z(x_i, y_i) - \mu]^2} \qquad (1)$$

where $x$, $y$ and $z$ denote the image coordinates, $\mu$ is the average height level and $N$ is the number of data points of the image in the $x$- and $y$-directions [28].

In addition to $\sigma_{rms}$, which characterizes vertical roughness only, the lateral correlation length $\xi$ is introduced to quantify the lateral separation for which two heights are correlated. $\xi$ can be used as a measure for lateral height fluctuations and is calculated from the height-height-correlation function [28]. For a random rough surface the height-height correlation function $C(x)$ can be approximated by [29]

$$C(x) = \sigma_{rms}^2 e^{\left[-(|x|/\xi)^{2\alpha}\right]} \qquad (2)$$

where $\alpha$ is the Hurst-parameter. $\xi$ corresponds to the $x$-value where $C(x)$ decays to $\sigma_{rms}^2/e$. Note that $\xi$ is smaller than the average lateral size of the surface structures (e.g. crystallites) but can be used as a parameter to characterize changes in lateral structure size. It should be noted that the presented data for the rms-roughness and the lateral correlation length are mean values of three independent $10 \times 10$ μm$^2$

images, excluding the polished LNO-sample and the LNO-sample annealed for 1000 h in dry, Cr- and Si-containing atmosphere, which were averaged from three $1 \times 1\ \mu m^2$ images. In the latter cases the samples exhibit a much smoother surface and the averaged rms-roughness of $1 \times 1\ \mu m^2$ images is considered to be sufficiently representative.
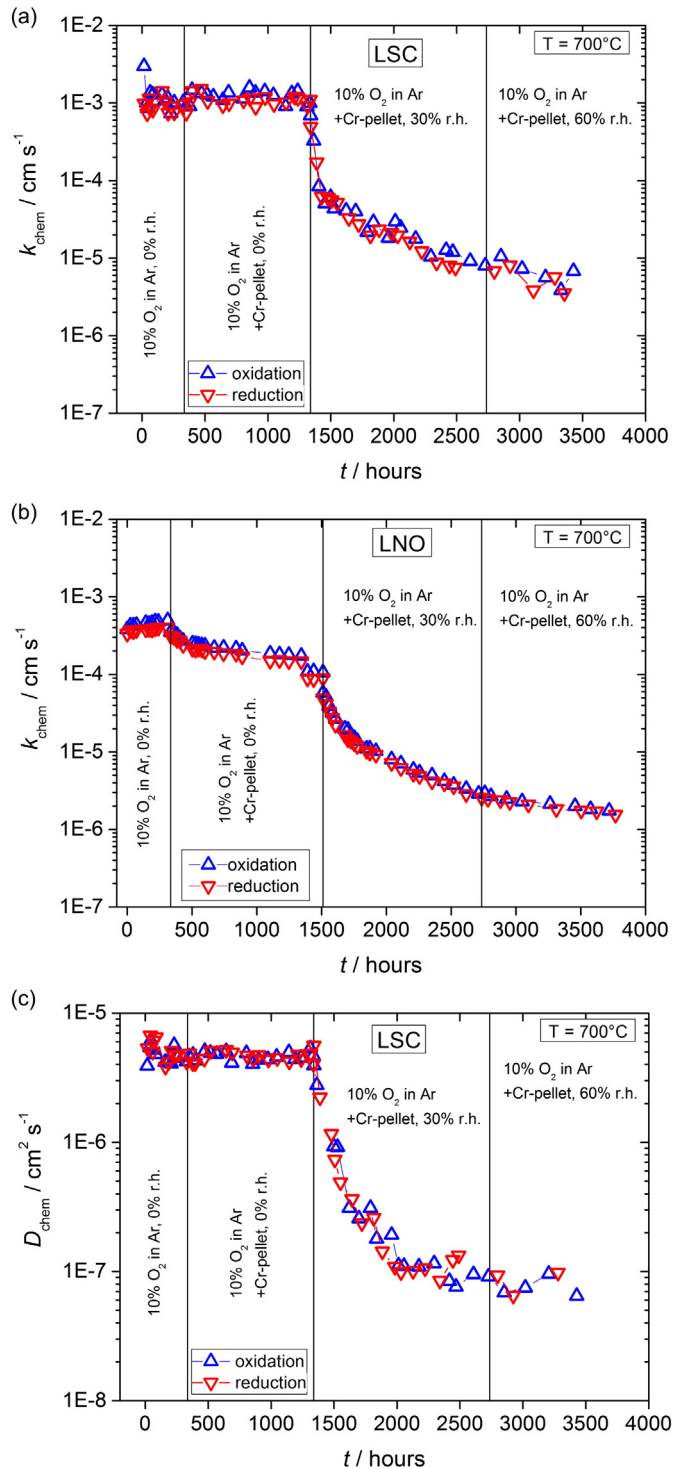


**Fig. 1.** Chemical surface exchange coefficients of oxygen of (a) LSC and (b) LNO and chemical diffusion coefficient of oxygen of (c) LSC at 700 °C and $p(O_2) = 0.1$ bar as a function of time. A silicon source was present for the entire duration of the experiment. Chromium was introduced after approximately 300 h.

## 2.4. X-ray photoelectron spectroscopy

X-ray photoelectron spectroscopy (XPS) measurements were performed with a Perkin Elmer PHI 5600 ESCA system with a hemispherical analyzer. A standard X-ray source was used to record the spectra with Mg-Kα radiation (1253.6 eV). The analyzed area was restricted to a spot with a diameter of 400 μm by the Omnifocus lens. Survey scans were conducted to check for potential unknown contaminants prior to depth profiling. During data acquisition the analyzer was operated at constant pass energy of 58.7 eV. For depth profiling an Atomika WF 421 Microfocus Ion Gun was used to automatically scan a sample area of $1.2 \times 1.5$ mm$^2$ with a 10 kV Ar$^+$ ion beam of approximately 150 μm diameter, irradiating the surface at an ion current of 125 nA under an angle of incidence 20° off surface normal. A sputter rate was estimated from the Ar$^+$-fluence by assuming a yield of 2 target atoms per impinging Ar$^+$, considering the volume density of the bulk composition [30]. It should be mentioned that with different sample compositions the sputter rates might deviate significantly. Especially oxides exhibit high binding energies which can prevent atoms from leaving the sample surface. However, the depth information from the XPS profiles is in good agreement with the crystallite heights determined by AFM (compare Sections 3.2 and 3.3). Despite the limitations of the present method, it is still possible to extract information on degradation-associated changes in the surface elemental composition. A Shirley background function was applied for the background subtraction. Subsequently, the concentrations of the specific elements were obtained from the core-level peak
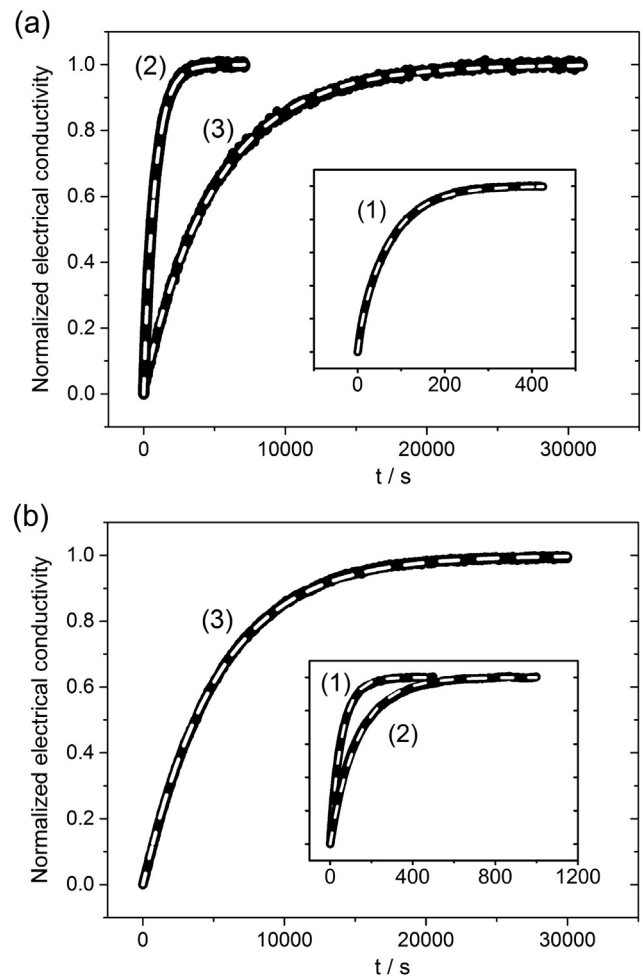


**Fig. 2.** Examples of conductivity relaxation curves, (a) LSC after aging for (1) 60 h, (2) 1213 h, and (3) 2442 h; (b) LNO after (1) 72 h, (2) 1176 h, and (3) 2448 h. Non-linear least square fits of the solution of the diffusion equation (dashed lines) to the experimental data (solid lines) are shown.
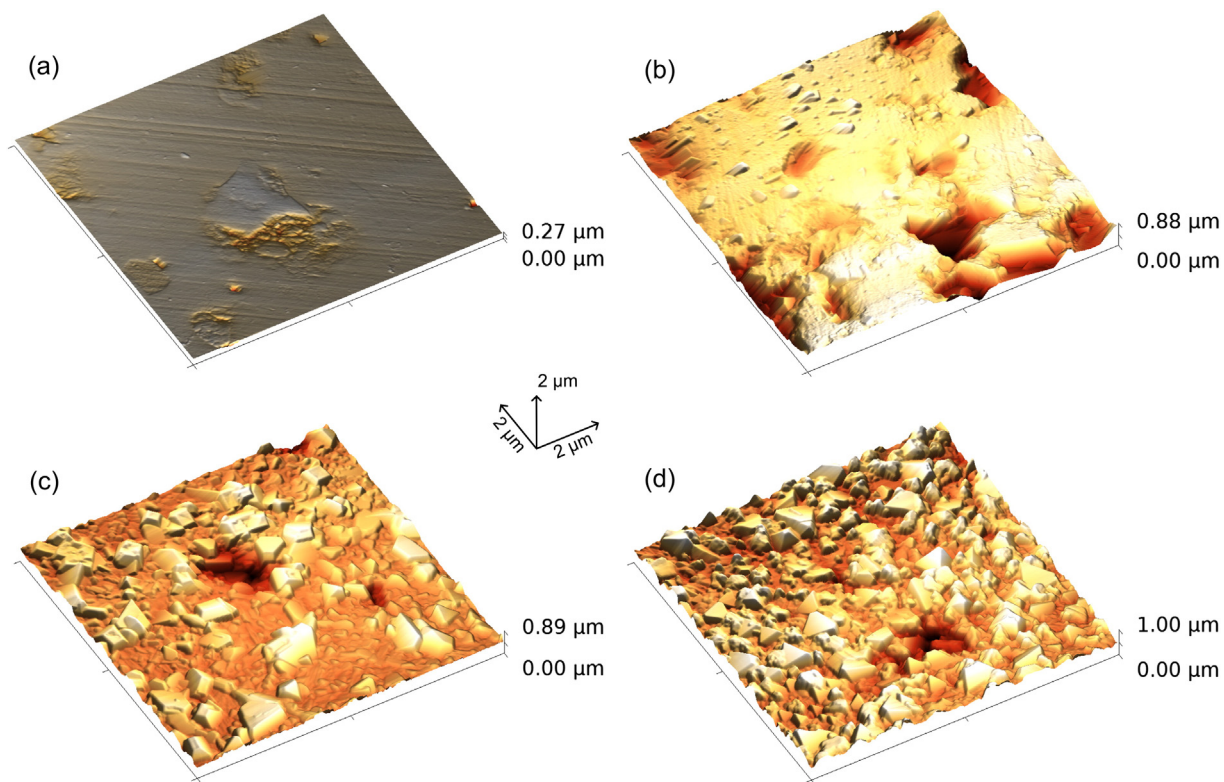
**Fig. 3.** Surface morphology of different LSC samples; AFM scans (10 × 10 μm²) in three-dimensional illuminated presentation of (a) the fresh, polished surface, (b) after 1000 h in dry atmospheres in presence of a Cr- and Si-source, (c) after an additional 1000 h of exposure to a Cr- and Si-source in a moderately humidified atmosphere (30% r.h.) and (d) after another 1000 h with Cr and Si in a strongly humidified atmosphere (60% r.h.). Equal scales are used for all axes.
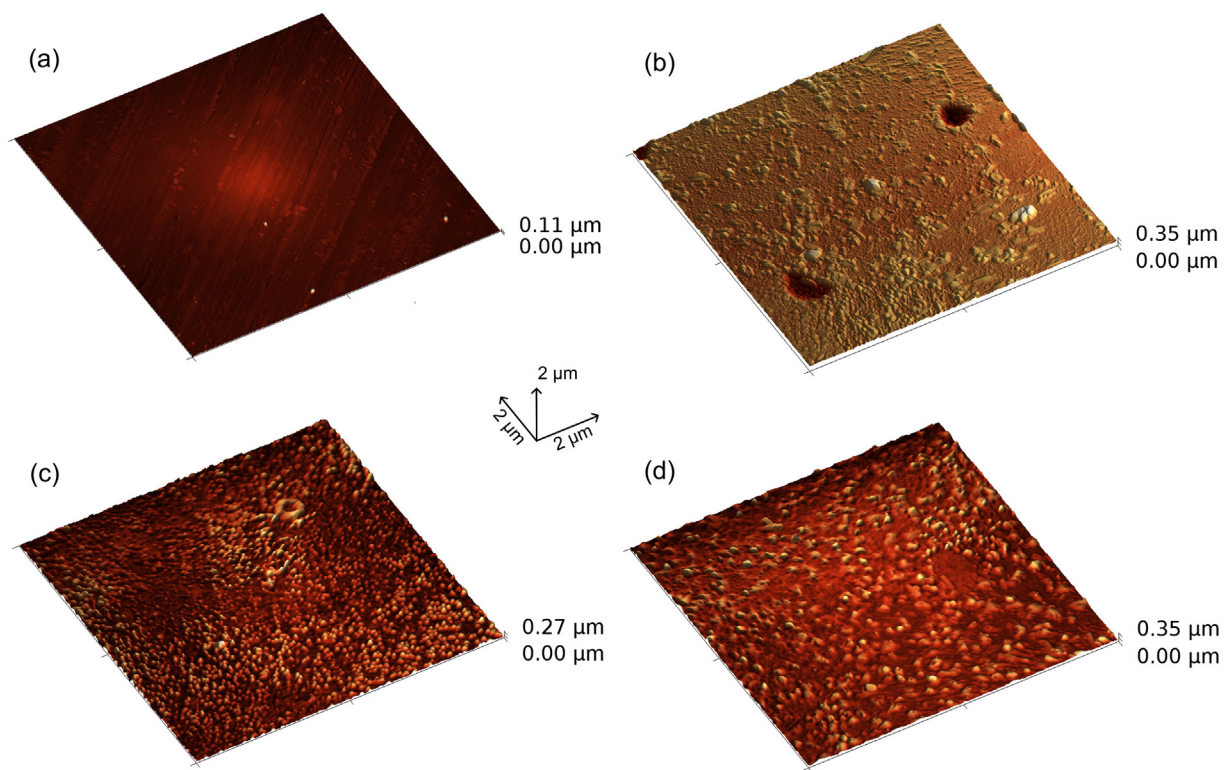


**Fig. 4.** Surface morphology of different LNO samples; AFM scans (10 × 10 μm²) in three-dimensional illuminated presentation of (a) the fresh, polished surface, (b) after 1000 h in a dry atmosphere in the presence of a Cr- and Si- source, (c) after an additional 1000 h of exposure to a Cr- and Si-source in a moderately humidified atmosphere (30% r.h.) and (d) after another 1000 h with Cr and Si in a strongly humidified atmosphere (60% r.h.). Equal scales are used for all axes.

areas by using standard relative sensitivity factors supplied by the manufacturer for the specific instrument. The reproducibility of the XPS-quantification is about 1%.

### 2.5. Scanning electron microscopy–energy dispersive X-ray spectroscopy

Scanning electron microscopy with energy dispersive and wavelength dispersive X-ray spectroscopy (SEM-EDXS, SEM-WDXS) analyses of LSC were performed by using a Zeiss Ultra 55 microscope with an EDAX Phoenix EDXS-detector and an EDAX TEX WDXS-detector at acceleration voltages of 12 kV. Elemental distribution maps of LNO were recorded at acceleration voltages of 10 kV by using a FEI Quanta 200 microscope with an EDAX Genesis detector for EDXS. High resolution images of LSC and LNO were recorded in secondary electron (SE) and backscattered electron (BSE) mode at acceleration voltages of 5 kV.

## 3. Results and discussion

### 3.1. Oxygen exchange kinetics

The results of the electrical conductivity relaxation measurements conducted over a period of about 3500 h are illustrated in Fig. 1. For LSC both the chemical surface exchange coefficient $k_{chem}$ of oxygen and the chemical diffusion coefficient $D_{chem}$ of oxygen could be determined simultaneously, indicating mixed-controlled kinetics. For the LNO sample, however, only $k_{chem}$ was obtained because the kinetics was found to be surface-exchange controlled [31,32].

In Fig. 1, the results for $k_{chem}$ of (a) LSC and (b) LNO are presented as a function of time at 700 °C and an oxygen partial pressure of $p(O_2) = 0.1$ bar. Both samples showed high initial $k_{chem}$-values of $1.1 \times 10^{-3}$ cm s$^{-1}$ (LSC) and $3.6 \times 10^{-4}$ cm s$^{-1}$ (LNO). During the first 200–300 h the experiments were performed without any chromium source to check the intrinsic stability of the materials. Both samples showed fairly stable surface exchange kinetics in the absence of chromium, thus indicating negligible intrinsic degradation. During the following 1000 h, the samples were exposed to a Cr- and Si-source in dry gas flow. For LSC, no Cr- and Si-induced degradation was observed under dry conditions. Post-test analyses of the sample after treatment in dry atmospheres revealed that deposited amounts of Cr and Si, if present, were below the detection limit of XPS (see Section 3.3). In comparison, $k_{chem}$ of LNO decreased by a factor of 2.8 and subsequent XPS-analyses confirmed the presence of Cr-species on the surface. After the introduction of moderate humidity (30% r.h.), a pronounced decrease of $k_{chem}$ by a factor of 110 and 40 was observed for LSC and LNO, respectively. As will be discussed in Section 3.2, the decrease of $k_{chem}$ can be attributed to Cr-induced changes of the surface morphology and phase decompositions in the regions near the surface. In addition, the deposition of poorly conducting Si-species released from the quartz glass reactor in humid atmospheres contribute to the deterioration of the surface exchange reaction. After exposure to increased levels of humidity (60% r.h.) the total decrease of $k_{chem}$ amounts to a factor of 250 and 230 for LSC and LNO, respectively. The increase in humidity does not accelerate the degradation rate, which is not surprising considering the actual changes in partial pressure of the most abundant volatile Cr- and Si-species released in humid atmospheres. At 700 °C and a $p(O_2)$ of 0.1 bar the change in partial pressure of chromic acid ($H_2CrO_4$) from $5.4 \times 10^{-8}$ bar (30% r.h.) to $1.1 \times 10^{-7}$ bar (60% r.h.) is relatively small (partial pressures were calculated with FactSage v.6.4 based on data by Ebbinghaus [14]). Similarly, the partial pressure of $H_4SiO_4$ increases from $3.1 \times 10^{-11}$ bar (30% r.h.) to $1.3 \times 10^{-10}$ bar at 60% r.h. (calculations based on data from Jacobson et al. [11]).

In the case of LSC, the simultaneous determination of surface exchange coefficients and chemical diffusion coefficients was possible. The initial value for $D_{chem}$ of $4.7 \times 10^{-6}$ cm$^2$ s$^{-1}$ remained constant during the exposure to Cr-containing atmospheres without humidification (Fig. 1c). Once humidity was added to the gas stream, $D_{chem}$ started to

**Table 1**
Root mean square roughness $\sigma_{rms}$ and lateral correlation length $\xi$ of LNO and LSC samples, determined at different stages of the degradation experiments.

| Material | Treatment | $\sigma_{rms}$/nm | $\xi$/nm | Image size/μm$^2$ |
|---|---|---|---|---|
| LNO | Polished | 3 | 60 | 1 × 1 |
| | + 1000 h Cr/Si, dry | 18 | 96 | 1 × 1 |
| | + 1000 h Cr/Si, 30% r.h. | 34 | 88 | 10 × 10 |
| | + 1000 h Cr/Si, 60% r.h. | 32 | 141 | 10 × 10 |
| LSC | Polished | 48 | 665 | 10 × 10 |
| | + 1000 h Cr/Si, dry | 123 | 778 | 10 × 10 |
| | + 1000 h Cr/Si, 30% r.h. | 167 | 691 | 10 × 10 |
| | + 1000 h Cr/Si, 60% r.h. | 136 | 393 | 10 × 10 |

decrease. Over the entire duration of the experiment, $D_{chem}$ dropped by a factor of 65 which can probably be ascribed to the formation a relatively thick layer of Cr-containing compounds on the sample surface (Fig. 6c and d) which exhibits a much smaller $D_{chem}$ compared to the bulk phase. Similar behavior was also observed in a previous study [20].

Selected examples of experimental conductivity relaxation curves and the corresponding fits are given in Fig. 2a and b for LSC and LNO, respectively. It should be considered that, due to the observed formation of secondary phases, the assumption of diffusion in a homogeneous medium is not strictly valid. One must be aware that the measured kinetic parameters of the more strongly degraded samples, which contain variable amounts of different phases in the surface-near region, are to be understood as effective rate constants which give overall trends for the changes in a multi-phase sample. Even though the values of $k_{chem}$ (and $D_{chem}$) of the more strongly degraded samples may thus be influenced by increased measurement uncertainties, the fits to the models (mixed-controlled kinetics for LSC, surface-controlled kinetics for LNO) describe the experimental data very well (compare examples in Fig. 2). This seems to indicate that at least the overall trends and magnitudes of the kinetic parameters are correct.
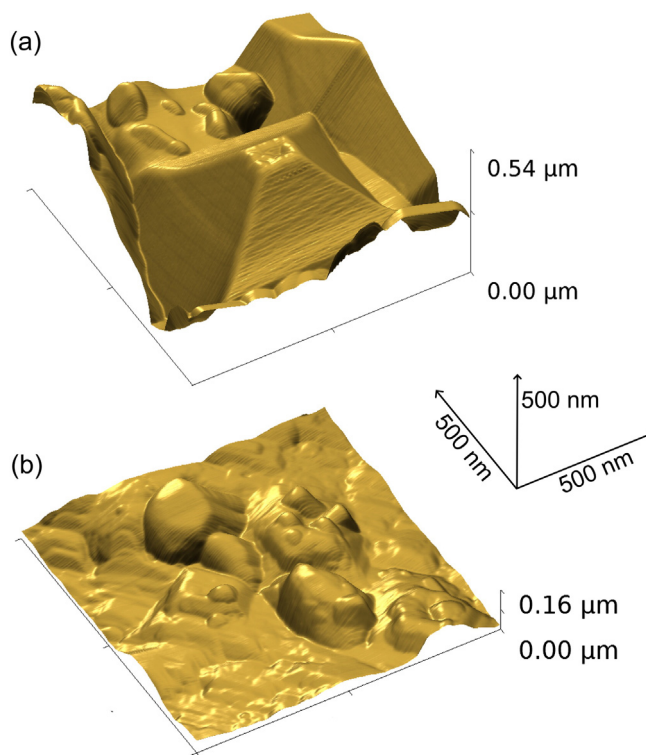


**Fig. 5.** Comparison of surface structures of degraded LSC and LNO samples; high resolution 3D AFM images (1 × 1 μm$^2$) of (a) LSC and (b) LNO after 3000 h in dry and humid atmospheres in close proximity to a Cr-pellet and a Si-source. Axes are to scale.

### 3.2. Atomic force microscopy

In order to examine degradation-associated changes in surface morphology, pre- and post-test analyses of LSC and LNO were performed by using AFM. Figs. 3 and 4 present large area surface scans ($10 \times 10$ µm$^2$) of LSC and LNO (a) of the fresh, polished surface, (b) after 1000 h in a dry atmosphere in the presence of chromium and silicon, (c) after an additional 1000 h of exposure to a Cr- and Si-source in a moderately humidified atmosphere (30% r.h.) and (d) after further 1000 h of exposure to a Cr- and Si-source in a strongly humidified atmosphere (60% r.h.). The corresponding root mean square surface roughness $\sigma_{rms}$ and the lateral correlation length ξ are listed in Table 1.

The fresh LSC sample depicted in Fig. 3a shows fine scratches caused by the polishing procedure. Small cavities from residual porosity with a maximum depth of approx. 200 nm can be observed in some regions. In other areas shallow, irregularly structured craters (presumably due to grain pull-out during polishing) are visible which result in a relatively high surface roughness for a polished surface. In comparison, a freshly prepared sample of LNO features a relatively smooth surface with $\sigma_{rms}$ and ξ being smaller by one order of magnitude (Fig. 4a).

After 1000 h of exposure to Cr and Si in dry atmospheres, $\sigma_{rms}$ and ξ of LSC are increased by a factor of 2.5 and 1.2, respectively, indicating an increase in the number of surface features. The AFM-image in Fig. 3b reveals sharp-edged craters, and small crystallites in their early state of growth with a height of approximately 120 nm (determined by line

profile analysis) are protruding from the surface. Similarly, for the LNO sample (Fig. 4b) $\sigma_{rms}$ and ξ increase after 1000 h in dry Cr- and Si-containing atmospheres by a factor of 6 and 1.5, respectively and the surface features small rod-like crystallites. Some areas show cavities of approximately 1 µm diameter which are surrounded by a cluster of crystals along the circumference.

Fig. 3c illustrates the surface of LSC after an additional 1000 h at 30% r.h. The surface is covered with faceted crystals of 0.15 to 2 µm lateral extension and an average crystallite height of approximately 140 nm as obtained by analysis of the height histogram (not shown) of the AFM data (for details of this procedure see [28], page 348). Furthermore, the surface roughness increases by a factor of 1.4 whereas the lateral correlation length decreases by a factor of 1.1, indicating not only an increase in the height of the growing crystallites, but also an increase in number. The same general trend was also found for the LNO sample, where $\sigma_{rms}$ increases by a factor 1.8 and ξ decreases by a factor of 1.1. Compared to the rather coarse crystallites formed on the LSC surface, the AFM image of LNO (Fig. 4c) reveals a surface that is densely covered with roundish grains with a lateral extension between 50 and 300 nm.

Exposure of the LSC sample to 60% r.h. over the course of another 1000 h results in promoted crystal growth which is illustrated in Fig. 3d, accompanied by a decrease in the surface roughness and the lateral correlation length (Table 1). The crystals found on the LSC sample surface bear a resemblance to truncated pyramids in different sizes
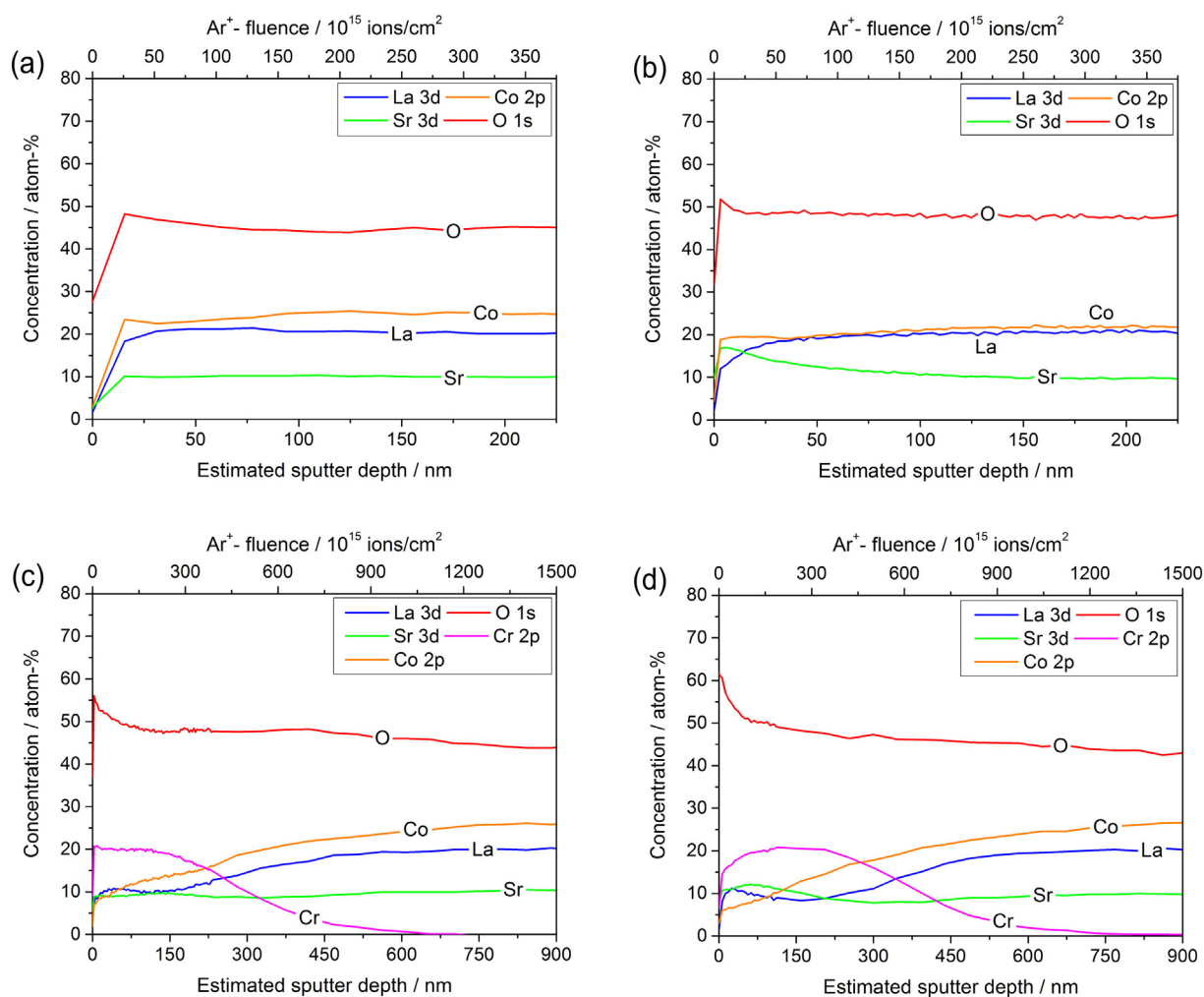


**Fig. 6.** XPS elemental depth profiles of La, Sr, Co and O in LSC and Cr-impurities in (a) the fresh sample, (b) after 1000 h of exposure to a dry atmosphere in the presence of a Cr- and Si-source at 700 °C, (c) after an additional 1000 h of exposure to a Cr- and Si-source in a moderately humidified atmosphere (30% r.h.) and (d) after another 1000 h in vicinity to a Cr-pellet and Si-source in a strongly humidified atmosphere (60% r.h.).

with square and rectangular bases (see also Fig. 5a) and an average crystallite height of approximately 195 nm obtained by height histogram analysis (not shown), whereas the surface of LNO is covered with round protrusions of irregular shape and size (Figs. 4d and 5b). Compared to the condition of the LNO surface after treatment in moderately humidified atmosphere (30% r.h.), $\xi$ is increased while $\sigma_{rms}$ remains constant, indicating that the crystallites grow rather in the lateral than in the vertical direction.

### 3.3. X-ray photoelectron spectroscopy

For the analytical investigation of the surface composition along different stages in the degradation process, XPS-depth profiles were recorded after 1000 h at 700 °C in a dry gas flow of 10% $O_2$/Ar with a Cr- and Si-source, after additional 1000 h in a moderately humidified (30% r.h.) gas stream and after further 1000 h under strongly humidified conditions (60% r.h.). Depth profiles of freshly polished, non-degraded samples were recorded for comparison. XPS-profiling was extended to sputtering depths where a constant bulk composition was reached. It should be mentioned that due to preferential sputtering of lighter elements by the Ar-beam the measured bulk compositions are deviating from the nominal compositions of the investigated materials. Nevertheless, the method provides general trends regarding changes in surface composition among different samples. Moreover, XPS-analysis is a valuable analytical technique by complementing results from EDX-

spectroscopy (see next section) in that XPS provides accurate identification of Cr but has lower sensitivity for silicon while EDXS can be used to reliably identify Si-species but is less suitable for detecting Cr-signals due to the overlap of Cr-lines with those of La and O.

Fig. 6a shows elemental depth profiles of as-prepared LSC, confirming a homogenous composition within the first 200 nm of the sample. Abrupt changes in the topmost layer are an artefact originating from carbon or hydrate/hydroxyl species adsorbed at the surface [20]. Indeed, significant amounts of carbon have been detected by XPS before the first sputtering step but are not shown in the profiles in Figs. 6 and 7. Similarly, small amounts (usually < 3 at.%) of Bi (on LSC) and Bi and Cd (on LNO) originating from the contacting gold paste were found within the topmost surface layer of all degraded samples and have been omitted from the XPS-profiles for reasons of clarity.

After exposing LSC for 1000 h to Cr and Si under dry conditions, significant changes in the surface composition can be gathered from the depth profiles. However, care should be taken in the interpretation of such profiles, since for small sputtering depths XPS-analysis captures signals from both the crystallites formed on the surface (see AFM-results) and the uncovered sample surface. The depth profiles of LSC in Fig. 6b show significant enrichment of Sr within the topmost 100 nm, caused by a segregation of Sr to the surface during the annealing interval. The segregation of A-site cations (mostly Sr) from the bulk towards the surface of $La_{1-x}Sr_xCoO_{3-\delta}$ and similar mixed conducting perovskites (ABO₃) has also been reported in the literature in various
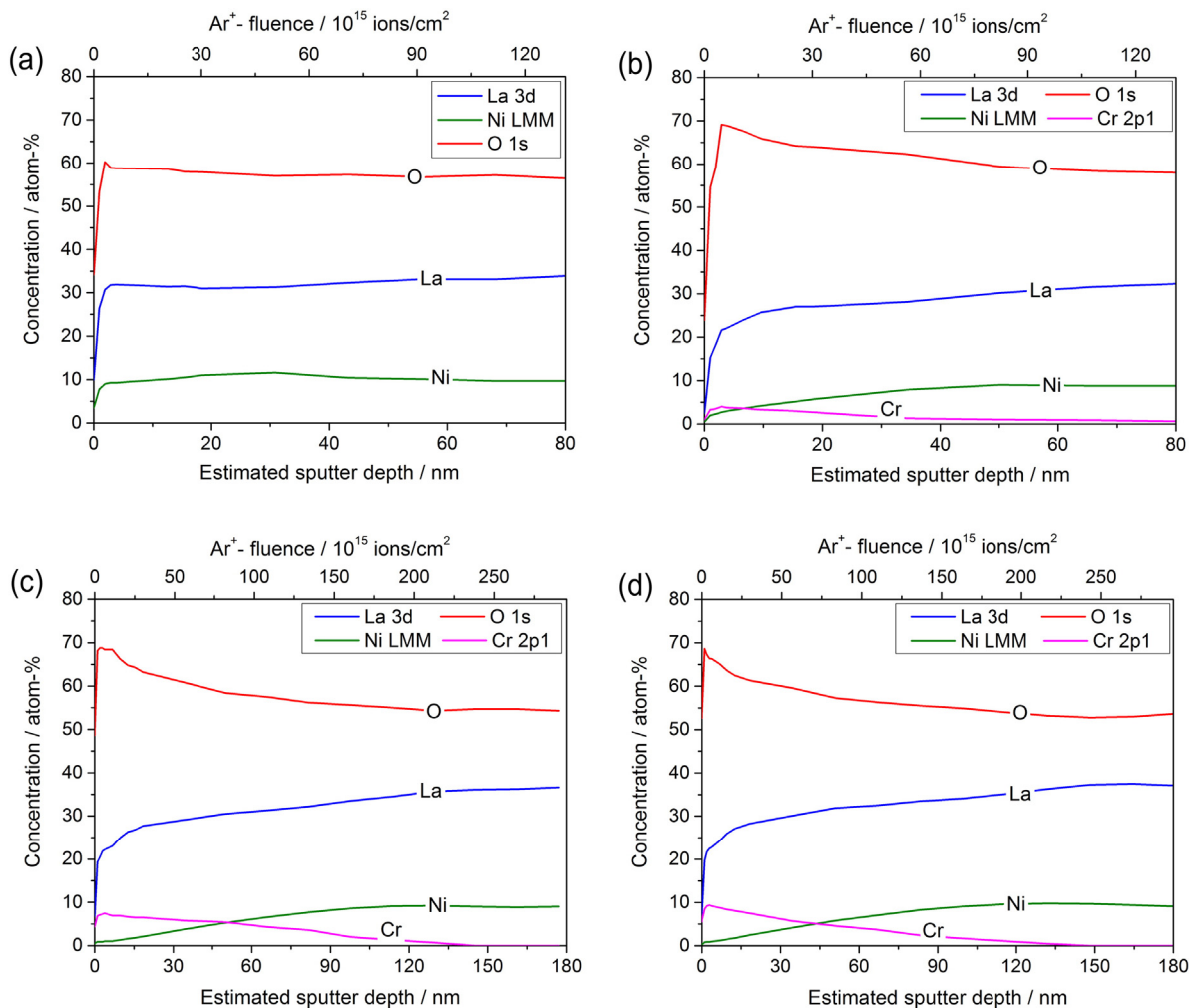


Fig. 7. XPS elemental depth profiles of La, Ni and O in LNO and Cr-impurities in (a) the fresh sample, (b) after 1000 h of exposure to a dry atmosphere in the presence of a Cr- and Si-source at 700 °C, (c) after an additional 1000 h of exposure to a Cr- and Si-source in a moderately humidified atmosphere (30% r.h.) and (d) after another 1000 h in vicinity to a Cr-pellet and Si-source in a strongly humidified atmosphere (60% r.h.).

experimental studies, for instance [17,19,20,33–40], as well as in theoretical calculations [41]. It has further been observed that the Sr-segregation may be enhanced by humidified atmospheres [35,39] and that Sr-rich surface particles may represent nucleation sites for the formation of secondary phases [39]. Similar to the reports of Sr-segregation, La-segregation in LNO was recently found by Druce et al. [42].

With LSC the formation of Sr-chromate/silicate crystallites appears to be less relevant at this stage of degradation, based on the AFM-image in Fig. 3b showing only a few small crystals on the surface and the absence of Cr/Si-signals in the XPS-spectra (Fig. 6b). In comparison, XPS-analysis of LNO confirms the deposition of small amounts of Cr even under dry conditions (Fig. 7b), in agreement with the observed decrease of $k_{chem}$ in dry atmospheres (see Section 3.1). Moreover, close inspection of the data reveals an increase in the La/Ni-ratio within a surface zone of 40 nm, indicating segregation of lanthanum to the surface and/or the incipient formation of La/Cr-containing crystallites (see also Fig. 4b).

Depth profiles of the LSC-sample annealed at 700 °C in 30% r.h. (Fig. 6c) show significant Cr-signals up to a distance of 500–600 nm from the surface. In the case of LSC, the main portion of Cr is found in the topmost 200 nm which is in good agreement with the mean crystallite height of 140 nm and suggests that Cr is mainly located in the surface crystallites developed during Cr-poisoning under humid conditions (see Fig. 3c). Furthermore, the superficial increase in Cr-concentration correlates well with the slight enrichment of Sr and strong depletion of La and Co, suggesting Sr-chromate as main component in the newly formed crystallites, which is in agreement with results reported in literature [2,21]. This may also be an indication that, due to the increased segregation of Sr, the affinity of the surface towards reaction with Cr-impurities is increased, as suggested for the similar IT-SOFC cathode material $La_{0.6}Sr_{0.4}Co_{0.2}Fe_{0.8}O_{3-\delta}$ [35,39].

XPS-analysis of the degraded LNO-surface (Fig. 7c) finds significantly lower amounts of Cr regarding both magnitude and extension as compared to LSC. This is not surprising considering the differences in surface morphology with finely dispersed crystallites grown on the LNO-surface yielding a much lower surface roughness of 34 nm (cf. Figs. 3c and 4c). Correlated with the increase in Cr-concentration is a decrease in the Ni-content which drops to almost zero at the immediate surface. Based on this finding it may be hypothesized that the small crystallites are composed of La-chromate. It is interesting to note that the Cr-trace of LNO does not show a distinctive drop-off as observed for LSC but is rather uniformly decreasing with increasing sputter depth.

XPS-results of LSC and LNO after additional 1000 h at 700 °C under strongly humidified conditions (60% r.h.) are shown in Figs. 6d and 7d, respectively. While depth profiles resemble those of specimens annealed in 30% r.h., their trends are more pronounced. For LSC Sr-enrichment on the surface can now be clearly discerned, but Cr-levels have only slightly shifted to greater sputter depths. The AFM-image of LSC in Fig. 3d and corresponding changes in values of $\sigma_{rms}$ and $\xi$ indicate that crystallite growth does not further increase crystal heights but advances mainly laterally by increasing the surface coverage. While coarsening of the surface crystallites appears to have taken place for LNO (Fig. 4d), Cr-contamination has only been slightly aggravated and is still much less pronounced than for LSC.

### 3.4. Scanning electron microscopy

After the long-term oxygen exchange experiments, SEM-EDXS and -WDXS analyses were performed on strongly degraded samples (60% r.h.) to gain further insight into modifications of the sample surface. Fig. 8 shows the BSE image of a section of the degraded surface of LSC as well as the corresponding elemental distribution maps of La, Sr, Co, O, Si and Cr. Dark areas in the images of La and Co coincide with brighter areas in the maps of O and Cr, which agrees well with trends observed in the XPS-profiles. Some Sr-rich areas appear to be depleted
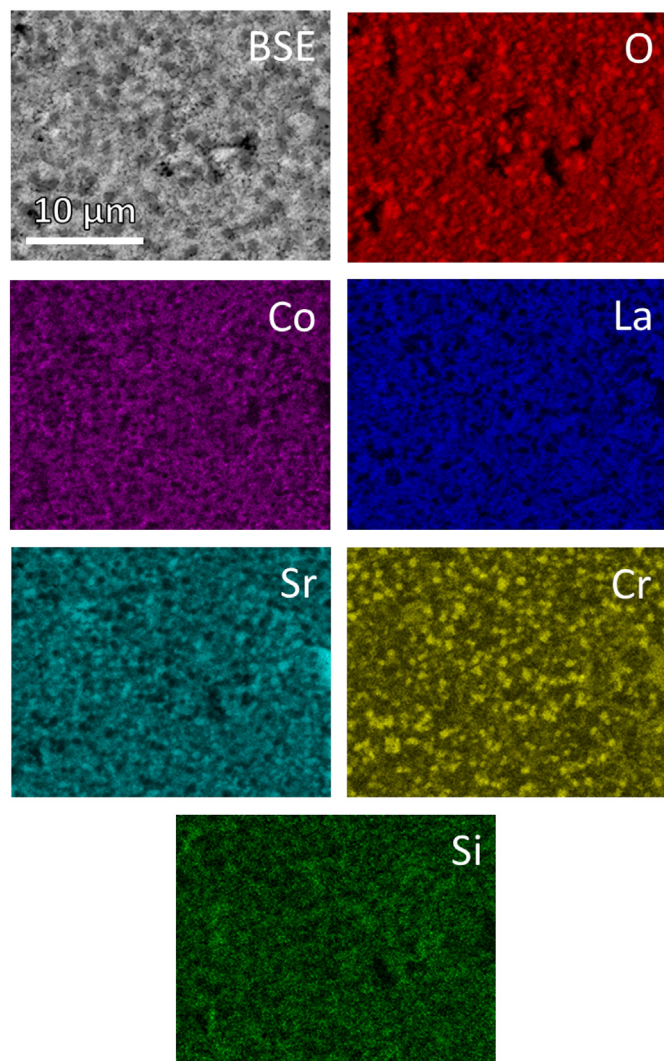


**Fig. 8.** Post-test SEM-BSE image (top left) and SEM-EDXS elemental distribution maps of LSC after degradation at 700 °C in 60% r.h.; the Si-map was acquired by SEM-WDXS. The width of all images is 27.14 μm.

of La and Co, but enriched with Cr. This could be evidence of the formation of $SrCrO_4$ which was also reported for similar, Cr-poisoned SOFC cathode materials [3,43,44]. However, the resolution of EDXS is too low to determine the actual composition in this area reliably. Moreover, it should be mentioned that the Cr-L peak (0.573 eV) overlaps with the O–K peak (0.523 eV) which limits the accuracy of quantification for both Cr and O. Si is distributed over the entire surface and was confirmed separately by WDXS. Preliminary TEM-results of surface regions on degraded LSC give further evidence of the formation of $SrCrO_4$ and will be dealt with in a forthcoming publication.

Fig. 9 presents SEM-BSE image and elemental distribution maps of strongly degraded LNO. The BSE image shows individual grains which are visible due to channeling contrast, as well as some isolated particles on top of the surface. Small dark spots coincide with bright areas in the Ni-map and correspond to NiO-inclusions. NiO has also been detected using SEM-EDXS on a fresh sintered sample obtained from the same pellet used for the preparation of the LNO sample and thus originates either from Ni-excess in the raw powder or is formed during sintering. However, room temperature X-ray diffraction measurements indicate that NiO is not present in the raw powder (XRD-pattern not shown). La and O seem to be homogenously distributed over the entire surface. Si was also confirmed and found to be spread in concentrated patches across the entire surface. The quantification of Cr by EDXS-mapping
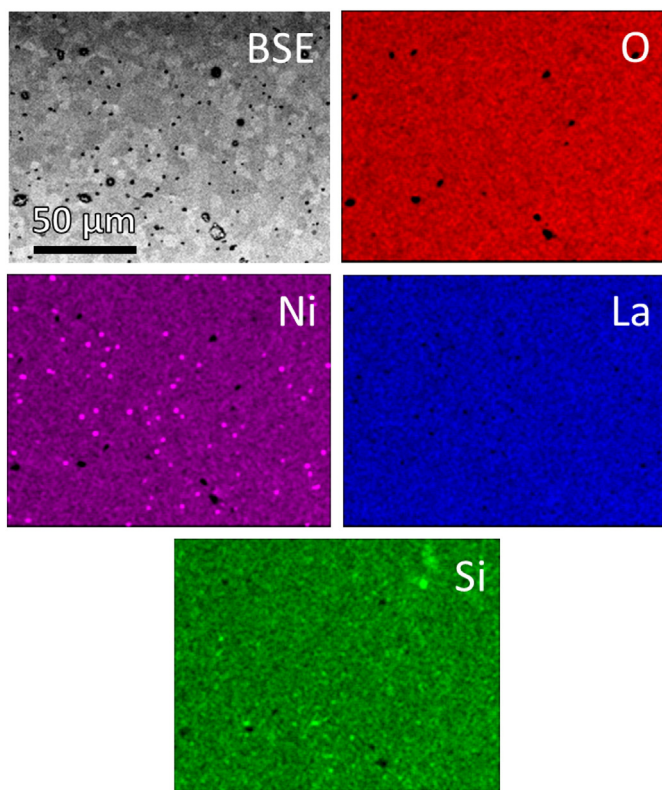
**Fig. 9.** Post-test SEM-BSE image (top left) and SEM-EDXS elemental distribution maps of LNO after degradation at 700 °C in 60% r.h. The width of all images is 155.90 μm.

turned out to be unreliable due to the strong overlap of Cr-peaks with lines of O and La. In addition, the amounts of Cr on degraded LNO determined by XPS-measurements are significantly smaller than for LSC (see Section 3.3).

## 4. Conclusions

The long-term stability against simultaneous Cr- and Si-poisoning of the promising IT-SOFC cathode materials $La_{0.6}Sr_{0.4}CoO_{3-\delta}$ (LSC) and $La_2NiO_{4+\delta}$ (LNO) was investigated at 700 °C in dry and humidified $O_2$/Ar gas streams for more than 3000 h by using dc-conductivity relaxation experiments. The chemical surface exchange coefficient ($k_{chem}$) and the chemical diffusion coefficient ($D_{chem}$) of oxygen were determined as a function of time to monitor the degradation process. At different stages of the experiment, AFM-images of the sample surface were recorded and XPS-depth profiles were measured. In addition, elemental distribution maps of strongly degraded samples were obtained by using SEM-EDXS and SEM-WDXS. The results of the long-term stability measurements show that both materials exhibit excellent stability under dry, Cr-free conditions. In the presence of a Cr- and Si-source, LSC and LNO are fairly stable under dry conditions for a time period of 1000 h. LNO shows a slight decrease in $k_{chem}$ which can be attributed to small quantities of Cr deposited on the surface as confirmed by XPS. However, after the humidification of the gas stream, both compounds experience a severe degradation of the surface exchange reaction, with LSC being slightly stronger affected than LNO. AFM images show the formation of a relatively thick surface layer of large crystals on LSC. In comparison, the Sr-free material LNO forms significantly smaller crystals and exhibits lower amounts of Cr deposited on the surface. It can therefore be concluded that LSC seems to be more susceptible towards Cr-poisoning in a humidified atmosphere than LNO. However, the absence of Sr does not prevent Cr-induced degradation in LNO. Volatile

Si-species released from the quartz glass reactor and deposited on the surface additionally contribute to the decline of the surface exchange rate. Experiments in this work thus simulate the conditions encountered in real SOFC-systems where both Cr- and Si-contaminants are present simultaneously in the gas phase of the cathode side. The deterioration through Cr- and Si-poisoning is significantly intensified in humid atmospheres, due to the coupled effects of segregation of Sr and La from the bulk towards the surface of LSC and LNO, respectively, and increased gas phase transport of volatile Cr- and Si-compounds. Hence, it can be concluded that maintaining dry operating conditions by pre-drying the oxidant flow would be beneficial for improving the long-term stability of SOFC-cathodes.

## Acknowledgments

## References

[1] M. Stanislowski, E. Wessel, K. Hilpert, T. Markus, L. Singheiser, J. Electrochem. Soc. 154 (2007) A295–A306.
[2] S.P. Jiang, X. Chen, Int. J. Hydrog. Energy 39 (2014) 505–531.
[3] E. Konysheva, H. Penkalla, E. Wessel, J. Mertens, U. Seeling, L. Singheiser, K. Hilpert, J. Electrochem. Soc. 153 (2006) A765–A773.
[4] R. Trebbels, T. Markus, L. Singheiser, J. Fuel Cell Sci. Technol. 7 (2009) 011013/1–6.
[5] Z. Wuillemin, A. Nakajo, A. Müller, A.J. Schuler, S. Diethelm, J. Van Herle, D. Favrat, Proc. 11th Intern. Symp. Solid Oxide Fuel Cells (SOFC-XI) 2009, pp. 457–466.
[6] T. Horita, H. Kishimoto, K. Yamaji, M.E. Brito, Y. Xiong, H. Yokokawa, Y. Hori, I. Miyachi, J. Power Sources 193 (2009) 194–198.
[7] M. Backhaus-Ricoult, Solid State Sci. 10 (2008) 670–688.
[8] J.A. Schuler, C. Gehrig, Z. Wuillemin, A.J. Schuler, J. Wochele, C. Ludwig, A. Hessler-Wyser, J. Van Herle, Proc. of the 9th European Solid Oxide Fuel Cell Forum 2010, pp. 7111–7127.
[9] P.J. Howard, I. Szkoda, J. Fuel Cell Sci. Technol. 9 (2012) 041009/1–4.
[10] J.A. Schuler, Z. Wuillemin, A. Hessler-Wyser, J. Van herle, Electrochem. Solid-State Lett. 14 (2011) B20–B22.
[11] N.S. Jacobson, E.J. Opila, D.L. Myers, E.H. Copland, J. Chem. Thermodyn. 37 (2005) 1130–1137.
[12] E.J. Opila, N.S. Jacobson, D.L. Myers, E.H. Copland, JOM 58 (2006) 22–28.
[13] K. Hilpert, D. Das, M. Miller, D.H. Peck, R.R. Weiss, J. Electrochem. Soc. 143 (1996) 3642–3647.
[14] B.B. Ebbinghaus, Combust. Flame 93 (1993) 119–137.
[15] M.M. Viitanen, R.G.v. Welzenis, H.H. Brongersma, F.P.F. van Berkel, Solid State Ionics 150 (2002) 223–228.
[16] H. Yokokawa, N. Sakai, T. Horita, K. Yamaji, in: W. Vielstich, H. Yokokawa, H.A. Gasteiger (Eds.), Handbook of Fuel Cells—Fundamentals, Technology and Applications, John Wiley & Sons, Ltd 2009, pp. 979–991.
[17] D. Oh, E. Armstrong, D. Jung, C. Kan, E. Wachsman, in: S.C. Singhal (Ed.), Proc. 11th Intern. Symp. Solid Oxide Fuel Cells (SOFC-XI), The Electrochemical Society 65 South Main Street, Building D Pennington, NJ 08534-2839, USA, Vienna, Austria 2009, pp. 2871–2879.
[18] I. Kaus, K. Wiik, M. Dahle, M. Brustad, S. Aasland, J. Eur. Ceram. Soc. 27 (2007) 4509–4514.
[19] E. Bucher, W. Sitte, F. Klauser, E. Bertel, Solid State Ionics 191 (2011) 61–67.
[20] E. Bucher, W. Sitte, F. Klauser, E. Bertel, Solid State Ionics 208 (2012) 43–51.
[21] Z. Yang, G. Xia, P. Singh, J.W. Stevenson, J. Power Sources 155 (2006) 246–252.
[22] A.M. Azad, R. Sudha, O.M. Sreedharan, Thermochim. Acta 194 (1992) 129–136.
[23] B.C.H. Steele, Mater. Sci. Eng. B 13 (1992) 79–87.
[24] H.J.M. Bouwmeester, H. Kruidhof, A.J. Burggraaf, Solid State Ionics 72 (1994) 185–194.
[25] W. Preis, M. Holzinger, W. Sitte, Monatsh. Chem. 132 (2001) 499–508.
[26] A. Egger, W. Sitte, F. Klauser, E. Bertel, J. Electrochem. Soc. 157 (2010) B1537–B1541.
[27] E. Bucher, BHM 156 (2011) 423–428.
[28] C. Teichert, Phys. Rep. 365 (2002) 335–432.
[29] Y. Zhao, G.-C. Wang, T.-M. Lu (Eds.), Characterization of Amorphous and Crystalline Rough Surface: Principles and Applications, Academic Press, 2001.
[30] R. Behrisch, W. Eckstein, Sputtering by Particle Bombardment, Topics in Applied Physics, Vol. 110, Springer, Berlin Heidelberg, 2007.
[31] A. Egger, W. Sitte, Solid State Ionics 258 (2014) 30–37.

[32] A.L. Shaula, E.N. Naumovich, A.P. Viskup, V.V. Pankov, A.V. Kovalevsky, V.V. Kharton, Solid State Ionics 180 (2009) 812–816.

[33] P.A.W. van der Heide, Surf. Interface Anal. 33 (2002) 414–425.

[34] S.P. Simner, M.D. Anderson, M.H. Engelhard, J.W. Stevenson, Electrochem. Solid-State Lett. 9 (2006) A478–A481.

[35] R.-R. Liu, Y. Shiratori, T. Oshima, K. Sasaki, Proc. 9th European Solid Oxide Fuel Cell Forum 2010, pp. 7148–7155.

[36] M. Kubicek, A. Limbeck, T. Fromling, H. Hutter, J. Fleig, J. Electrochem. Soc. 158 (2011) B727–B734.

[37] Z. Cai, M. Kubicek, J. Fleig, B. Yildiz, Chem. Mater. 24 (2012) 1116–1127.

[38] L. Zhao, J. Drennan, C. Kong, S. Amarasinghe, S.P. Jiang, ECS Trans. 57 (2013) 599–604.

[39] L. Zhao, J. Drennan, C. Kong, S. Amarasinghe, S.P. Jiang, J. Mater. Chem. A 2 (2014) 11114–11123.

[40] C.C. Wang, T. Becker, K. Chen, L. Zhao, B. Wei, S.P. Jiang, Electrochim. Acta 139 (2014) 173–179.

[41] M.S.D. Read, M.S. Islam, G.W. Watson, F. King, F.E. Hancock, J. Mater. Chem. 10 (2000) 2298–2305.

[42] J. Druce, H. Téllez, M. Burriel, M.D. Sharp, L.J. Fawcett, S.N. Cook, D.S. McPhail, T. Ishihara, H.H. Brongersma, J.A. Kilner, Energy Environ. Sci. 7 (2014) 3593–3599.

[43] S.P. Jiang, S. Zhang, Y.D. Zhen, J. Electrochem. Soc. 153 (2006) A127–A134.

[44] H. Yokokawa, K. Yamaji, M.E. Brito, H. Kishimoto, T. Horita, J. Power Sources 196 (2011) 7070–7075.
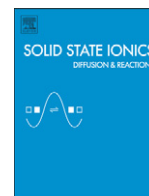
# Phase decomposition in the chromium- and silicon-poisoned IT-SOFC cathode materials La$_{0.6}$Sr$_{0.4}$CoO$_{3-\delta}$ and La$_2$NiO$_{4+\delta}$

Nina Schrödl [a], Edith Bucher [a,*], Christian Gspan [b], Andreas Egger [a], Christian Ganser [c], Christian Teichert [c], Ferdinand Hofer [b], Werner Sitte [a]

[a] Chair of Physical Chemistry, Montanuniversitaet Leoben, Franz-Josef-Straße 18, 8700 Leoben, Austria
[b] Institute for Electron Microscopy and Nanoanalysis (FELMI), Graz University of Technology and Graz Centre for Electron Microscopy (ZFE), Steyrergasse 17, 8010 Graz, Austria
[c] Institute of Physics, Montanuniversitaet Leoben, Franz-Josef-Straße 18, 8700 Leoben, Austria

## ARTICLE INFO

## ABSTRACT

Chromium- and silicon-poisoned samples of the intermediate temperature solid oxide fuel cell (IT-SOFC) cathode materials La$_{0.6}$Sr$_{0.4}$CoO$_{3-\delta}$ (LSC) and La$_2$NiO$_{4+\delta}$ (LNO) were investigated by transmission electron microscopy (TEM) with energy dispersive X-ray spectroscopy (EDXS), electron energy loss spectroscopy (EELS), convergent beam electron diffraction (CBED), as well as by atomic force microscopy (AFM). Analytical TEM revealed phase decomposition of the original, oxygen exchange-active materials LSC and LNO, and the formation of secondary phases after 3500 h of testing at 700 °C. In the case of LSC, the phases SrCrO$_4$, Co$_3$O$_4$, and CoCr$_{2-x}$Co$_x$O$_4$ as well as a La-chromate phase with unknown stoichiometry were found in the near-surface region and at the grain boundaries. Transport of cations, especially Sr and Cr, along the grain boundaries seems to play a key role in the degradation of LSC. AFM was used to determine the three-dimensional shape including interplanar facet angles of SrCrO$_4$ crystallites. In the case of the Sr-free material LNO, the formation of La-silicate and La-Ni-chromate phases was observed, which seems to proceed from the surface toward the bulk. Based on the experimental results, tentative mechanisms for the degradation processes are suggested.

© 2016 Elsevier B.V. All rights reserved.

## 1. Introduction

The mixed conducting perovskite La$_{0.6}$Sr$_{0.4}$CoO$_{3-\delta}$ (LSC) and the K$_2$NiF$_4$-type oxide La$_2$NiO$_{4+\delta}$ (LNO) are considered as promising cathode materials for intermediate temperature solid oxide fuel cells (IT-SOFC) due to their fast oxygen exchange kinetics at temperatures in the range of 600–800 °C [1–6]. The reduced operating temperatures of IT-SOFCs allow the use of less expensive and mechanically more stable metallic interconnects, compared to the ceramic interconnects employed in high temperature SOFCs. However, chromium poisoning, caused by the release of volatile Cr-species from metallic components in SOFC stacks, has been identified as an important degradation mechanism limiting the life-time of IT-SOFC cathodes. Diffusion barriers applied as coatings or formed in situ on interconnects have been found to reduce the release of Cr-compounds but not to eliminate it completely [7,8]. In addition, the release of Si-species from silicate-based sealing materials that are necessary for the separation of fuel and oxidant gases in SOFC stacks may cause similar degradation, especially in the presence of humidity. Previous investigations showed that both Cr- and Si-poisoning affect the cathode materials by forming electrically insulating secondary phases and changing the local surface

composition [9,10]. In a recent study, the effects of combined Cr- and Si-poisoning on the long-term stability of LSC and LNO were investigated at 700 °C using the dc-conductivity relaxation (CR) method while exposing the samples to a Cr- and a Si-source in dry and humid atmospheres [11]. By monitoring the chemical surface exchange coefficient ($k_{chem}$) of oxygen with time, the detrimental effects of combined Cr- and Si-poisoning were found to be especially severe under humid conditions due to the enhanced gas phase transport of volatile Si- and Cr-species. At 700 °C, both materials exhibited a significant decrease of $k_{chem}$ over a period of 3500 h. Post-test analysis using atomic force microscopy (AFM) showed an increase in surface roughness compared to freshly polished samples due to the formation of small crystallites on the surface. X-ray photoelectron spectroscopy (XPS) combined with depth profiling revealed that the newly formed crystallites contain significant amounts of Cr. Additionally, elemental mappings generated using scanning electron microscopy with energy and wavelength dispersive X-ray analysis (SEM-EDXS, SEM-WDXS) confirmed the presence of Si-containing phases on LSC and LNO [11].

The current study presents new results on the phase decomposition and secondary phase formation in LSC and LNO after long-term degradation due to exposure to Si-/Cr-containing atmospheres at 700 °C. The identification of the secondary phases and their spatial distribution in the near-surface region was performed by analytical transmission electron microscopy (TEM) using electron energy loss spectroscopy

(EELS), energy dispersive X-ray spectroscopy (EDXS), and convergent beam electron diffraction (CBED). Three-dimensional shape analysis of secondary phase crystals was made by AFM. Based on these results, degradation mechanisms for LSC and LNO are suggested.

## 2. Experimental

### 2.1. Sample preparation and previous degradation studies

$La_{0.6}Sr_{0.4}CoO_{3-\delta}$ (LSC) and $La_2NiO_{4+\delta}$ (LNO) powders obtained from EMPA (Dübendorf, Switzerland) and Treibacher Industrie AG (Althofen, Austria) were pressed into cylindrical pellets. The LSC tablet was sintered for 10 h at 1200 °C in air. The LNO pellet was sintered twice for 10 h at 1350 °C in air to obtain the required density. Heating and cooling rates of 2 K min$^{-1}$ were used for both LSC and LNO. The sintered tablets with relative densities of above 95% were cut into square slabs and subsequently polished to a mirror finish. The gold contacted samples were annealed at 700 °C in a quartz-glass reactor acting as Si-source with and without the presence of chromium in dry and humid $O_2$-Ar gas atmospheres for time periods of 1000 h for each step. The effects of the progressing degradation on the oxygen exchange kinetics were monitored via the chemical surface exchange coefficient of oxygen, which was determined by means of dc-conductivity relaxation measurements. The chemical and morphological changes of the sample surface at different stages in the degradation process were studied using XPS, SEM-EDXS, and AFM. Further details on the sample preparation and other experimental details can be found in an earlier publication [11].

### 2.2. Transmission electron microscopy (TEM)

A TEM lamella was prepared with the Focused Ion Beam (FIB) NOVA 200 Nanolab dual beam microscope. Investigations on the TEM were performed both on an FEI Tecnai F20 (operating at 200 kV) and an FEI Titan$^3$ G2 60–300 (operating at 300 kV). The Titan$^3$ G2 has a $C_S$ probe corrector (DCOR) for high-resolution STEM imaging with a sub-Ångström resolution and is equipped with a high-end post-column electron energy filter (GIF Quantum ERS™) from Gatan Inc. For analytical investigations, EDXS and EELS measurements were performed on the Tecnai F20 and the Titan$^3$ G2. For EDXS quantification, the spectra from the Tecnai F20 and for the elemental mapping the EDX and EEL spectra from the Titan$^3$ G2 were used. Results from convergent beam electron diffraction (CBED) experiments were compared with CBED simulations calculated with the software package JEMS [12].

### 2.3. Atomic force microscopy (AFM) and crystal facet analysis

The surface morphology of the degraded electrodes was analyzed using AFM under ambient conditions [11]. The three-dimensional imaging capabilities of AFM were employed to obtain information [13,14] on facet orientation of well-developed crystallites formed on the surface of degraded LSC. For this purpose, small-scale AFM images of a selected micrometer-sized, randomly oriented crystallite were recorded using high-resolution AFM tips (Olympus AC160 with tip radius of 9 ± 2 nm). Angles between the crystal facets were determined using the AFM image analysis software Gwyddion [15]. The procedure involves plotting the density of the surface normals on a two-dimensional map with azimuthal and polar angles in a polar coordinate system. The facets of preferentially occurring orientations are identified in the map and the interplanar angles are calculated using the average surface normals of each facet. The surface normals were averaged over a region of ± 5° in both angles. On the basis of the interplanar angles, the facets were assigned to faces of the assumed crystal structure.

## 3. Results and discussion

### 3.1. Phase decomposition of LSC

TEM investigations were performed on a dense sample of LSC, which was exposed to a Cr- and Si-source at 700 °C for 1000 h in dry $O_2$-Ar atmosphere, 1000 h in $O_2$-Ar with 30% relative humidity (r.h.) and additional 1000 h in $O_2$-Ar with 60% r.h. Previous CR measurements showed a significant decrease in $k_{chem}$ during 3500 h of testing, which could be correlated to changes in the surface chemical composition and microstructure [11]. Fig. 1a shows the TEM bright-field image of a cross section of the near-surface region of the degraded LSC after 3500 h. EFTEM elemental distribution maps of La and Cr indicate that the topmost layer of crystallites contains significant amounts of Cr, but no La. This is in good agreement with previous SEM-EDXS results indicating the formation of a Sr- and Cr-rich top layer in humid and Cr-containing atmospheres [11]. The resulting layer of Sr-Cr-O crystallites exhibits a thickness of up to 600 nm, as determined by TEM in agreement with previous XPS depth profiling results [11]. To obtain the actual chemical composition, the Sr-Cr-O crystallites were analyzed using EDXS. In Fig. 1b, a STEM-HAADF image of a Sr-Cr-O crystallite is depicted. EDXS spectra confirm the presence of $SrCrO_4$ (1) on top of the LSC matrix (2). The formation of $SrCrO_4$ on LSC and similar Sr-containing perovskites under Cr-poisoning conditions is also well documented in the literature [7,16–18] and is supported by thermodynamic calculations [19,20].

The structure of the $SrCrO_4$ crystals was further analyzed using convergent beam electron diffraction (CBED). In Fig. S1a (Supplementary material), the CBED pattern of a $SrCrO_4$ crystal in zone axis [−111] is depicted, which shows good agreement with the simulated CBED pattern of monazite-type $SrCrO_4$ (SG 14: $P2_1/n$, ICSD #40,922) in Fig. S1b. The interplanar facet angles of a $SrCrO_4$-crystallite were determined by facet analysis of an AFM image shown in Fig. 2a. The facets could be assigned to low-index crystal faces based on calculations using crystal structure data of $SrCrO_4$ as determined by CBED. The faces (-1,-1,0), (-1,-1,2), (1,-2,0), and (1,-2,-1) (Fig. 2b) give the closest match to experimental angles within the index range of $-2 \leq h, k, l \leq +2$ (see Table S1 for details; Supplementary material).

A STEM-HAADF cross-sectional image of the near-surface region of degraded LSC is depicted in Fig. 3a. The Z-contrast of this imaging mode indicates the formation of different secondary phases at the surface and at the grain boundaries. The white frame marks a magnified area showing several different decomposition products of LSC. Fig. 3b displays a distribution map of the formed secondary phases, which were identified by quantification of their corresponding EDX spectra as $SrCrO_4$ (red), $La_xCr_yO_z$ (blue), $Co_3O_4$ (light green), $CoCr_{2-x}Co_xO_4$ (dark green), and LSC (lilac). Table S2 (Supplementary material) shows the chemical composition for each phase in atomic percent, as determined by quantification of the corresponding EDX spectra, with the exception of $La_xCr_yO_z$ (quantification of the stoichiometry was not possible). This is in good agreement with thermodynamic calculations [19], which predict $SrCrO_4$, $Co_3O_4$, $CoCr_2O_4$, $LaCrO_3$, and $La_{1-x}Sr_xCoO_3$ ($x < 0.4$) as the secondary phases formed under the given experimental conditions.

Similar to results of a previous study on the phase decomposition of LSC under $SO_2$-poisoning conditions [21], the Cr-related degradation of the LSC perovskite phase appears to start at the surface and at the grain boundaries. Previous investigations also showed that the phase decomposition of LSC is preceded by the segregation of Sr to the surface [11], leaving a Sr-poor and La-enriched layer of LSC underneath. A-site cation segregation to the surface of perovskite-type mixed conductors is a well-known phenomenon and has been reported in various studies [16,22–31], but the role that grain boundaries play in this process is not yet clear. To gain further insight into the decomposition behavior at the grain boundaries, EELS and EDXS line profiles across a region showing phase decomposition at a selected grain boundary of the
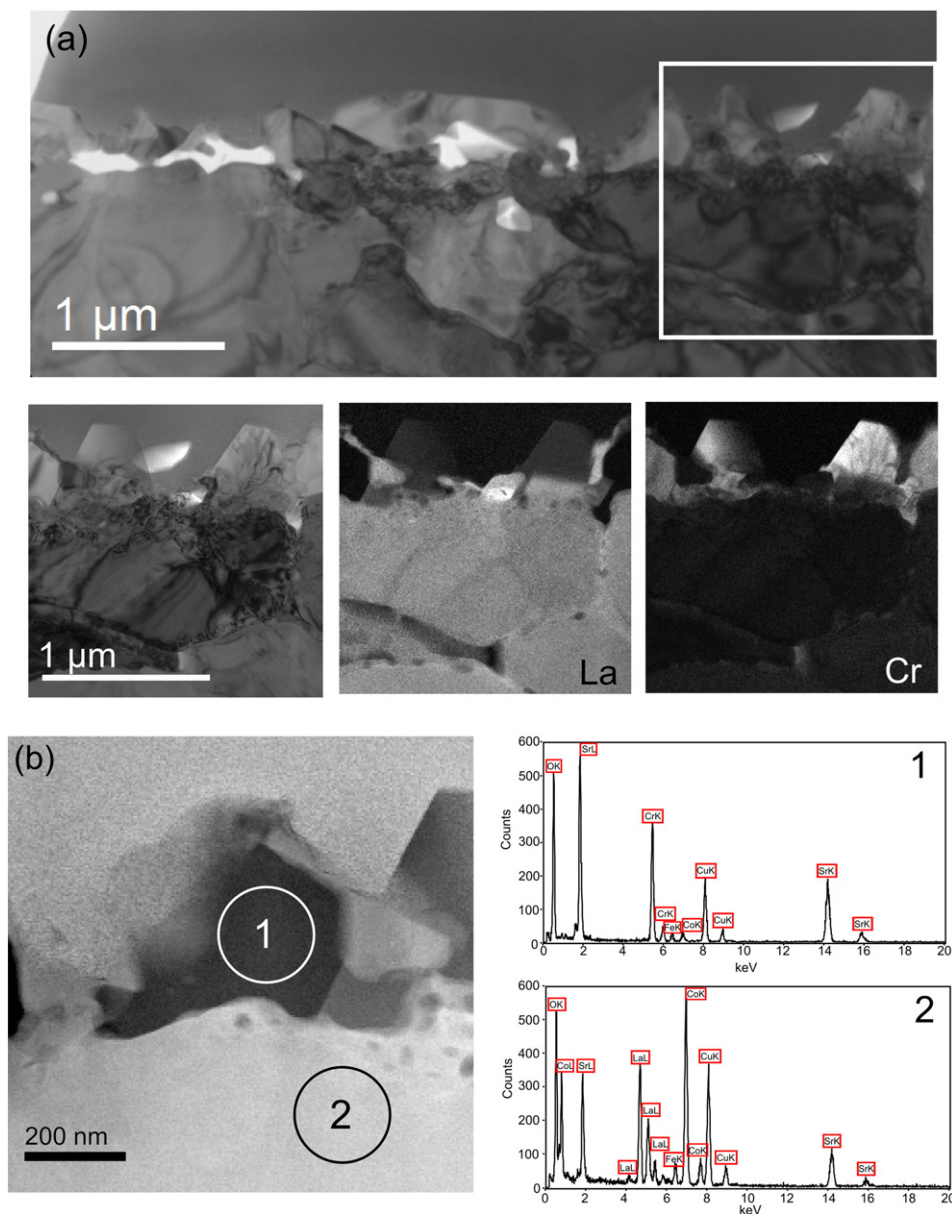
**Fig. 1.** (a) TEM bright-field image of the degraded LSC near-surface region and corresponding EFTEM elemental distribution maps from the region marked by the white rectangle. (b) STEM-HAADF image of the degraded LSC surface with EDX spectra of regions (1) $SrCrO_4$ and (2) LSC matrix; the weak Fe and Cu signals in the spectra originate from the microscope and the sample holder, respectively.

degraded LSC were acquired (Fig. 4). In the vicinity of the $SrCrO_4$ secondary phase formed at the grain boundary interface, a Sr-depleted and La-rich region was found. The results suggest that Sr, which accumulates at the surface and at grain boundaries, reacts with Cr and that the grain boundaries also act as a pathway for the diffusion of Cr from the surface toward the bulk. Chromium was found down to depths of 600–700 nm in the dense, degraded LSC sample after 3500 h at 700 °C [11], which indicates that the Cr transport from the surface to deeper regions of the sample occurs by diffusion. STEM-EDXS and STEM-EELS analyses show that chromium is enriched at the grain boundaries (see Figs. 3 and 4), which indicates that Cr diffusion occurs preferentially along the grain boundaries. To the authors' knowledge, grain boundary diffusion coefficients for Cr in LSC are not available in the literature. However, a number of studies on A- and B-site diffusion coefficients in similar perovskites have been performed, which confirmed that grain boundaries act as fast transport pathways for cations, including Cr.

Sakai et al. [32] measured Sr, Ca, and Cr tracer diffusion coefficients in $La_{0.95}Sr_{0.05}CrO_3$ and $La_{0.75}Ca_{0.25}CrO_3$ at 1000 °C by secondary ion mass spectrometry (SIMS). In both materials, the grain boundary diffusion coefficient of Cr was found to be approximately one order of magnitude higher than the bulk diffusion coefficient. However, the grain boundary diffusion coefficients of Sr-Ca interdiffusion or Ca diffusion were even higher. In a later study, Sakai et al. [33] determined tracer diffusion coefficients of Ca and Cr in $(La,Ca)CrO_3$ at 900 °C. In this study, the grain boundary diffusivity of Cr was found to be $10^4$–$10^5$ times higher than the bulk diffusivity. Wærnhus et al. [34] measured A- and B-site impurity tracer diffusion coefficients in $La_{1-x}Sr_xFeO_{3-\delta}$ ($x = 0$ and 0.1) at 900–1100 °C by SIMS using $Y^{3+}$ and $Cr^{3+}$ tracer ions, respectively. The grain boundary diffusion coefficients were by a factor of $10^5$ higher than the bulk diffusion coefficients. Cr (B-site impurity) diffusion was found to be faster than Y (A-site impurity) diffusion. Recently, Kubicek et al. [35] investigated Sr, Fe, and Sm diffusion in LSC thin films on YSZ
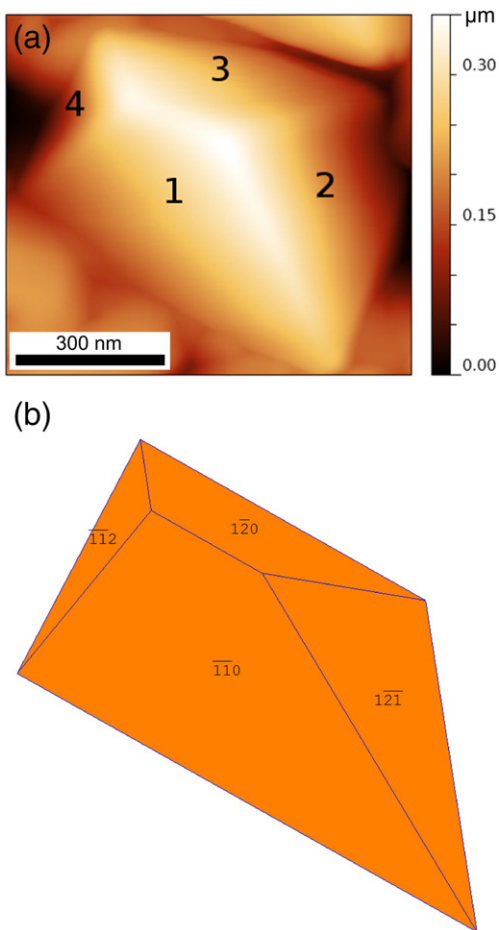
Fig. 2. (a) AFM image of a SrCrO$_4$ crystal on the surface of degraded LSC and (b) model of a SrCrO$_4$ single crystal with indexed faces (see Table S1 (Supplementary material) for details).



Fig. 3. (a) STEM-HAADF cross-sectional image of degraded LSC. (b) EDXS analyses show the distribution of secondary phases at the surface and at grain boundaries. Identified phases are (1) SrCrO$_4$ (red), (2) La$_x$Cr$_y$O$_z$ (blue), (3) Co$_3$O$_4$ (light green) and (4) CoCr$_{2-x}$Co$_x$O$_4$ (dark green), and (5) LSC matrix (lilac).

at 625–800 °C by time of flight-secondary ion mass spectrometry (ToF-SIMS). Grain boundary diffusion of A- and B-site cations was found to be about 10$^3$ times faster than their respective bulk diffusion. The highest diffusion coefficients were found for B-site Fe/Co interdiffusion, followed by those of the A-site cations Sr and Sm/La. Kishimoto et al. [36] studied interdiffusion between Co and Fe in La$_{0.8}$Sr$_{0.2}$CoO$_3$ (LSC82) and La$_{0.8}$Sr$_{0.2}$FeO$_3$ (LSF82) at 800–1100 °C. At 1000 °C Fe diffusion into the LSC82 was found to occur mainly via the grain boundaries.

As a consequence of the decomposition of the perovskite phase LSC, a number of other binary and ternary oxides and Cr-containing phases are formed in addition to SrCrO$_4$. The presence of the cobalt spinel Co$_3$O$_4$ was confirmed via EDXS quantification (Table S2; Supplementary material) and is shown in light green color in Fig. 3b. As the degradation of LSC progresses, Co$_3$O$_4$ incorporates Cr into its structure to form a mixed CoCr$_{2-x}$Co$_x$O$_4$ spinel [37], depicted in the dark green regions in Fig. 3b. Formation of a spinel secondary phase is also supported by thermodynamic calculations based on data available for stoichiometric CoCr$_2$O$_4$ [19]. However, EDXS quantification indicates the formation of the mixed Co-Cr-spinel with the composition CoCr$_{2-x}$Co$_x$O$_4$ (see Table S2; Supplementary material) [37].

Considering that the analyzed LSC sample was also exposed to volatile Si-species during the investigation of its long-term stability, it is to be expected that small amounts of Sr-La-silicates are formed under the applied experimental conditions, in analogy to results from similar studies [10,38,39]. However, Si was not identified in any of the recorded EDX spectra. Since the detection of small amounts of Si in a
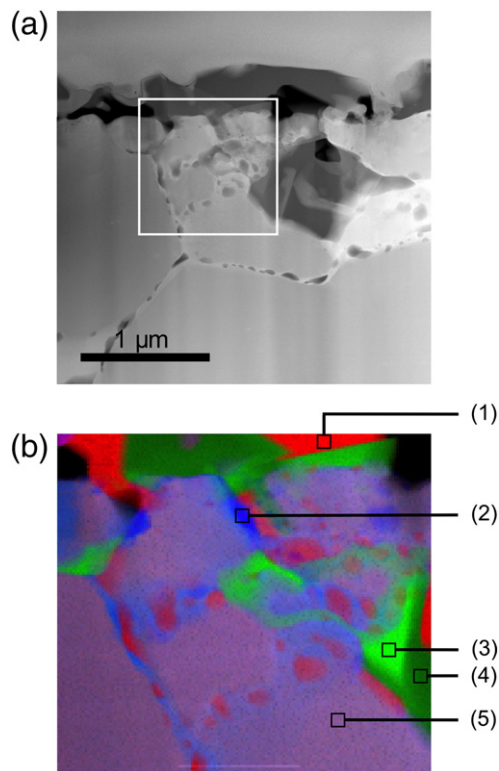
Sr-containing matrix by EDXS is difficult due to an overlap of the Sr L-lines with Si K-lines, EFTEM was applied to acquire an elemental distribution map of Si, but Si was not found in the EFTEM image either. However, elemental distribution mapping using scanning electron microscopy with wavelength dispersive X-ray spectroscopy indicated the presence of Si in form of insular patches across the LSC sample surface [11].

The formation of Cr-containing decomposition products on the surface and grain boundaries has a detrimental effect on the oxygen exchange kinetics of LSC. As a result of combined Cr-/Si-poisoning under humid conditions, the chemical surface exchange coefficient of oxygen decreased by a factor 250 [11]. In addition to impeding oxygen exchange at active surface sites of the material, the formed secondary phases also exhibit poor electrical conductivity (SrCrO$_4$: $1.5 \times 10^{-5}$ S cm$^{-1}$ at 700 °C and pO$_2$ = 0.21 bar [40], LaCrO$_3$: 0.89 S cm$^{-1}$ at 700 °C in air [41], Co$_3$O$_4$: below 1 S cm$^{-1}$ for $T > 700$ °C [42], CoCr$_{2-x}$Co$_x$O$_4$: 0.01 S cm$^{-1}$ at 700 °C [43]) in comparison to LSC (1900 S cm$^{-1}$ at 700 °C and pO$_2$ = 0.10 bar [44]). Preis et al. demonstrated that electrically blocking grain boundaries, which may be formed by impurities penetrating the cathode along the grain boundaries, lead to a significant increase of the area specific resistance (ASR) of a porous cathode [45]. Therefore, with respect to the application of LSC as SOFC cathode material, the ASR of cells is expected to increase dramatically.

### 3.2. Phase decomposition of LNO

Previous investigations of LNO treated for 1000 h in dry and additional 2000 h in humid O$_2$-Ar atmospheres (30–60% r.h.) containing volatile Cr- and Si-species revealed an LNO surface covered with small crystallites of irregular shapes [11]. The presence of significant amounts
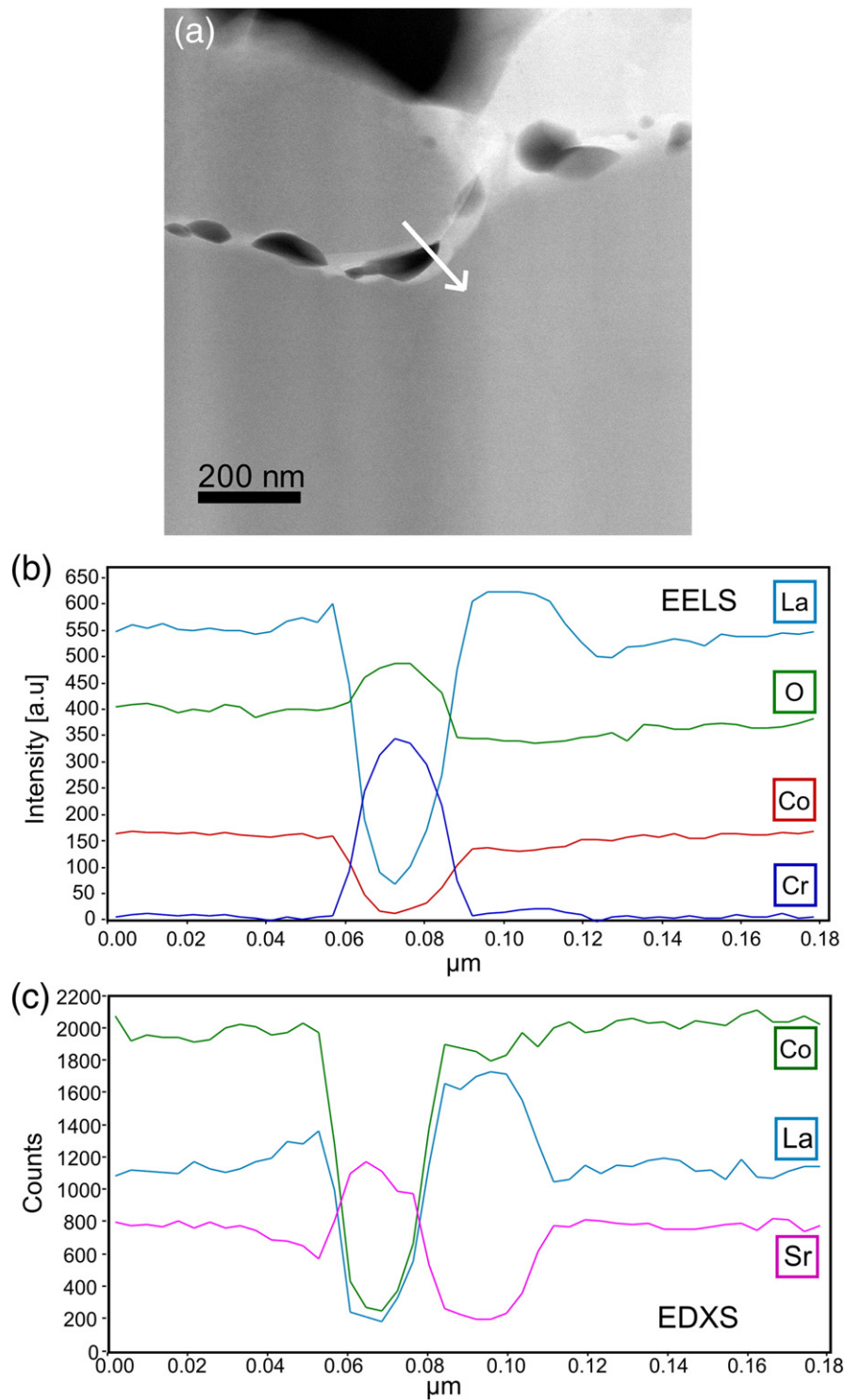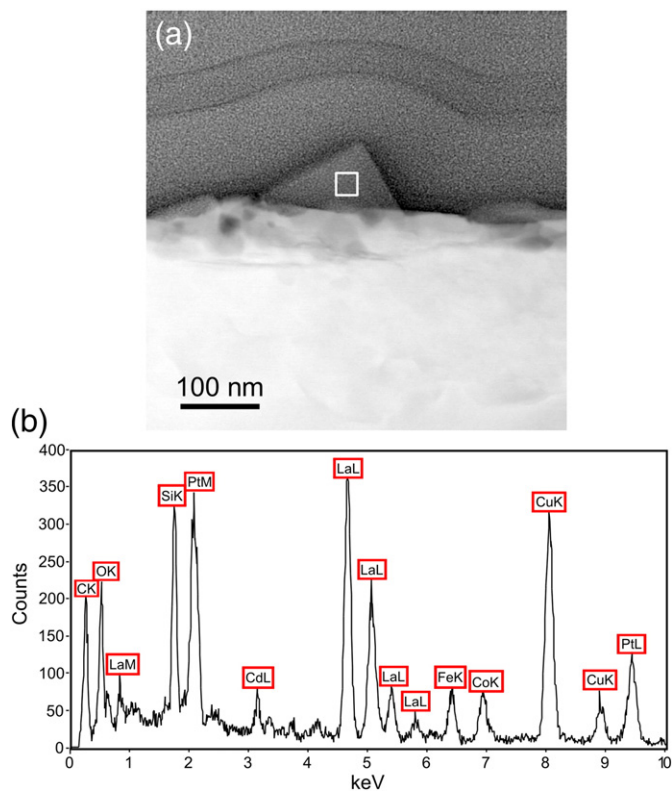
**Fig. 4.** (a) STEM-HAADF cross-sectional image of degraded LSC; (b) EELS and (c) EDXS line profiles across a selected grain boundary of LSC (marked by the white arrow in image a).

of Cr and Si on the sample surface was confirmed by XPS and SEM-EDXS. The Cr-content was found to decrease with increasing depth [11]. Thermodynamic modeling of the system La-Ni-Cr-O-H at 700 °C suggests the formation of $LaCrO_3$ [19]. A STEM-HAADF image of the degraded LNO sample surface reveals an approximately 100 nm thick degraded near-surface region (Fig. 5a). According to EDXS analysis the small, faceted crystallite on top is composed mainly of La and Si

(Fig. 5b). Small amounts of Cd-impurities are introduced via the gold paste used for contacting the sample for conductivity relaxation measurements. Pt-peaks are a result of the applied coating on top of the sample surface for the FIB process. EDXS analysis of the underlying layer shows a secondary phase containing La, Ni, and O, as well as small amounts of Si, but no Cr (Fig. 6a and b). At this point, it should be mentioned that the detection of Cr-impurities using EDXS in

**Fig. 5.** (a) STEM-HAADF cross-sectional image showing secondary phases on degraded LNO; (b) EDXS analysis from the region marked by the white rectangle in image a confirms the presence of Si, La, and O; the weak Fe and Cu signals in the EDX spectrum originate from the microscope and the sample holder, respectively.

former XPS results, which show a continuous increase of Ni-content and the decrease in Cr-content with increasing sputter depth [11]. The elemental distribution of La, Cr, Ni, and O within this degraded region might suggest the formation of a mixed $LaCr_{1-x}Ni_xO_3$ perovskite phase, where Cr is partially replaced by Ni cations on the B-site in the $ABO_3$ perovskite structure [46].

Based on the present results, the following degradation mechanism for LNO under Cr- and Si-poisoning conditions is proposed. Long-term treatment in dry $O_2$-Ar atmosphere at 700 °C leads to La enrichment on the surface [11], leaving probably La depleted, Ni-rich Ruddlesden–Popper phases like $La_3Ni_2O_{7-\delta}$ and $La_4Ni_3O_{10-\delta}$ [47] underneath. Similar surface enrichment of cations on the A-site in $K_2NiF_4$-type rare earth nickelates was found in earlier investigations by our group [48,49] and has also been reported by other authors [50–52]. Volatile Cr- and Si-species are released in significant amounts under humid conditions from Cr- and Si-sources and are transferred to the sample via gas phase transport where they react with the La-enriched surface to form La-silicates and La-chromates. The rather continuous decrease in Cr content toward the bulk [11] is consistent with the proposed formation of $La(Cr,Ni)O_3$ as reaction product since this compound is known to form a solid solution over the entire B-site composition range [46].
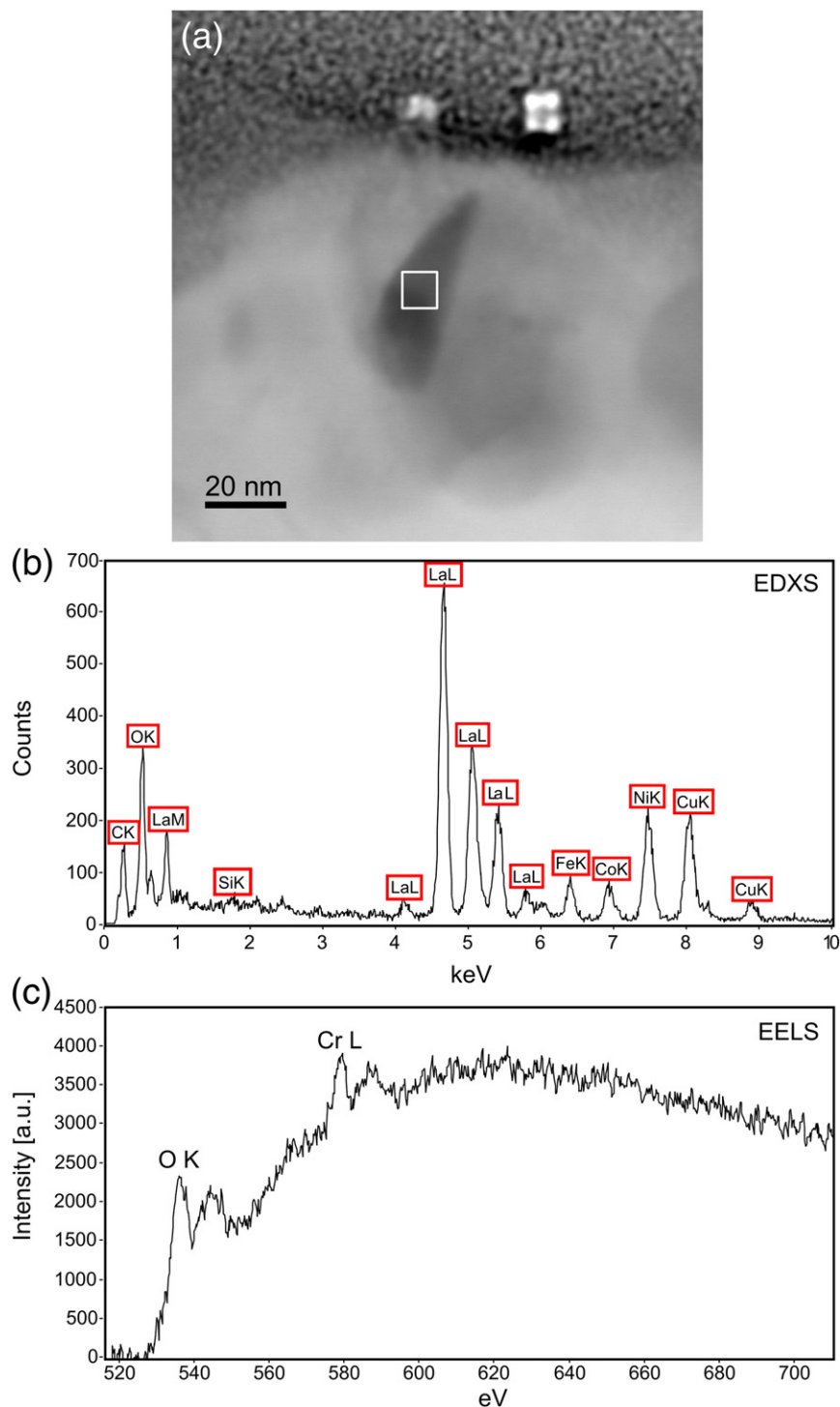
According to Čebašek et al., the diffusion of A-site cations in LNO is bulk diffusion dominated [53,54], thus indicating that – unlike Sr in LSC (compare results in section 3.1 of the present study and the literature [55]) – La does not show enhanced grain boundary diffusion in LNO. The resulting lower rate of La surface segregation could also be the reason for the relatively thin degradation layer on LNO, compared to LSC degraded under similar conditions.

As discussed above for LSC, the oxygen-exchange-active surface sites of the degraded LNO are no longer exposed to the gas due to the decomposition of the surface and the formation of Cr- and Si-containing phases. This is expected to have a detrimental impact on the surface oxygen exchange rate. Indeed, a significant decrease of the chemical surface exchange coefficient of oxygen by a factor of 230 was observed for LNO by Cr-/Si-poisoning at 700 °C in humid atmospheres [11].

## 4. Conclusions

In previous investigations, $La_{0.6}Sr_{0.4}CoO_{3-\delta}$ (LSC) and $La_2NiO_{4+\delta}$ (LNO) samples tested for 3500 h at 700 °C in the presence of chromium and silicon sources showed a strong decrease of the surface exchange activity of oxygen [11]. In order to get more insight into the degradation mechanisms of LSC and LNO, detailed analytical investigations by TEM and AFM were performed on the Cr- and Si-poisoned samples. It could be shown that the long-term degradation of the oxygen exchange kinetics of LSC is a result of the phase decomposition in the near-surface region. The secondary phases $SrCrO_4$, $La_xCr_yO_z$, $CoCr_{2-x}Co_xO_4$, and $Co_3O_4$ were found. In comparison to LSC, these compounds exhibit poor electrical conductivity and low to negligible activity for oxygen exchange. The TEM analysis of the lateral distribution of the secondary phases in LSC indicates that the phase decomposition takes place at the grain boundaries, which also act as fast transport path for cations (including Cr). In the degraded LNO sample, TEM shows the formation of La-silicate and La-chromate phases. In contrast to LSC, no enrichment of secondary phases was found at the grain boundaries of LNO. Rather, the degradation of LNO appears to proceed homogeneously from the sample surface to the interior, probably caused by the formation of a $La(Cr,Ni)O_3$ perovskite of variable B-site composition.

These results are also of interest for the long-term stability of LSC, LNO, and similar mixed conducting oxides in various applications (SOFC or SOEC air electrodes, oxygen permeable membranes, etc.). The segregation of A-site elements (Sr and/or La) toward the surface and grain boundaries is a major driver for the degradation due to the strong affinity of these elements toward reaction with impurities. Therefore, an improvement of the long-term stability could be reached

materials containing La is difficult due to an overlap between La and Cr peaks in the energy spectrum. Therefore, the more sensitive EEL spectroscopy was applied for the detection of Cr impurities. In Fig. 6c, an EEL spectrum of the area outlined by a white frame in Fig. 6a confirms the presence of Cr. Elemental distribution mapping on a different part of the degraded layer (see Fig. S2, Supplementary material) confirms that Si-deposits are located on top of the surface and that the Cr-level decreases, whereas the Ni-content increases from the surface toward the bulk, which is in good agreement with the previous XPS analysis [11]. The actual chemical composition of the decomposed layer, however, could not be determined by EDXS or EELS due to the small crystallite size.

In Fig. 7a, a STEM-HAADF image of a larger part of the decomposed near-surface zone reveals a degraded layer of 100–250 nm thickness. This is in good agreement with results from XPS depth profiling, where Cr is found to be present within a surface zone of approximately 150 nm thickness [11]. The round-shaped grain in the bottom left corner of the image is a Zr-O inclusion caused by the abrasion of $ZrO_2$ grinding balls during sample preparation. To gain more insight into the distribution of the elements, STEM-HAADF distribution maps of La, Ni, O, Cr, and Si were acquired using EDXS and EELS data (Fig. 7b). Silicon was found to be distributed in insular patches and, with few exceptions, on the very top of the degraded layer, which consists of Cr, O, Ni, and La. La as well as O are present in both, the Si-containing and the Cr-containing regions, which indicates the formation of La-silicate and La-chromate phases with a yet undetermined stoichiometry. Cr-rich areas appear to be depleted of Ni, whereas the Ni-containing zones seem to contain only small amounts of Cr (Fig. 7b), again confirming

Fig. 6. (a) STEM-HAADF cross-sectional image of a near-surface zone on degraded LNO; (b) EDX spectrum from the region marked by the white rectangle in image a confirming the elements La, Ni, O, and small amounts of Si; (c) EEL spectrum from the same area showing small quantities of Cr which are not detected by EDXS.

either by the prevention of Sr-/La-segregation or by the reduction of the Cr- and Si-content in the gas phase.
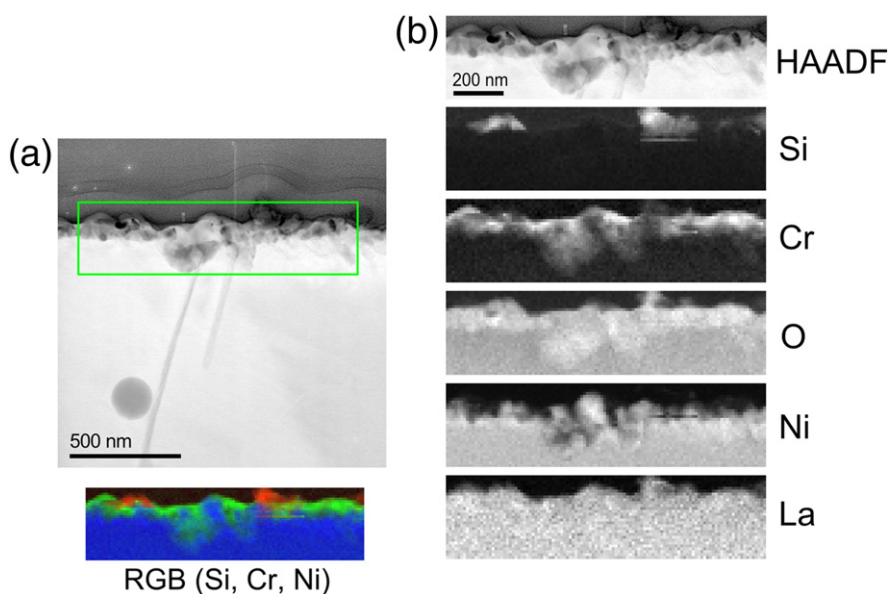
## Appendix A. Supplementary data

Supplementary data to this article can be found online at http://dx.doi.org/10.1016/j.ssi.2016.01.006.

**Fig. 7.** (a) STEM-HAADF cross-sectional image of degraded LNO; Si, Cr, and Ni distribution are indicated by red, green, and blue, respectively. (b) HAADF image and elemental distribution maps from the zone marked in panel a; Si, La, O, and Ni distribution maps were derived from EDX, and the Cr-map was determined from EEL spectra.

## References

[1] J. Januschewsky, M. Stöger-Pollach, F. Kubel, G. Friedbacher, J. Fleig, Z. Phys. Chem. 226 (2012) 889–899.
[2] J. Januschewsky, M. Ahrens, A. Opitz, F. Kubel, J. Fleig, Adv. Funct. Mater. 19 (2009) 3151–3156.
[3] C. Peters, A. Weber, E. Ivers-Tiffee, J. Electrochem. Soc. 155 (2008) B730–B737.
[4] A. Egger, E. Bucher, M. Yang, W. Sitte, Solid State Ionics 225 (2012) 55–60.
[5] E. Boehm, J.M. Bassat, P. Dordor, F. Mauvy, J.C. Grenier, P. Stevens, Solid State Ionics 176 (2005) 2717–2725.
[6] F. Mauvy, C. Lalanne, J.M. Bassat, J.C. Grenier, H. Zhao, P. Dordor, P. Stevens, J. Eur. Ceram. Soc. 25 (2005) 2669–2672.
[7] E. Konysheva, H. Penkalla, E. Wessel, J. Mertens, U. Seeling, L. Singheiser, K. Hilpert, J. Electrochem. Soc. 153 (2006) A765–A773.
[8] R. Trebbels, T. Markus, L. Singheiser, J. Fuel Cell, Sci. Technol. 7 (2009) 011013/1–011013/6.
[9] T. Horita, H. Kishimoto, K. Yamaji, M.E. Brito, Y. Xiong, H. Yokokawa, Y. Hori, I. Miyachi, J. Power Sources 193 (2009) 194–198.
[10] M.M. Viitanen, R.G.v. Welzenis, H.H. Brongersma, F.P.F.v. Berkel, Solid State Ionics 150 (2002) 223–228.
[11] N. Schrödl, E. Bucher, A. Egger, P. Kreiml, C. Teichert, T. Höschen, W. Sitte, Solid State Ionics 276 (2015) 62–71.
[12] P.A. Stadelmann, Ultramicroscopy 21 (1987) 131–145.
[13] M.A. Lutz, R.M. Feenstra, P.M. Mooney, J. Tersoff, J.O. Chu, Surf. Sci. 316 (1994) L1075–L1080.
[14] C. Teichert, Phys. Rep. 365 (2002) 335–432.
[15] D. Nečas, P. Klapetek, Cent. Eur. J. Phys. 10 (2012) 181–188.
[16] C.C. Wang, T. Becker, K. Chen, L. Zhao, B. Wei, S.P. Jiang, Electrochim. Acta 139 (2014) 173–179.
[17] J.A. Schuler, H. Yokokawa, C.F. Calderone, Q. Jeangros, Z. Wuillemin, A. Hessler-Wyser, J. Van Herle, J. Power Sources 201 (2012) 112–120.
[18] J.W. Fergus, Int. J. Hydrog. Energy 32 (2007) 3664–3671.
[19] FactSage© 6.4, thermodynamic software package, © 1976–2013 Thermfact and GTT Technologies.
[20] H. Yokokawa, T. Horita, N. Sakai, K. Yamaji, M.E. Brito, Y.P. Xiong, H. Kishimoto, Solid State Ionics 177 (2006) 3193–3198.
[21] E. Bucher, C. Gspan, W. Sitte, Solid State Ionics 272 (2015) 112–120.
[22] D. Oh, E. Armstrong, D. Jung, C. Kan, E. Wachsman, Proc. 11th Intern. Symp. Solid Oxide Fuel Cells (SOFC-XI) edited by S.C. SinghalVienna, Austria, 2009 2871–2879.
[23] E. Bucher, W. Sitte, F. Klauser, E. Bertel, Solid State Ionics 191 (2011) 61–67.
[24] E. Bucher, W. Sitte, F. Klauser, E. Bertel, Solid State Ionics 208 (2012) 43–51.
[25] P.A.W. van der Heide, Surf. Interface Anal. 33 (2002) 414–425.
[26] S.P. Simner, M.D. Anderson, M.H. Engelhard, J.W. Stevenson, Electrochem. Solid-State Lett. 9 (2006) A478–A481.
[27] R.-R. Liu, Y. Shiratori, T. Oshima, K. Sasaki, Proc. 9th European Solid Oxide Fuel Cell Forum, 2010 7148–7155.
[28] M. Kubicek, A. Limbeck, T. Frömling, H. Hutter, J. Fleig, J. Electrochem. Soc. 158 (2011) B727–B734.
[29] Z. Cai, M. Kubicek, J. Fleig, B. Yildiz, Chem. Mater. 24 (2012) 1116–1127.
[30] L. Zhao, J. Drennan, C. Kong, S. Amarasinghe, S.P. Jiang, ECS Trans. 57 (2013).
[31] L. Zhao, J. Drennan, C. Kong, S. Amarasinghe, S.P. Jiang, J. Mater, Chem. A 2 (2014) 11114–11123.
[32] N. Sakai, K. Yamaji, T. Horita, H. Negishi, H. Yokokawa, Solid State Ionics 135 (2000) 469–474.
[33] N. Sakai, T. Horita, K. Yamaji, Y.P. Xiong, H. Kishimoto, M.E. Brito, H. Yokokawa, Solid State Ionics 177 (2006) 1933–1939.
[34] I. Waernhus, N. Sakai, H. Yokokawa, T. Grande, M.-A. Einarsrud, K. Wiik, Solid State Ionics 178 (2007) 907–914.
[35] M. Kubicek, G.M. Rupp, S. Huber, A. Penn, A. Opitz, J. Bernardi, M. Stöger-Pollach, H. Hutter, J. Fleig, Phys. Chem. Chem. Phys. 16 (2014) 2715–2726.
[36] H. Kishimoto, N. Sakai, T. Horita, K. Yamaji, M.E. Brito, H. Yokokawa, Solid State Ionics 178 (2007) 1317–1325.
[37] P. Bracconi, L.-C. Dufour, J. Phys. Chem. 79 (1975) 2400–2405.
[38] E. Bucher, C. Gspan, F. Hofer, W. Sitte, Solid State Ionics 230 (2013) 7–11.
[39] Y. Liu, X. Zhu, M. Li, W. Li, Y. Yang, J. Membr. Sci. 492 (2015) 173–180.
[40] W. Liu, E. Konysheva, ECS Trans. 59 (2014) 327–332.
[41] S.P. Jiang, L. Liu, K.P. Ong, P. Wu, J. Li, J. Pu, J. Power Sources 176 (2008) 82–89.
[42] Co3O4: electrical conductivity, Seebeck coefficient, in: O. Madelung, U. Rössler, M. Schulz (eds.), Landolt-Börnstein - Group III Condensed Matter, SpringerMaterials.
[43] W. Qu, L. Jian, J.M. Hill, D.G. Ivey, J. Power Sources 153 (2006) 114–124.
[44] A. Egger, E. Bucher, W. Sitte, J. Electrochem. Soc. 158 (2011) B573–B579.
[45] W. Preis, E. Bucher, W. Sitte, Fuel Cells 12 (2012) 543–549.
[46] J. Yang, Acta Crystallogr. B 64 (2008) 281–286.
[47] N. Gauquelin, T.E. Weirich, M. Ceretti, W. Paulus, M. Schroeder, Monatsh. Chem. 140 (2009) 1095–1102.
[48] A. Egger, W. Sitte, F. Klauser, E. Bertel, J. Electrochem. Soc. 157 (2010) B1537–B1541.
[49] A. Egger, W. Sitte, Proc. 10th European Solid Oxide Fuel Cell Forum, 2012 B05104–B05114.
[50] J. Choisnet, N. Abadzhieva, P. Stefanov, D. Klissurski, J.M. Bassat, V. Rives, L. Minchev, J. Chem. Soc., Faraday Trans. 90 (1994) 1987–1991.
[51] J. Druce, H. Téllez, M. Burriel, M.D. Sharp, L.J. Fawcett, S.N. Cook, D.S. McPhail, T. Ishihara, H.H. Brongersma, J.A. Kilner, Energy Environ. Sci. 7 (2014) 3593–3599.
[52] M. Burriel, S. Wilkins, J.P. Hill, M.A. Muñoz-Márquez, H.H. Brongersma, J.A. Kilner, M.P. Ryan, S.J. Skinner, Energy Environ. Sci. 7 (2014) 311–316.
[53] N. Čebašek, R. Haugsrud, Z. Li, T. Norby, J. Am. Ceram. Soc. 96 (2013) 598–605.
[54] N. Čebašek, R. Haugsrud, T. Norby, Solid State Ionics 231 (2013) 74–80.
[55] M. Kubicek, G.M. Rupp, S. Huber, A. Penn, A.K. Opitz, J. Bernardi, M. Stöger-Pollach, H. Hutter, J. Fleig, Phys. Chem. Chem. Phys. 16 (2014) 2715–2726.

Contents lists available at ScienceDirect

# Solid State Ionics

# Phase decomposition of $La_2NiO_{4+\delta}$ under Cr- and Si-poisoning conditions

N. Schrödl[a], A. Egger[a,*], C. Gspan[b], T. Höschen[c], F. Hofer[b], W. Sitte[a]

[a] Chair of Physical Chemistry, Montanuniversitaet Leoben, Franz-Josef-Straße 18, 8700 Leoben, Austria
[b] Institute for Electron Microscopy and Nanoanalysis (FELMI), Graz University of Technology, Graz Centre for Electron Microscopy (ZFE), Steyrergasse 17, 8010 Graz, Austria
[c] Max Planck Institute for Plasma Physics, Boltzmannstraße 2, 85748 Garching, Germany

## ABSTRACT

The influence of simultaneous Cr- and Si-poisoning on the oxygen exchange kinetics of $La_2NiO_{4+\delta}$ was studied at 800 °C in dry and humid $O_2/Ar$ atmospheres over a period of 4000 h by means of dc-conductivity relaxation measurements. Chemical and morphological changes of the $La_2NiO_{4+\delta}$ surface exposed to increasingly harsh ambient conditions were investigated using X-ray photoelectron spectroscopy (XPS) depth profiling, scanning electron microscopy with energy dispersive X-ray spectroscopy (SEM-EDXS) and high-resolution scanning transmission electron microscopy with energy dispersive X-ray and electron energy loss spectroscopy (HR-STEM EDXS/EELS). In the presence of Cr/Si-sources and under dry conditions, $La_2NiO_{4+\delta}$ shows good stability for more than 1000 h. However, as soon as humidity is introduced into the system a strong decline of the oxygen exchange activity is observed. Post-test analyses reveal newly formed partially blocking Cr- and Si-rich secondary phases on the surface of $La_2NiO_{4+\delta}$ which impede the surface exchange of oxygen.

## 1. Introduction

Solid oxide fuel cells (SOFCs) are highly efficient energy conversion devices for stationary and mobile applications, which are usually operated in a temperature range of 800–1000 °C. However, limitations to long-term stability at these high temperatures as well as high production costs pose a serious hindrance to large-scale commercialization of this promising technology. The need to develop advanced fuel cells with improved durability and lower production costs has led to a reduction of operating temperatures to 600–800 °C, which allows for the use of cheaper materials in SOFC stacks. Metallic interconnects made of ferritic stainless steels exhibit high electronic and thermal conductivity as well as good machinability at intermediate temperatures and thus can replace ceramic interconnects [1]. Interconnect alloys usually contain large amounts of Cr in order to resist high temperature corrosion through $Cr_2O_3$ scale formation under typical SOFC operating conditions [2]. Chromia-rich scales can produce volatile, hexavalent Cr-species like chromium oxide ($CrO_3$) and – in the presence of air moisture – chromium oxyhydroxide ($CrO_2(OH)_2$) [3], which can be deposited on the cathode surface and lead to a long-term decrease in cell performance [4–6]. The application of protective barrier coatings based on rare earth perovskite or spinel structures has successfully reduced the emanation of Cr-species from interconnects [7,8], but poor layer adhesion, residual porosity or crack formation in these coatings

can lead to Cr-migration and Cr-poisoning of the SOFC cathode [9,10].

Similar performance deterioration has been observed in conjunction with the deposition of volatile Si-species [11–13]. Present as an impurity in raw materials – often introduced by powder and ceramics processing – as well as in silicate-based SOFC glass sealings, Si tends to form $H_4SiO_4$ as the dominant gas species in humid, oxidizing atmospheres [14,15]. Both Si and Cr effectively inhibit the incorporation of oxygen into the cathode material by blocking active sites for the oxygen exchange reaction and by forming electrically insulating reaction products with the cathode material.

In the literature, Cr-poisoning has frequently been associated with the segregation of a nucleation agent to the active surface, facilitating the deposition of Cr-species [16]. In strontium-containing state-of-the-art cathode materials like LSC and LSCF, SrO has been identified as nucleation agent for volatile Cr-species [4,17,18]. Moreover, Sr has been found to react readily with $H_4SiO_4$ forming silicate phases [19–22]. Given the important role of Sr in the phase decomposition of these cathode materials, the investigation of Sr-free materials for SOFC cathode applications seems highly appropriate.

The mixed ionic electronic conductor $La_2NiO_{4+\delta}$ (LNO) has been proposed as promising cathode material for SOFCs with a higher tolerance for Cr-poisoning [23]. LNO is the first member of the Ruddlesden-Popper series $A_{n+1}B_nO_{3n+1}$ (n = 1, 2, 3…) with high oxygen diffusivity and sufficient electronic conductivity for SOFC cathode

applications [24,25]. However, reports on the long-term stability of LNO against the combined effects of Cr- and Si-poisoning have been scarce. In a previous work, prolonged exposure of LNO to Cr and Si in dry and humid atmospheres at 700 °C has been shown to cause a significant decrease in surface activity due to a partial decomposition of the material [4,19].

This study intends to expand the existing knowledge on the influence of Cr- and Si-contaminants on LNO under SOFC operating conditions at 800 °C. Test samples are exposed to Cr- and Si-sources in dry and humid $O_2$/Ar atmospheres and the degradation process is investigated via monitoring the chemical surface exchange coefficient of oxygen over time. Microstructural and chemical changes occurring on the sample surface are characterized using various analytical techniques and the crystal structures as well as the chemical composition of newly formed degradation phases are identified.

## 2. Experimental

### 2.1. Sample preparation

LNO powder (Treibacher Industrie AG) was isostatically pressed into a cylindrical pellet at 200 MPa and sintered two times for 10 h at 1350 °C with heating and cooling rates of 2 K min$^{-1}$. The relative density of the sintered pellet was 98%. A rectangular sample with the dimensions $6 \times 6 \times 10$ mm$^3$ was cut with a diamond wire saw and the four larger faces were polished using polymer-embedded diamond lapping films with 30, 6 and 1 µm particle size. Electrical contacts (gold) were attached to both smaller faces using gold paste (Metalor) and two voltage probes were placed between the gold contacts at a distance of 5.2 mm from one another.

### 2.2. Electrical conductivity relaxation measurements

The influence of surface contamination via Cr- and Si-species on the oxygen exchange kinetics was determined at 800 °C in dry and humid $O_2$/Ar atmospheres. The electrical conductivity ($\sigma$) of the LNO sample was obtained from V/I characteristics in linear four-point geometry. Chemical surface exchange coefficients ($k_{chem}$) and chemical diffusion coefficients ($D_{chem}$) of oxygen were measured using the dc-conductivity relaxation method [26]. Oxidation and reduction steps were realized by changing the oxygen partial pressure around the sample ($0.1 \leq p\mathrm{O}_2$/ bar $\leq 0.15$). A constant current of 300 mA was applied and the electrical conductivity of the sample was recorded as a function of time. The gas flow was kept constant at 2 dm$^3$ h$^{-1}$. SOFC operation with undried air was simulated by passing the gas streams through washing bottles filled with deionized water which were thermostatted at 6 °C or 17 °C, to achieve relative humidities (r.h.) of 30% and 60%, respectively (100% r.h. corresponds to the equilibrium vapor pressure of $H_2O$ at 25 °C). The kinetic parameters $k_{chem}$ and $D_{chem}$ were calculated from the conductivity response to sudden changes in oxygen content around the sample using non-linear regression analysis of the corresponding solutions of the two-dimensional diffusion equation [27]. The effects of simultaneous Cr- and Si-poisoning were simulated by placing the sample next to Cr-pellets in a quartz glass reactor, which served as a constant Si-source under humid conditions. Two additional samples of LNO positioned close to the measured sample were removed at different stages during the degradation study for chemical analysis. For a more in-depth description of the measurement procedure see Bucher [28].

### 2.3. X-ray photoelectron spectroscopy (XPS)

A Perkin Elmer PHI 5600 ESCA system with a hemispherical analyzer and a standard X-ray source (Mg-Kα radiation, 1253.6 eV) was used to record XPS spectra of an area with 400 µm in diameter in constant analyzer mode. To check for impurities, survey scans were performed before depth profiling. For depth profiling an Atomica WF

421 Microfocus Ion Gun was used to automatically scan a sample area of $1.2 \times 1.5$ mm$^2$ with a 10 kV Ar$^+$ ion beam of approximately 150 µm diameter, irradiating the surface at an ion current of 125 nA. A sputter rate was estimated from the Ar$^+$-fluence by assuming a yield of 2 target atoms per impinging Ar$^+$, taking into account the volume density of the bulk composition [29]. The background was subtracted using a Shirley background function and the concentrations of the specific elements were obtained from the core-level peak areas by using standard relative sensitivity factors. The reproducibility of the XPS quantification amounts to about 1%.

### 2.4. Scanning electron microscopy with energy-dispersive X-ray spectroscopy (SEM-EDXS)

SEM images and EDXS analyses of sample surfaces were obtained using a Zeiss EVO50, equipped with a LaB$_6$ cathode and an Oxford Instrument INCA EDX detector at acceleration voltages of 15 kV. Elemental distribution maps of LNO were recorded at acceleration voltages of 10 kV using a Zeiss Ultra 55 microscope with an EDAX Phoenix EDXS detector.

### 2.5. High resolution scanning transmission electron microscopy (HR-STEM)

A Focused Ion Beam (FIB) NOVA 200 Nanolab dual beam microscope was used for TEM lamella preparation. Energy dispersive X-ray spectroscopy (EDXS) and electron energy loss spectroscopy (EELS) analyses were conducted using a FEI Tecnai F20 microscope operated at 200 kV in STEM mode. High resolution imaging was realized using a FEI Titan$^3$ G2 60-300 microscope (operated at 300 kV) equipped with a C$_s$ probe corrector (DCOR) for sub-Ångström resolution and a post-column energy filter (GIF Quantum ERS™) from Gatan Inc. To determine the chemical composition of secondary phases, high resolution images were compared with high angle annular dark field (HAADF) simulations calculated with the software package JEMS [30].

## 3. Results and discussion

### 3.1. Oxygen exchange kinetics

Conductivity relaxation measurements were performed over a period of approximately 4000 h. A set of typical conductivity relaxation curves measured at different stages of the degradation study together with the corresponding fitting curves is given in Fig. 1. The sample geometry was optimized to allow for the simultaneous determination of the oxygen transport properties $k_{chem}$ (Fig. 2a) and $D_{chem}$ (Fig. 2b). Results obtained from the oxidation steps ($p\mathrm{O}_2$ change from 0.1 to 0.15 bar) are indicated in blue while parameters obtained from the reduction steps ($p\mathrm{O}_2$ change from 0.15 to 0.1 bar) are shown as red symbols. The electrical conductivity (Fig. 2c) was recorded between oxidation and reduction steps to check for changes in the bulk of the material during the degradation study. For the first 600 h, the sample was kept in a dry $O_2$/Ar mixture at 800 °C without a chromium source in order to determine the intrinsic stability of LNO. It should be mentioned that, since the measurements were conducted in a quartz glass reactor, a potential Si-source was always present at every step of the experiment. However, under dry conditions the volatilization of $SiO_2$ is practically negligible [14]. In dry atmospheres, $k_{chem}$ and $D_{chem}$ remained constant at values of $3.4 \times 10^{-3}$ cm s$^{-1}$ and $1.5 \times 10^{-4}$ cm$^2$ s$^{-1}$ (average of oxidation and reduction steps), respectively, indicating excellent intrinsic stability of the material. Fig. 3 presents a comparison of average $k_{chem}$ values obtained in this study with data reported by Li and Haugsrud [31] and data from an earlier study by our group [32]. Arithmetic means and standard deviations were calculated based on 12 $k_{chem}$ values measured in dry atmospheres at 800 °C for oxidation and reduction steps separately, as oxidation steps yield systematically higher $k_{chem}$ values. The standard deviations amount to 7% for both oxidation and reduction reactions
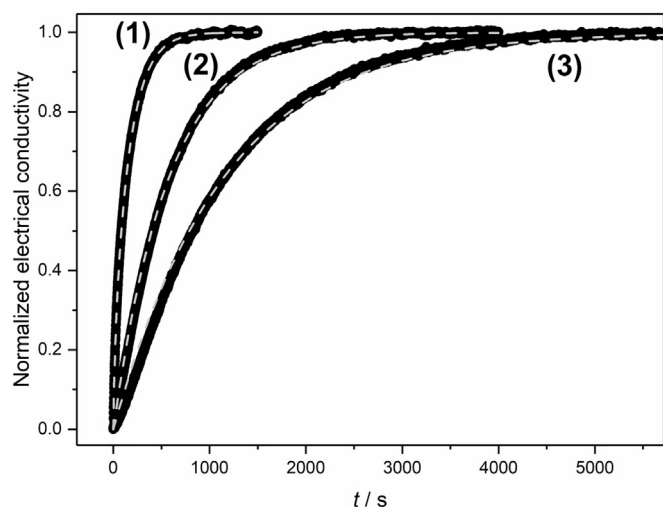
**Fig. 1.** Conductivity relaxation curves of the oxidation process after (1) 552 h, (2) 1872 h and (3) after 3960 h. Measured data points are shown as black symbols while fitting curves applied for the calculation of $k_{chem}$ values are plotted as grey dashed lines.

($k_{chem}$ (ox): $3.6 \times 10^{-3} \pm 2.4 \times 10^{-4} \, cm \, s^{-1}$; $k_{chem}$ (red): $3.2 \times 10^{-3} \pm 2.4 \times 10^{-4} \, cm \, s^{-1}$). Although $k_{chem}$ depends on several factors such as surface properties (quality of the polishing process, presence of impurities) and oxygen partial pressure, the values obtained in this study are in good agreement with published data. Cooling down to room temperature to repair a broken contact and reheating to 800 °C did not have any impact on the measured parameters. After 600 h a Cr-source was added, and the relaxation measurements were continued under dry conditions for 1000 h, resulting in a slight reduction of $k_{chem}$ by a factor of 1.3. This is a clear indication of degradation processes affecting the sample surface. Since both $D_{chem}$ and $\sigma$ remained quite stable, there appears to be no impact on the bulk of the material. Similar observations were made in an earlier study, in which the slight decrease in oxygen exchange activity could be attributed to the formation of small chromium-containing crystallites on the sample surface [4]. However, once the test gas was humidified (30% r.h.) a sudden decrease of $k_{chem}$ by a factor of 18 was recorded. As a result, $D_{chem}$ could no longer be extracted from the measured conductivity profiles, indicating that the oxygen exchange reaction changed into a surface-controlled process. This can be attributed to the enhanced gas phase transport of volatile Cr-species ($CrO_2(OH)_2$) as well as the formation of volatile Si-compounds ($H_4SiO_4$) in the presence of water vapor [3,14]. After 1000 h under humid conditions in the presence of a Cr- and a Si-source the surface exchange coefficient stabilized at a value of $1.4 \times 10^{-4} \, cm \, s^{-1}$. A further increase in humidity to 60% r.h. resulted in only a slight decrease in $k_{chem}$ over the course of another 1000 h. This is not very surprising considering that at 800 °C the partial pressure of the most abundant Cr-vapor species ($CrO_2(OH)_2$) only increases from $1.9 \times 10^{-8}$ bar at 30% r.h. to $3.9 \times 10^{-8}$ bar at 60% r.h. [6]. The electrical conductivity of the sample (Fig. 2c) remained quite constant during all stages of the experiment. In comparison to an earlier study by our group on the influence of Cr and Si on the oxygen exchange kinetics of LNO, where a decrease in $k_{chem}$ by a factor of 230 was observed at 700 °C [4], LNO seems to be much less prone to Cr/Si-degradation at 800 °C, showing an overall drop in $k_{chem}$ by only a factor of 25 under similar experimental conditions.

Since all measurements were performed in a quartz reactor acting as Si-source, the influence of humidity alone on the oxygen exchange properties of LNO could not be determined in this work. However, long-term tests on symmetrical cells with porous LNO electrodes under Si-free conditions at 800 °C and 30% r.h. conducted by our group (data not yet published) showed that exposure to humidity in the absence of a Cr- and Si-source had no significant influence on the area specific resistance
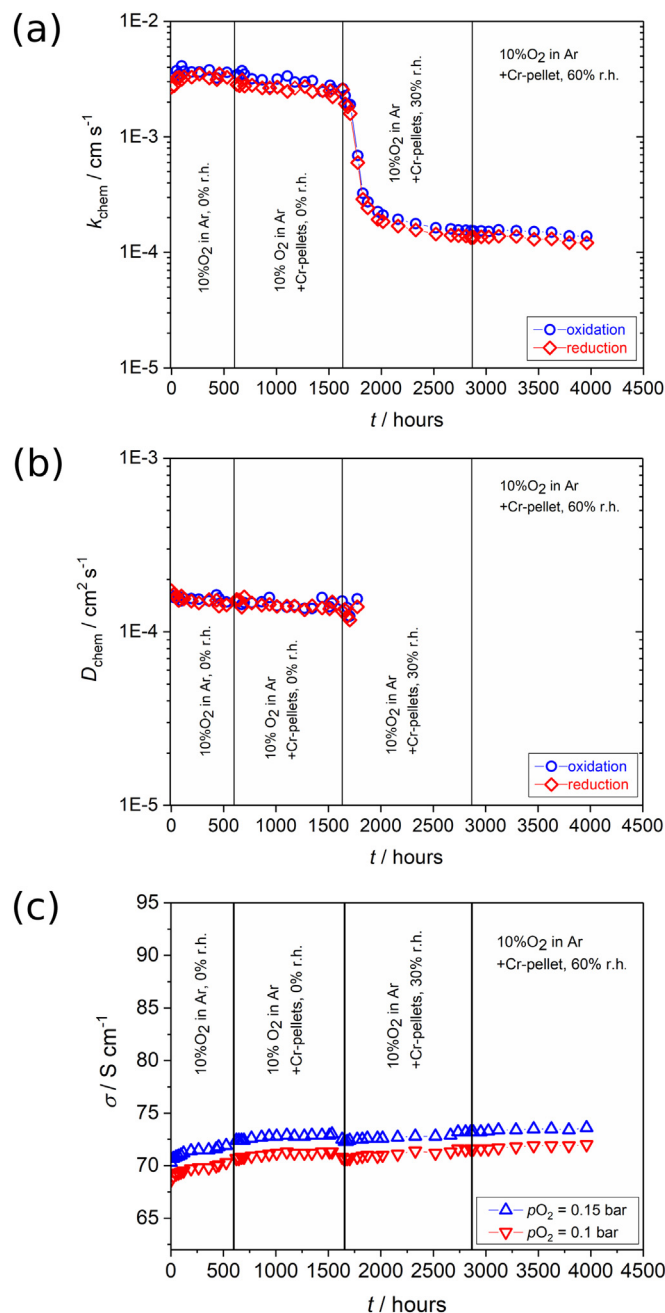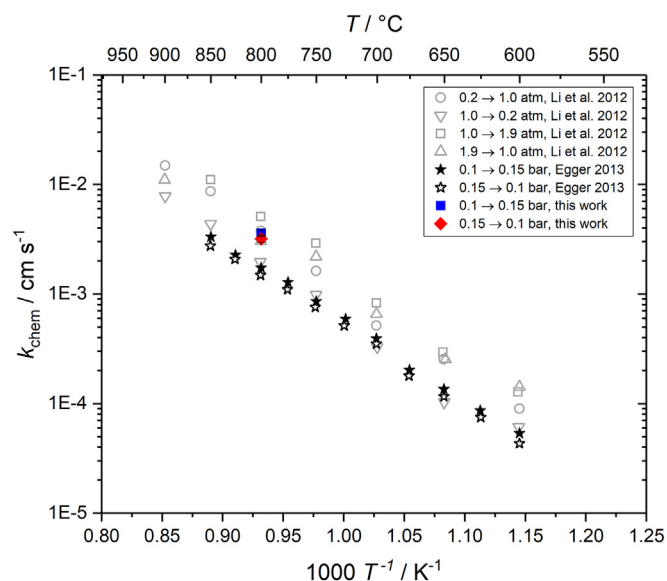


**Fig. 2.** (a) Chemical surface exchange coefficients of oxygen, (b) chemical diffusion coefficient of oxygen and (c) electrical conductivity of LNO at 800 °C and $pO_2 = 0.1$ bar as a function of time. Chromium was introduced after approximately 600 h. Experiments were conducted in a quartz glass reactor which served as a Si-source.

(ASR) of the electrodes over a period of 650 h. Once a Cr-source was introduced in addition to humidity, a strong increase in the ASR was observed. This is consistent with the findings presented in this work and suggests that humidity alone does not affect the oxygen surface exchange process of LNO in a significant way.

### 3.2. Scanning electron microscopy with energy dispersive X-ray spectroscopy

To determine the cause for the reduction in oxygen surface exchange rates, SEM images of degraded samples removed at different stages of the degradation study were recorded. Fig. 4 displays images

**Fig. 3.** Comparison of published chemical surface exchange coefficients of oxygen for LNO. Open grey symbols represent data from Li and Haugsrud [31], black stars are data taken from Egger [32]. The blue and red filled symbols illustrate average values of $k_{chem}$ for the oxidation (blue square) and the reduction (red diamond) reaction, calculated from $k_{chem}$ values measured at 800 °C in dry $O_2$/Ar mixtures over a period of 22 days. (For interpretation of the references to color in this figure legend, the reader is referred to the web version of this article.)

taken in backscattered electron (BSE) mode of (a) a polished and thermally etched LNO sample, (b) a sample tested for 600 h without and 1000 h with a Cr-source present in dry conditions, (c) a sample exposed for another 1000 h to Cr in moderately humidified atmospheres (30% r.h.) and (d) a sample subjected for additional 1000 h to a strongly humidified atmosphere (60% r.h.).

The polished and etched sample displayed in Fig. 4a features grains with diameters of 5 to 10 μm. Analysis of the sample surface using EDXS reveals a La:Ni cation ratio of 2:1, while impurity levels are well below the detection limit of the method. A second analysis of a polished sample of the same sintered compact, however, revealed the presence of small NiO inclusions along the grain boundaries of LNO grains (data not shown). The second sample (Fig. 4b) – exposed to Cr/Si-sources for a period of 1000 h in dry atmospheres – shows large LNO grains covered with smaller crystallites as well as sporadic patches of dark contrast, identified as Zr- und Si-containing phases by EDXS. These secondary phases are believed to be formed from material impurities and not to be the result of contamination via gas phase transport, as traces of Si (90 ppm) were found in the raw material and Zr was likely introduced by powder milling. As already mentioned, Si and $SiO_2$ do not form volatile gas species in $O_2$/Ar in the absence of water vapor [14] and thus the quartz glass reactor cannot be the source of Si-compounds formed on the sample surface in dry atmospheres.

In addition, small amounts of Bi are detected in regions of fine crystalline structures, originating from the gold paste used for contacting the sample. However, neither the Bi-contaminants nor the corresponding morphological changes seem to have a significant influence on the oxygen exchange reaction. Fig. 4c and d depict sample surfaces exposed to $O_2$/Ar gas streams with 30% and 60% r.h., respectively. The surfaces are densely covered in fine crystallites. EDXS point analyses at several different regions of the degraded surfaces confirm the presence of Cr, Si and Bi.
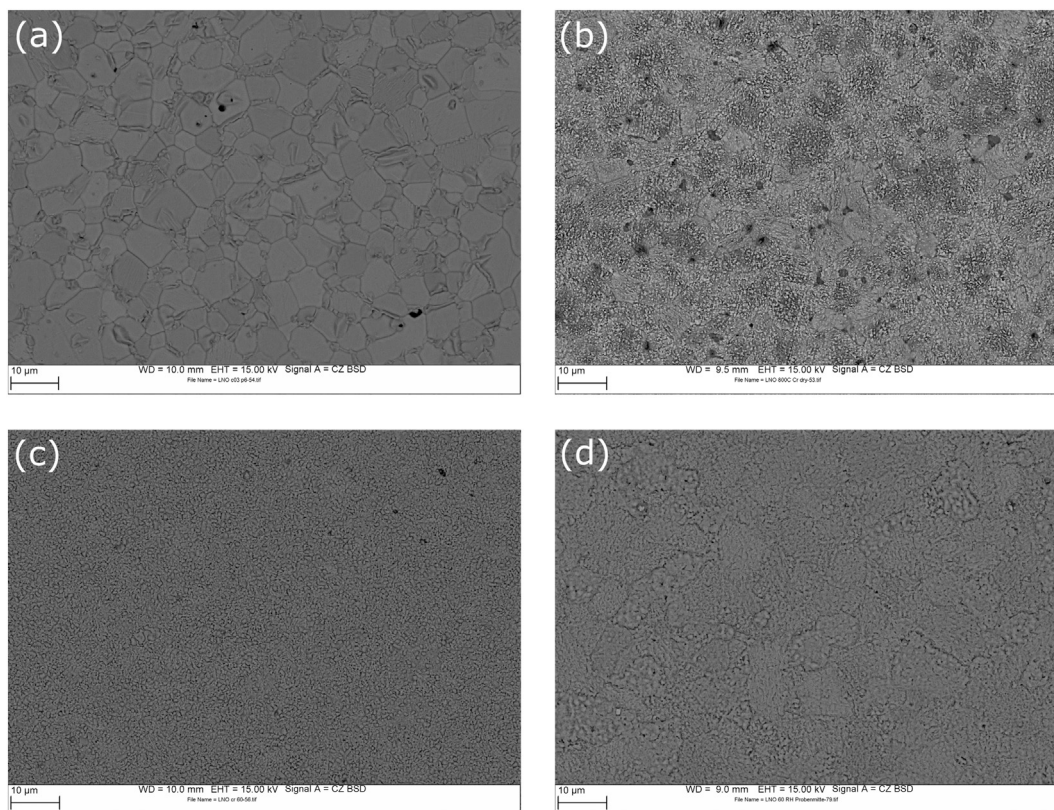


**Fig. 4.** SEM images in BSE imaging mode of (a) a polished and thermally etched LNO sample, (b) after 600 h in dry atmosphere without Cr (but with Si) and 1000 h in a dry $O_2$/Ar mixture with Cr and Si at 800 °C, (c) after an additional 1000 h in a humidified $O_2$/Ar gas mixture with 30% r.h. and (d) after another 1000 h in a humidified $O_2$/Ar gas mixture with 60% r.h.
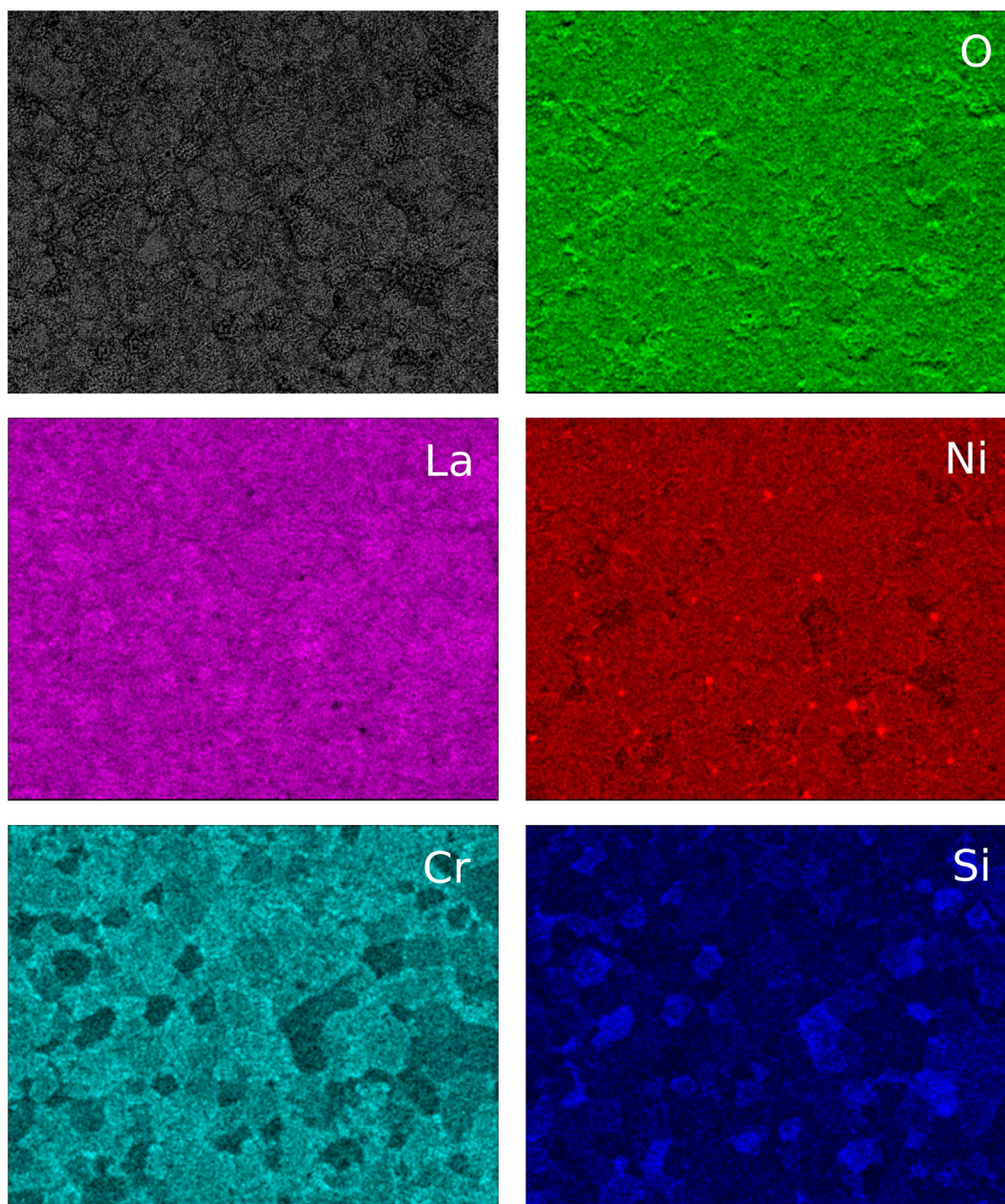
**Fig. 5.** Post-test SEM image (top left) and corresponding SEM-EDXS elemental distribution maps of LNO after degradation at 800 °C in 60% r.h. The width of all images is 108.54 μm.

To obtain a clearer picture about the distribution of elements on the degraded sample surface, detailed EDXS analyses of the sample subjected to 60% r.h. in the presence of Cr and Si were conducted. Fig. 5 displays a secondary electron (SE) image of a selected surface region as well as the corresponding elemental distribution maps of La, Ni, O, Cr and Si. Finely dispersed dark spots in the La-map – indicating a local depletion of La and coinciding with high concentrations of Ni in the Ni-map – are caused by NiO impurities. On a larger scale, La as well as O appear to be evenly distributed across the surface. Dark areas in the Cr-map correspond to high concentrations of Si in the Si-map and vice versa, thus indicating the formation of at least one Cr-rich and one Si-rich secondary phase, both of which also contain La and O. Furthermore, Ni seems to be depleted in areas rich in Si, but not in areas where Cr is present. Also, Bi was found in areas rich in Cr and devoid of Si (data not shown). It must be mentioned that parts of the La-signal may have been attributed to the Cr-map due to a strong overlap of the Cr-Kα peak (5.410 keV) with the La-Lβ peak (5.372 keV) in the acquired EDX spectra. In a similar way, part of the Cr-signal may have been integrated into the O-map due to an overlap of the Cr-Lα peak (0.573 keV) and the O-Kα peak (0.525 keV). Nevertheless, these results are in good agreement with TEM results of an earlier study on the phase decomposition of LNO under Cr- and Si-poisoning conditions at 700 °C [19], which confirmed the formation of La-chromate and La-silicate phases but did not permit the determination of their exact composition or crystal structure.

### 3.3. X-ray photoelectron spectroscopy

To gain some depth resolution regarding the composition of the near-surface degradation layer, XPS elemental depth profiles of La, Ni, O, Cr and Si were recorded at different stages during the long-term study (Fig. 6). Sputtering of the samples was continued until constant concentrations for La, Ni and O were reached.

The XPS depth profile of a fresh, undegraded sample presented in
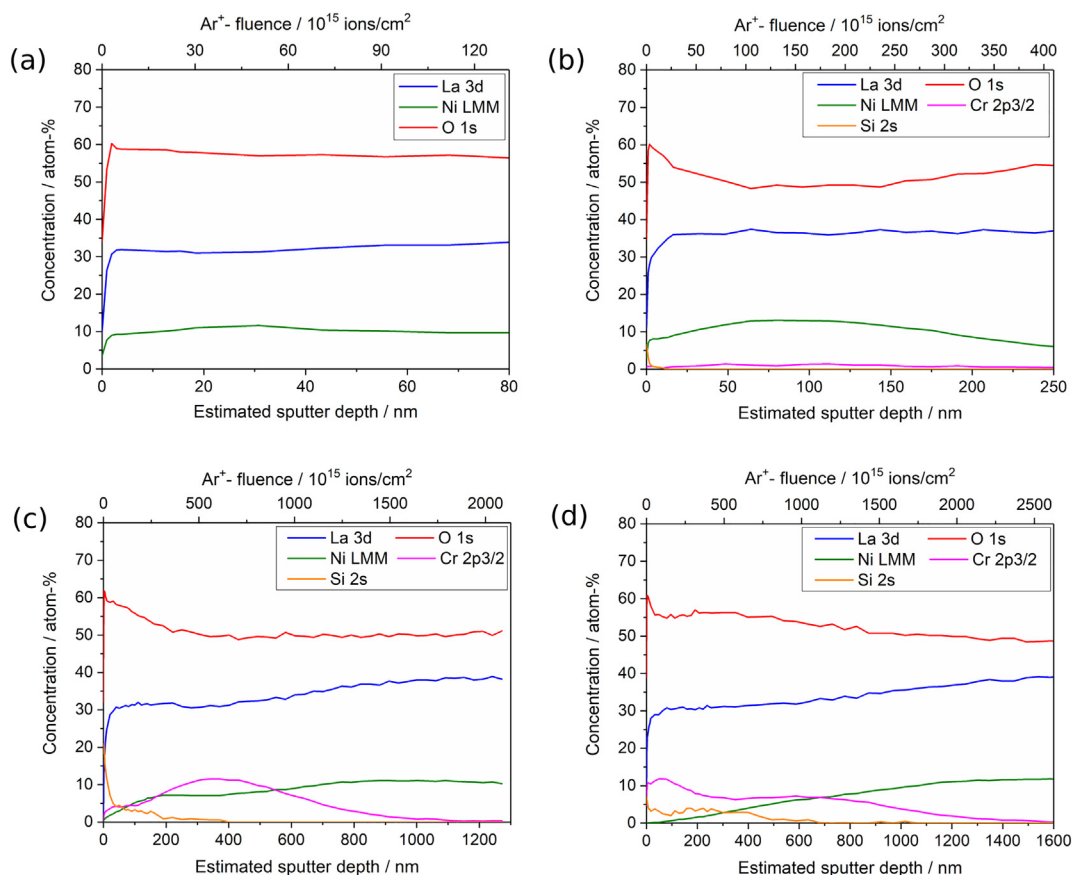
**Fig. 6.** XPS elemental depth profiles of La, Ni and O in LNO and Cr/Si-impurities of (a) the freshly polished sample, (b) after 600 h in dry atmosphere without Cr (but with Si) and 1000 h in a dry $O_2$/Ar mixture with Cr and Si at 800 °C, (c) after an additional 1000 h in a humidified $O_2$/Ar gas mixture with 30% r.h. and (d) after another 1000 h in a humidified $O_2$/Ar gas mixture with 60% r.h.

Fig. 6a shows a uniform depth distribution of La, Ni and O. The steep profile slopes at the immediate surface are due to high levels of carbon detected on the sample surface, which might be remnants of materials used for sample preparation or molecules adsorbed during storage in ambient air [22]. Fig. 6b displays the sample treated for 1600 h in dry $O_2$/Ar with a Cr- and Si-source present. An increased La:Ni ratio within the first 15 nm from the surface, followed by a zone with higher Ni content, indicates La segregation towards the surface. This phenomenon has been reported in the literature by several authors [33–36]. Small amounts of Cr and Si are detected which may be responsible for the slight decline of $k_{chem}$ in dry atmospheres (see Section 3.1).

After additional 1000 h in moderately humidified atmosphere (30% r.h.) a degradation layer of approximately 800 nm thickness is formed, followed by a fairly constant concentration of La, Ni and O (Fig. 6c). The degraded surface layer shows an increased La:Ni ratio compared to the bulk and large amounts of Cr are found with a maximum at depths of approximately 400 nm. Si-species were detected up to 400 nm from the sample surface, with a large accumulation within the first 50 nm. Elemental profiles of the sample treated for another 1000 h in strongly humidified $O_2$/Ar atmosphere (60% r.h.) are presented in Fig. 6d. The degradation layer has grown by approximately 200 nm in this last phase of the degradation study, which surprisingly did not cause a further decline in oxygen surface exchange rates (see Section 3.1). The near-surface layer is almost completely depleted of Ni while the Cr-profile indicates a pronounced accumulation of chromium within the first 200 nm, followed by a broad plateau. Si-species were found to be deposited at the immediate surface and interspersed with Cr-rich regions up to depths of 600 nm.

Fig. 7 shows the evolution of peaks selected for the quantification of Cr ($2p_{3/2}$) and Si (2s) together with Bi (4f) during XPS depth profiling.

Hatched areas mark the range of measured binding energies for oxides of Cr, Si and Bi taken from the NIST X-ray Photoelectron Spectroscopy database [37].

XPS spectra of the Cr $2p_{3/2}$ region recorded in the near-surface zone (Fig. 7, left) suggest the presence of Cr(III) oxide compounds, while no signals of Cr(VI) species (e.g. chromate $CrO_4^{2-}$ or dichromate $Cr_2O_7^{2-}$) are detected. With increasing sputtering depths, a second peak emerges at lower binding energies which can be attributed to metallic Cr. The deposition of Cr in metallic form is highly implausible considering the high temperatures and oxidizing conditions applied in the degradation study and is most likely an artifact caused by prolonged $Ar^+$ ion bombardment in the course of the sputtering process during depth profiling. The reduction of metal oxides due to sputtering with $Ar^+$ ions has been described in the literature for Cr [38,39] and other transition metals [21,22,40–42]. Other elements with similar binding energies as metallic Cr would be Ag ($3p_{3/2}$) and Te ($3d_{5/2}$) which, however, are not contained in any of the materials used in the experimental setup and have not been detected by any of the other analytical methods applied in this work.

Signals at binding energies consistent with Si(IV) oxides have been identified (Fig. 7, right) which – together with results from SEM analysis – points to the formation of a lanthanum silicate phase. No evidence of metallic silicon can be found. Signals of bismuth are also clearly visible in the surface scan, but quickly disappear after the first few sputtering steps, indicating that Bi contaminations are only present at the topmost surface layer.

Based on the XPS results it is difficult to get a conclusive picture about the elemental distributions within the surface layer. Looking at Fig. 6c (after 1000 h at 30% r.h.) it appears that the topmost reaction layer is composed of a Si-compound beneath which a Cr-containing
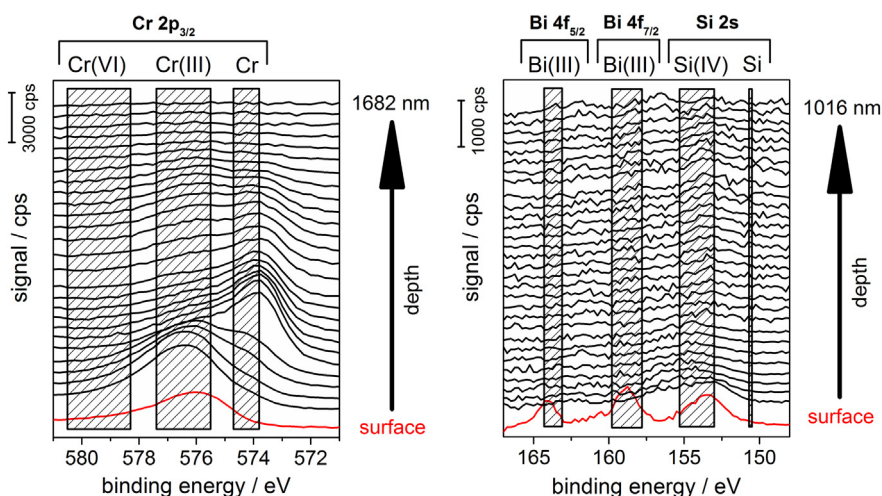
**Fig. 7.** XPS spectra of the LNO sample after completion of the degradation study showing the evolution of signals of Cr 2p$_{3/2}$, Si 2s and Bi 4f during surface depth profiling.

phase is located. This is plausible, considering the higher volatility of $CrO_3$ in dry atmospheres as compared to $SiO_2$, which should lead to preferential Cr-poisoning in the early stages of the degradation study (dry atmospheres) while Si is deposited at a later stage when humidity is added to the gas stream. This model, however, is somewhat contradicted by the XPS depth profiles recorded after exposition to 60% r.h. (Fig. 6d).

It should be mentioned that due to the large lateral averaging of the XPS technique (400 × 400 μm$^2$) the interpretation of the depth profiles is not straightforward, as it would have to be based on the assumption of a rather evenly layered structure of the surface zone. This, however, seems not to be the case according to SEM results presented in the previous section, which show the degraded surface layer to be laterally inhomogeneous at a length scale smaller than the area analyzed by XPS (see Fig. 5).

In order to get a clearer picture about the make-up of the near-surface region and to allow for phase identification of the Cr- and Si-containing secondary phases, TEM analyses were conducted.

### 3.4. High resolution scanning transmission electron microscopy

A STEM HAADF cross section image of the decomposed surface layer is displayed in Fig. 8a. The HAADF $Z$-contrast reveals an approximately 1 μm thick near-surface degradation zone containing

various phases of different chemical composition. In the topmost layer, marked as region 1 in Fig. 8a, La, Si and O are confirmed by EDXS. Complementary electron energy loss spectroscopy (EELS) measurements indicate that neither Cr nor Ni are present within this layer (data not shown). The small grains marked as region 2 below the topmost layer are identified as La-Cr-Ni-oxide. Due to the small crystallite size, the exact chemical composition could not be reliably determined by EDXS. Dark grains in region 3 are identified as NiO by EDXS and EELS. Similar inclusions are also clearly visible in the elemental distribution map of Ni presented in Section 3.2. Since NiO was also found in a fresh sample, its presence cannot be unambiguously assumed to be caused by secondary phase formation during the degradation process. For comparison, an EDX spectrum of the bulk composition (region 4) is depicted in Fig. 8b.

Detailed structural information of the La-Si-O and La-Cr-Ni-O secondary phases were obtained in HR-STEM mode (Figs. 9 and 10). The Si-rich layer (analyzed area marked by a white circle in Fig. 9a) is identified as silicon oxyapatite La$_{9.33}$(SiO$_4$)$_6$O$_2$ with space group $P6_3/m$ (176) by comparison of an HAADF-simulation (white rectangle in Fig. 9b) of this compound with the acquired high resolution image. The comparison of a calculated Fast Fourier Transformation (FFT) based on the HR-STEM image with the simulated diffraction pattern of La$_{9.33}$(SiO$_4$)$_6$O$_2$ in [2 −1 −1 3] zone axis further supports this result. Interestingly, this highly anisotropic material exhibits significant ionic



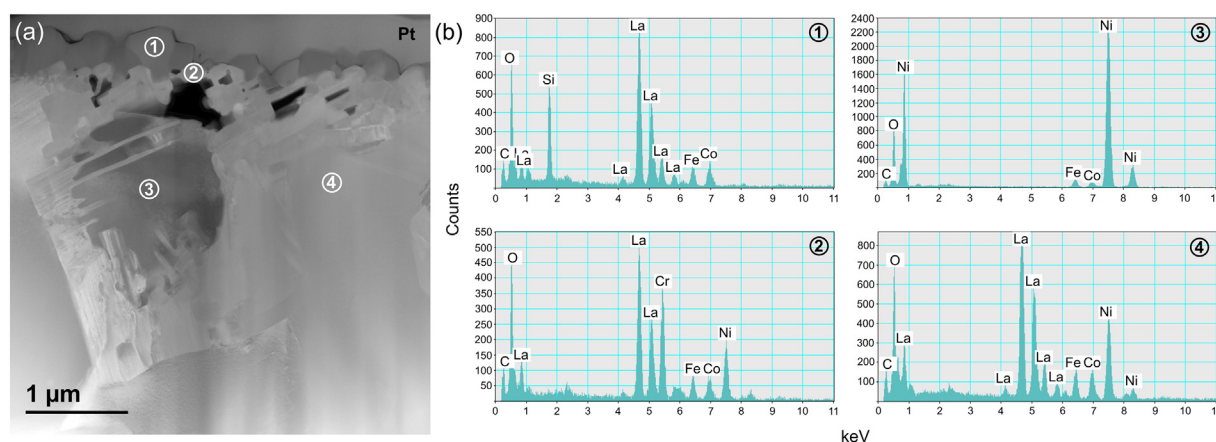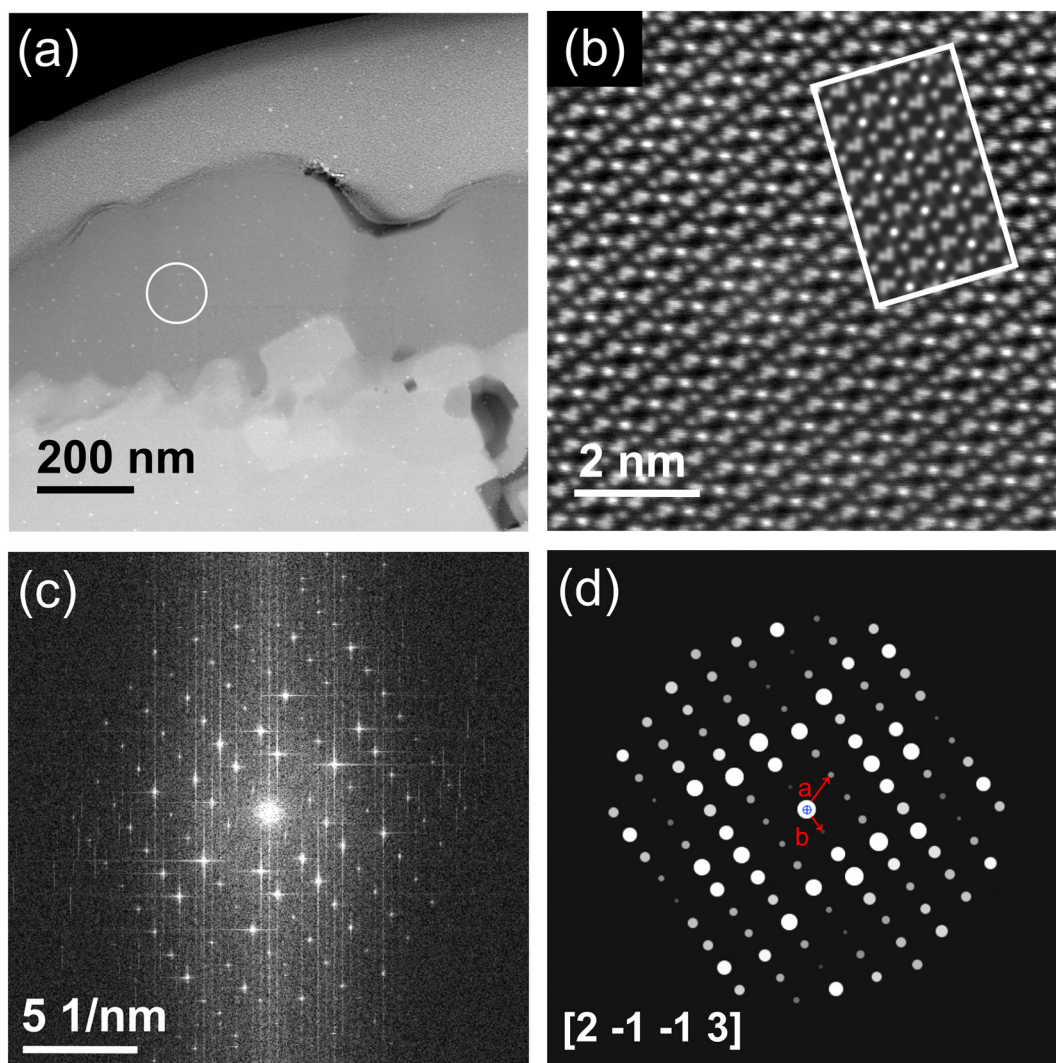**Fig. 8.** Post-test STEM HAADF image of (a) the near-surface region of LNO after degradation at 800 °C in 60% r.h. and (b) corresponding EDX spectra of secondary phases. Additional peaks of Fe and Co originate from the interior lining of the microscope.

**Fig. 9.** (a) STEM HAADF image of the near-surface region of LNO with a white circle marking an area within the Si-rich secondary phase, (b) HR-STEM HAADF image of the marked area with HAADF simulation overlay (white rectangle), (c) FFT image of the selected area and (d) simulated diffraction pattern of $La_{9.33}(SiO_4)_6O_2$ in [2 −1 −1 3] zone axis. The red arrows a and b indicate the diffraction planes (−1 0 1) and (0 1 0), respectively. (For interpretation of the references to color in this figure legend, the reader is referred to the web version of this article.)

conductivity (10–20 mS cm$^{-1}$ at 800 °C [43]) – similar to that of YSZ – and has been investigated as electrolyte material for intermediate-temperature solid oxide fuel cells [44,45].

A similar procedure was carried out for the Cr-containing phase depicted in Fig. 10a. A HRTEM image of the area marked with a black circle is shown in Fig. 10b. The calculated FFT image (Fig. 10c) was successfully matched to the simulated diffraction pattern of a La(Cr,Ni)O$_3$ perovskite with space group *Pnma* (62) (Fig. 10d) as suggested by results from EDXS and EELS analysis. EDXS line-scans from the top of a La(Cr,Ni)O$_3$ crystal towards the bulk phase show a decreasing Cr-concentration and a corresponding increase in Ni-content (data not shown), which is easily established since $LaCr_{1-x}Ni_xO_3$ supports complete solid solution on the perovskite B-site [46]. It is difficult to conclude from the available data whether the observed chromium phases are formed by Cr-diffusion into a LaNiO$_3$ degradation phase, Ni-diffusion into a LaCrO$_3$ secondary phase or by a more complicated reaction scheme. The Cr-rich end member of the $LaCr_{1-x}Ni_xO_3$ series is a p-type electronic conductor which is used for interconnector plates in high-temperature SOFCs [47]. Compared with LNO, however, the electrical conductivity of LaCrO$_3$ is rather low (0.96 S cm$^{-1}$ at 800 °C in air [48]). A tendency for the formation of LaCrO$_3$ has also been reported for Cr-poisoning of symmetrical LNO half cells by Lee et al. [23]. The

formation of secondary phases with some levels of ionic or electronic conductivity may explain why – despite the strong decomposition of the sample surface – significant activity for the oxygen surface exchange reaction is still retained.

Light grey stripes in the bulk phase directly below the degraded surface zone (see Fig. 11a) are identified in HR-STEM images as stacking anomalies in the LNO phase (Fig. 11b). Monolayers of the n = 3 member of the $La_{n+1}Ni_nO_{3n+1}$ Ruddlesden-Popper series (Fig. 11c) are found to be embedded between regular (n = 1) LNO layers. The formation of these monolayers can probably be attributed to the initially observed and continuously propagating segregation of La to the sample surface, which also has been reported in the literature [49].

## 4. Conclusions

The influence of Cr and Si on the long-term stability of $La_2NiO_{4+\delta}$ (LNO) was investigated at 800 °C in dry and humidified O$_2$/Ar atmospheres. The degradation was monitored by measuring the chemical surface exchange ($k_{chem}$) and the chemical diffusion coefficient ($D_{chem}$) of oxygen using the dc-conductivity relaxation technique over a period of approximately 4000 h. Moreover, ancillary pieces of LNO have been mounted close to the sample and were removed at different stages of
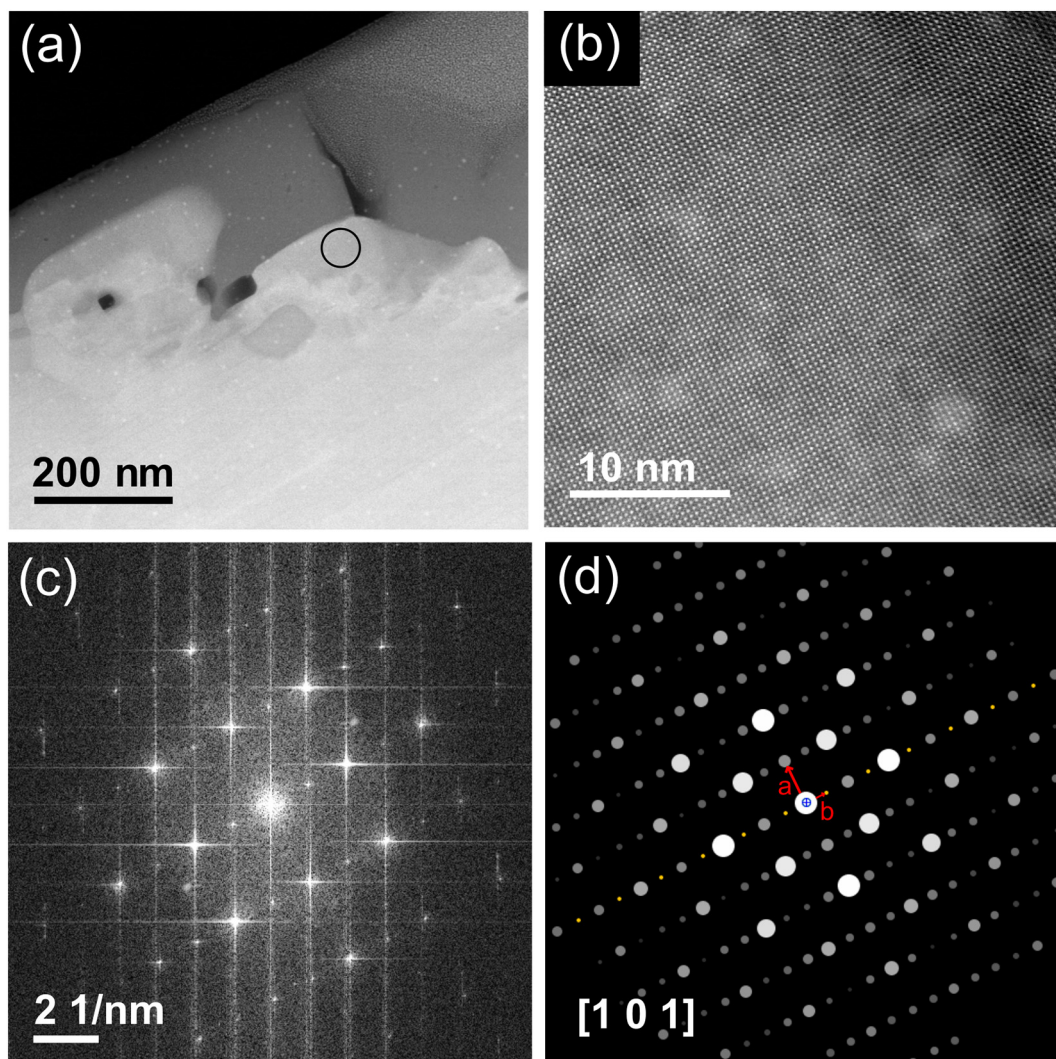
**Fig. 10.** (a) STEM HAADF image of the near-surface region of LNO with a black circle marking an area within the Cr-rich secondary phase, (b) HR-STEM HAADF image of the marked area, (c) FFT image of the selected area and (d) simulated diffraction pattern of a perovskite structure with space group *Pnma*. Red arrows a and b indicate the diffraction planes (1 0 −1) and (0 −1 0), respectively. (For interpretation of the references to color in this figure legend, the reader is referred to the web version of this article.)
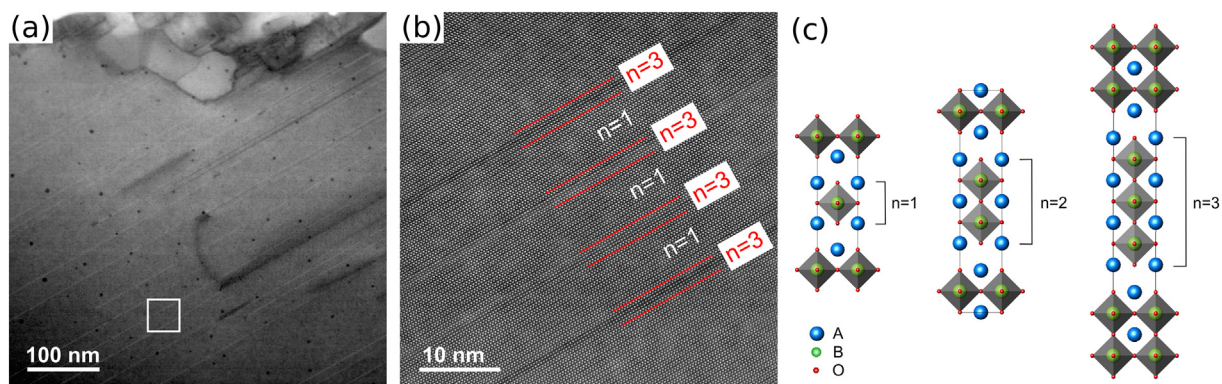


**Fig. 11.** (a) STEM HAADF image of the bulk area below a degraded surface region of LNO after degradation at 800 °C in 60% r.h., (b) HR-STEM HAADF image of the selected area with red lines indicating boundaries between the $La_2NiO_{4+\delta}$ main phase (n = 1) and $La_4Ni_3O_{10}$-type stacking faults and (c) crystal structure of the first three Ruddlesden-Popper phases $A_{n+1}B_nO_{3n+1}$ (n = 1, 2, 3). (For interpretation of the references to color in this figure legend, the reader is referred to the web version of this article.)

the degradation study for SEM-EDX analysis and XPS depth profiling.

While LNO exhibits good stability in the presence of Cr/Si-sources under dry conditions, a strong reduction of the oxygen exchange activity occurs when humidity is added to the gas stream, as evidenced by a decrease in $k_{chem}$ by a factor 25 over the course of 4000 h. HR-STEM imaging in combination with EDXS and EELS measurements was employed to identify the reaction phases formed on the sample surface after combined Cr/Si-poisoning. The main finding is a decomposition of the LNO surface layer into a predominantly oxide ion conducting phase $La_{9.33}(SiO_4)_6O_2$ and a predominantly electronic conducting compound $LaCr_{1-x}Ni_xO_3$, resulting in the observed decrease in oxygen surface exchange activity. Below the degraded surface zone, stacking faults consisting of higher order Ruddlesden-Popper phases are visible in HR-STEM images and are probably caused by La-segregation to the surface. It has been shown in this work that LNO is strongly affected by contaminants transported via the gas phase when treated with humidified test gases. Since this has also been reported for other SOFC cathode materials [6,27,50,51], it can be concluded that operation of such systems with pre-dried air or oxygen would significantly improve the long-term stability of cathodes.

## Acknowledgements

## References

[1] N. Shaigan, W. Qu, D.G. Ivey, W. Chen, J. Power Sources 195 (2010) 1529–1542.

[2] S. Frangini, A. Masci, S.J. McPhail, T. Soccio, F. Zaza, Mater. Chem. Phys. 144 (2014) 491–497.

[3] B.B. Ebbinghaus, Combust. Flame 93 (1993) 119–137.

[4] N. Schrödl, E. Bucher, A. Egger, P. Kreiml, C. Teichert, T. Höschen, W. Sitte, Solid State Ionics 276 (2015) 62–71.

[5] S.-N. Lee, A. Atkinson, J.A. Kilner, J. Electrochem. Soc. 160 (2013) F629–F635.

[6] E. Bucher, C. Gspan, T. Höschen, F. Hofer, W. Sitte, Solid State Ionics 299 (2017) 26–31.

[7] A. Kruk, A. Adamczyk, A. Gil, S. Kąc, J. Dąbek, M. Ziąbka, T. Brylewski, Thin Solid Films 590 (2015) 184–192.

[8] S.N. Hosseini, F. Karimzadeh, M.H. Enayati, N.M. Sammes, Solid State Ionics 289 (2016) 95–105.

[9] E. Konysheva, H. Penkalla, E. Wessel, J. Mertens, U. Seeling, L. Singheiser, K. Hilpert, J. Electrochem. Soc. 153 (2006) A765–A773.

[10] R. Trebbels, T. Markus, L. Singheiser, J. Fuel Cell Sci. Technol. 7 (2009) 011013(1-6).

[11] E. Bucher, C. Gspan, F. Hofer, W. Sitte, Solid State Ionics 230 (2013) 7–11.

[12] A.J. Schuler, Z. Wuillemin, A. Hessler-Wyser, J. Van Herle, Electrochem. Solid-State Lett. 14 (2011) B20–B22.

[13] T. Horita, H. Kishimoto, K. Yamaji, M.E. Brito, Y. Xiong, H. Yokokawa, Y. Hori, I. Miyachi, J. Power Sources 193 (2009) 194–198.

[14] N.S. Jacobson, E.J. Opila, D.L. Myers, E.H. Copland, J. Chem. Thermodyn. 37 (2005) 1130–1137.

[15] E.J. Opila, N.S. Jacobson, D.L. Myers, E.H. Copland, JOM 58 (2006) 22–28.

[16] S.P. Jiang, Y.D. Zhen, Solid State Ionics 179 (2008) 1459–1464.

[17] D. Oh, E. Armstrong, D. Jung, C. Kan, E. Wachsman, S.C. Singhal (Ed.), Proc. 11th Intern. Symp. Solid Oxide Fuel Cells (SOFC-XI), 2009, pp. 2871–2879 (Vienna, Austria).

[18] C.C. Wang, T. Becker, K. Chen, L. Zhao, B. Wei, S.P. Jiang, Electrochim. Acta 139 (2014) 173–179.

[19] N. Schrödl, E. Bucher, C. Gspan, A. Egger, C. Ganser, C. Teichert, F. Hofer, W. Sitte, Solid State Ionics 288 (2016) 14–21.

[20] I. Kaus, K. Wiik, M. Dahle, M. Brustad, S. Aasland, J. Eur. Ceram. Soc. 27 (2007) 4509–4514.

[21] E. Bucher, W. Sitte, F. Klauser, E. Bertel, Solid State Ionics 191 (2011) 61–67.

[22] E. Bucher, W. Sitte, F. Klauser, E. Bertel, Solid State Ionics 208 (2012) 43–51.

[23] S.-N. Lee, A. Atkinson, J. Kilner, ECS Trans. 57 (2013) 605–613.

[24] E. Boehm, J.M. Bassat, P. Dordor, F. Mauvy, J.C. Grenier, P. Stevens, Solid State Ionics 176 (2005) 2717–2725.

[25] F. Mauvy, C. Lalanne, J.M. Bassat, J.C. Grenier, H. Zhao, P. Dordor, P. Stevens, J. Eur. Ceram. Soc. 25 (2005) 2669–2672.

[26] A. Egger, W. Sitte, Solid State Ionics 258 (2014) 30–37.

[27] A. Egger, W. Sitte, F. Klauser, E. Bertel, J. Electrochem. Soc. 157 (2010) B1537–B1541.

[28] E. Bucher, BHM 156 (2011) 423–428.

[29] R. Behrisch, W. Eckstein, Sputtering by Particle Bombardment, Topics in Applied Physics, vol. 110, Springer, Berlin Heidelberg, 2007.

[30] P.A. Stadelmann, Ultramicroscopy 21 (1987) 131–145.

[31] Z. Li, R. Haugsrud, Solid State Ionics 206 (2012) 67–71.

[32] A. Egger, Rare Earth Nickelates as Cathodes for Solid Oxide Fuel Cells (PhD thesis), University of Leoben, Austria, Department of General, Analytical and Physical Chemistry, 2013.

[33] J. Druce, H. Téllez, M. Burriel, M.D. Sharp, L.J. Fawcett, S.N. Cook, D.S. McPhail, T. Ishihara, H.H. Brongersma, J.A. Kilner, Energy Environ. Sci. 7 (2014) 3593–3599.

[34] T. Akbay, A. Staykov, J. Druce, H. Tellez, T. Ishihara, J.A. Kilner, J. Mater. Chem. A 4 (2016) 13113–13124.

[35] G. Amow, P.S. Whitfield, I.J. Davidson, R.P. Hammond, C.N. Munnings, S.J. Skinner, Ceram. Int. 30 (2004) 1635–1639.

[36] J. Choisnet, N. Abadzhieva, P. Stefanov, D. Klissurski, J.M. Bassat, V. Rives, L. Minchev, J. Chem. Soc. Faraday Trans. 90 (1994) 1987–1991.

[37] NIST X-ray Photoelectron Spectroscopy Database, NIST Standard Reference Database Number 20, Gaithersburg MD, 20899, (2000), http://dx.doi.org/10.18434/T4T88K retrieved Feb. 2018.

[38] J.F. Weaver, H.A.E. Hagelin-Weaver, G.B. Hoflund, G.N. Salaita, Appl. Surf. Sci. 252 (2006) 7895–7903.

[39] S. Suzuki, M. Oku, Y. Waseda, Surf. Interface Anal. 25 (1997) 161–166.

[40] T.J. Chuang, C.R. Brundle, K. Wandelt, Thin Solid Films 53 (1978) 19–27.

[41] S. Suzuki, K. Sugiyama, Y. Waseda, J. Surf. Anal. 9 (2002) 455–458.

[42] S. Hashimoto, C. Tanaka, A. Murata, T. Sakurada, J. Surf. Anal. 13 (2006) 14–18.

[43] S. Nakayama, M. Sakamoto, J. Eur. Ceram. Soc. 18 (1998) 1413–1418.

[44] X.G. Cao, S.P. Jiang, Int. J. Hydrog. Energy 41 (2016) 1203–1212.

[45] D. Marrero-López, M.C. Martín-Sedeño, J. Peña-Martínez, J.C. Ruiz-Morales, P. Núñez, M.A.G. Aranda, J.R. Ramos-Barrado, J. Power Sources 195 (2010) 2496–2506.

[46] J. Yang, Acta Crystallogr. B 64 (2008) 281–286.

[47] T.S. Zhao, N. Meng (Eds.), Solid Oxide Fuel Cells: From Materials to System Modeling, RSC Publishing, Cambridge, UK, 2013.

[48] S.P. Jiang, L. Liu, K.P. Ong, P. Wu, J. Li, J. Pu, J. Power Sources 176 (2008) 82–89.

[49] N. Gauquelin, T.E. Weirich, M. Ceretti, W. Paulus, M. Schroeder, Monatsh. Chem. 140 (2009) 1095–1102.

[50] L. Zhao, J. Zhang, T. Becker, S.P. Jiang, J. Electrochem. Soc. 161 (2014) F687–F693.

[51] X. Chen, Y. Zhen, J. Li, S.P. Jiang, Int. J. Hydrog. Energy 35 (2010) 2477–2485.